# UNITED STATES AIR FORCE

# SUMMER RESEARCH PROGRAM -- 1991

# GRADUATE STUDENT RESEARCH PROGRAM (GSRP) REPORTS

## VOLUME 7

ADA 248770

## PHILLIPS LABORATORY
## CIVIL ENGINEERING LABORATORY


RESEARCH & DEVELOPMENT LABORATORIES

5800 Uplander Way

Culver City, CA 90230-6608

Program Director, RDL
Gary Moore

Program Manager, AFOSR
Lt. Col. Claude Cavender

Program Manager, RDL
Claude Baum

Program Administrator, RDL
Gwendolyn Smith





Submitted to:

AIR FORCE OFFICE OF SCIENTIFIC RESEARCH

Bolling Air Force Base

Washington, D.C.

December 1991

AFOSR-TR- 92 0174

AIR FORCE OFFICE OF SCIENTIFIC RESEARCH (AFSC)
NOTICE OF TRANSMITTAL TO DTIC
This technical report has been reviewed and is
approved for public release IAW AFR 190-12
Distribution is unlimited.
STINFO Program Manager

Approved for public release;

92 4 08 013

92-09032

# REPORT DOCUMENTATION PAGE

Form Approved
OMB No 0704-0188



| 1. AGENCY USE ONLY (Leave blank) | 2. REPORT DATE | 3. REPORT TYPE AND DATES COVERED |
|---|---|---|
| | 9 January 1992 | 30 Sep 90-30 Sep 91 |

**4. TITLE AND SUBTITLE**

1991 Graduate Student Research Program (GSRP)
Volumes 6-9 Vol. 7

**5. FUNDING NUMBERS**

F49620-90-C-0076

**6. AUTHOR(S)**

Mr Gary Moore

**7. PERFORMING ORGANIZATION NAME(S) AND ADDRESS(ES)**

Research Development Laboratories (RDL)
5800 Uplander Way
Culver City CA 90230-6608

**8. PERFORMING ORGANIZATION REPORT NUMBER**

AFOSR-TR- 92 0174

**9. SPONSORING/MONITORING AGENCY NAME(S) AND ADDRESS(ES)**

AFOSR/NI
Bldg 410
Bolling AFB DC 20332-6448
Lt Col V. Claude Cavender

**SPONSORING/MONITORING AGENCY REPORT NUMBER**

**11. SUPPLEMENTARY NOTES**

**12a. DISTRIBUTION/AVAILABILITY STATEMENT**

UNLIMITED

**12b. DISTRIBUTION CODE**

**13. ABSTRACT (Maximum 200 words)**

This program was started in 1982 as an adjunct to the SFRP. Its objectives are to permit graduate students to participate in research under the direction of a faculty member at an Air Force laboratory; stimulate professional association among graduate students, their supervising professors, and professional peers in the Air Force; to further research objectives of the Air Force; and to expose graduate students to potential thesis topics in areas of interest to the Air Force.

During the summer of 1991 142 graduate students performed research for 10 weeks at Air Force laboratories. Their reports were submitted to RDL and consolidated into this annual report.

**14. SUBJECT TERMS**

**15. NUMBER OF PAGES**

**16. PRICE CODE**

| 17. SECURITY CLASSIFICATION OF REPORT | 18. SECURITY CLASSIFICATION OF THIS PAGE | 19. SECURITY CLASSIFICATION OF ABSTRACT | 20. LIMITATION OF ABSTRACT |
|---|---|---|---|
| UNCLASSIFIED | UNCLASSIFIED | UNCLASSIFIED | UL |

# UNITED STATES AIR FORCE

# SUMMER RESEARCH PROGRAM – 1991

# GRADUATE STUDENT RESEARCH PROGRAM (GSRP) REPORTS

## VOLUME 7

## PHILLIPS LABORATORY
## CIVIL ENGINEERING LABORATORY


RESEARCH & DEVELOPMENT LABORATORIES

5800 Uplander Way

Culver City, CA 90230-6608



Program Director, RDL
Gary Moore

Program Manager, AFOSR
Lt. Col. Claude Cavender

Program Manager, RDL
Claude Baum

Program Administrator, RDL
Gwendolyn Smith





Submitted to:

AIR FORCE OFFICE OF SCIENTIFIC RESEARCH

Bolling Air Force Base

Washington, D.C.

December 1991

# PREFACE

Reports in this document are numbered consecutively beginning with number 1. Each report is paginated with the report number followed by consecutive page numbers, e.g., 1-1, 1-2, 1-3; 2-1, 2-2, 2-3.

This document is one of a set of 13 volumes describing the 1991 AFOSR Summer Research Program. The following volumes comprise the set:

| VOLUME | TITLE |
|---|---|
| 1 | Program Management Report |
| | *Summer Faculty Research Program (SFRP) Reports* |
| 2 | Armstrong Laboratory, Wilford Hall Medical Center |
| 3 | Phillips Laboratory, Civil Engineering Laboratory |
| 4 | Rome Laboratory, Arnold Engineering Development Center, Frank J. Seiler Research Laboratory |
| 5 | Wright Laboratory |
| | *Graduate Student Research Program (GSRP) Reports* |
| 6 | Armstrong Laboratory, Wilford Hall Medical Center |
| 7 | Phillips Laboratory, Civil Engineering Laboratory |
| 8 | Rome Laboratory, Arnold Engineering Development Center, Frank J. Seiler Research Laboratory |
| 9 | Wright Laboratory |
| | *High School Apprenticeship Program (HSAP) Reports* |
| 10 | Armstrong Laboratory |
| 11 | Phillips Laboratory, Civil Engineering Laboratory |
| 12 | Rome Laboratory, Arnold Engineering Development Center |
| 13 | Wright Laboratory |

# 1991 GRADUATE STUDENT RESEARCH REPORT

## Phillips Laboratory, Civil Engineering Laboratory

| Report Number | Report Title | Author |
|---|---|---|
| | *Phillips Laboratory (Cont.)* | |
| 16 | Assembly and Operation of the Working Fluid Experiment | John Crawford |
| 17 | An Experiment to Determine Angular Distribution of Backscattered Electrons as a Function of Energy & Material | Robert Davies |
| 18 | Mitigation Techniques to Minimize Damage Resulting from Explosive Loading on Structures Founded on Piles in Standard Soils | Nathan Dowden |
| 19 | Stimulated Emission Pump Spectroscopy of Iodine | Shawn Gaffney |
| 20 | Finite-Difference Time-Domain Solutions to Maxwell's Equations for Complex Geometries | Michael Governale |
| 21 | Parallelization of a Two Dimensional Vlasov Code | James Koga |
| 22 | Troubleshooting the Spectra Physics 5800 Tunable Diode Laser | John McCord |
| 23 | Implementing a Closed Loop Adaptive Optics System | Scott Peterson |
| 24 | Single Quantum Well, GRIN-SCH Semiconductor Optical Amplifier Gain Characterization | Keith Ver Steeg |
| 25 | Neural Network Programs Installed on the KHOROS Environment | Paul Wheeler |
| 26 | Integrating Neural Network Algorithms into the KHOROS Environment | Carla Williams |
| | *Civil Engineering Laboratory* | |
| | **Engineering & Services Center (ESC)** | |
| 27 | Stress Wave Transmission in Partially Saturated Soils | Kara Olen |
| 28 | Estimation of Contaminant Transport Parameters from Laboratory Studies: Batch and Column Techniques with Sorbing Organic Solutes | Dirk Young |

1991 USAF-RDL SUMMER FACULTY RESEARCH PROGRAM/

GRADUATE STUDENT RESEARCH PROGRAM

Sponsored by the

AIR FORCE OFFICE OF SCIENTIFIC RESEARCH

Conducted by the

Research and Development Laboratories, Inc.

FINAL REPORT

# RESEARCH IN VIBRATION IDENTIFICATION, ISOLATION, AND SUPPRESSION FOR LARGE SPACE STRUCTURES


| | |
|---|---|
| Prepared by: | James Michael Argento<br>Robert Alan Carlin<br>Marco David D'Amore<br>Ephrahim Garcia, Ph.D. |
| Academic Rank: | Assistant Professor |
| Department and | Department of Mechanical Engineering |
| University: | Vanderbilt University, Nashville, TN |
| Research Location: | Edwards Air Force Base<br>Phillips Laboratory, ASTREX division<br>Edwards AFB, Lancaster, California |
| Date: | August 23, 1991 |

# I. INTRODUCTION

The loads and vibrations that impinge upon a payload during launch have historically been the focus of structural and design engineers. My summer research focused on one particular Air Force satellite, and the possibility of reducing the loads from the two launch vehicles currently used: the Titan IV, and the Space Shuttle. The first step in this ongoing project was to learn about the structure of this satellite and perform an eigenanalysis using Nastran, NASA's Structural Analysis program. The next step involves a parametric study of the passive and/or active system that would be required to reduce said loads. It is assumed that this vibration isolator would be positioned between the satellite and the Inertial Upper Stage (IUS) upon which the satellite sits during launch in both vehicles.

Every satellite and its own substructures must be designed in such a way that they can withstand "launch cycle loads", and be able to perform their duties once they reach orbit. A considerable savings could be gained if these loads were reduced by some means. The savings are numerous and could include a decreased mass for the main load bearing members in the satellite, and in turn, an increased allowable mass for other components, such as electronics and propellant for attitude rockets. Another benefit is longer satellite life, since more propellant could mean a greater number of attitude adjustments while on orbit. The electronics on board might also exhibit longer life and have an even greater endurance, since the dynamic loading on the circuitry during launch would be reduced. With this in mind, the investigation into a vibration isolator for satellite sytems has great potential.

## DISCUSSION

Modeling The satellite chosen for this study is a geosynchronous Air Force satellite (Figure 1.1). Several Nastran models of this satellite have been analyzed in the past to obtain a reasonable structural analysis and mode shapes. The models used initially in this investigation had on the order of 18,000 degrees of freedom (DOFs), and were used to obtain mode shapes and a general feel for the dynamics of the satellite and its components. Once this was accomplished, it was determined that much simpler models would suffice, since the scope of this investigation involves only a parametric study of the vibration isolator. In the process, we are aiming to obtain similar responses to that given by the more complex models.

One of these simpler models was designed using MSC/PAL2, another finite element analysis package, and has approximately 150 DOFs in its current configuration (Figure 1.2). This model consists of the main load bearing members and mass simulators at the top, using very similar dimensions to those used in the Nastran models. Other components have obviously been left out of this model, but we have already obtained similar mode shapes to those in the 18,000 DOFs models for the components modelled, and continue to work on the details of this model.

Another modelling case being studied is a simple 2-D, undamped, lumped parameter model (Figure 1.3). This four DOF model and its equations of motion can be used to study the trends and tradeoffs of the isolator in a general way. The equivalent mass, stiffness and inertia of the modelled components (i.e. $m_1 J_1$, $k_1$) can be adjusted until they match those exhibited in previous models. The trends exhibited by the isolator can be studied in the same way, by adjusting $k_2$. The equation of motion, in matrix form, is:

$$M \ddot{x} + K x = B y$$

where

$$M = \begin{bmatrix} m_1 + 4J_1/d_1^2 & m_1 - 4J_1/d_1^2 & 0 & 0 \\ m_1 - 4J_1/d_1^2 & m_1 + 4J_1/d_1^2 & 0 & 0 \\ 0 & 0 & m_2 + 4J_2/d_2^2 & m_2 - 4J_2/d_2^2 \\ 0 & 0 & m_2 - 4J_2/d_2^2 & m_2 + 4J_2/d_2^2 \end{bmatrix}$$

$$K = \begin{bmatrix} 4k_1 & 0 & -4k_1 & 0 \\ 0 & 4k1 & 0 & -4k_1 \\ -4k_1 & 0 & 4(k_1+k_2) & 0 \\ 0 & 4k_1 & 0 & 4(k_1+k_3) \end{bmatrix}$$

$$B = \begin{bmatrix} 0 & 0 \\ 0 & 0 \\ 4k_3 & 0 \\ 0 & 4k_3 \end{bmatrix}$$

Damping terms (i.e. $c_1$ and $c_2$) will be added in future studies, and in turn, can be varied to study trends in the isolator design.

Excitation The load cycle of the launch vehicle is of key importance in this study. We will be using an internal report published by the Aerospace Corporation, which contains data obtained from the Titan IV booster during several previous missions. While much of this data is not intended for external release, we have obtained permission to use it and will discuss only that information which is deemed appropriate for a report such as this. There are several flight event times during a Titan IV launch that involve significant transients in the loading induced onto the payload. These are liftoff, stage I ignition, solid rocket motor separation, payload fairing separation, stage I shutdown, stage II ignition and stage II shutdown. While these events cover short periods of time during the launch cycle, they are the most important time periods, since large magnitude changes in the loading forces occur. The largest strains, and thus, the largest deformations will also occur at these times. The other time periods are relatively sedentary, and are probably unimportant in our study. The data obtained includes accelerations (i.e. g forces) in the principal directions of roll, pitch and yaw as recorded by several accelerometers at locations close to the payload compartment. This information will be used when we begin to evaluate the parameters of the isolation system.

Passive Control As mentioned earlier, the most significant elements of the launch load cycle are a select few time periods during which transients play an important role. In our passive control considerations, we will be looking to optimize our isolator design with the following considerations: designing the isolator strictly for these transients vs. designing the isolator for the transients *and* the time periods in between, during which the excitation is more sedentary. The available data indicates that the excitation forces during the sedentary periods are in a higher frequency range than the transients, but their amplitude is of a much smaller magnitude, making these secondary loads. While both cases will be considered in our optimization, the inclusion of the sedentary loads will probably prove unneccessary. The optimization process will involve tuning our system parameters (i.e. $k_s$ and $c_s$, shown in Figure 1.4) until we achieve an overall minimum of displacement ($x_s$) of the bottom of the satellite.

Active Control A greater isolator performance could most likely be achieved by including active control. A feedback control loop would allow for an on-line "active" isolator, and would prove more robust for this satellite suspension system. By generating a force $F_G$ (see Figure 1.4), such that

$$F_G = -k_G \dot{x}_s$$

that is, a force proportional to the velocity of the satellite, we could greatly reduce the excitation forces being transmitted to the satellite. Once the active control is properly tuned, the effects on the passive control would also be analyzed.

## RESULTS

Since this project will continue for approximately one more year, the results will not be complete for some time. As of mid-August however, we have obtained results from the extensive Nastran model, such as natural frequencies and mode shapes for 0 to 300 Hz. We are examining the Nastran results for mode shapes that may prove significant in determining which parts of the satellite might violate tolerances within the payload fairing shroud during launch. We have found two modes (14.8 and 30.4 Hz) in which the equipment compartment at the top of the satellite displaces as a rigid body with the supporting trusses in a swaying motion. Other modes involve the displacement of the main solar panel, configured as a cylinder around the main load bearing trusses of the satellite. The displacements of the solar paddles at the base of the satellite, which are stowed upward during launch, are also of concern. The current rigid assembly used as the interface between the satellite and the launch vehicle, has not allowed the satellite to violate any of the payload fairing tolerances, and the isolation system we intend to define during this investigation must conform in the same way. Information on the allowable deflections within the payload fairing has been obtained and will be used as a guide for our research.

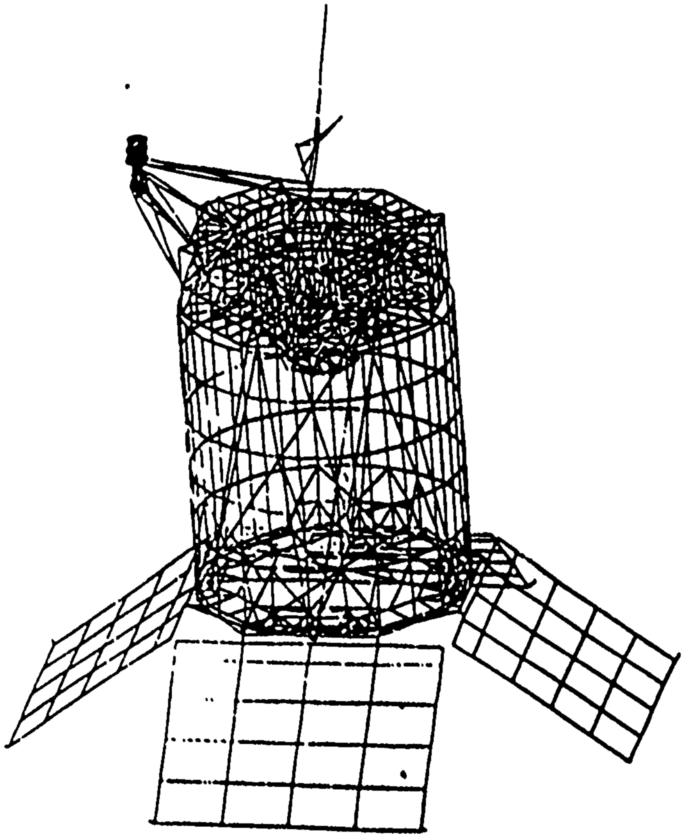

Figure 1.1
Geosynchronous Air Force Satellite, Nastran Model

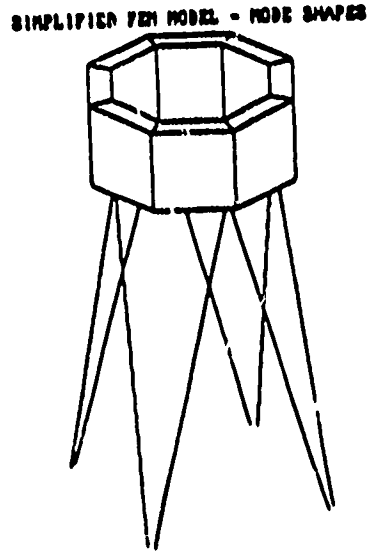


Figure 1.2
MSC/PAL2 FEM Model

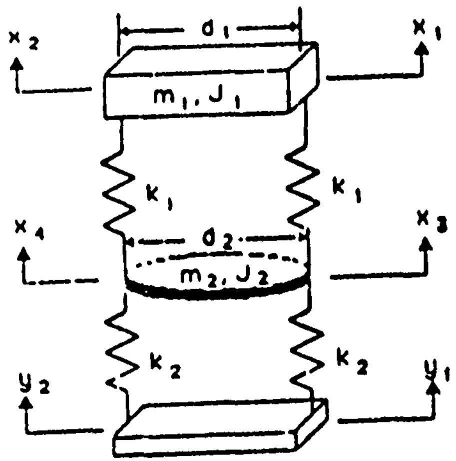


**Figure 1.3**
**2-Dimensional, 4 DOF**
**lumped parameter model**

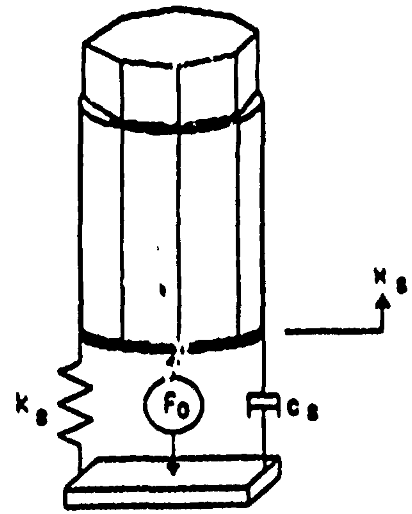


**Figure 1.4**
**Schematic of satellite and passive/active**
**vibration isolator**

## II. INTRODUCTION

The field of large space structures is very diverse. It encompasses modelling, testing, fabrication and operation of extremely complex mechanisms. Before anything can be built, however, extensive testing must be done to ensure that no unforeseen problems occur. To this end, modal analysis is used to determine a particular structure's natural frequencies of vibration, damping ratios, and mode shapes. However, each test requires that enormous amounts of data be collected in order to obtain a reasonable identification of these properties.

In order to reduce the amount of space necessary to store the tests, as well as save time in processing the data, the technique of data compression has been introduced. Although the idea of data compression is not new, it has not previously been used in parameter identification. The basic premise behind data compression (DC) is that data is eliminated from the original signal, thereby saving a combination of volume, time, and/or bandwidth (see section b).

Preliminary studies have shown that this application can be very useful in both ground tests and on-orbit identification. Telemetry data is, by necessity, extremely redundant; partial compression will not only save disk space (allowing more tests for less initial monetary outlay) but will not be much of a hindrance in analysis.

## DISCUSSION

Data Compression: Background The definition of data compression states that it is simply a reduction in the amount of storage space needed to save a given data set. This data can be in several forms. It can be physical, such as the volume that data takes up on a computer's hard drive; an interval of time, such as the time needed to transmit the data; or a part of the electromagnetic spectrum, like the bandwidth necessary to transmit the data. These three forms are interrelated, using the following analogy:

$$\text{Volume} = f(\text{time} \times \text{bandwidth})$$

Therefore, a reduction in volume affects either the transmission time or bandwidth. The parameter of interest - in our case, the volume - determines where the compression operation is performed in the system.

Data compression is performed for one of two major reasons. The first reason is to bypass a design constraint, such as limited storage space; the second is to obtain a significant savings in the design of a new system. In the performance aspect, data compression methods can be grouped into two 'classes' - reversible (called *redundancy reduction*) and irreversible (called *entropy reduction*). Irreversible techniques deal with the entropy of a system, where the entropy is defined as the average information. An example of an irreversible compression algorithm is the use of a threshold when obtaining responses of a system. In this case, the data is only transmitted when a particular sample exceeds the threshold. If very few values cross that level, a large amount of compression is achieved, but the original signal can't be reconstructed. Reversible techniques, on the other hand, allow for the restoration of the original data by removing only that data which is redundant. An example of this method is the elimination of repetitive data - for example, a square wave. In a redundancy-reduction operation, only the significant points - such as the 'corners' of the square wave - are retained, along with their relative positions in the original signal. [1]

Algorithm Background For our studies, a redundancy reduction algorithm was used to obtain significant amounts of compression of frequency response functions. This algorithm was implemented using a PC-based matrix manipulation program called MATLAB. MATLAB was chosen for both its comprehension and its functionality. A block diagram of the steps used in the modal analysis procedure may be seen in Figure 2.1. Time history responses are fast Fourier transformed into transfer functions and then averaged. This averaged transfer function (TF) can then either be analyzed (the right 'fork' of Figure 2.1) or it can first be compressed and then analyzed. Figure 2.2 shows the steps taken in the compression and analysis of the data. The TF is first compressed, and the compression ratio is calculated. The compression ratio, CR, is defined as:

$$CR = \frac{\text{number of data points before compression}}{\text{number of data points after compression}}$$

This means that for a CR of 30, only 1 data point in 30 is saved, and the compressed TF has only $\frac{1}{30}$th of the spectral lines of the original TF. The data is next decompressed using a new algorithm based on the compression algorithm. At this point, the data is analyzed using one of two methods. The first method requires that each 'peak' in the TF be separately identified and run through a SDOF Nyquist circle fit algorithm to obtain natural frequencies and damping ratios. The other method necessitates using an inverse fast Fourier transform to return the data to a time history format and then entering it into the Eigensystem Realization Algorithm (ERA).

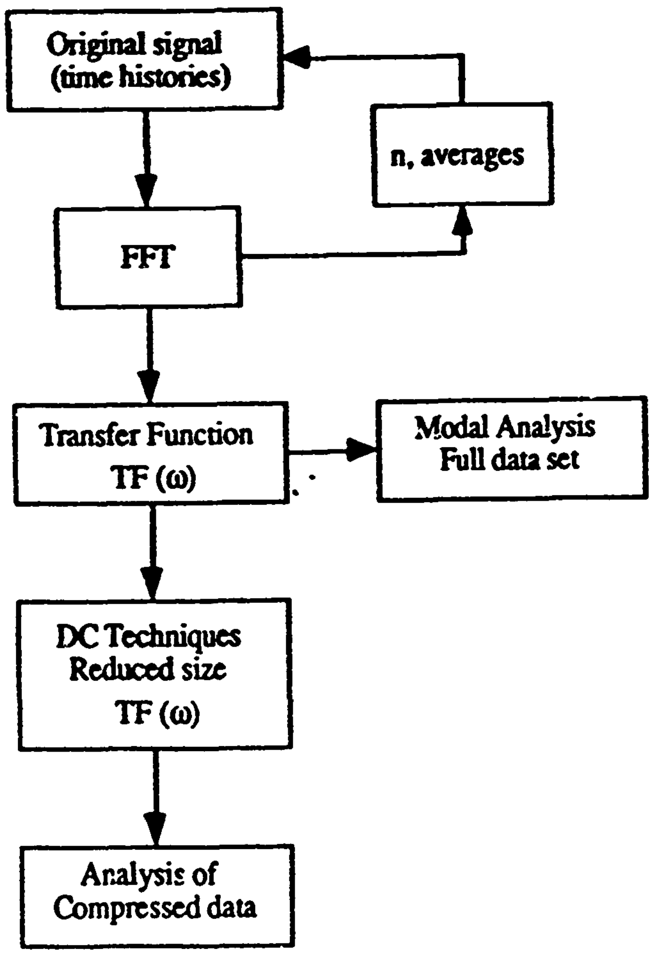

Figure 2.1. Steps used in the modal analysis procedure.

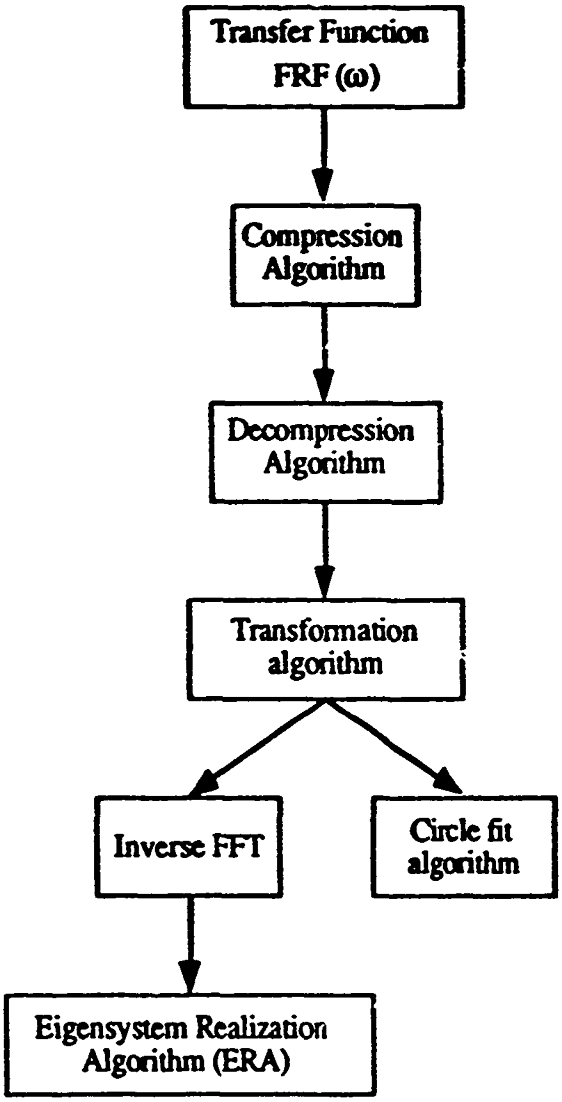


Figure 2.2. Steps used in the compressed data analysis procedure.

Initially, several frequency response functions were modelled in MATLAB, for both single- and multiple-degree-of-freedom (SDOF and MDOF, respectively) cases. Modal models were chosen for ease of reliability comparisons. The single degree of freedom test was done using a TF with a natural frequency of 10 Hz and a damping ratio of 0.02. Compression ratio values between 4 and 64 were obtained, and the results may be shown in Table 2.1, below. Please note that the actual identified value of the damping was determined to be 0.0195, and that the % errors are measured with respect to this value.

| CR, comp. ratio | ω, decompressed (Hz) | ω, % error | ζ, decompressed (% critical) | ζ, % error |
|---|---|---|---|---|
| 4 | 10.000 | 0.00 | 1.95 | 0.00 |
| 8 | 10.000 | 0.00 | 1.95 | 0.00 |
| 22 | 10.000 | 0.00 | 2.15 | 10.26 |
| 32 | 10.039 | 0.39 | 2.33 | 19.49 |
| 64 | 9.961 | 0.39 | 3.53 | 81.03 |

Table 2.1. Analysis of a SDOF model with respect to varying compression ratios.

Note that for large compression ratios, the modal parameter errors are relatively small. The maximum error obtained in the frequency determination is less that 0.5% at all times. This is not the case for the errors induced in the damping term. However, for compression ratios as high as 32, the error was only roughly 20%.

The multiple degree of freedom test was done with a TF which had natural frequencies of 1, 2, 10, and 16 Hz with $\zeta$=0.02 for modes 1 and 2, and $\zeta$=0.01 for modes 3 and 4. Results were obtained only for a compression ratio of approximately 4.0 and may be seen in Table 2.2.

| Mode | Natural frequency, Hz | % Error | Damping ratio | % Error |
|---|---|---|---|---|
| 1 | 1.0254 | 2.54 | 0.0238 | 19.00 |
| 2 | 2.0215 | 1.08 | 0.0217 | 8.50 |
| 3 | 10.0195 | 0.20 | 0.0112 | 12.00 |
| 4 | 16.0156 | 0.10 | 0.0101 | 1.00 |

Table 2.2. Identified natural frequencies and damping ratios, MDOF system, CR ≈ 4.0.

Astrex background The Phillips Laboratory at Edwards AFB is equipped with a one-half-scale model of a typical SDI satellite, shown in Figure 2.3. This model is called the ASTREX - Advanced Space Structures Technology Research Experiment. In order to prove the feasibility of the data compression technique in modal analysis, testing was performed with the help of the technicians at Edwards. The CDAC - Computer-controlled

Data Acquisition system - was used in conjunction with another matrix manipulation program called $MATRIX_x$ to obtain time history data for several positions on the model. These time histories were fast Fourier transformed and averaged to create usable transfer functions. At this time, analysis of these transfer functions has begun, but it is only preliminary. Initial analysis of one member from 0-40 Hz has shown 19 modes of vibration in this small frequency range. ERA was used to obtain a stability plot for the uncompressed data; this can be seen in Figure 2.4. Figure 2.5 shows the stability plot obtained by ERA for the compressed data, and Figure 2.6 shows a comparison of both stability plots. It can be seen from Figure 2.6 that the results obtained after compression are almost identical to those obtained before compression. This is a very good indication that the compression technique is reliable.

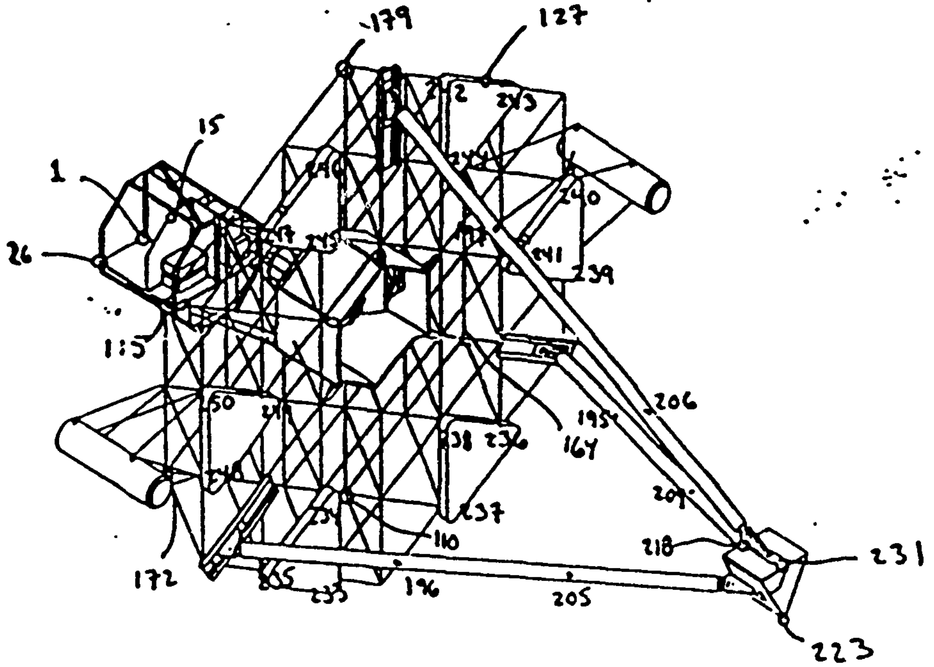


Figure 2.3. Diagram of the ASTREX test structure.

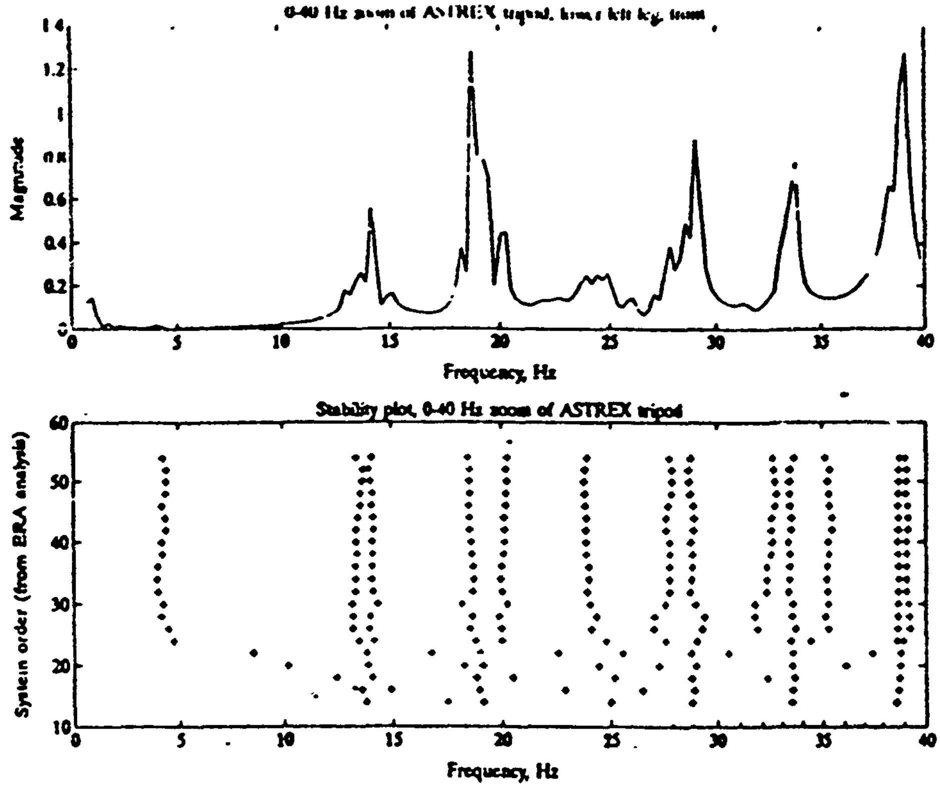


Figure 2.4. ERA stability plot, ASTREX structure,uncompressed data, 0-40 Hz.

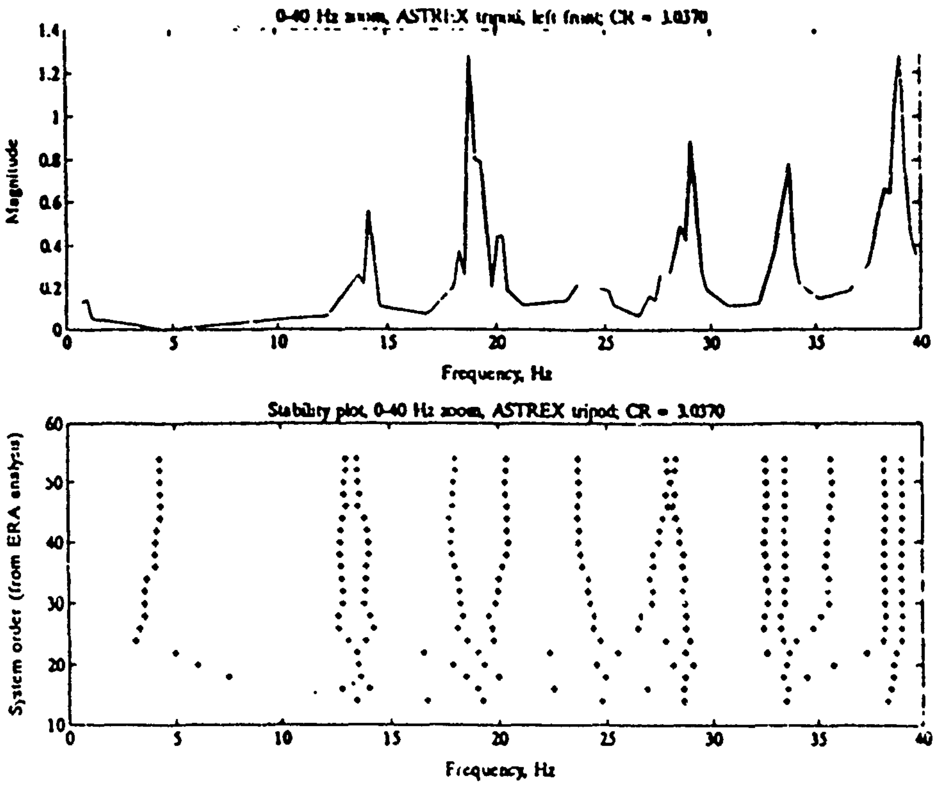


Figure 2.5. ERA stability plot, compressed data, ASTREX structure, 0-40 Hz.

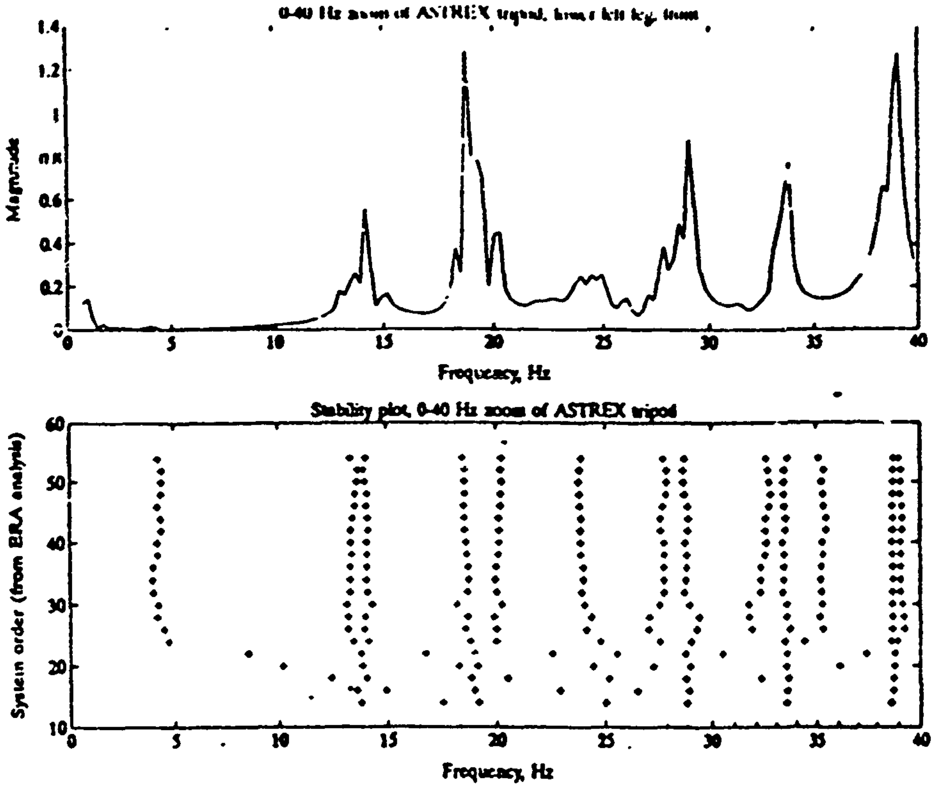


Figure 2.4. ERA stability plot, ASTREX structure,uncompressed data, 0-40 Hz.

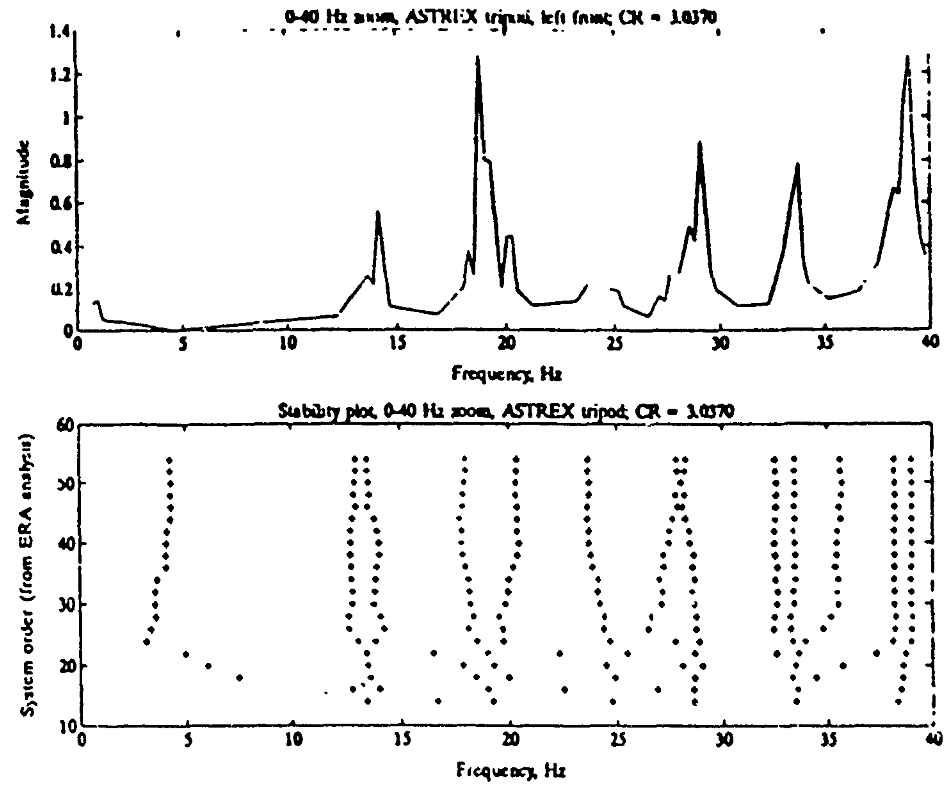


Figure 2.5. ERA stability plot, compressed data, ASTREX structure, 0-40 Hz.

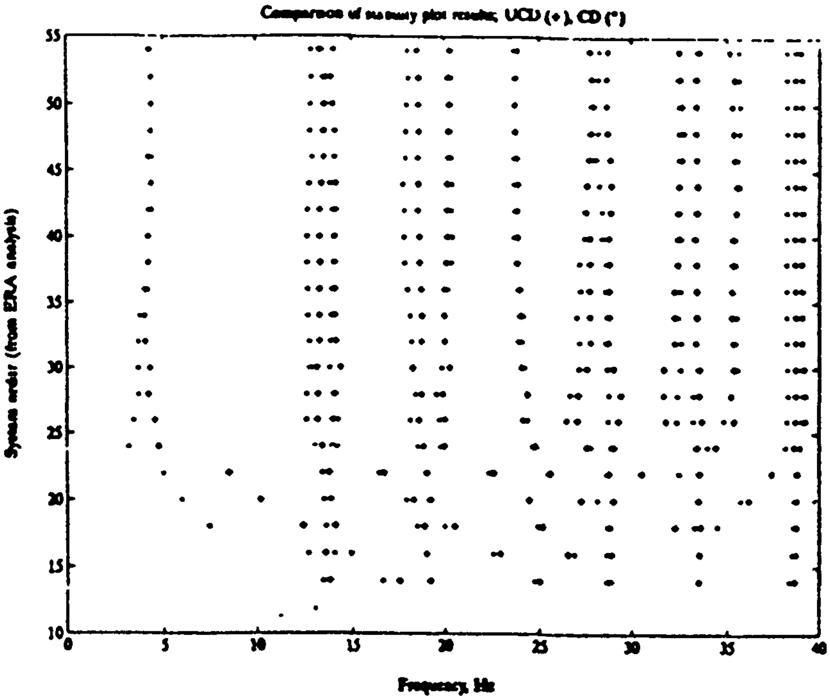


Figure 2.6. Comparison of stability plots, compressed and uncompressed data.

## CONCLUSIONS

It can be seen from the data presented here that data compression in modal analysis is a viable area of research. The identification of modal parameters is robust with respect to data compression. Also, a significant savings in volume, as well as time, is feasible with the use of certain compression methods. Potential applications for this theory are too numerous to mention, but include the topics of on-orbit testing, telemetry, and health monitoring.

## REFERENCES

[1] Lynch, Thomas J. Data Compression: Techniques and Applications. New York: Van Nostrand Reinhold, 1985.

[2] Ewins. D.J. Modal Testing: Theory and Practice. Letchworth, England: Research Studies Press Ltd./Brüel & Kjaer, 1986.

[3] Garcia, E, "System Identification for the Microcomputer Environment," M.S. Thesis, Department of Mechanical and Aerospace Engineering, State University of New York at Buffalo, Buffalo, New York 14260.

[4] Juang, J.-N. and Pappa, R.S., "An Eigensystem Realization Algorithm for Modal Parameter Identification and Model Reduction," AIAA Journal of Guidance, Control, and Dynamics, Vol. 8, No. 5, Sept.-Oct. 1985, pp. 620-627.

## III. INTRODUCTION

A very critical area is the suppression of vibrations in spacecraft with long flexible appendages. Many outside stimuli are responsible for such motions, such as dynamics induced by thermal gradients brought about by solar heating, solar winds, and or the vibrations induced by a slewing maneuver. The problems induced by such motions tend to wreak havoc with such systems used for signal transmission performed by antenna arrays. Not only can these dynamics cause accuracy problems in the performance of such systems but also high amplitude motions may prove fatal to these systems.

The ASTREX Facility (Advanced Structures Technology Research Experiment) is a structure specifically designed to investigate the aforementioned areas of research. The motivation of this study is to research and design a control algorithm for this structure using the existing actuators. The goal of these controllers will be to suppress vibrations using the reaction wheel and gas-jet thrusters. The induced slewing load will be a model which may prove important when using the thrusters for vibration suppression. The thrust of the vibration suppression scheme is to reduce the line of sight (LOS) error of the structure due to a disturbance response.

## DISCUSSION

Modeling In order to investigate the ASTREX and develop a control model, a finite element model of the structure must be developed. A full order model consisting of 2394 degrees of freedom (DOFs) was constructed using Cosmic NASTRAN. A diagram of the undeformed model can be seen in Fig. 3.1 at the end of this section. This diagram was produced via NASTRAN.

It is evident that this structure, as stated earlier, needs a very complicated FEM model to accurately perform a dynamic analysis of the structure and thus is the reason for having 399 nodal locations. However, while this makes for a very precise model to predict the experimental modes of the structure, the mass and stiffness matrices extracted from an analysis are unmanageable and not to be considered for use in the control design. Therefore the structural model must be reduced enough so that they can be manipulated into a state space model. The idea is to take the large mass and stiffness matrices and reduce them while still having them retain the ability to produce the lower modes given by the full order model or as close to these modes as possible .

The method of reduction chosen was Guyan reduction. This a very well known and common reduction method which was easily incorporated into the NASTRAN model via the ASET command. The way the ASET card works is that the node location that you desire to keep is entered in along with the retained DOFs associated with that node. The key to using the Guyan reduction is to choose the nodes and the corresponding DOFs at those points to render a good approximation to the full order model. Many trial runs were done to check which nodal locations should be kept with regards to the sensitivity of the model. The ultimate goal was to get a very accurate model with very small order, not forgetting that the line of sight investigation (LOS) is the main goal of this study. Therefore, the main nodes to be kept are those with which pointing is an issue, such as the secondary reflector, trackers, and positions on the primary structure where mirrors would be located.

| MODE NUMBER | FULL ORDER 2394 | 958 | 472 | 197 | 58 |
|---|---|---|---|---|---|
| 1 | 3.519 | 3.521 | 3.529 | 3.529 | 3.528 |
| 2 | 5.146 | 5.154 | 5.156 | 5.156 | 5.233 |
| 3 | 13.014 | 13.135 | 13.150 | 13.155 | 13.549 |
| 4 | 13.178 | 13.273 | 13.292 | 13.298 | 13.675 |
| 5 | 16.501 | 17.028 | 17.234 | 17.239 | 18.643 |
| 6 | 18.277 | 18.979 | 19.224 | 19.246 | 19.252 |
| 7 | 19.188 | 19.222 | 19.330 | 19.352 | 19.732 |
| 8 | 20.200 | 20.304 | 20.406 | 20.428 | 21.282 |
| 9 | 25.347 | 27.167 | 27.544 | 27.587 | 29.503 |
| 10 | 26.765 | 28.626 | 29.256 | 29.348 | 31.177 |

TABLE 3.1 Frequencies for Guyan reduced models

The lower modes, not including the rigid body pedestal modes, are tripod modes (motion between the secondary and the primary via the tripod configuration). It is for these reasons that it is felt that much time and effort should be concentrated in controlling these modes in order to control the LOS between the secondary and primary structures. For verification of this fact, refer to Table 3.1 and compare the modes of the model with 472 DOFs to the model with 197 DOFs. The model with 472 DOFs contains all primary and tripod nodes that the 197 DOF model contains. However the 472 DOF model contains all DOFs for the tertiary structure as well as the components connecting the tertiary to the hub. It is readily discerned from scrutinizing these two reductions that the large difference in DOFs had insignificant effect on the model to warrant the inclusion of these nodes in the model.

The 958 DOF model is an attempt to see that the inclusion of all nodes and corresponding DOFs for the primary had a significant effect on the lower eigenvalues. The reason for this model was to see whether or not perhaps a loss of mass in the reduced mass matrix caused an error when the eigenanalysis was performed using the new reduced mass and stiffness matrices. As is shown in Table 3.1,this run has little difference than the other runs at 472 and 197.

These previous examples of reductions were never considered to be a feasible model from the onset because of the large order matrices they would produce. They were simply done, as expressed earlier, for verification of the pertinent nodes to render a good model. Having done these studies, I was able to come up with a small but good approximation to the full order model of order 58. The model, as shown from Table 3.1, has a model that is as good, if not better than, the models of several magnitudes larger. The reason this final model was developed is to approximate the induced slewing loads in the structure, as well as the applied actuator loads, in order to arrive at a high fidelity model.

It should be pointed out that by no means does the author propose to develop a control using a 58 by 58 matrix or a 116 by 116 state matrix. Via the incorporation of damping from experimental data, the model of the system will be transformed into a modal model. This will also allow the model to be reduced even further through a modal reduction method in which the desired modes are kept along with their corresponding eigenvectors (mode shapes). This will finally allow manageability for a control study. This is also due to the fact that damping information is only available for the modes between 0 to 140 Hz.

Once the desired mass(M) and stiffness(K) matrices were extracted from NASTRAN a small program was written to transform them into a format that was readable by MATLAB. Doing an eigenanalysis

$$(M^{-1}K-\lambda I)\upsilon=0$$

the eigenvalues($\lambda$) and eigenvectors (u) were calculated, thus producing a diagonal matrix of eigenvalues ($\mathrm{diag}(\omega^2{}_i)$) and also a matrix of eigenvectors, $U=(u_i)$. Using this eigenvector matrix, a mass weighted similarity transformation matrix ($S_m = M^{-1/2}U$) was formed which has the following properties.

$$S^T{}_m M S_m = I$$

$$S^T{}_m D S_m = \mathrm{diag}(2\zeta\omega)$$

$$S^T{}_m K S_m = \mathrm{diag}(\omega^2{}_i)$$

The D is the damping matrix and the $\zeta$ is damping ratio. From the methods expressed in Section II, the damping ratios may be found and by using the second equation above, the damping matrix may be formulated using this transformation matrix. Knowing what eigenvector is associated with what mode and what the order of M and K was as determined by NASTRAN, the second order system can be produced and then ultimately transformed into state space form.

$$\dot{x} = \begin{bmatrix} 0 & I \\ -M^{-1}K & -M^{-1}D \end{bmatrix} x + \begin{bmatrix} 0 \\ M^{-1} \end{bmatrix} f$$

## RESULTS

In addition to the work mentioned above, a model of the torque wheel was produced via SIMULAB and a model of the thruster is presently under development. These models will be used to develop a control scheme by using a comparison of Linear Velocity Feedback (LVF) and Linear Quadratic Gaussian (LQG) methods. The ultimate goal is to suppress the lower modes of vibration, which predominantly affect the tripod, in order to improve line of sight accuracy. Also, the effects of slewing induced vibrations will be considered in this study Due to space considerations, the aforementioned material has not been included.

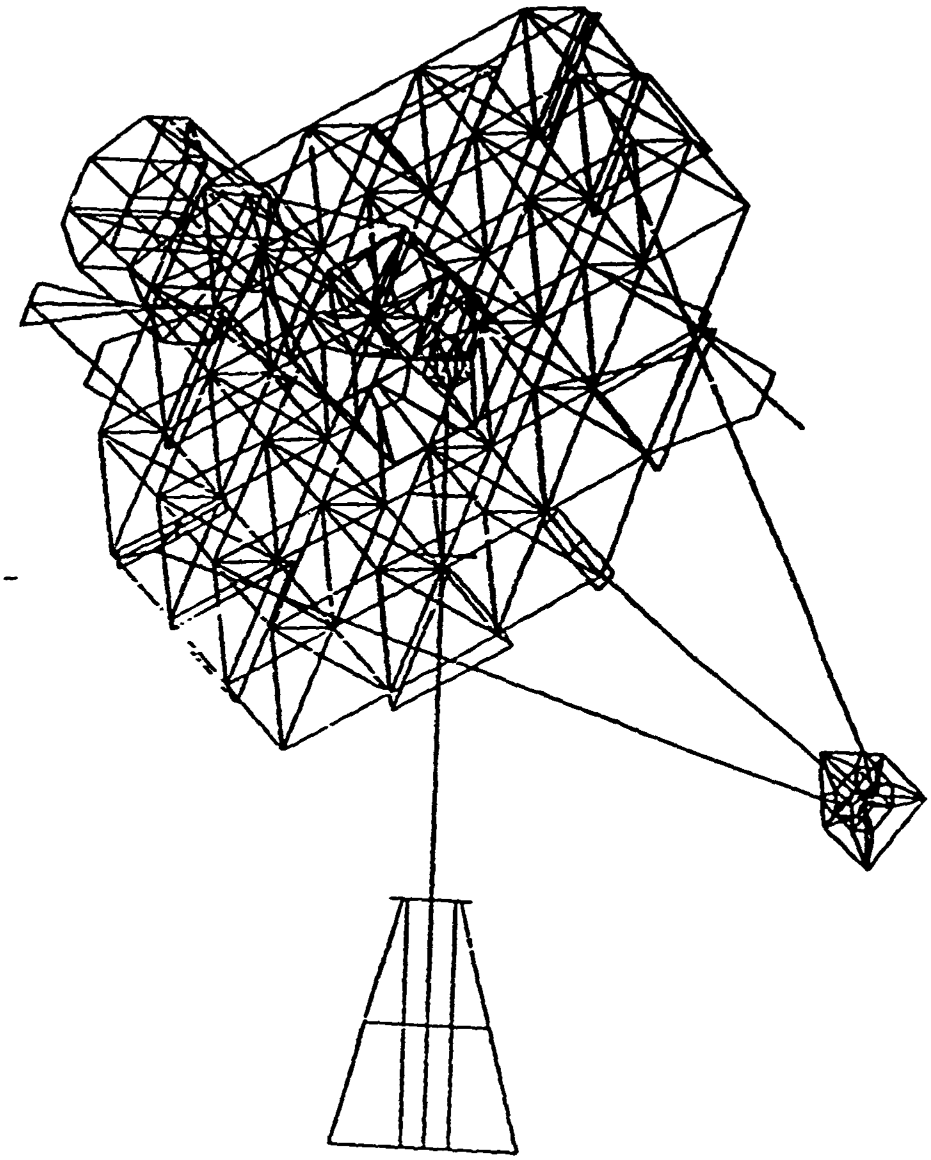

Figure 3.1. Full order finite element model of the ASTREX structure.

# RESEARCH IN VIBRATION IDENTIFICATION, ISOLATION, AND SUPPRESSION FOR LARGE SPACE STRUCTURES

BY

Robert A. Carlin
Marco D. D'Amore
James M. Argento
Ephrahim Garcia, Ph.D

**SEE: JAMES M. ARGENTO**

# RESEARCH IN VIBRATION IDENTIFICATION, ISOLATION, AND SUPPRESSION FOR LARGE SPACE STRUCTURES

BY

Marco D. D'Amore
Robert A. Carlin
James M. Argento
Ephrahim Garcia, Ph.D

**SEE: JAMES M. ARGENTO**

# XAFS Analysis of Propellant Materials
## RDL Final Report

by
Guy A. DeRose
employee number 398

Summer, 1991

## ABSTRACT

The technique of X-ray Absorption Fine Structure (XAFS) spectroscopy was used to determine local structure and short range order at the Cl K-edge in rocket fuel oxidizers - namely ammonium perchlorate (AP) - , oxidizer/binder systems, and new polymer materials of vital interest to the Air Force. Data was collected at the National Synchrotron Light Source, Brookhaven National Laboratory and analyzed at the Phillips Laboratory, Edwards Air Force Base. This Faculty/Graduate Student Summer research Project also resulted in the acquisition, by the Air Force, of state-of-the-art analysis programs for reducing EXAFS (Extended XAFS) data to a reportable form. Theory of XAFS and a detailed description of the analysis procedure is presented herein, along with limitations of the single-scattering formalism as applied to near-edge structure and suggestions for future work.

## INTRODUCTION

Extended X-ray Absorption Fine Structure (EXAFS) spectroscopy, the modulation of the absorption coefficient above an absorption edge, has found wide ranging application in solving structural problems in recent years. EXAFS spectroscopy is a very useful tool for studying complex or dilute systems whose structures cannot be determined by conventional x-ray diffraction techniques.

Post-absorption edge fine structure was first observed by Kronig[1] on 1931, but it wasn't until the 1970's that the short range order theory was fully worked out.[2,3] These new theoretical developments, coupled with the emergence of dedicated synchrotron radiation sources for x-ray absorption spectroscopies in general, have led to the transformation of EXAFS from a laboratory curiosity available to a very small group of scientists, to a widely available, quantitative tool for structural investigation.

This technique is well suited for studying the structure of rocket fuel oxidizers such as ammonium perchlorate in various local environments and new advanced polymer component materials currently of interest to the Air Force, as a thorough, quantitative understanding of the chlorine-local structure of these complex systems is required for consistent device fabrication.

# THEORY OF EXAFS

The oscillatory structure of the absorption coefficient is attributed to the scattering of the photoelectron emitted due to the absorption of the incident x-ray by the atoms surrounding the absorbing atom. By comparing experimental data with theory and/or model compounds, information about the local (~5Å) structure of a material can be obtained with a high degree of accuracy (~0.01Å). By comparing the structures obtained for the various binders in the oxidizer/binder system, a very detailed body of information about the oxidizer's local structure can be constructed.

It has been determined[3,4] that for energies sufficiently high above the absorption edge (≥ 50eV) the single scattering approximation adequately describes the structure. An additional simplification also manifests itself in this region, namely the plane wave approximation. The EXAFS oscillations, following the single-scattering and outgoing plane wave approaches, are given for K-edges as a function of photoelectron wave number k by[4]

$$\chi(k)=\sum_j -\frac{N_j}{kR_j^2}|f_j(k,\pi)|\, e^{-2\sigma^2k^2}e^{\frac{-2R_j}{\lambda}}\sin(2kR_j+\delta_j(k)) \tag{1}$$

where $N_j$ is the number of equivalent scatterers of type j a mean distance $R_j$ from the absorber, $f_j(k,\pi)$ is the (energy dependent) backscattering function, $e^{-2\sigma^2k^2}$ is a Debye-Waller term describing thermal disorder, $e^{-2R/\lambda}$ is a term which accounts for inelastic scattering effects over the photoelectron mean free path $\lambda$, and $\sin(2kR_j+\delta_j(k))$ is the interference term, where $\delta_j(k)$ is the (energy dependent) phase shift. The photoelectron wave number, k, is given by

$$k=\left(\frac{2m}{\hbar^2}(E-E_0)\right)^{\frac{1}{2}} \tag{2}$$

where m is the mass of the electron, $\hbar$ is Planck's Constant divided by $2\pi$, E is the incident x-ray energy, and $E_0$ is the edge energy.

## EXPERIMENTAL PROCEDURE

As the experimental setup, sample preparation, data collection, and associated complexities are described in detail in the report of the faculty half of this faculty/graduate student team, namely Professor R. W. Hoffman, the reader is directed to that work for details. All data for this experiment was collected in the fluorescence mode on beamline X19-A at the National Synchrotron Light Source, Brookhaven National Laboratory between 7 and 13 August, 1991. A pictorial description of a "typical" synchrotron XAFS experimental layout and fluorescence detector is given in Figure 1.

## DATA ANALYSIS

Many complications may hinder one's progress towards quantitative analysis of EXAFS. One must be very careful when stating results to include some particulars about how the analysis was performed. The procedure used here can be divided into two main parts. The first includes the initialization and background removal to obtain normalized EXAFS oscillations. This normalized data can then be analyzed by the theory developed above. The second major step in the analysis extracts the parameters of interest. The analyst has several tools at his disposal for this part of the analysis. These include: Fourier Transform (FT) and Fourier filtering to get radial structure functions, direct comparison of EXAFS spectra, isolation of single shells, and curve fitting or calculation.

## PRELIMINARY ANALYSIS

### INITIALIZATION

The programs used in this study to analyze the data were FORTRAN codes developed over the course of about a decade. They enable one to analyze data from many different synchrotron radiation (SR) beamlines by putting the data into a standard format. After the raw data has been initialized, the analysis proceeds without regard to the origin of the particular data set. A plot of a fluorescence spectrum of AP is shown in Figure 2(A).

### PRE-EDGE SUBTRACTION

Below the absorption edge of interest, the measured background contains contributions from several sources, such as Compton scattering and other (lower energy) absorption edges. It is useful, especially for near-edge studies, to remove this pre-edge background. This is done by fitting the data below the edge to a suitable function and extrapolating to the end of the data set. It is found that a quadratic pre-edge function is a good approximation to this background for transmission, and for fluorescence even a linear function will suffice[5]. Usually this curve is fit between two points in the data set; the first "good" point and the point at which the absorption edge begins to occur. It is possible for the analyst to specify both of these points. This is especially useful when comparing several spectra at the same absorption edge to provide consistency in the analysis. The curve from Figure 2(A) is shown in Figure 2(B) with the pre-edge function over-plotted.

### EDGE ENERGY DETERMINATION

Even though the EXAFS technique is relatively insensitive to the absolute energy calibration of the monochromator it is useful, again to maintain consistency, to define a threshold energy $E_0$. This is done by mathematically determining the inflection point in the absorption edge spectrum. When analyzing materials with different chemical or crystallographic compositions it is useful to use the same number for $E_0$ for the entire group. Therefore, one lets the computer program determine the inflection point of the "pure" or "control" sample, and then manually assigns that number for $E_0$ to subsequent samples. A plot showing the inflection point for AP X-ray Absorption Near-Edge Structure (XANES) appears in Figure 3(A). Figure 3(B) shows the fluorescence spectrum of AP with the pre-edge function subtracted.

**DEJUMPING**

Sometimes one finds that the data contains absorption edges other than that or those of interest. This was the case in this study, due to the closeness of the chlorine k-edge (2823 eV) to that of argon (3205 eV). Since a typical EXAFS scan extends to approximately 1000 eV above the edge, this could cause a problem due to EXAFS arising from the other element(s). Fortunately, Ar is a noble gas and as such there is no fine structure above the edge, so this edge can be carefully "dejumped" or subtracted PRIOR to isolation of the EXAFS oscillations. Since the amplitudes of these features are larger than the EXAFS oscillations themselves at this energy, it is useful to dejump when possible to avoid contaminating the FT performed later. The Ar edge in an AP scan is shown in Figure 4(A) and the dejumping process is illustrated in Figure 4(B).

**BACKGROUND REMOVAL**

The background above the edge is more complex than that below it, and must be carefully removed in order to properly normalize the data and later extract structural parameters. There are several methods for determining the post-edge background function, and in this work the background is obtained as a cubic smoothing-spline approximant to the data[6]. This method, as well as the several others available to the general EXAFS community, depends on the background being slowly varying with respect to the EXAFS oscillations.

Two parameters may be varied by the user- one determines the smoothness of the fit and the other is an inverse weighting parameter. In practice the weighting parameter is held fixed at a small value to force the spline to go through the first data point and the smoothing parameter is varied. The smoothing parameter is varied by an iterative process by which one examines the FT and background derivative. Using a smoothing parameter that is too small will cause non-physical peaks at small radial distance R in the FT, while if the smoothing parameter is too large the oscillations in the background derivative will too closely follow the EXAFS.

The procedure is to visually compare plots of the FT and background derivative and determine what final value to use for the smoothing parameter. Also important is the k-range used in the FT. Usually one specifies the k-range to start at the first zero of $\chi(k)$ and extend to a k-value dependent on the quality of the high-k data. Plots showing the effect of varying the smoothing parameter on the FT and background derivative are shown in Figure 5.

## NORMALIZATION

After the background has been subtracted from the data, the next step is to normalize the EXAFS oscillations to enable meaningful comparison of spectra collected from different samples. This is done by choosing a point beyond the near edge structure region, and dividing each data point by the $\chi$ value of the normalization point. When studying several samples of a given system it is important that the same energy value be used for each to maintain consistency.

Once the data has been normalized it must then be written in a form conducive to detailed Fourier analysis. This procedure writes only the normalized, isolated EXAFS data into a file that can be read by a program that analyzes and fits the $\chi$ data. Plots of the normalized $\chi$ for AP and AP/TET are shown in Figure 6.

## FOURIER ANALYSIS AND EXTRACTION OF STRUCTURAL PARAMETERS

Once a careful preliminary analysis has been completed, detailed Fourier analysis and quantitative comparison may commence. It is well established[2,7] that the Fourier transform can be used to extract information from equation 1 since it is essentially a sum of sines and exponentials. The reason that it is possible to isolate data corresponding to different radial distances is that the sine term in equation 1 contains the strongest k dependence[8].

There are several ways to extract information from equation 1, and the method(s) used for a given study will depend on what information is needed. Three well-known techniques are: curve fitting, $\chi$ calculation and visual comparison. Often, two or more of these methods are used together. The program used in this part of the analysis enables one to overplot several EXAFS ($\chi$) or Fourier transform (RSF) spectra, fit data to a reference material or theoretical information, and calculate EXAFS spectra given a reference material or theoretical information. This also includes Fourier filtering and backtransformation to isolate single shell data.

For a theoretical treatment one may use the calculated phase shifts and backscattering amplitudes of Teo and Lee[9] (plane wave approximation) or McKale *et al*[10] (full curved-wave formalism). This is particularly useful when a suitable reference compound is difficult or impossible to obtain, although one must particularly careful to properly normalize the data in this case. The use of reference materials for fitting or calculation is quite useful for comparing an unknown sample to a well-characterized standard. In addition to providing a reference for phase shifts and backscattering amplitudes, the use of model compounds allows the analyst to visually compare the experimental and calculated or fitted data to the model.

## DISCUSSION AND CONCLUSIONS

### XANES ANALYSIS

Analysis of the XANES gives information about the density of unoccupied states near the edge. A major complication of XANES analysis is that the full matrix operators must be used and summation over *all* scattering paths is required, unlike EXAFS in which a single scattering process will suffice. It is apparent that most of the information contained in the interaction between AP and various binders is contained in the XANES region. This is a limitation of the present analysis process as well as the general XAFS community and should form an impetus for future work in this rapidly developing field.

### SUMMARY

A powerful experimental technique, that of X-ray Absorption Fine Structure spectroscopy and analysis, was added to the list of in-house capabilities available at Phillips Laboratory OLAC for the investigation of a new set of materials of vital interest to the Air Force. As well as providing computer programs for performing the data analysis chlorine K-edge XAFS was shown, for the first time, in oxidizers and a new class of synthesized polymers. An X-ray fluorescence spectrum for a newly synthesized polymer is shown in Figure 7. As this is part of an ongoing project providing relatively recent data (13 AUG 91), the final analysis is not yet complete. There is additional synchrotron beamtime available this Autumn, and a careful and detailed XANES study should be carried out at that time, as well as a demonstration of the versatile tool of structural determination known as XAFS on other new materials and oxidizer/binder systems at that time.

ACKNOWLEDGEMENTS

I would like to thank my focal point at the Phillips Laboratory OLAC, Dr. J. Rusek, for giving me the opportunity to work with him this Summer on this exciting project as well as S. Osborn, K. Chaffee and many others at Edwards AFB for being extremely helpful and receptive to new ideas. I would also like to thank my thesis advisor, Prof. R. W. Hoffman of Case Western Reserve University, who also participated in this program with me for all of his help, useful conversations and advice in countless matters over the Summer. This research was funded through the Summer Faculty/Graduate Student Research project of RDL Research and Development Laboratories and the NSLS is supported by the U.S. Department of Energy, Office of Basic Energy Sciences.

## REFERENCES


1) Kronig, R. de L., Z. Phys., **70**, (1931), 317.

2) Sayers, D. E., Stern, E. A. and Lytle, F. W., Phys. Rev. Lett., **27**, (1971), 1204.

3) Lee, P.A. and Pendry, J. B., Phys. Rev. B, **11**, (1975), 2795.

4) Ashley, C. A. and Doniach, S., Phys. Rev. _ **11**, (1975), 1279.

5) Sayers, D. E. and Bunker, B. A. in *X-ray Absorption: Principles, Applications, Techniques of EXAFS, SEXAFS and XANES*, Koningsberger, D. C. and Prins, R., eds., (John Wiley, New York, 1988), 216.

6) ibid, Sayers and Bunker, 217.

7) Stern, E. A., Sayers, D. E., and Lytle, F. W., Phys. Rev. B, **11**, (1975), 4836.

8) ibid, Sayers and Bunker, 227.

9) Teo, B. K and Lee, P A., J. Amer. Chem. Soc., **101**, (1979), 2815.

10) Mckale, A. G. *et al*, J. Amer. Chem. Soc., **110**, (1988), 3763.


## FIGURE CAPTIONS

1) (A) Beamline setup for a typical absorption experiment
(B) Diagram of a Lytle type fluorescence detector

2) (A) X-ray fluorescence vs photon energy in eV of AP
(B) X-ray fluorescence and quadratic pre-edge vs photon energy in eV of AP

3) (A) Cl K-edge XANES of AP
(B) X-ray fluorescence spectrum minus pre-edge background of AP

4) (A) Ar edge appearing in AP data vs photoelectron energy in eV
(B) Removal of Ar edge by the dejumping process

5) (A) Post-edge background derivative and
(B) Fourier transform magnitude of AP as a function of smoothing parameter

6) Normalized EXAFS data of (A) AP and (B) AP with 1 mL of TET diffused

7) X-ray fluorescence vs photon energy in eV of "SYN 14"

# SCHEMATIC OF AN X-RAY ABSORPTION EXPERIMENT AT A SYNCHROTRON RADIATION FACILITY

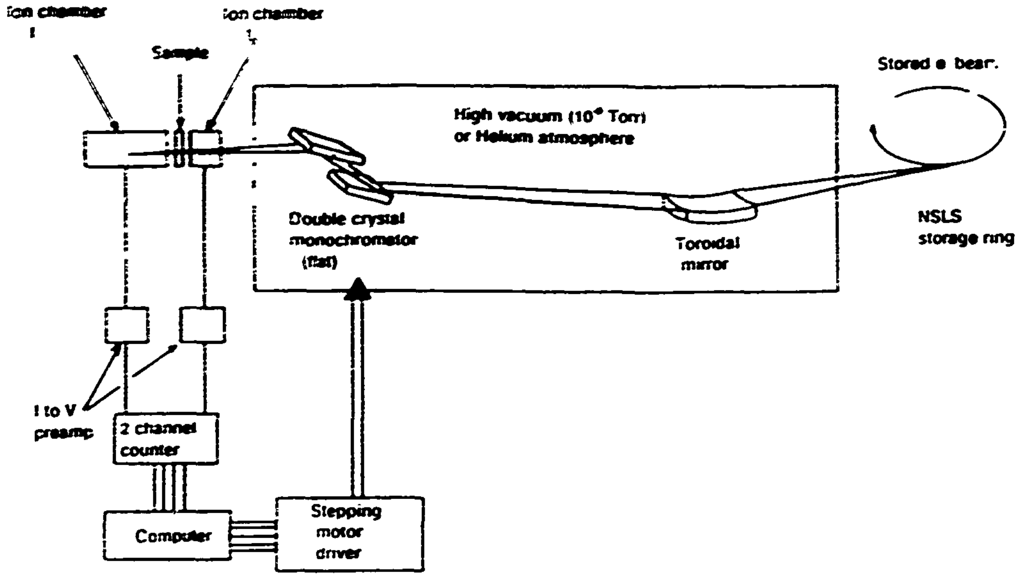


( A )

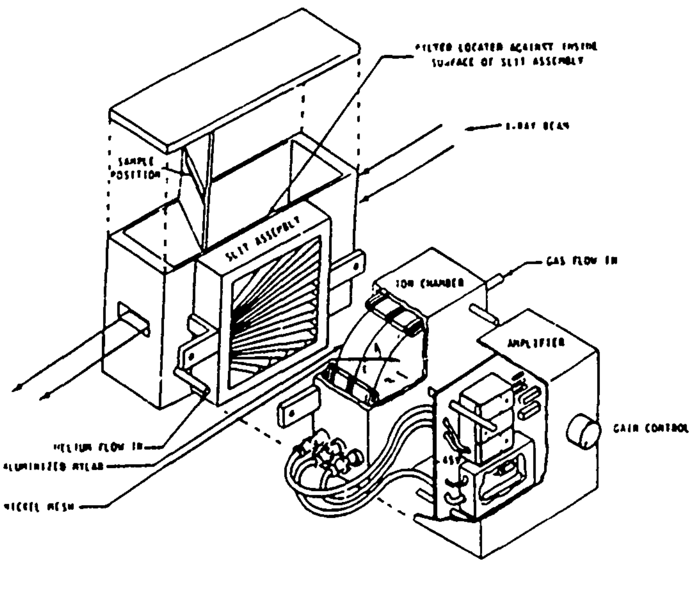


FIGURE 1

( B )

X-RAY FLUORESCENCE SPECTRUM OF $NH_4ClO_4$

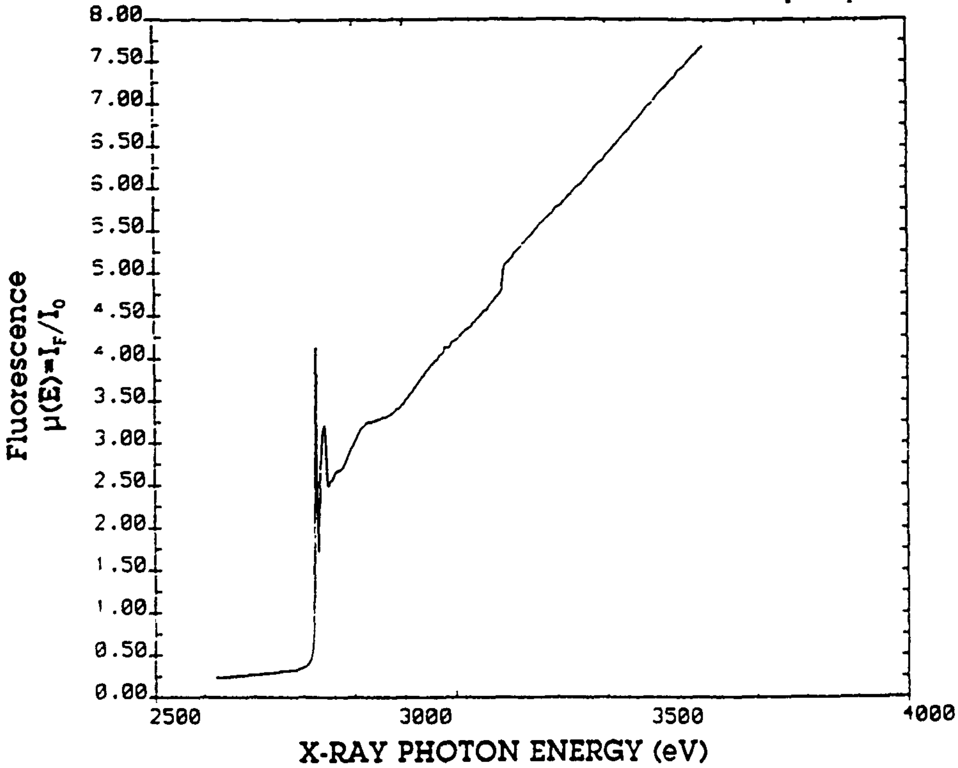


( A )

X-RAY FLUORESCENCE SPECTRUM OF $NH_4ClO_4$
WITH QUADRATIC PRE-EDGE BACKGROUND OVERPLOTTED

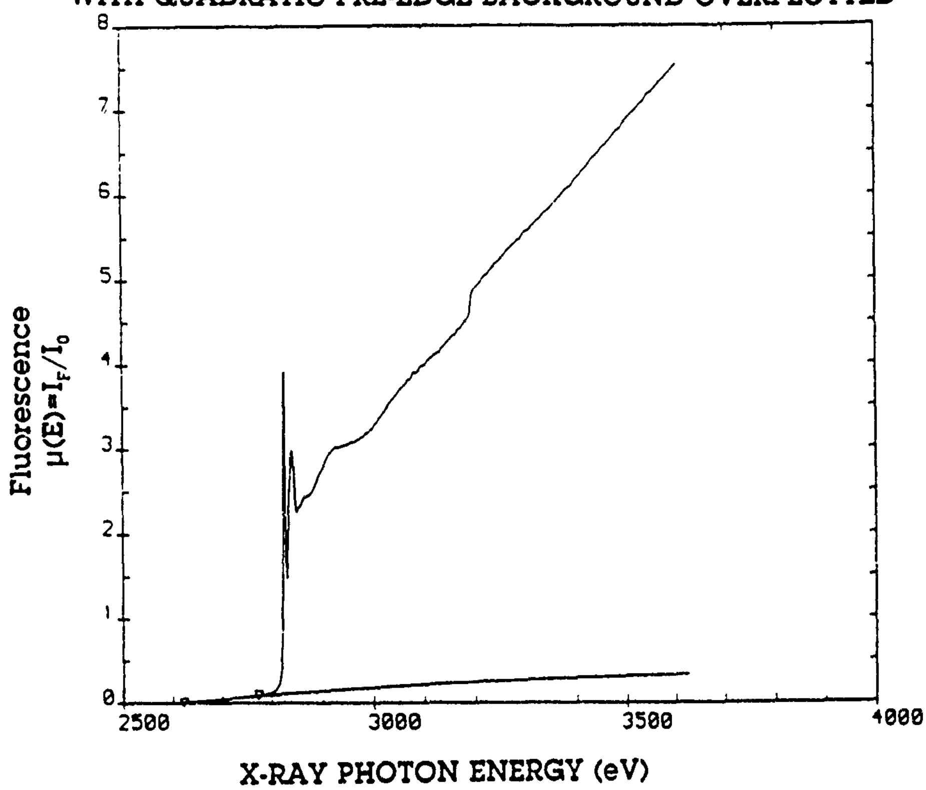


( B )

FIGURE 2

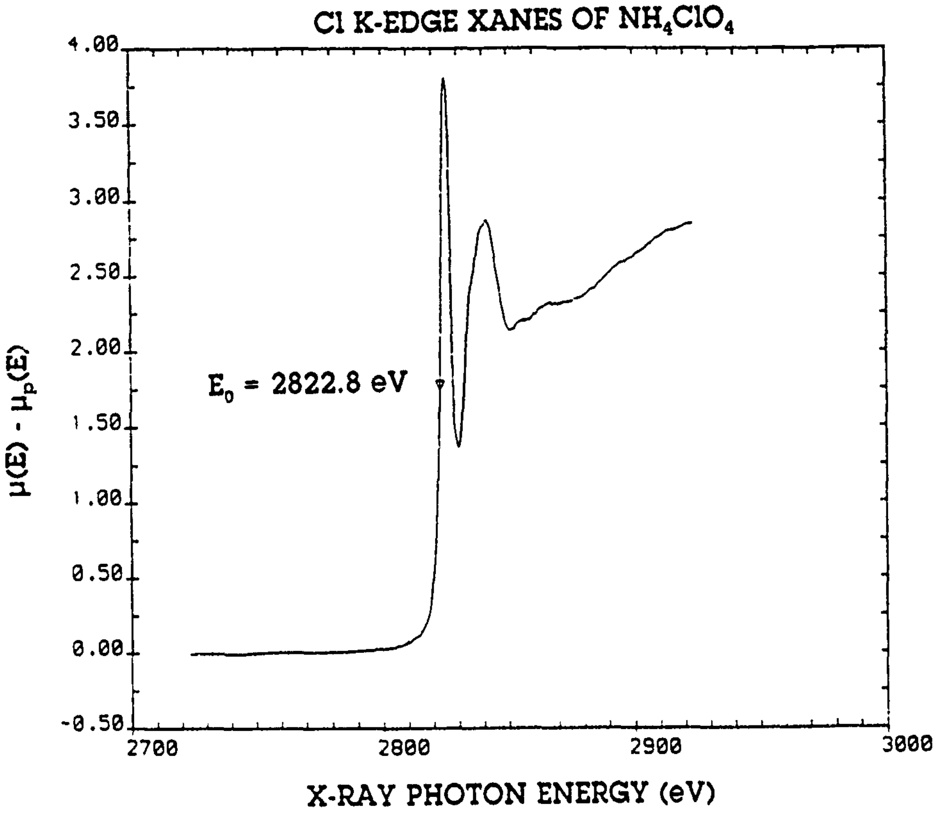
Cl K-EDGE XANES OF $NH_4ClO_4$
$\mu(E) - \mu_p(E)$
$E_0$ = 2822.8 eV
4.00
3.50
3.00
2.50
2.00
1.50
1.00
0.50
0.00
-0.50
2700
2800
2900
3000
X-RAY PHOTON ENERGY (eV)

( A )

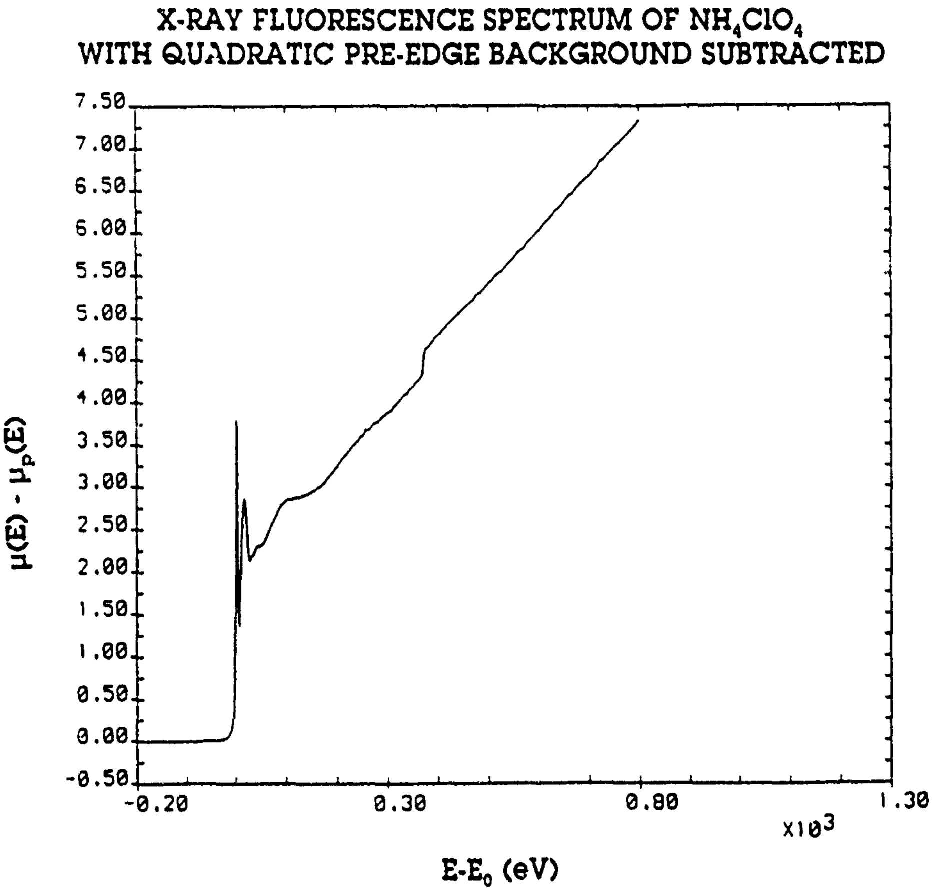
X-RAY FLUORESCENCE SPECTRUM OF $NH_4ClO_4$
WITH QUADRATIC PRE-EDGE BACKGROUND SUBTRACTED
$\mu(E) - \mu_p(E)$
7.50
7.00
6.50
6.00
5.50
5.00
4.50
4.00
3.50
3.00
2.50
2.00
1.50
1.00
0.50
0.00
-0.50
-0.20
0.30
0.80
1.30
X10$^3$
$E-E_0$ (eV)

( B )

FIGURE 3

X-RAY FLUORESCENCE SPECTRUM OF $NH_4ClO_4$
WITH QUADRATIC PRE-EDGE BACKGROUND SUBTRACTED

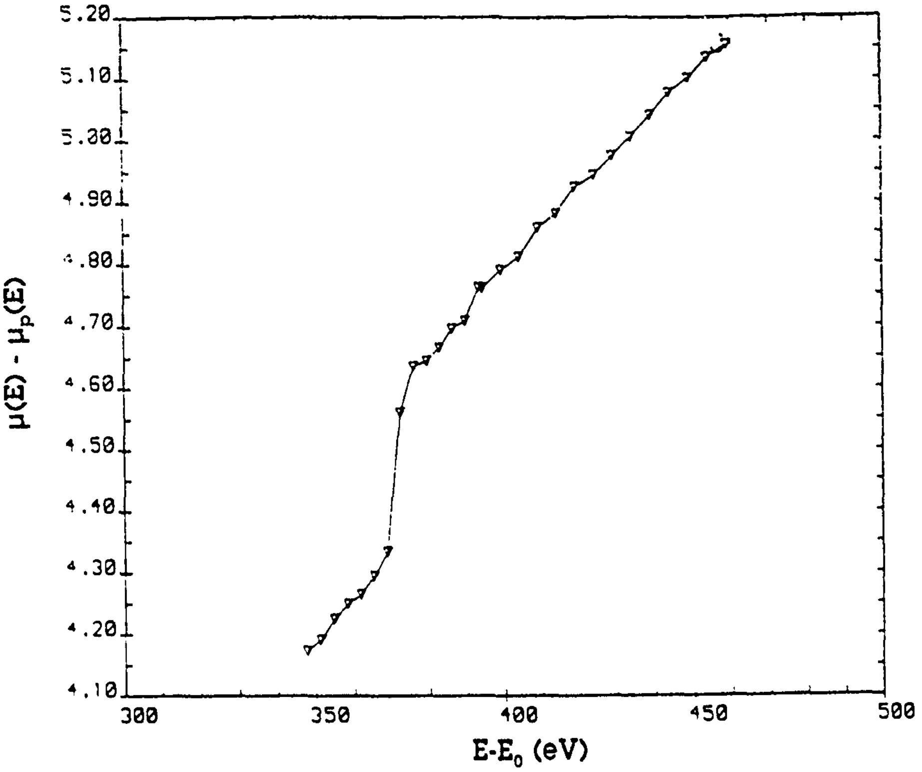


( A )

X-RAY FLUORESCENCE SPECTRUM OF $NH_4ClO_4$
WITH QUADRATIC PRE-EDGE BACKGROUND SUBTRACTED

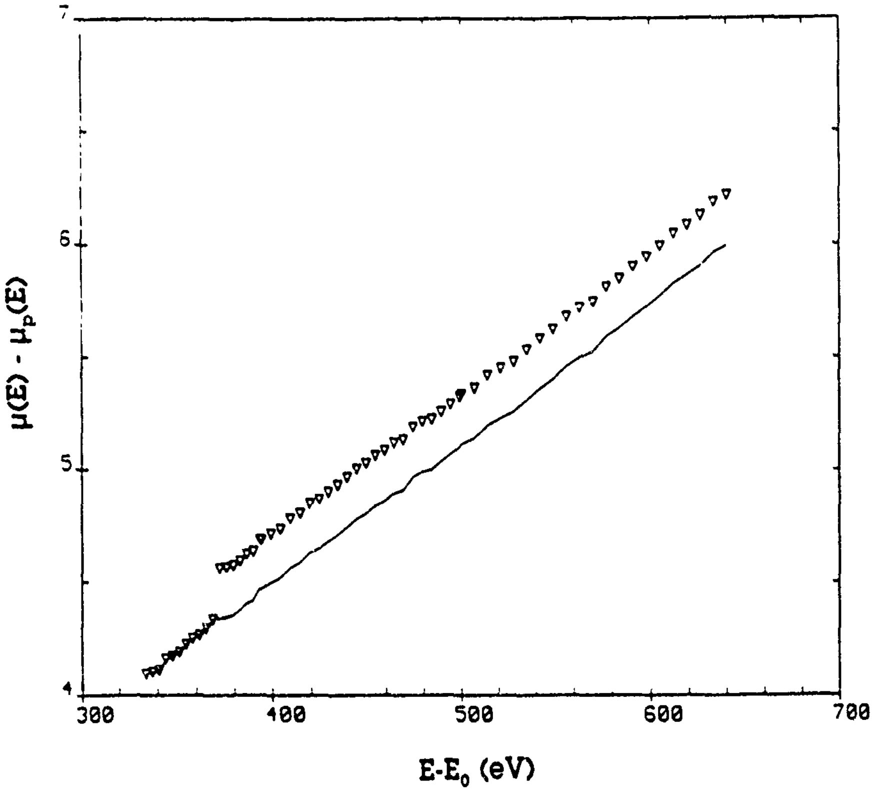


( B )

FIGURE 4

POST-EDGE BACKGROUND DERIVATIVE vs PHOTOELECTRON WAVE NUMBER FOR $NH_4ClO_4$ AS A FUNCTION OF SMOOTHING PARAMETER

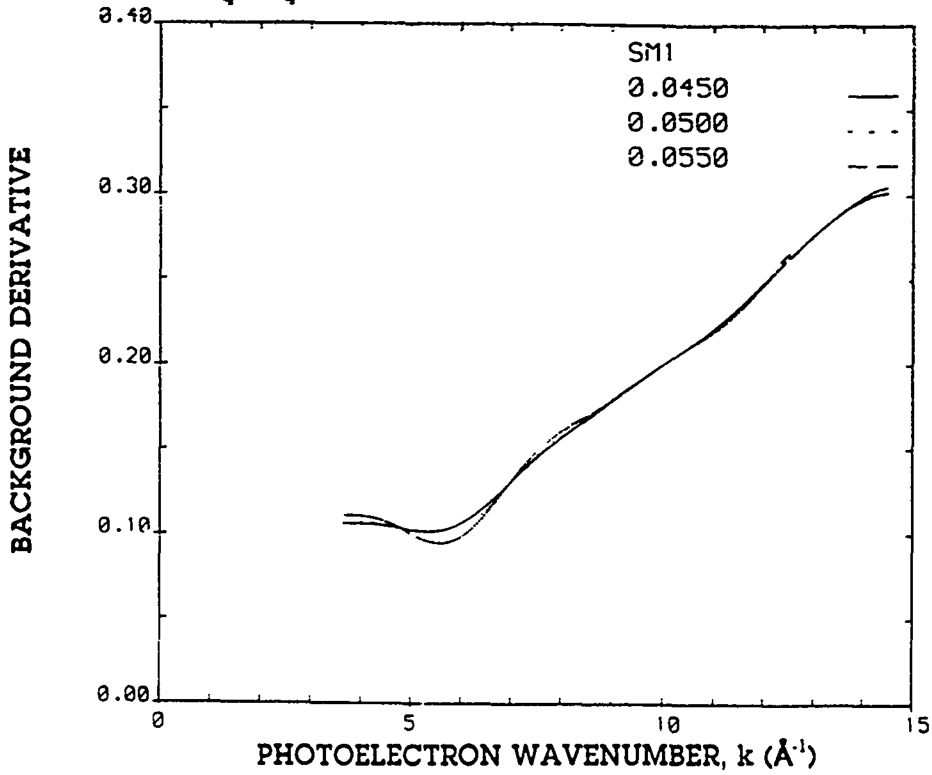


( A )

FOURIER TRANSFORM MAGNITUDE VS RADIAL DISTANCE IN Å FOR $NH_4ClO_4$ AS A FUNCTION OF SMOOTHING PARAMETER

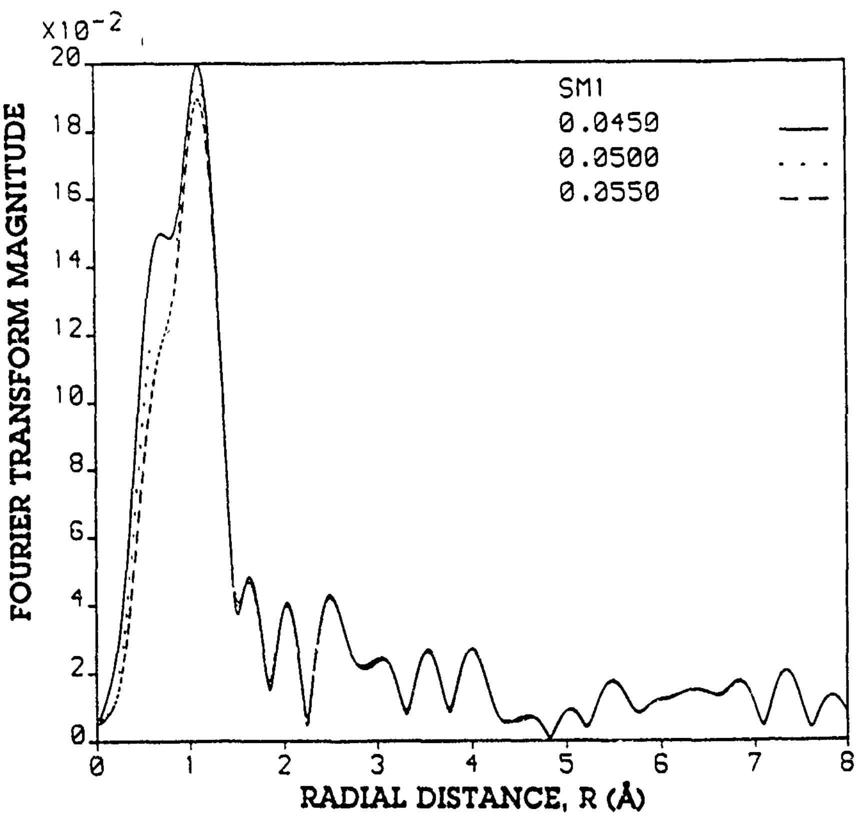


( B )

FIGURE 5

NORMALIZED EXAFS DATA $\chi(k)$ vs PHOTOELECTRON WAVE NUMBER IN $Å^{-1}$

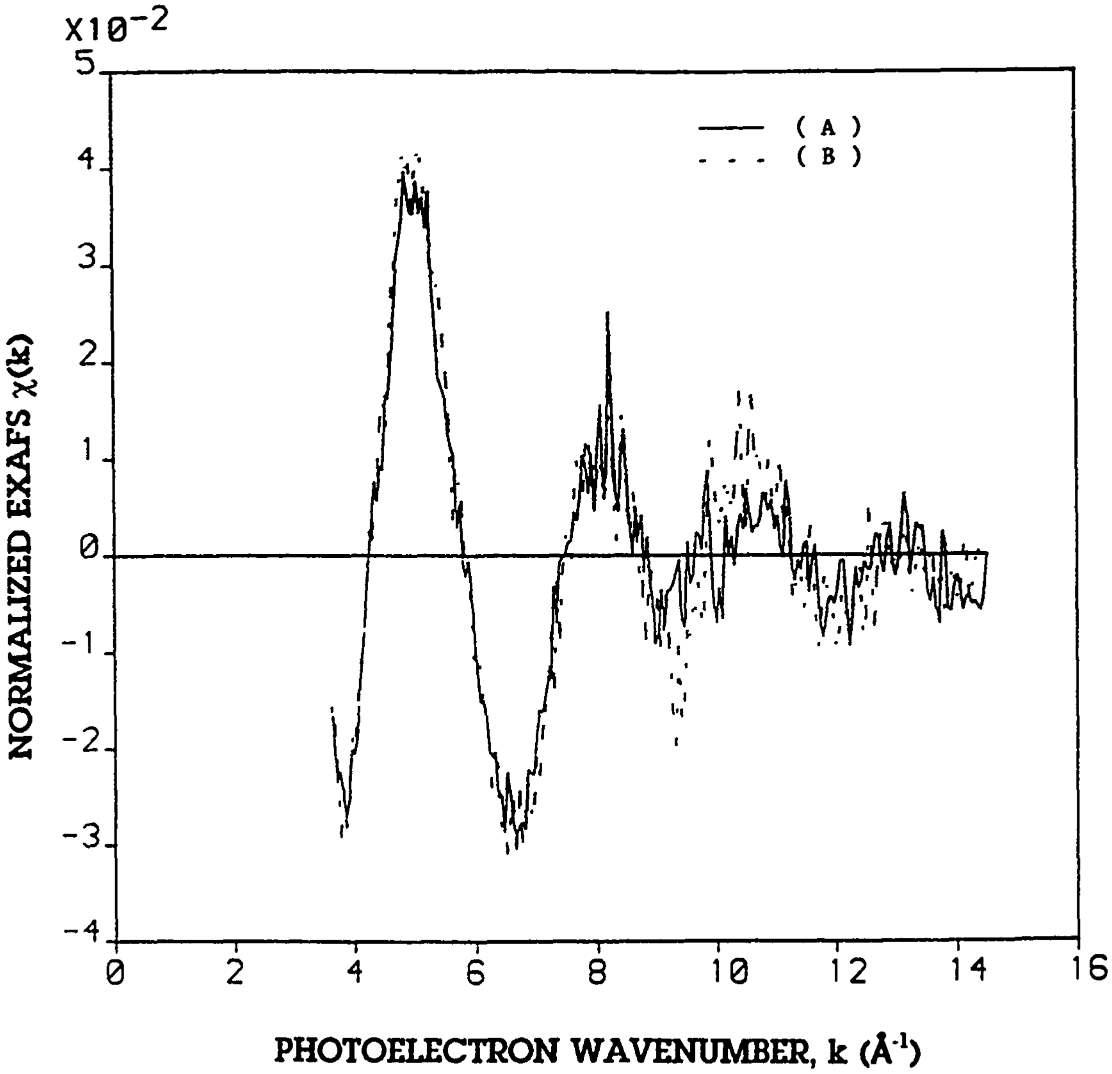


FIGURE 6

## X-RAY FLUORESCENCE SPECTRUM OF NEWLY SYNTHESIZED POLYMER

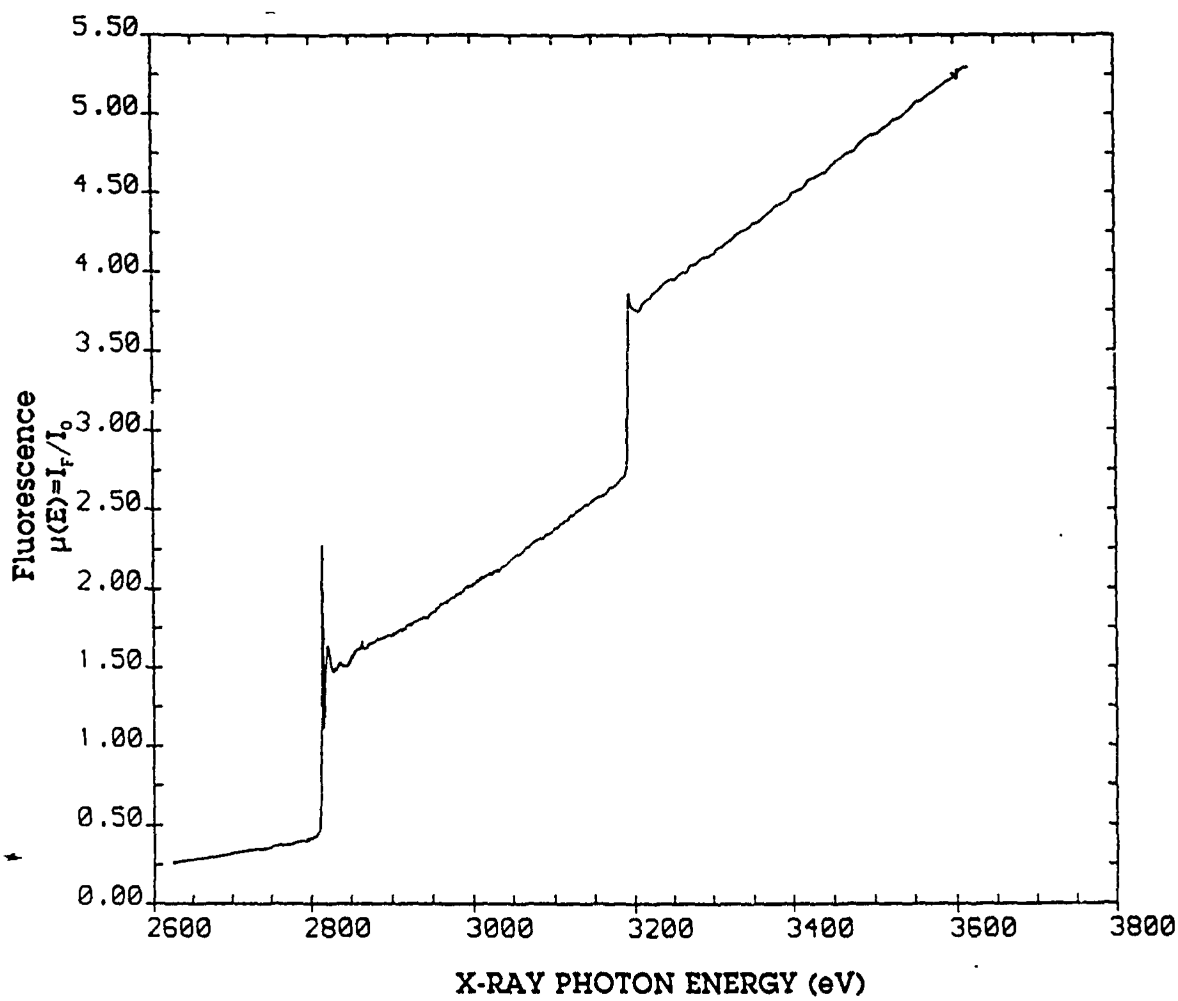

ALKALI METAL VAPOR SPECTROSCOPY
AND
SOLAR PLASMA PROPULSION

Paul S. Erdman
Candidate
Doctor of Philosophy
University of Iowa

ABSTRACT

The solar plasma propulsion concept involves absorbing solar energy directly into the propellant of the rocket. Materials which would work well as solar absorbers and high specific impulse propellant would be alkali metals, particularly lithium, combined with hydrogen. To study the various $Li_xH_y$ species which may be formed in the high temperature and pressure environment of the rocket, the Plasma Spectroscopy Cell (PSC) has been constructed. The PSC has been successfully tested and spectroscopic observations have been performed. There are indications that lithium hydrides have been formed, but wider spectral ranges and additional spectroscopic techniques will need to be employed in future experiments to fully study the $Li_xH_y$ species.

## INTRODUCTION

One of the proposed methods of using solar energy in space propulsion is to absorb the radiant energy directly into the propellant [1]. Because of its low mass, hydrogen offers a high specific impulse when used as a propellant. However, hydrogen absorbs well only in the ultraviolet region of the spectrum. The majority of emitted solar radiant energy is in the visible and infrared regions. Thus, to couple the visible radiant energy to hydrogen, a seed element with appropriate solar radiation absorption properties must be mixed with the hydrogen.

Studies have been made which show the alkali metals to be powerful absorbers in the region of the solar spectrum. In the application to solar plasma propulsion, lithium would be the best candidate as a hydrogen seedant, considering its low mass would provide a higher specific impulse. The lithium would form additional absorbing species such as LiH. In fact, the high temperature and high pressure environment that would be produced in a solar plasma propulsion absorption chamber would likely result in species such as $Li_2H$, $Li_2H_2$, $Li_3H$, and ionized species such as $Li_2^+$, $Li_2H^+$, $LiH_2^+$, $Li_3^+$ [2]. Many of these species have never been studied, because the high temperature and pressure environment required to produce a significant density of them has not existed in a laboratory until now.

The development of the Plasma Spectroscopy Cell (PSC) at the Phillips Laboratory at Edwards Air Force Base has opened opportunities to observe these $Li_xH_y$ species. The PSC (see Figure 1) is designed to produce a gas flow mixture of hydrogen, alkali metal vapor, and neutral carrier gases at temperatures up to 3000 K and pressures up to 100 atmospheres. The design also includes optical access to the interactive region, allowing quantitative spectroscopic observation of the various species formed.

Thus, through spectroscopic study of the many lithium-hydrogen species produced in the PSC, the absorption cross section of the plasma mixture can be determined. Comparison to the solar spectrum will reveal how well the plasma may perform as a solar propulsion propellant.

## PROBLEM

The original design of the PSC included a system for pumping liquid alkali metal into the atomizer region where it would be vaporized using a molybdenum heating element, and carried to the hot zone with a neutral entrainment gas. This system was redesigned because of the difficulties in pumping liquid alkali metals. Instead, the alkali metal was loaded into the atomizer in solid form and evaporated, entrained in an inert carrier gas, and delivered to the hot zone.

An initial test of the PSC resulted in failure of the evaporator. The short term goal for the project thus became the replacement of the evaporator. For this purpose, a new rhenium heating element was manufactured for installation in the evaporator.

The PSC was disassembled and the evaporator replaced. Lithium was loaded into a zirconium crucible with a covering of octane and placed into the atomizer chamber. The PSC was then reassembled and ready to be tested.

## RESULTS

The PSC was successfully tested in the vacuum and atmospheric pressure range. The maximum temperatures reached during the many tests were 1100 C in the evaporator and 1520 C in the hot zone. Helium and Argon were used as entrainment gases.

Spectroscopic observations showed that the lithium was indeed vaporized and carried into the hot zone. Figure 2 shows an overlay of several of the absorption spectra that were measured at different hot zone temperatures. The main features to note are the strong Li absorption at 670 nm and the broad $Li_2$ absorptions in the 490 nm (for the X to B transition) and 713 nm (for the X to A transition) regions. The absorption line at 589 nm results from Na, which was present as an impurity in the lithium source. A subtle but noteworthy feature is behavior of the bottom absorption curve (labeled F2551) on the 450 nm line. Whereas the three curves immediately above all converge near 0.85 transmittance, the bottom curve stops at 0.7 transmittance. The bottom curve was measured when hydrogen was introduced into the system, and hence it is believed that the additional absorption seen in the 450 nm region is due to LiH.

## CONCLUSION

The Plasma Spectroscopy Cell performed successfully. The modifications to the design worked well. Lithium species were observed with absorption spectroscopy and show strong absorption in the optical and infrared regions of the spectrum.

The spectrometer used had only a limited range of 450 to 750 nm. For future work, it will be worthwhile to look above and below this range to see more of the expected absorption features. The LiH species should show up more strongly around 385 nm, and $Li_3$ absorption may already be taking place above 750 nm in the present experiments. Additionally, experiments with Laser Induced Fluorescence could provide information which could be used to calculate the identity and properties of the various $Li_xH_y$ species. These and many more experiments are good possibilities for future work with the Plasma Spectroscopy Cell.

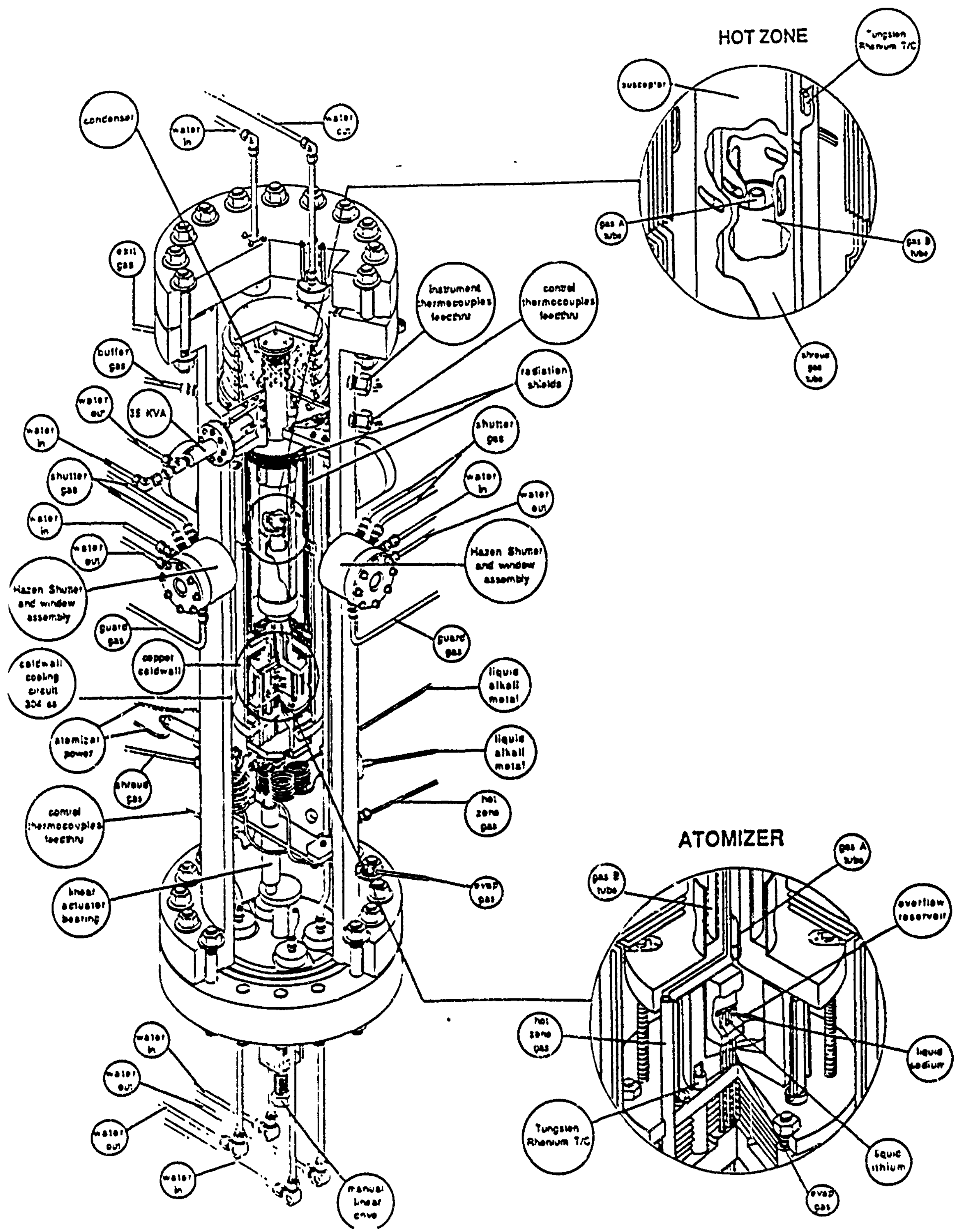


**FIGURE 1**
The Plasma Spectroscopy Cell showing enlargements of the Hot Zone and Atomizer.

## FIGURE 2

Absorption spectra of Li and LiX species in the Plasma Spectroscopy Cell hot zone.

Pertinent temperatures are :

| Curve Number | Evaporator T (C) | Hot Zone T (C) |
|---|---|---|
| F2537 | 962 | 1320 |
| F2549 | 1124 | 1410 |
| F2546 | 1110 | 1301 |
| F2540 | 1005 | 1321 |
| F2551 | 1124 | 1410 |

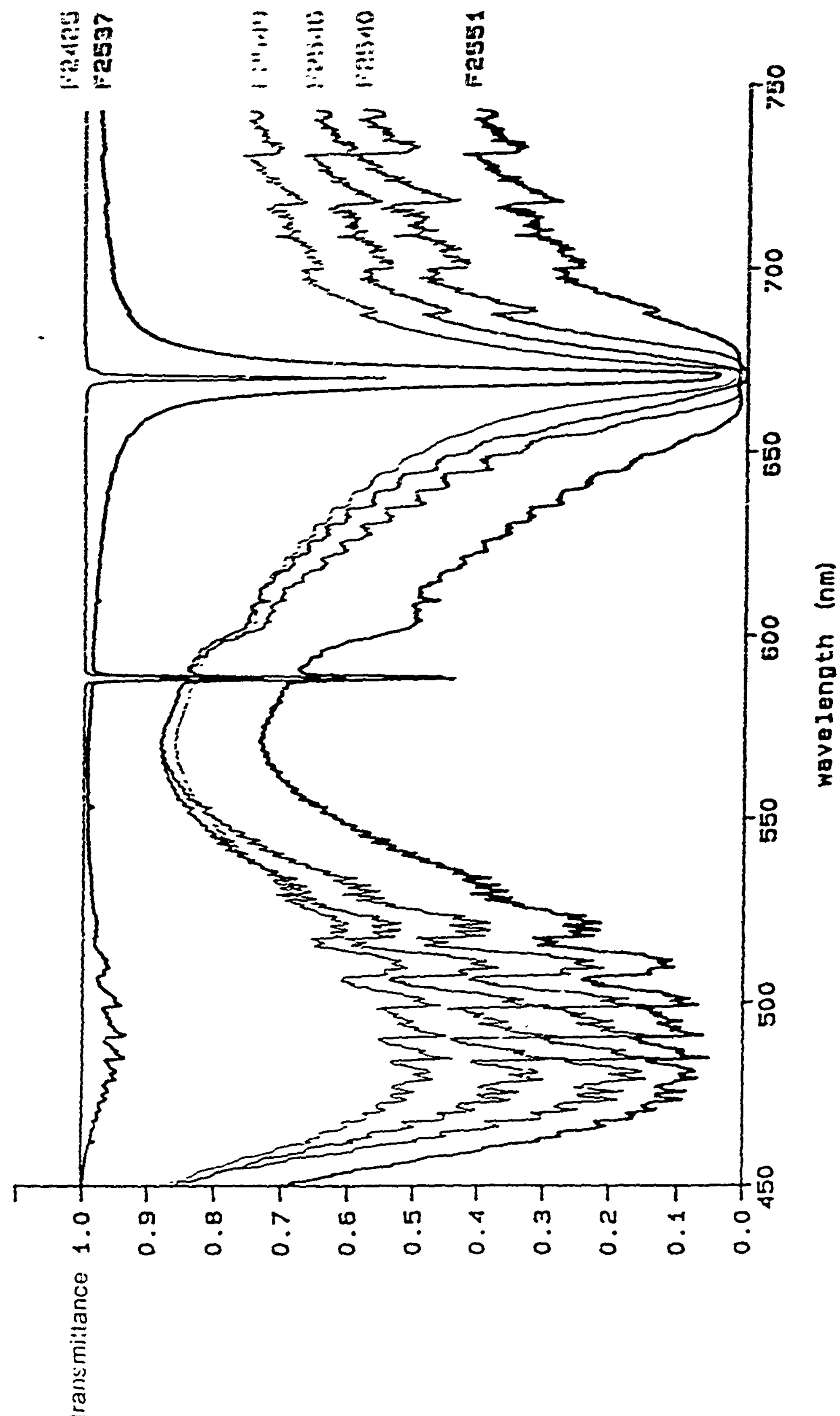
transmittance
wavelength (nm)
F2537
F2551
F2540
1.0
0.9
0.8
0.7
0.6
0.5
0.4
0.3
0.2
0.1
0.0
450
500
550
600
650
700
750

FIGURE 2

## REFERENCES


[1] C. W. Larson, "Solar Plasma Propulsion", Report AFRPL TR-85-096 of the Air Force Rocket Propulsion Laboratory, Edwards Air Force Base (1987).

[2] C. W. Larson, "The Spectroscopy of Hydrogen/Metal-Vapor Mixtures at High Temperatures and Pressures", Report AL-TR-88-080 of the Air Force Astronautics Laboratory, Edwards Air Force Base (1988).

# A STUDY OF THE CATALYTIC GROWTH

# OF CARBON FILAMENTS

A Project Report

Presented to

Research and Development Laboratories

by

Patricia Meng-Fu Liu

September 1991

# ABSTRACT

## A STUDY OF THE CATALYTIC GROWTH OF CARBON FILAMENTS

Patricia Meng-Fu Liu

In this project, the catalytic growth of carbon filaments on a graphite substrate was studied. To grow the filaments, gas mixtures of actelyene and hydrogen or propane and hydrogen were passed through the growth reactor at 950° C and angstrom sized iron oxide particles were used as catalysts. Experimental results indicate that carbon filament formation is inhibited when an acetylene-hydrogen gas mixture is used in the growth reactor at 950°C. However, when acetylene is replaced with propane what appeared to be carbon filaments with a hollow core and an approximate diameter size of 3 microns were grown. The hollow structure of the filaments are indicative of carbon filaments grown from catalyst particles.

# A STUDY OF THE CATALYTIC GROWTH OF CARBON FILAMENTS

Patricia Meng-Fu Liu

Summer Intern

## Introduction

In recent years, the study of the growth of carbon filaments has increased significantly as a result of numerous new applications for this material. Among the potential applications of most interest to the aerospace industry is the use of filamentous carbon grown on primary carbon fibers in the creation of a new generation of composites with unique chemical, electrical, and physical properties. There are many advantages to producing a composite with a network of cross-linked fibers over an existing carbon fiber pre-form. By providing channels for crack growth, the secondary filaments would promote crack bifurcation and retardation. They would also make it more feasible to separately control the strength and toughness of a composite. Since the filaments and fibers form an integrated, multidirectional network, thereby contributing to the through-the-thickness strength of the composite, the common problems of delamination as well as weak strength in the through-the-thickness direction will be alleviated or, perhaps, even eliminated.

One method of growing carbon filaments on carbon fibers is by the metal-catalyzed decomposition of hydrocarbons. The key step in the growth mechanism is believed to be the diffusion of carbon atoms through the bulk of the catalyst particle from the exposed face on which the hydrocarbons decompose to the opposite face at which the carbon precipitates out of solution. Whether a temperature or concentration gradient drives the diffusional flow is a question that remains to be answered conclusively. An extremely influential model proposed by Baker, Barber, Harris, Feates, and Waite [1] assumes that diffusional flow is primarily driven by a temperature gradient created in the particle by the exothermic decomposition of the hydrocarbon at the exposed leading faces and endothermic deposition of carbon at the rear faces, which is initially in contact with the surface of the support. Experiments performed by Yang and Yang [2] using the gold decoration technique to study the growth of carbon deposits from the interaction of nickel with different hydrocarbons seem to support the idea that a temperature gradient is the driving force. In contrast, a model proposed by Tibbetts, Devour, and Rodda [3] assumes that the diffusional flux is primarily driven by a concentration gradient, a view in agreement with that of Rostrup-Nielson and Trimm [4]. Tibbetts et. al. argue that the hydrocarbon decomposition enthalpy is insufficient to drive carbon atoms through the particle. Thus, supersaturation of the particle by carbon is required and a concentration gradient is the driving force for the diffusional process. Excess carbon which accumulates at the exposed surfaces of the particles is transported by surface diffusion around the peripheral surfaces to form the graphitic skin of the filament. If the transport process is slow, then the available catalyst surface for adsorption and decomposition of hydrocarbons decreases. Eventually, the leading face is encapsulated by a layer of carbon preventing further decomposition of hydrocarbons and growth ceases.

The present study grew out of a desire by the Composites Lab at Phillips Laboratory to obtain a fundamental understanding of the growth mechanisms for filamentous carbon, which is essential in order to determine the optimum experimental parameters for producing carbon filaments. Eventually, the Lab would like to be able to control the direction of growth for a number of reasons. First, a 3-D composite made by growing carbon fibers through composite lay-ups in the third direction would be much more feasible to produce than one in which the conventional method of hand weaving the fibers into a 3-D network is used. Second, if growth could be controlled, straight carbon whiskers could be grown and compacted together to form a high fiber-volume carbon-carbon composite with very high electrical conductivity. Thus, the objective of my research effort this past summer at the Phillips Laboratory was to devise a method of growing filamentous carbon. As part of my project, I helped to construct an apparatus in which vapor-grown carbon filaments could be produced.

## APPARATUS

The apparatus, shown in Figure 1, was devised to allow graphite substrates on which carbon fibers are to be grown to be inserted and removed from the furnace in a controlled atmosphere. After placing the substrates in a specially designed graphite boat, the sample prechamber can be sealed. Once the growth reactor has been purged with Argon, a ball valve can be opened to allow the substrate to be pushed into the furnace with a sample push rod.

The apparatus was constructed using a 4 ft. fused silica tube with a bore of 2 in. and an inner diameter of 1 in. The tube was placed in a Linberg single-zone 36 in. tube heater. On the outside of the tube, a solenoid consisting of 10 turns was wound on top of another ten turns of K-type heavy duty insulated thermocouple wire. A high-voltage stainless steel electrode was also added to the outside of the tube. The flare fitting was made from standard 1 1/2 in. stainless steel tubing and glued on with silicone rubber cement. The thermocouple wire, which is of the 20 gauge type K, has a high temperature NEXTEL braided insulation and can be used to approximately 2200°F. A diagram of the tube with the dimensions given is shown in Figure 2.

## Experimental Procedure

Twelve substrates were cut from graphite scrap to dimensions of 1.375 in. x 0.75 in. x 0.1875 in. and then ground and polished on one of the surfaces. The iron oxide particles that were used as catalysts were obtained from an aqueous 100 gauss ferrofluid EMG807, which has a particle concentration of 1.65% by volume. The particle size is 1000 Å 10%. The ferrofluid was diluted with distilled water before use. The mixture ratio of ferrofluid to distilled water was 1:250. The substrates were placed in a pyrex dish and submersed in the diluted ferrofluid. After evaporation of the liquid for 5 hours at 100°C, the iron oxide particles adhere to the substrate surface as can be seen in Figure 3 and act as catalysts for the decomposition of acetylene or propane and the deposition of carbon. The treated substrates were placed in a tube furnace through which an acetylene-hydrogen or propane-hydrogen mixture flowed. Three experimental runs were conducted.

In the first run, substrate #2 was inserted into the furnace at a temperature of 950°C under a rapidly flowing Argon purge of 330 cc/min. After two minutes, the argon flowmeter was shut off, and a mixture of hydrogen with a flowrate of 90 cc/min and acetylene with a flowrate of 10 cc/min was introduced to the system. Under these conditions, the filaments should lengthen without substantial thickening. After 35 minutes, the hydrogen flowrate was decreased to 10 cc/min while the acetylene flowrate was increased to 24 cc/min. Under these conditions, with the hydrocarbon concentration increased very high, the catalyst should be rapidly buried under a passivating layer of carbon. Thus, lengthening of the filaments should stop and only an increase in diameter should occur. After 25 minutes, the hydrogen and acetylene flowmeters were turned off and argon was once again used to purge the tube of reactive gases.

The ball valve was opened after five minutes and the push rod was inserted to push the substrate out of the furnace to the end of the tube, where it was allowed to cool in flowing Argon for 15 minutes before removal.

In the second run, substrate #3 was subjected to the same procedure as substrate #2 except that the lengthening period was increased to an hour and the thickening period was eliminated.

In the third run, substrate #4 was also subjected to basically the same procedure as substrate #2 with the following changes: acetylene was replaced by propane, the lengthening period was increased to an hour, and the thickening period was eliminated.

## RESULTS

After removal from the growth reactor, substrates 2, 3, and 4 were viewed with the scanning electron microscope (SEM). Figure 4 is an SEM micrograph of the surface of substrate #2. The surface seems to be covered with only finely divided carbon soot. It seems that during the thickening period, the acetylene concentration was increased to such a high level that the atmosphere above the substrate consisted mainly of ionized acetylene molecules. There were few unreacted acetylene molecules. The ionized molecules reacted with eachother before they would even see the substrate surface, which resulted in soot formation rather than fiber growth. Thus, for run #2, it was decided that the thickening period would be eliminated to decrease the amount of soot formation so that the filaments, if they had formed, would be more readily visible. The lengthening period was increased to aid in making the fibers more visible.

With the elimination of the thickening phase, the level of soot formation on substrate #3 was dramatically decreased. However, there was still no evidence of fiber growth. It is believed that the temperature at which the first and second runs were performed is too high for acetylene to undergo the desired reaction that results in fiber growth. Decreasing the temperature might be one way to enhance the conditions for fiber growth. However, at low temperatures, the kinetics would not be favorable for the growth of fibers. Thus, the next logical step would be to decrease either the concentration of acetylene or the pressure. The first possibility is not feasible for two reasons. First, the rate of reaction is a function of concentration and would thus be slowed down tremendously if the concentration of acetylene were decreased to an appropriate level. Second, the minimum attainable concentration of acetylene was limited by the flow controllers used in these experiments. With regard to the second alternative, the experimental set-up used did not allow for the pressure to be varied. Thus, it was decided that, since acetylene is too reactive a species for the experimental conditions, switching to a less reactive gas such as propane in run #3 would be the only feasible alternative.

Figure 5 is an SEM micrograph of carbon fibers that were grown on substrate #4. It seems that by using propane, the concentration of ionized molecules in the atmosphere was effectively reduced enough that the molecules were able to reach the surface, where decomposition of the hydrocarbon can take place at the leading surface of the catalytic sites and deposition of carbon can occur at the opposite surface. Figure 6 shows the cross section of one of the fibers that was formed by vapor deposition of carbon on a hollow filament. The central filament itself was grown by catalytic action on an iron oxide particle. The hollow structure seen in Figure 6 has been widely observed. However, no valid explanation has been advanced to account for such a structure. Many researchers believe that the hollow core is caused by surface diffusion of carbon molecules around the catalytic particle.

## CONCLUSIONS

An apparatus in which vapor grown carbon fibers can be produced was constructed. For the reaction conditions used, it was found that when the iron oxide catalyst was reacted in acetylene and hydrogen, carbon filament formation was inhibited. Replacing acetylene with propane, a less reactive gas, resulted in the growth of fibers. However, the fibers did not grow in abundance. They were sparsely scattered along the edges of the substrate surface. Thus, it will be necessary to explore the conditions for which the yield will be increased. It is recommended that the duration of the experimental runs, the temperature at which the experiments are conducted, and the propane concentration be varied to investigate the influence of these variables on fiber growth. Furthermore, the effect of different catalyst-hydrocarbon systems should also be addressed.


## Acknowledgments

I would like to extend my appreciation to the Air Force Systems Command, Air Force Office of Scientific Research, and the Phillips Laboratory for their sponsorship of this research and to Research and Development Laboratories for their help with the administrative aspects of this program.

I would also like to thank Dr. Pete Pollock and Dr. Phillip Wapner for their invaluable help and support, which made my experience at the Phillips Laboratory a rewarding and enriching one, and Joe Maher for his help with the scanning electron microscopy.

## Figure Captions

Figure 1. Apparatus in which the filaments were grown. Flowmeters (FM) feed appropriate mixture of gases into the growth reactor.

Figure 2. Silica tube that was constructed for use in the growth reactor.

Figure 3. SEM micrograph of the iron oxide catalysts on the surface of a graphite substrate. The catalytic particles appear to have agglomerated together during evaporation of the ferrofluid. (Magnification-1340x)

Figure 4. SEM micrograph showing only soot formation on the surface of a graphite substrate that was reacted in an acetylene-hydrogen mixture at 950° C. No carbon filaments are visible. (Magnification-1570x).

Figure 5. Vapor grown carbon filaments grown from propane by an iron oxide catalytic particle. (Magnification-2460x)

Figure 6. SEM micrograph of the cross-section of a vapor grown carbon filament. (Magnification-4270x)

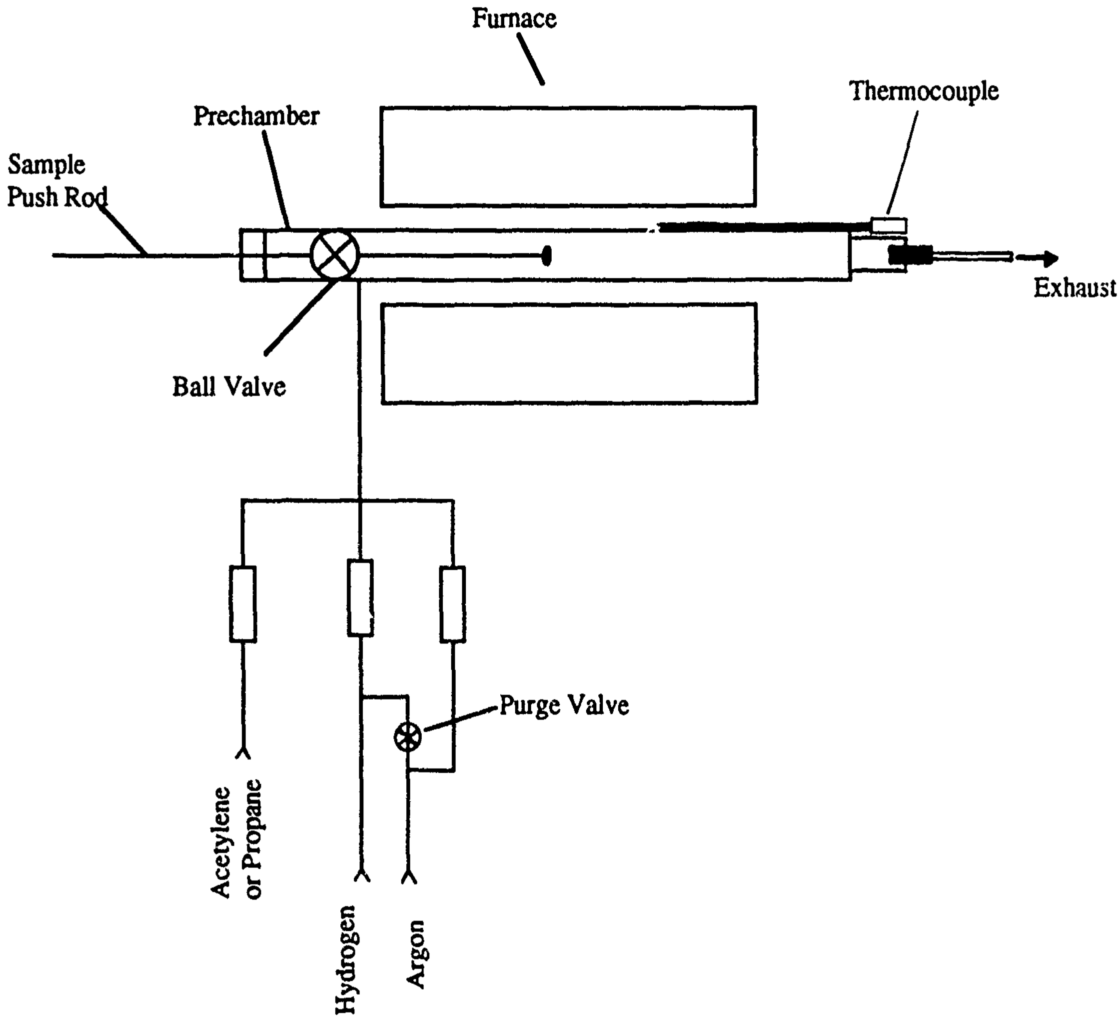


Figure 1. Apparatus in which the filaments were grown. Flowmeters (FM) feed appropriate mixture of gases through the silica tube into the furnace.

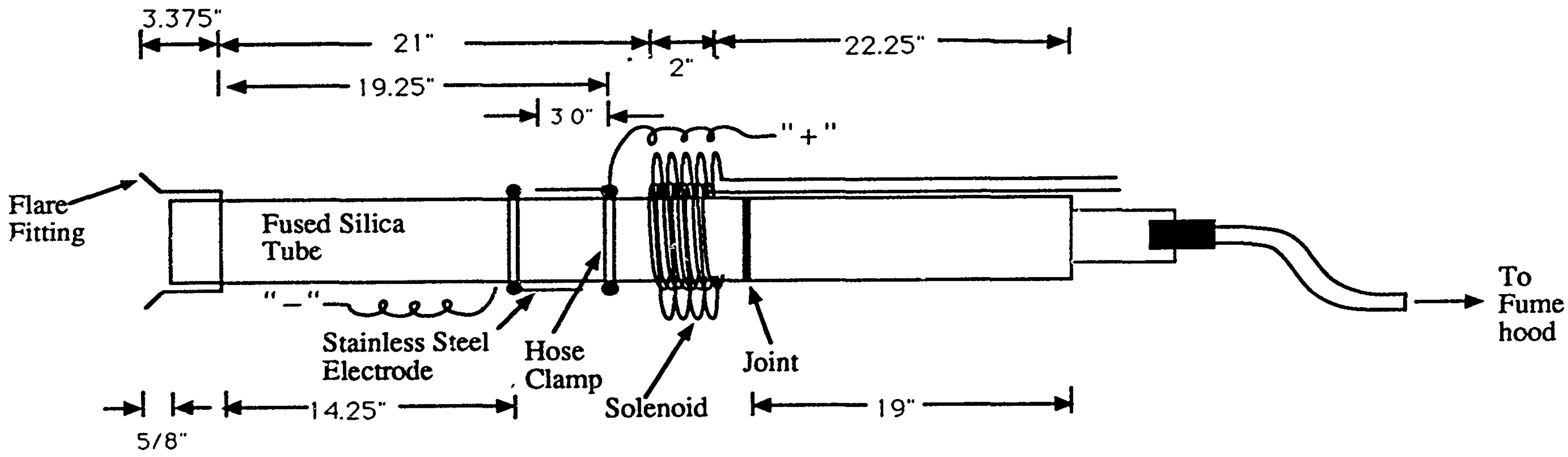


Figure 2. Silica tube that was constructed for use in the growth reactor.

Figure 3. SEM micrograph of the iron oxide catalysts on the surface of a graphite substrate. The catalytic particles appear to have agglomerated together during evaporation of the ferrofluid. (Magnification-1340x)

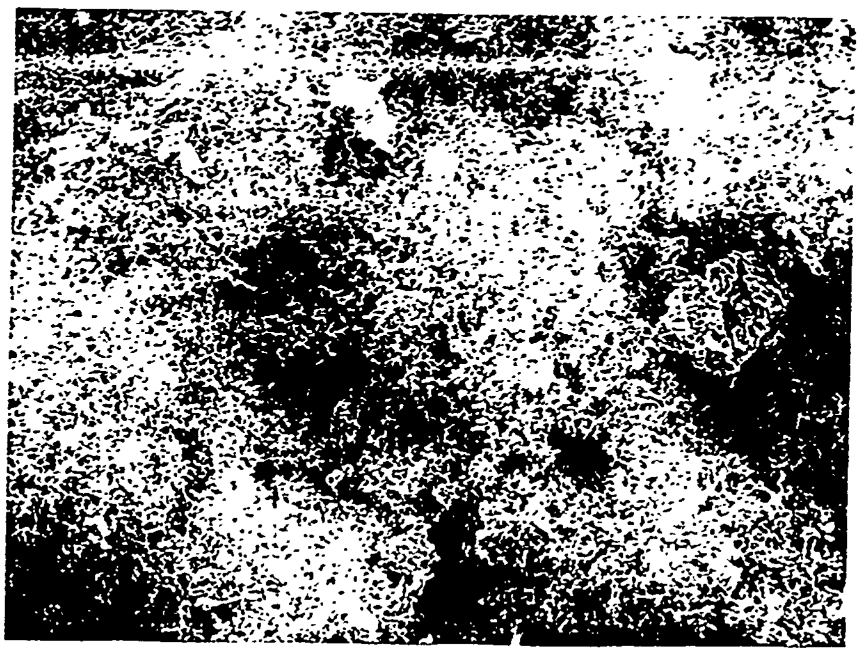

Figure 4. SEM micrograph showing only soot formation on the surface of a graphite substrate that was reacted in an acetylene-hydrogen mixture at 950° C. No carbon filaments are visible. (Magnification-310x)

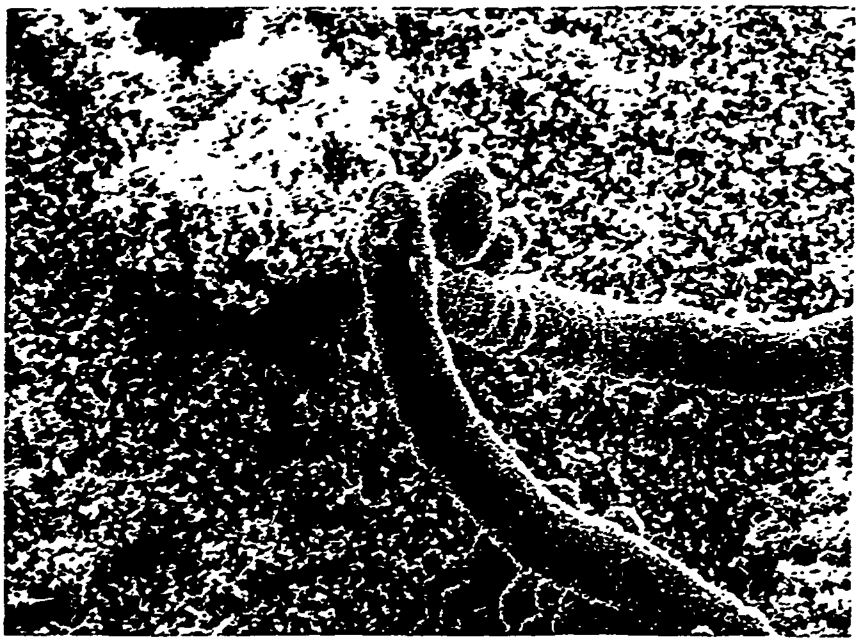

Figure 5. Vapor grown carbon filaments grown from propane by an iron oxide catalytic particle. (Magnification-2460x)

Figure 6. SEM micrograph of the cross-section of a vapor grown carbon filament. (Magnification-4270x)

## References


1. R. T. K. Baker, M. A. Barber, P. S. Harris, F. S. Feates, and R. J. Waite, *J. Catalysis* **26**, 51 (1972).
2. J. R. Rostrup-Nielson and D. L. Trimm, *J. Catalysis* **48**, 155 (1977).
3. G. G. Tibbetts, M. G. Devour and E. J. Rodda, *Carbon* **25**, 367 (1987).
4. R. T. Yang and K.L. Yang, *J. Catalysis* **93**, 182 (1985).

# SYNTHESIS OF PHOTOCROSSLINKABLE POLYMER FILMS FOR INFLATABLE SOLAR COLLECTORS

RODNEY MASON

## INTRODUCTION

Phillips Laboratory Directorate of Rocket Propulsion has been interested in solar propulsion since 1956. By the end of 1963, the program was dropped due to the lack of interest in the scientific community. It was't until 1978 when the AFOSR funded an information gathering project with Rocketdyne that solar propulsion was again recognized as a viable alternative to chemical rocketery.

. Rocketdyne determined that shuttle would be a good vehicle for getting solar experiments to low earth orbit. Since1984, the AFRPL has redirected attention from earth based concentrator to space flight orientated inflatable reflector. The solar propulsion concept is the means by which solar powered propulsion can accomplish interorbital linear and interplantery transfer missions. The main advantage of solar propulsion verses chemical propulsion is cost. The SPC is composed of three parts: the concentrators are inflatable and hollow, resembling large clam shells made of transparent films.

The thruster is designed to capture the solar energy from both collectors at the same time. The single propellant/tank contains a working fluid which is fed into the thruster where it is heated and expelled in producing thrust. The problems are that inflatable collectors are susceptible to micrometeroid penetration and loss of inflatable gas by diffusion through the thin polymer film(6 micron).

This will result in loss of reflector shape. The purpose of the project is to develop a polymer for use in the solar collection that will be rigidized by exposure to ultraviolet (UV) light after inflation mitigating the effect of gas loss.

## OBJECTIVE

As the recipient of the AFOSR summer research fellowship program, I have been instrumental in assisting to this laboratory's efforts in the synthesis of photocrosslinkable polymeric materials for inflatable solar collectors.

## DISCUSSION

The photocrosslinkable monomers that were used included: 2,3,5,6-tetramethyl-1,4-phenylene diamine (TMPDA); tetraethylmethylene dianiline (TEMDA); 2,6-diaminoanthraquinone (2,6-DAQ); and 1,4 diaminoanthraquinone (1,4-DAQ). The above monomers were reacted with 3,3',4,4'-benzophenone tetracarboxylic dianhydride (BTDA) to make polyamic acids which were then converted into polyimides by a solution imidization technique. A photocrosslinkable monomer (dihydroxychalcone-DHC) for the synthesis of a polyester was also prepared. Below illustrates the reactions of the polyimide and DHC syntheses:

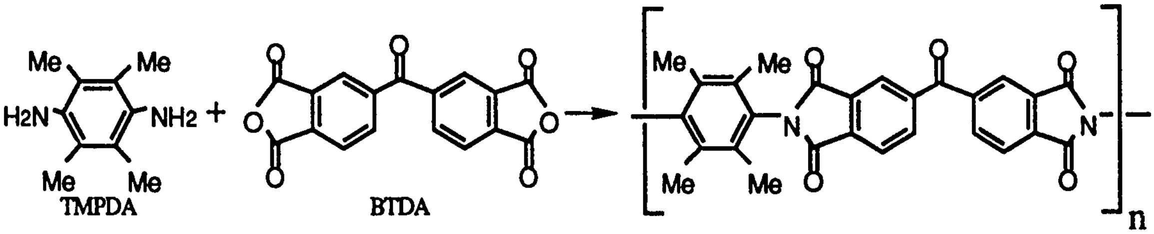
TMPDA
BTDA

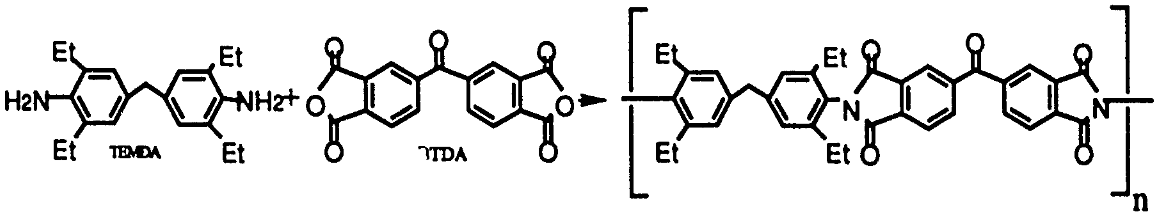
TEMDA
BTDA

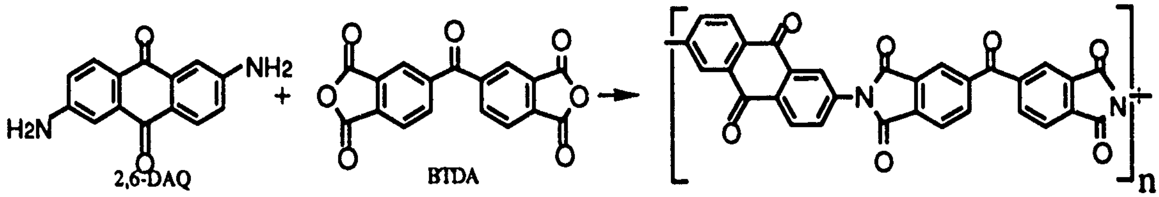
2,6-DAQ
BTDA

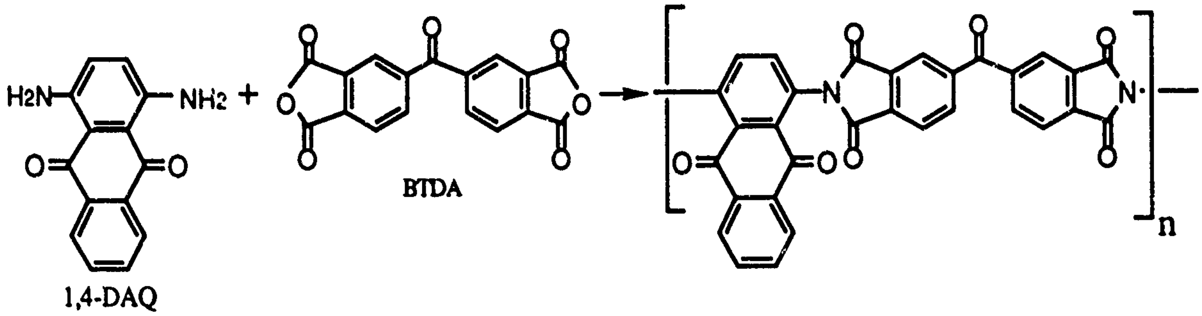
1,4-DAQ
BTDA

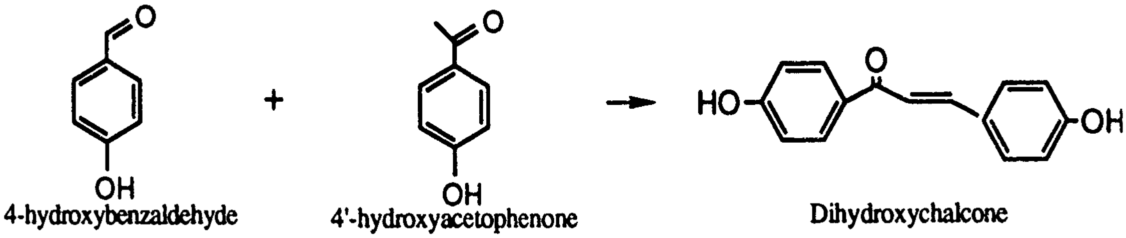
4-hydroxybenzaldehyde
4'-hydroxyacetophenone
Dihydroxychalcone

## PROCEDURES

Dihydroxychalcone

6.009 grams of 4-hydroxylbenaldehyde, 6.602 grams of 4'-hydroxylacetophenone and a 50% (13.196 grams ) potasium hydroxide (KOH) solution were added to a 500 milliliter erlymeyer flask. The reaction under magnetic stirring ran for several days while being closely monitored by thin layer chromatography. To initiate crystallization a 10% hydrochloric acid (HCL) solution was added until oily droplets appeared. The crystals were than dried in a vacuum oven and a melting point determined. The recrystallization was repeated until a constant melting point was achieved.

TMPDA Based Polyimide

The polymerization involved 2.0 grams (0.0122moles) of TMPDA crystallized from diethyl ether ($Et_2O$), dissolved in 20 milliliters of 1-methyl-2 pyrrolidinone (NMP) Along with 3.93 grams (0.01219 moles) of 3,3',4,4' benzophenone tetracarboxylic dianhydride purified by sublimation. Actually, the solids were added under a reduced nitrogen ($N_2$) flow rate and NMP was injected through a rubber septum. In insuring an inert atmosphere a vacuum pump followed by $N_2$ purging was repeatly generated.

In addition to, imidization followed which is a process of dehydration in converting a polyamic acid mixture to a polyimide. The imidization involved the addition of the polyamic acid mixture to a 20% solution of cyclohexyl pyrrolidinone (CHP) in NMP. The mixture was than heated to 165 C and dehydration carried out with a Dean Stark Trap. To induce precipitation, the solution was added to a 3:1 $MeOH/H_2O$ solution by means of a separatory funnel followed by filtering and drying. Finally, a soxhlet extraction appartus was set up to extract NMP with hexane.

2,6-Diaminoanthraquinone Based Polyimide

2,6-DAQ was recrystallized from absolute (EtOH) ethanol. Filtering and drying of crystals accompanied by a melting point determination followed. The melting point observation indicated a range of 335-339C which coincides with the literture. The crystals were added under a reduced nitrogen (N2) flow rate and the dimethylacetamide (DMAc) was injected through a rubber septum. Polymerization is the process in which the polyamic acid is formed. The polyamic acid formed here, involved the reaction of 0.435 grams of DAQ (0.00183 moles) and 0.591 grams BTDA (0.00183 moles) dissolved in DMAC. Stated earlier solution imidization is a process in which dehydration (-H2O) in converting a polyamic acid to a polyimide is formed.

20 milliliters of DMAC was added to the 2,6-DAQ based polyamic acid solution and the mixture was refluxed with a Dean Stark trap packed with molecular sieves. Next, to induce precipitation, a 3:1 MeOH/H2O solution was prepared and the viscous polymer was allowed to drip from a separatory funnel into solution. The precipitate was filtered and dried in a vacuum oven. Residuai DMAc was removed by soxhlet extraction.

1,4-Diaminoanthraquinone Based Polyimide

1,4-DAQ was recrystallizated from absolute ethanol (EtOH). The crystals were filtered and dried in a vacuum oven. The melting range was 255-263C verses the given literature range of 263-265C. The crystals were added under a reduced nitrogen ($N_2$) flow rate and the DMAC was injected through a rubber septum. The polyamic acid formed here involved the reaction of 0.679 grams DAQ (0.002849 moles) and 0.9183 grams of BTDA (0.002849 moles) dissolved in DMAC.

The polyamic acid was solution imidized by adding 2 milliliters of cyclohexyl pyrrolindinone in 20 milliliters of DMAC to the polymer solution and refluxing overnight with a Dean Stark trap packed with molecular sieves. The viscous solution was then added dropwise with stirring to a 3:1 $MeOH/H_2O$ solution to induce precipitation. Finally, a soxhlet extraction apparatus was set up to extract residual DMAC.

## RESULTS/CONCLUSIONS

Results of $^1H$, $^{13}C$ NMR , gas chromotography-mass spectroscopy, and Fourier transform infrared spectroscopy confirmed the structure of the polymers that were based on the diamines TEMDA; TMPDA; 2,6-DAQ; 1,4-DAQ; and the monomer DHC. Ultimately, the DHC will be polymerized with terephthaloyl chloride to form a polyester. The polymers will be cast into thin films and the mechanical properties of the films will be determined by dynamic mechanical analysis (DMA). The films will then be exposed to ultraviolet light to induce photocrosslinking and the DMA's will be run again to determine how the mechanical properties have changed. From these results it can be determined if any of these polymers will be suitable materials for inflatable solar concentrators.

# INCREASED DAMPING IN COMPOSITE TUBES THROUGH STRESS COUPLING AND CO-CURED DAMPING LAYERS: FORTRAN PROGRAM AND MEASUREMENTS

Dennis Duane Olcott
Graduate Student, Brigham Young University

ABSTRACT

A unique tube design which uses the stress coupling properties of composite materials and the high loss factors of viscoelastics was studied. A computer program was written to solve previously derived equilibrium equations for the tube. The damping loss factor and resonant frequency of four tubes were measured. The measured values corresponded well with those from the computer program, indicating that this unique tube design has great potential for providing high stiffness, high damping, and low weight tubes for space structures.

## 1.0 INTRODUCTION

Large space structures can suffer from vibration induced problems such as antenna and laser misalignment, blurry photographs and radar images, as well as premature fatigue damage. The control of such structures is a current area of research at the Phillips Laboratory, Edwards Air Force Base, California, primarily in the form of active, but also in passive, damping applications.

Active damping involves sensing vibrational movements and then controlling actuators to reduce the vibrations. The advantage of active damping is the potentially large damping achievable. The disadvantages of active damping include the need to imbed the sensors and actuators within the structure, the requirement for an external power source, and the narrow frequency range under which a particular active damping application is effective.

Passive damping is usually effective under very wide frequency ranges and no external power source is required. Previously, however, passive damping techniques had achieved relatively low damping loss factors using techniques suitable for space structures.

A passive damping technique suitable for space structures with higher potential damping was proposed by Barrett (Barrett, 1989). This technique uses the shear coupling properties inherent in fiber-reinforced composites to induce large shear strains across viscoelastic materials. Specifically, a viscoelastic material is sandwiched between two layers of high-stiffness composite layers in a tube. As the tube is loaded axially, the inner and outer composite layers rotate differentially, thus shearing the middle viscoelastic layer. Hysteretic losses in the viscoelastic layer convert the vibrational kinetic energy to heat, thus reducing the vibrations. Problems with the concept include the lack of significant shearing along the entire length of the tube and also that simple end fixtures restrict differential rotations, thus eliminating the shear in the viscoelastic layer.

A unique, new design was proposed by the author and subsequently analyzed at Brigham Young University. By placing several short tubes (similar to Barrett's) in series, a total tube is created which has many effective "ends." See Figure 1. Since the significant shearing in Barrett's tubes occurred at the ends, this new tube contains many regions of significant shearing along its entire length, thus increasing the total damping loss factor.

Several tubes were manufactured by the author prior to working in the Air Force Summer Research Program and several patents regarding concept and manufacturing technique are currently being prepared.

## 2.0 DISCUSSION OF PROBLEM

Two primary issues were addressed while working at Edwards Air Force Base:

1. Completion of a FORTRAN code (initiated at Brigham Young University) which allows design studies to be conducted, and
2. Initial testing of previously manufactured tubes using both Air Force and Brigham Young University equipment.

The primary goal was to design tubes with sufficient damping loss factors to warrant further study and eventual inclusion in future space-based platforms considering factors of: performance, cost, weight, and active damping reduction or elimination.

## 2.1 FORTRAN Code

A FORTRAN code, DAMTUBE, was created to solve the equilibrium equations derived by the author (Olcott, 1991). This program was designed to conduct parametric studies involving material properties and tube geometries.

Program inputs include material properties, tube geometry, and tube end constraints. Outputs include the axial stiffness and loss factor. The axial stiffness, $k_z$, is computed from

$$k_z = \frac{P}{w_L} \tag{1}$$

where $w_L$ is the axial displacement at the end of the tube and P is the applied axial load. Since the displacement contains both real and imaginary components, the stiffness in Equation (1) is a complex value. The loss factor is the ratio between the imaginary and real components of the stiffness:

$$\eta = \frac{k_z''}{k_z'} \tag{2}$$

where ' and " indicate the real and imaginary components of $k_z$.

## 2.2 Measurement Technique

A simple method for testing the axial dynamic properties of composite tubes was first documented by Andriulli (Andriulli 1989). A tube is hung from elastic bands at both ends to simulate free-free boundary conditions, Figure 2. For axial testing, an accelerometer is affixed to one end of the tube with beeswax and the end of the tube is struck with an impulse hammer. The frequency response function of the tube (measured by the accelerometer) with respect to the input load (measured by the hammer) is calculated using a spectrum analyzer. The damping loss factor, $\eta$, is calculated using either standard log decrement or half-power methods. Material modulus is determined as a function of the measured resonant frequency.

# 3.0 RESULTS AND DISCUSSION

## 3.1 Parametric Studies

Parametric studies were conducted using DAMTUBE by varying the ply orientation angle $\phi$ from $0^{\circ}$ to $35^{\circ}$, and the number of segments in the tube from 1 to 25. The tubes modelled were identical to the tubes eventually tested, except in length where the modelled tubes were 0.6 inches shorter. The geometry of the tube model was:

1. 14.0 inches length
2. 1.0 inch inner diameter
3. 5 plies (0.0055 inch thickness per ply) in each of the two stiffness (composite) layers
4. 0.01 inch thick damping (viscoelastic) layer.

The material properties used in the analysis are contained in Table 1.

### 3.1.1 Axial Stiffness

The effect of the number of segments on the axial stiffness and loss factor is contained in Figures 3 and 4. The axial stiffness plot shows that increasing the number of segments has a mild effect on reducing total stiffness. The reduced stiffness occurs, however, as the loss factor increases dramatically. The loss factor reaches a peak and then declines when the individual segments become so short and closely packed that they begin inhibiting shearing in neighboring segments, thus limiting the overall damping. A factor not considered by the computer program is the effect of joint length between adjacent segments. If the individual segments become too short, they will consist entirely of joints. Therefore, the recommended number of segments for the modelled tube considering both loss factor and section length is eight (8).

### 3.1.2 Orientation Angle

The effect of the orientation angle on the axial stiffness, imaginary axial stiffness, and loss factor is contained in Figures 5, 6, and 7. The axial stiffness reduces at a rate approximately proportional to the increase in loss factor as the orientation angle increases. Thus, some intermediate angle provides the best compromise between maximum axial stiffness and maximum loss factor, depending on the appropriate design constraints.

The dynamic displacement of a structure is determined by the imaginary axial stiffness. The imaginary stiffness of the tube in this study reached a peak around 15°. Since these damped tubes are designed for vibration, not static, applications, a wind angle of 15° is recommended.

### 3.2 Physical Testing

Four tubes were tested, each differing in their fiber orientation angle, the number of segments, and the type of damping material used, if any:

**0° Tube:** The first tube constructed contained only 0° plies with no damping layer. An extra 90° was also added to the outside of the tube to prevent axial cracks from forming during the cure cycle.

**±10° Tube:** The second tube contained an inner stiffness layer with +10° fiber orientations and an outer layer with -10°. Again, no damping layer was used.

**±10° Tube, Three Segments, AF-32:** The third tube contained three (3) segments of ±10° wind angles which alternated along the length and between the inner and outer layers as has previously been discussed to enhance damping. The two end segments were each 4.30 inches long, with a center segment 6.00 inches long. One 0.01 inch thick layer of AF-32 film adhesive was placed between the inner and outer stiffness layers.

**±16° Tube, Sev. . Segments, ISD112:** The final tube contained seven (7) segments alternating between positive and negative 16° along the length. Again, the inner and outer layers had opposite angles. A 0.01 inch thick sheet of ISD112 viscoelastic material was sandwiched between the two stiffness layers.

All tests were conducted at the Applied Composite

Structures Laboratory of the Phillips Laboratory at Edwards Air Force Base, California. Equipment used included: a dynamic signal analyzer (Hewlett-Packard HP35660A); an accelerometer (Endevco Model 2250-A); an impulse hammer (PCB Piezotronics, Inc. Model 086B01); two power/signal conditioners (PCB Piezotronics, Inc. Model 480D06); and a digital scale (Mettler Instrument Corp. Type AE 160).

Each tube tested was suspended from rubber bands to simulate free-free boundary conditions, similar to the method used by Andriulli. The signal analyzer calculated the frequency response function of the tube (acceleration over force) by averaging the results from 25 impacts.

The weight of each tube was measured by the digital scale and converted to mass assuming a gravitational acceleration of 32.2 ft/sec$^2$.

The results of the physical testing, including natural frequency, loss factor, and coherence, are recorded in Table 2. The real and imaginary parts of the frequency response functions for an example specimen, specifically the ISD112 damped specimen, are recorded in Figures 8 and 9. The coherence plot for this specimen is contained in Figure 10.

### 3.2.1 Natural Frequency, $f_r$

The measured frequency of the first resonant mode, in this case an axial extension mode, corresponded very well with the analytically predicted values, Table 2. For the 0° tube, the reason for the excellent correspondence was that the unidirectional modulus used in the model was obtained from the $0^\circ$ tests. For the other tubes, the resonant frequencies were predicted within 1% of the measured frequencies. This indicates that the mass increase and axial stiffness loss in the damped tubes is accurately modelled in the computer program.

### 3.2.2 Loss Factor $\eta$

The loss factor in the $\pm 16^\circ$ tube with ISD112 was the only tube fabricated with a predicted high loss factor. The measured loss factor, however, was 30% lower than predicted.

The optimistic loss factor prediction can be explained by two factors. First, joints exist in the actual test specimens which are not accounted for in the computer model. These locations will not experience as large of shear deformations as the model predicts, thus reducing the total loss factor. Second, the model allows the slope (first derivative with respect to axial position) of the displacement function to be discontinuous. Since continuous fibers will prevent such "hinge" action, the maximum displacements at the joints will be slightly reduced, again reducing the overall loss factor.

### 3.2.3 Coherence

The coherence plots for all four tubes showed relatively constant values above 92% in the 800 Hz span around the resonant frequency. The coherence function reports the repeatability of the measurements taken from the 25 individual hammer strikes. One rule-of-thumb is that coherence levels above 80% are acceptable, thus the 92% and above levels obtained in these tests were all acceptable.

### 3.2.4 Mass Increase

A significant result of the physical tests was the extremely low, less than 2%, increase in the mass of the damped tubes relative to the mass of the undamped tubes. This indicates that damped tubes can be fabricated with damping material added, but without stiffness layer material being removed to maintain a constant total mass.

## 3.3 ASTREX Application

The United States Air Force built a test facility specifically to study the vibration and control of large space structures. This facility, called the Advanced Space Structure Technology Research Experiment or ASTREX, is located at the Phillips Laboratory on Edwards Air Force Base, California. The facility consists of a 40x40x40 ft enclosure with a spherical air bearing capable of supporting 14,500 lb structures. The air bearing isolates the supported structure from outside vibrations, thus more closely simulating a satellite floating in space.

A simulated space based laser satellite is currently being studied in the ASTREX facility. The major components of this structure are the primary and secondary mirrors, three long booms connecting the two mirrors, and associated thrust motors and computer equipment necessary to support the laser. See Figure 11.

The three primary booms are 198 inches long, have a 5.00 inch outer diameter, a 0.120 inch wall thickness, and an overall modulus of 11.2 Msi (Jacoy 1991). The modulus is created using T300 graphite fibers and Ciba-Geigy ARALDITE AMIME epoxy with combined properties of $E_1$=34.5 Msi, $E_2$=1.96 Msi, $\upsilon_{12}$=0.28, $G_{12}$=1.36 Msi and a ply layup, from the inner to the outer ply, of ±15, ±15, ±38, ±38, ±15, and ±15. Each ply is 0.01667 inches thick. An overlap 90° ply is also added for protection which is 0.020 inches thick. Assuming a typical loss factor for graphite/epoxy of 0.5%, the currently used booms would also have a 0.5% loss factor.

Using the unique, new, damped tube concept, replacement tubes could be constructed with identical stiffness, slightly lower weight, and a much higher loss factor. By maintaining the length, diameter, and wall thickness constant, replacement tubes were designed with inner and outer stiffness layers 0.05 inches thick, a damping layer 0.01 inches thick, and an overlap 90° layer which was also 0.01 inches thick. The slightly lower density of most viscoelastic materials relative to graphite epoxy would result in a slight decrease in overall structure weight.

A parametric study using DAMTUBE was conducted to find the various combinations of wind angle and total number of segments which would give an overall axial stiffness of 0.10406 Mlbf/in, identical to that of the original tubes, as well as the maximum possible loss factor.

The maximum number of segments was limited to 50, since this would give each individual segment a length of approximately 4 inches, considered reasonable for this size tube.

The tube which had the correct axial stiffness as well as the highest loss factor contained 50 segments and a wind angle of $24^{\circ}$. The predicted loss factor was 9.6%.

From the previous testing, the predicted loss factor was found to be overly optimistic. Assuming that the actual loss factor is only 70% of the predicted value, the best loss factor achievable in replacement booms for the laser platform is approximately 6.7%.

Therefore, replacement booms for the space based laser could be constructed and tested in the ASTREX facility with:

1. Axial stiffness identical to the current tubes
2. Slightly lower weight
3. Loss Factor of 6.7% or 13 times greater than the original booms.

## 4.0 CONCLUSIONS AND RECOMMENDATIONS

1. The computer code DAMTUBE performed well in predicting the stiffness of damped tubes, as was shown by the excellent correlation with measured natural frequencies. Although the predicted loss factors were optimistic, they were correct in predicting the order of magnitude. The final damped tube constructed (which contained $\pm 16^{\circ}$ wind angles, 7 segments, and ISD112 damping material) showed that the new damped tube concept actually works and merits further study.

2. The analysis technique and computer program should be

refined to more accurately predict the loss factor.

3. Full-scale testing of these tubes in a large structure would allow them to be tested both at much lower frequencies, which are of primary interest to the Air Force, and under combined loading conditions. An excellent test bed would be the U.S. Air Force's ASTREX program. A large-scale simulated space-based laser platform already exists for vibration control testing. Three 198 inch booms hold a critical secondary mirror at a precise location away from the primary mirror. By replacing these three booms with three damped tubes, a relatively low-cost test of their performance could be made.

## REFERENCES


Andriulli, J.B. "Measured Damping and Modulus of Composite Cylinders." Proceedings of Damping '89 (1989): BCC-1-26.

Barrett, David J. "A Design for Improving the Structural Damping Properties of Axial Members." Proceedings of Damping '89 (1989): HCB-1-18.

Jacoy, Paul. Jet Propulsion Laboratory. Telephone Interview (July 18, 1991).

Olcott, Dennis D., Rotz, Christopher A., and Barrett, David J. "Improved Damping in Composite Tubes Through Stress Coupling and Co-cured Damping Layers." To be published in 23rd International SAMPE Technical Conference (October 1991).

Table 1. Material Properties.

| Material | Mechanical Properties | |
|---|---|---|
| 6048 Graphite/ Epoxy Prepreg | $E_1$ (Msi) | (18.55,0.1855) |
| | $E_2$ (Msi) | (1.30,0.013) |
| | $G_{12}$ (Msi) | (1.03,0.0103) |
| | $\nu_{12}$ | 0.30 |
| AF-32 @ 10 kHz, 75°F | G (ksi) | (18.4,12.8) |
| ISD112 @ 10 kHz, 75°F | G (ksi) | (1.5,1.5) |

Table 2. Measured Physical Properties of Test Tubes.

| | | Specimen | | | |
|---|---|---|---|---|---|
| | | 0° | ±10° | ±10°,w/AF-32 | ±16° w/ISD112 |
| Calculated Values: | $\eta$ (%) | 1.00 | 1.00 | 1.28 | 6.22 |
| | $f_r$ (kHz) | 11.37 | 11.01 | 10.78 | 9.41 |
| | $k_z$ (Mlbf/in) | 0.2337 | 0.2209 | 0.2144 | 0.1628 |
| Measured Values: | Mass (g) | 79.234 | 79.143 | 80.983 | 80.644 |
| | $\eta$ (%) | 0.955 | 1.22 | 1.25 | 4.42 |
| | $f_r$ (kHz) | 11.30 | 10.96 | 10.68 | 9.46 |
| | Coherence (%) | 93.8 | 94.6 | 92.6 | 94.4 |

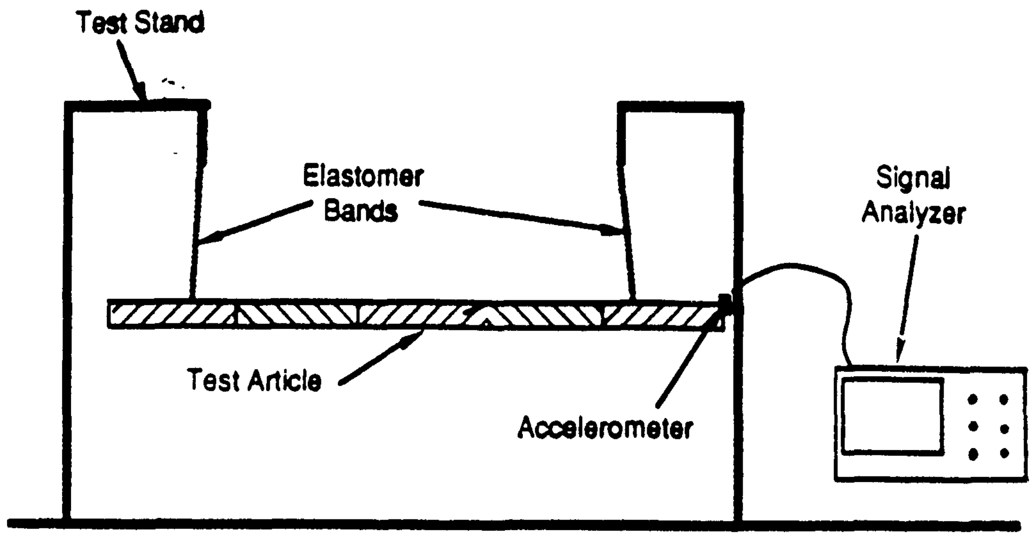


Figure 1. Unique Damped Tube Design with Varying Ply Orientation Angle along the Length of the Tube.

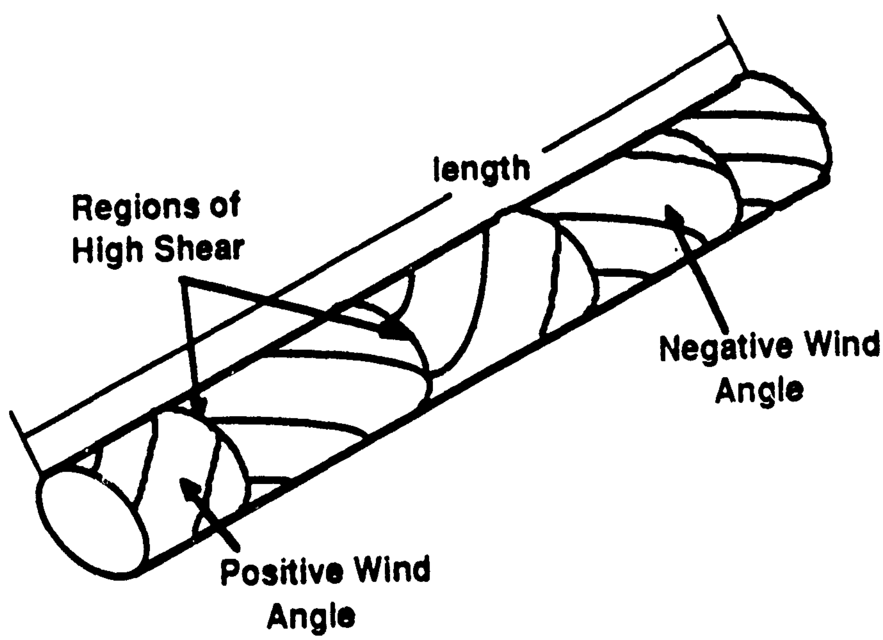


Figure 2. Andriulli's Composite Tube Test Setup.

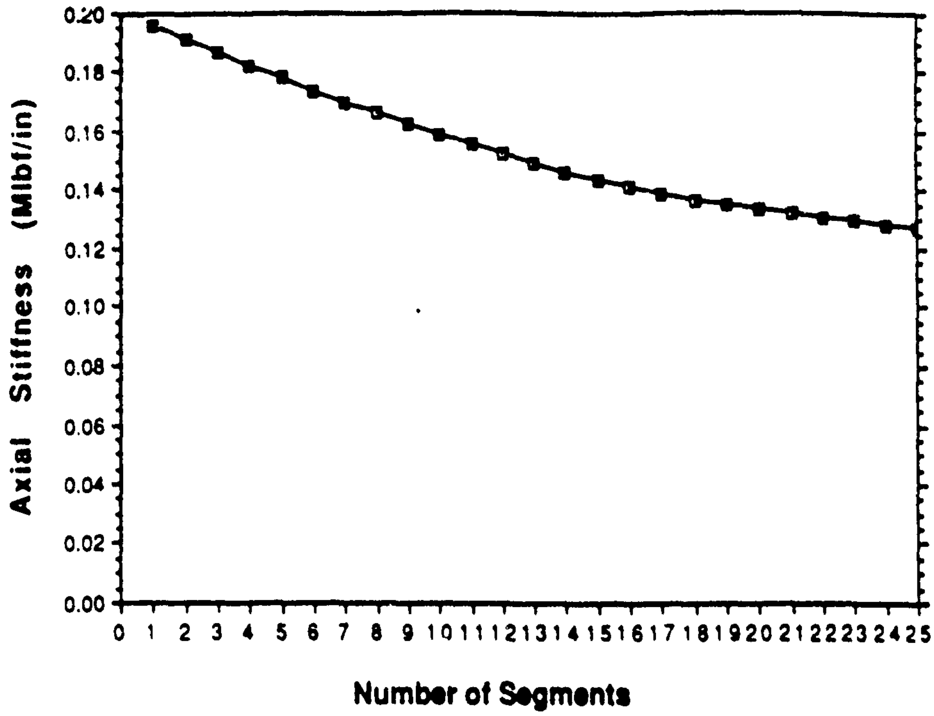


Figure 3. Predicted Axial Stiffness, $k_z$, versus the Number of Segments for a 16° ISD112 Tube.

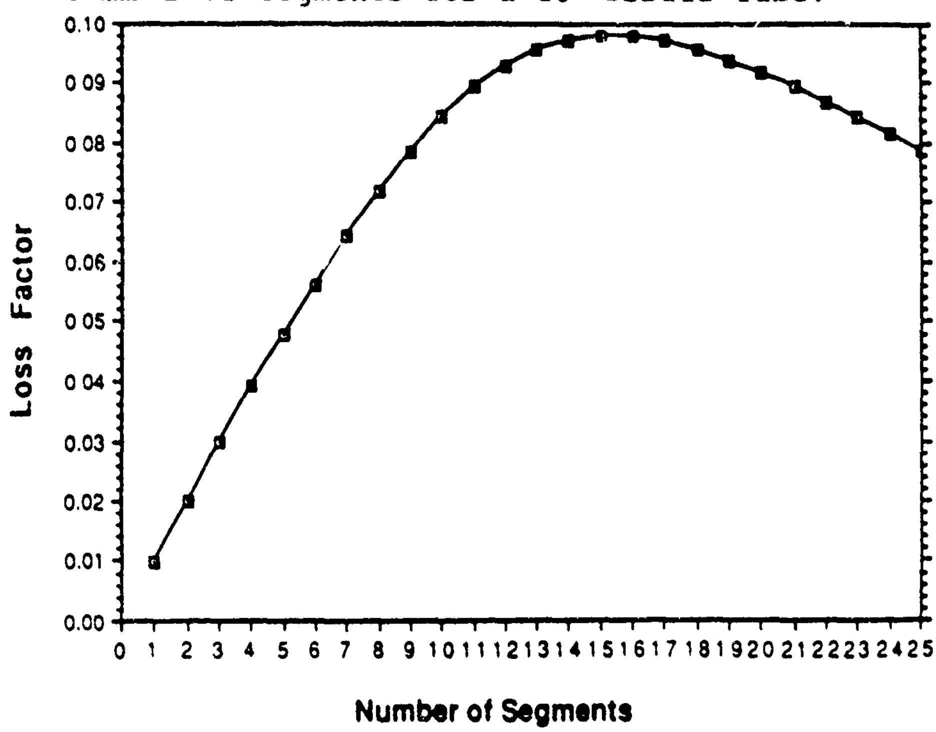


Figure 4. Predicted Loss Factor, $\eta$, versus the Number of Segments for a 16° ISD112 Tube.

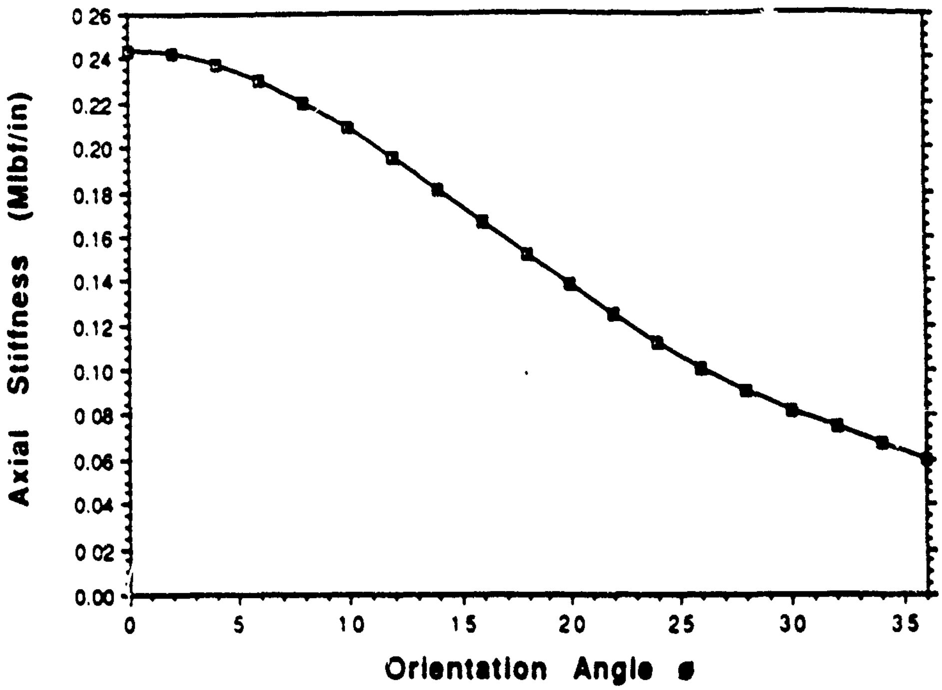


Figure 5. Predicted Axial Stiffness, $k_z$, versus the Orientation Angle for an Eight Segment, ISD112 Tube.

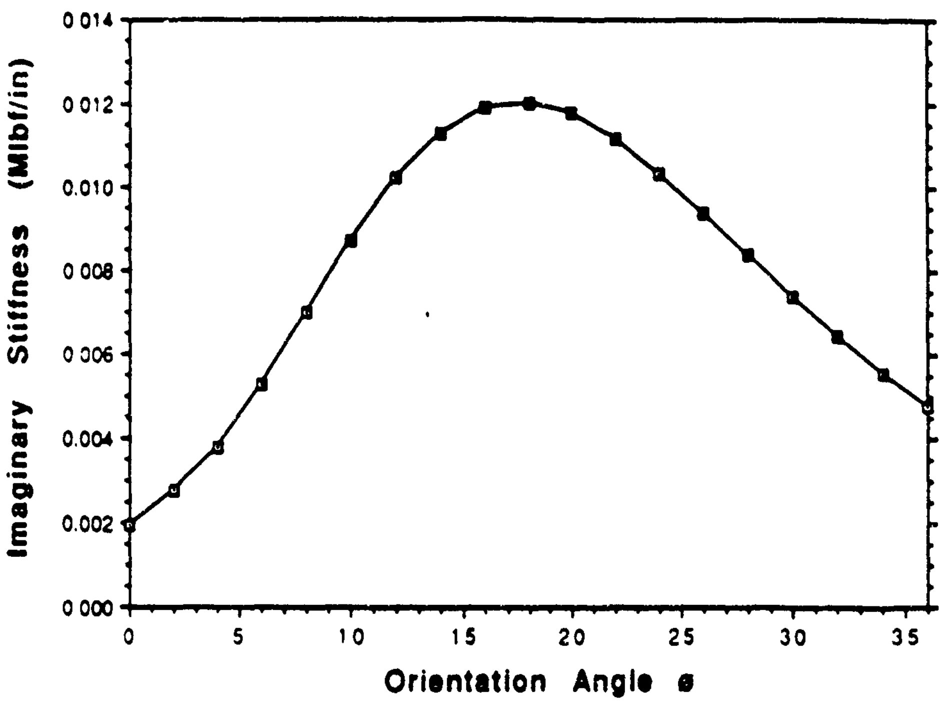


Figure 6. Predicted Imaginary Axial Stiffness, $k_z''$, versus the Orientation Angle for an Eight Segment, ISD112 Tube.

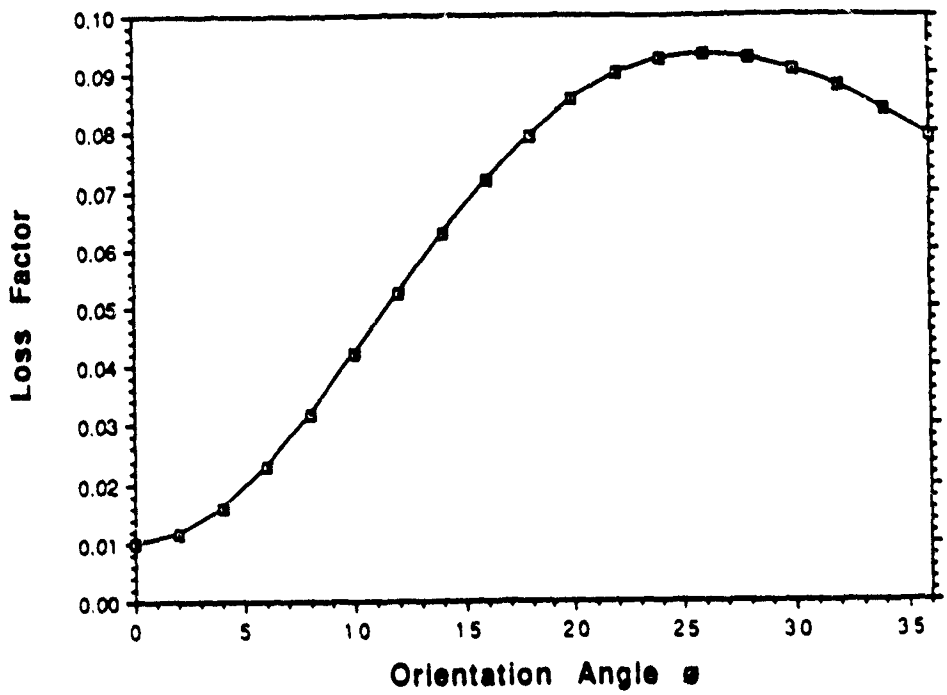


Figure 7. Predicted Loss Factor, $\eta$, versus the Orientation Angle for an Eight Segment, ISD112 Tube.

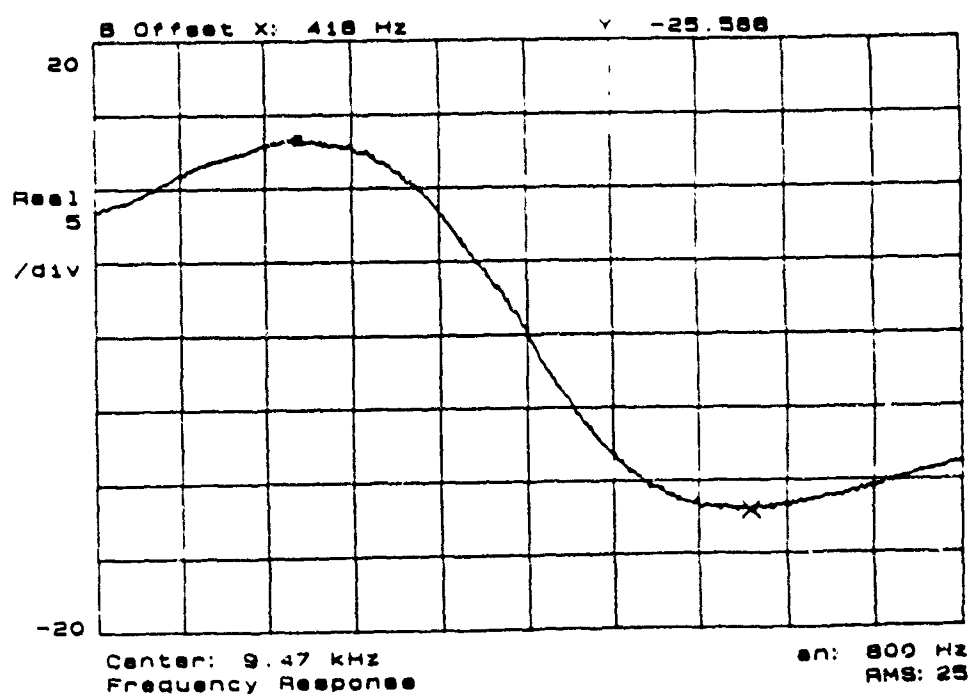


Figure 8. Real Components of the Frequency Response of the Seven Segment, $\pm 16^{\circ}$, ISD112 Tube.

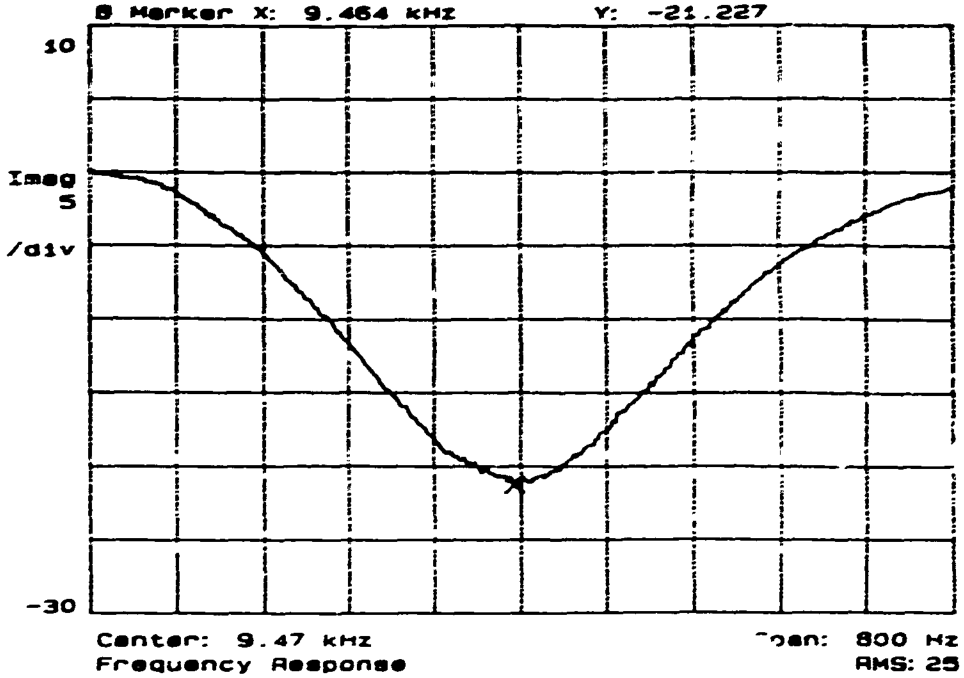


Figure 9. Imaginary Components of the Frequency Response of the Seven Segment, $\pm 16^{\circ}$, ISD112 Tube.

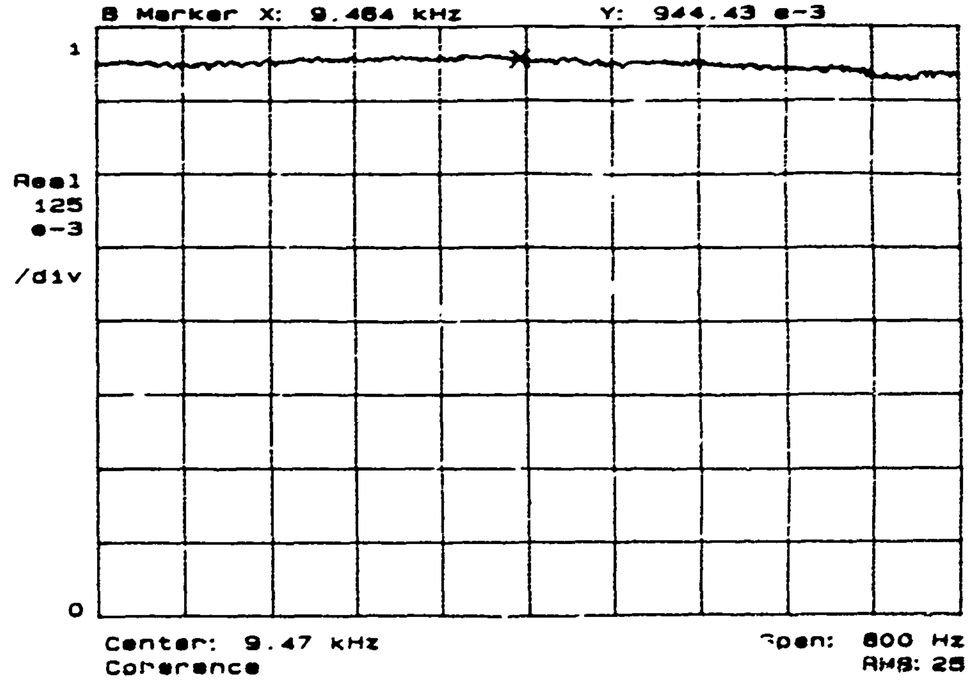


Figure 10. Coherence Plot for the Frequency Response of the Seven Segment, $\pm 16^{\circ}$, ISD112 Tube After 25 Hammer Strikes.

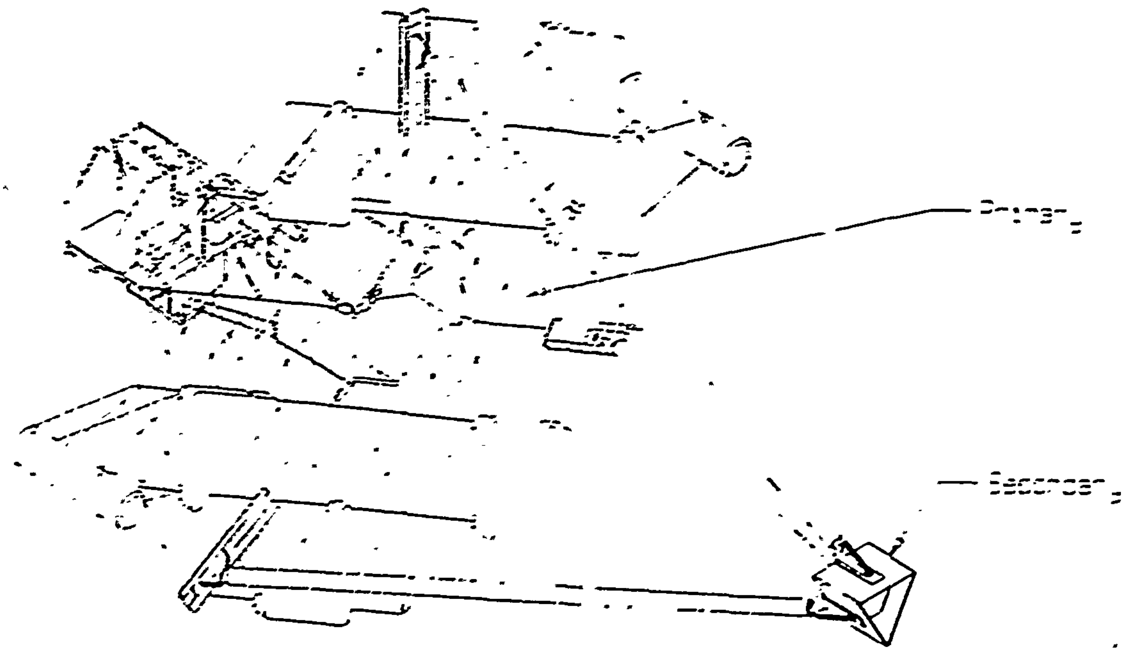

Figure 11. Diagram of Space Based Laser Currently Being Tested in the ASTREX Facility.

# Developmental Research on Differential Inversion

Thomas W. Drueding

August 13, 1991

**Abstract**

This report contains the progress of the summer research into the implementation of the differential inversion technique for temperature retrieval. The full derivations of the equations used are explored to determine what assumptions are involved in the initial implementation. The weakest assumption appears to be the representation of the weighting function as a convolution type kernel. Results from algorithms that account for the variation in the weighting function are reported and demonstrate a need for further research into the more general solution. A derivation of a differential inversion type solution to the more general weighting function is then shown. In addition the possible usefulness of a massively parrallel machine for doing temperature retrieval is determined.

# 1 Determination of Temperature Profiles

## 1.1 Introduction

Satellite observations provide a means of obtaining temperature profiles and other parameters in the atmosphere[2]. The satellite instrument observes the infared upwelling radiance. For the determination of temperature profiles, the region around the $CO_2$ absorption band at 15$\mu$m is used. The optical thickness in this region varies with the height in the atmosphere, which allows for the calculation of the temperature as a function of height.

The equation of radiative transfer that must be solved is a Fredholm integral equation. The standard technique used [3] [8] is a iterative relaxation method. The solution found is not unique, but will represent a solution that is "closest" to an initial guess used to begin the process. In this sense, the solution may be said to be biased towards the initial trial solution. The method suggested here was developed by Dr. Jean I. F. King of the Phillips Laboratory[6]. The solution proposed is based on the work of Eddington [4] and is further developed using *hyperdistribution* techniques, which were invented by Prof. Guido v. H. Sandri of Boston University [7].

## 1.2 Derivation of Fredholm Equation

We begin with the Schwarzchild equation which relates the Intensity, $I$, of the upwelling radiance and the Plank Intensity, $B$, as a function of height. The density of the atmospheric gas, $\rho$, and the absorption coefficient, $k_\nu$ are also functions of height

(*Assumption 1 : Local thermodynamic equilibrium*)

$$\frac{dI}{dz_1} = k_\nu \rho (B - I) \tag{1}$$

The solution for the intensity is given by

$$I_\nu(z_1) = e^{-\int_{z_0}^{z_1} k_\nu \rho dz'} I_0 + e^{-\int_{z_0}^{z_1} k_\nu \rho dz'} \int_{z_0}^{z_1} B_\nu(T(y))\, k_\nu \rho\, e^{\int_{z_0}^{y} k_\nu \rho dz'} dy \tag{2}$$

The observations are made at a height $z_1$ are dependent on a surface contribution of, $I_0$, at a surface height of $z_0$.

Rearrange the integrating factor knowing $y \leq z_1$ as

$$e^{-\int_{z_0}^{z_1} k_\nu \rho dz'} e^{\int_{z_0}^{y} k_\nu \rho dz'} = e^{-\int_{y}^{z_1} k_\nu \rho dz'} \tag{3}$$

to obtain the following

$$I_\nu(z_1) = e^{-\int_{z_0}^{z_1} k_\nu \rho dz'} I_0 + \int_{z_0}^{z_1} B_\nu(T(y))\, k_\nu \rho\, e^{-\int_{y}^{z_1} k_\nu \rho dz'} dy \tag{4}$$

The surface term can be expressed as an integral with $I_0 = B_\nu(T_0)$

$$e^{-\int_{z_0}^{z_1} k_\nu \rho dz'} I_0 = \int_{-\infty}^{z_0} B_\nu(T_0)\, k_\nu \rho\, e^{-\int_{y}^{z_1} k_\nu \rho dz'} dy \tag{5}$$

## 1.2 Derivation of Fredholm Equation

We begin with the Schwarzchild equation which relates the Intensity, $I$, of the upwelling radiance and the Plank Intensity, $B$, as a function of height. The density of the atmospheric gas, $\rho$, and the absorption coefficient, $k_\nu$ are also functions of height

(*Assumption 1 : Local thermodynamic equilibrium*)

$$\frac{dI}{dz_1} = k_\nu \rho (B - I) \tag{1}$$

The solution for the intensity is given by

$$I_\nu(z_1) = \mathrm{e}^{-\int_{z_0}^{z_1} k_\nu \rho\, dz'} I_0 + \mathrm{e}^{-\int_{z_0}^{z_1} k_\nu \rho\, dz'} \int_{z_0}^{z_1} B_\nu(T(y))\, k_\nu \rho\, \mathrm{e}^{\int_{z_0}^{y} k_\nu \rho\, dz'}\, dy \tag{2}$$

The observations are made at a height $z_1$ are dependent on a surface contribution of, $I_0$, at a surface height of $z_0$.

Rearrange the integrating factor knowing $y \leq z_1$ as

$$\mathrm{e}^{-\int_{z_0}^{z_1} k_\nu \rho\, dz'} \mathrm{e}^{\int_{z_0}^{y} k_\nu \rho\, dz'} = \mathrm{e}^{-\int_{y}^{z_1} k_\nu \rho\, dz'} \tag{3}$$

to obtain the following

$$I_\nu(z_1) = \mathrm{e}^{-\int_{z_0}^{z_1} k_\nu \rho\, dz'} I_0 + \int_{z_0}^{z_1} B_\nu(T(y))\, k_\nu \rho\, \mathrm{e}^{-\int_{y}^{z_1} k_\nu \rho\, dz'}\, dy \tag{4}$$

The surface term can be expressed as an integral with $I_0 = B_\nu(T_0)$

$$\mathrm{e}^{-\int_{z_0}^{z_1} k_\nu \rho\, dz'} I_0 = \int_{-\infty}^{z_0} B_\nu(T_0)\, k_\nu \rho\, \mathrm{e}^{-\int_{y}^{z_1} k_\nu \rho\, dz'}\, dy \tag{5}$$

substituted for

$$I_\nu(z_1) = \int_{-\infty}^{z_0} B_\nu(T_0)\, k_\nu\rho\, e^{-\int_y^{z_1} k_\nu\rho\, dz'}\, dy + \int_{z_0}^{z_1} B_\nu(T(y))\, k_\nu\rho\, e^{-\int_y^{z} k_\nu\rho\, dz'}\, dy. \tag{6}$$

Now define $B'_\nu$ as a function of $y$ with a range from $-\infty$ to $+\infty$

$$B'_\nu(y) = \begin{cases} B_\nu(T=0), & \text{if } y > z_1; \\ B_\nu(T(y)), & \text{if } z_1 \geq y > 0; \\ B_\nu(T_0), & \text{if } y \leq 0. \end{cases} \tag{7}$$

This is a standard technique to extend the limits of integration from $-\infty$ to $+\infty$ by replacing the definition for $B_\nu$ and combining terms

$$I_\nu(z_1) = \int_{-\infty}^{+\infty} B'_\nu(y) \left( k_\nu\rho\, e^{-\int_y^{z_1} k_\nu\rho\, dz'} \right) dy \tag{8}$$

Define $\tau$ the transmittance as

$$\tau_\nu(z_1, y) = e^{-\int_y^{z_1} k_\nu\rho\, dz'} \tag{9}$$

and define $W$ the weight function as

$$W_\nu(z_1, y) = \frac{\partial \tau_\nu(z_1, y)}{\partial y} = k_\nu\rho\, e^{-\int_y^{z_1} k_\nu\rho\, dz'} \tag{10}$$

We now have the following integral equation for the intensity,

$$I_\nu(z_1) = \int_{-\infty}^{+\infty} B'_\nu(y)\, W_\nu(z_1, y)\, dy \tag{11}$$

By assuming the observation is outside the atmosphere we can further simplify

(*Assumption 2: Evaluation of the upwelling radiance at infinity*)

$$I_\nu = I_\nu(+\infty),\ W_\nu(y) = W_\nu(+\infty, y) \tag{12}$$

for the weight function

$$W_\nu(y) = k_\nu \rho\, e^{-\int_y^\infty k_\nu \rho\, dz'} \tag{13}$$

The intensity is now expressible as follows

$$I_\nu = \int_{-\infty}^{+\infty} B'_\nu(y)\, W_\nu(y)\, dy \tag{14}$$

If we further assume that the Planck function is not dependent on the frequency within the range of the observations.

(*Assumption 3: The Planck function is not dependent on frequency*)

$$B'_\nu(y) = B'_{\bar{\nu}}(y) \tag{15}$$

By observing the the frequency relates to a specific height in the atmosphere defined as the height of the peak of the weight function, we write both the intensity and the weight as functions of this height $\zeta$. This allows us to go from a series of integral constraint equations to a functional integral equation. (*Assumption 4: peak height is a smooth function of frequency*)

$$I_\nu = I(\zeta),\ W_\nu(y) = W(\zeta, y) \tag{16}$$

We now have a Fredholm integral equation

$$I(\zeta) = \int_{-\infty}^{+\infty} B'_{\bar{\nu}}(y)\, W(\zeta, y)\, dy \tag{17}$$

## 1.3 King's solution

A particular functional form is chosen for the weighting function which makes the weighting function translation invariant, i. e. convolution type. The actual weighting functions are not translation invariant and dependent on several parameters in the atmosphere including the temperature profile, but the variation is negligible in some cases.

$$W(\zeta, y) = W(\zeta - y) \tag{18}$$

Using the the following generalized exponential weighting function where $\zeta - y = z$

$$W_m(z) = e^{-z}\, e^{-me^{-z/m}} \tag{19}$$

we can then use the solution

$$B(z) = I(z) + \sum_{n=1}^{N} \lambda_n \nabla^n I(z) \tag{20}$$

The $\lambda$ coefficients are determined by the inverse series of moments of the weighting function. The weighting function can be expanded as a *hyperdistribution* series and the inverse weighting function can then be determined by the inverse series, Bochner algebra[1].

$$W^{inv}(z) = \sum_{n=0}^{\infty} \lambda_n \nabla^n \delta(z) \tag{21}$$

This inverse weighting function is used to determine $B_{\bar{\nu}}(z)$ by substituting into the following inverse equation

$$B'_{\bar{\nu}}(z) = \int_{-\infty}^{+\infty} I(y)\, W(z-y)\, dy \tag{22}$$

## 1.4 Application of Differential Inversion to Data

Data from TIROS Operation Vertical Sounder (TOVS) were used for initial tests of differential inversion. TOVS data were provided by the National Environmental Satellite Data and Information Service (NESDIS) from the operational data processed bye NESDIS in routine daily operations. The particular radiance data which we used in this study were taken from a data sample collected during the period 16-18 October 1987. The sample consisted of 15 clear column radiance sets from each of three latitude bands.

The radiance data from each latitude band were accompanied by a set of transmittance profiles that were computed by NESDIS from the average temperature-moisture profile in that band. Weighting functions were determined from these transmittance profiles and a particular generalized exponential weighting function was fitted to the weighting functions. The inverse coefficients were calculated from the chosen generalized exponential function.

The differential inversion technique was applied to this data and was compared to corresponding RAOB data which was taken simultaneously with the radiance data. The differential inversion was first attempted using constant inversion coefficients for each band[5]. Due to the variation of the weighting functions with the peak height it was necessary to make corrections for the changes in the weight function shapes. By using different inversion coefficients in different regions of the atmosphere improvements were made to the solutions. The following table shows the average RMS error for each of the three bands using previous and current algorithms.

Average RMS Error degrees Kelvin

| band | previous | current |
|---|---|---|
| Low Latitude | 2.8 | 2.6 |
| Mid Latitude | 2.6 | 2.1 |
| High Latitude | 3.7 | 2.5 |

The methods which account for the variation the inverse coefficients show some improvement. This suggests that a full solution of the general Fredholm integral equation needs to be explored.

# 2 General Differential Inversion

## 2.1 The Problem

The previous results have demonstrated the need to solve a more general equation then that of convolution type. The Fredholm equation of the first kind with infinite limits

$$g(z) = \int_{-\infty}^{\infty} K(z,y) f(y)\, dy \tag{23}$$

Assume an Inverse

$$f(x) = \int_{-\infty}^{\infty} L(z,x) g(z)\, dz \tag{24}$$

In order to construct this inverse we multiply both sides of (23) by $L(z,x)\,dz$ and integrate with respect to $z$

$$\int_{-\infty}^{\infty} L(z,x)\, dz\, g(z) = \int_{-\infty}^{\infty} L(z,x)\, dz \int_{-\infty}^{\infty} K(z,y) f(y)\, dy \tag{25}$$

We can rearrange the order of integration on the right hand side

$$\int_{-\infty}^{\infty} L(z,x) g(z)\, dz = \int_{-\infty}^{\infty} f(y)\, dy \int_{-\infty}^{\infty} L(z,x) K(z,y)\, dz \tag{26}$$

In order to get the solution for $f(x)$ from (24), the following must be true

$$\int_{-\infty}^{\infty} L(z,x) K(z,y)\, dz = \delta(x-y). \tag{27}$$

## 2.2 Hyperdistribution Expansion of Kernels

Introduce a function $K'$ related to $K$ by a change in variables where $z = z' + y'$ and $y = y'$

$$K(z,y) = K'(z',y') = K'(z-y,y) \tag{28}$$

The variables in $K'$, $z'$ and $y'$ are independent, as can be verfied by considering the Jacobian for the change of variables.

$$L(z,x) = L'(z',x') = L'(x-z,x) \tag{29}$$

The hyperd expansions of $K$ and $L$

$$K(z,y) = \sum_{n=0}^{\infty} a_n(y)\nabla^n\delta(z-y) \tag{30}$$

$$a_n(y) = \frac{(-1)^n}{n!}\int_{-\infty}^{\infty} t^n K'(t,y)\,dt \tag{31}$$

$$L(z,x) = \sum_{m=0}^{\infty} b_m(x)\nabla^m\delta(x-z). \tag{32}$$

$$b_m(x) = \frac{(-1)^m}{m!}\int_{-\infty}^{\infty} t^m L'(t,x)\,dt \tag{33}$$

Insert hyperd series of both $K$ and $L$ into equation (27)

$$\int_{-\infty}^{+\infty} \sum_{n=0}^{\infty} a_n(x)\nabla^n\delta(x-z) \sum_{m=0}^{\infty} b_m(y)\nabla^m\delta(z-y)\,dz = \delta(x-y) \tag{34}$$

We can rearrange equation (34) to take the summations and the functions $a_n(y)$ and $b_m(x)$ outisde the integral, and then solve the integral

$$\delta(x-y) = \sum_{n=0}^{\infty}\sum_{m=0}^{\infty} a_n(y)b_m(x)\int_{-\infty}^{+\infty} \nabla^m\delta(x-z)\nabla^n\delta(z-y)\,dz \tag{35}$$

$$\delta(x-y) = \sum_{n=0}^{\infty}\sum_{m=0}^{\infty} a_n(y)b_m(x)\nabla^{n+m}\delta(x-y) \tag{36}$$

change of indeces

$$\delta(x-y) = \sum_{p=0}^{\infty}\sum_{q=0}^{p} a_{p-q}(y)b_q(x)\nabla^p\delta(x-y) \tag{37}$$

Make $x-y=\zeta$ and $x=\eta$ so $y=\eta+\zeta$

$$\delta(\zeta) = \sum_{p=0}^{\infty}\sum_{q=0}^{p} a_{p-q}(\eta+\zeta)b_q(\eta)\delta^{(p)}(\zeta) \tag{38}$$

Using the following relation

$$f(x)\delta^{(n)}(x) = \sum_{k=0}^{n}\binom{n}{n-k}(-1)^{n-k}f^{n-k}(0)\delta^{(k)}(x) \tag{39}$$

we can determine the matrix equation for solving $b_q$

$$\delta_{k0} = \sum_{q=0}^{\infty} A_{kq}(\eta)b_q(\eta) \tag{40}$$

$$A_{kq}(\eta) = \begin{cases} \sum_{p=0}^{\infty}\binom{p}{p-k}(-1)^{p-k}a_{p-q}^{(p-k)}(\eta) & q \le k \\ \sum_{p=q}^{\infty}\binom{p}{p-k}(-1)^{p-k}a_{p-q}^{(p-k)}(\eta) & q > k \end{cases} \tag{41}$$

This solution has several infinite series that must be truncated. The solution can not be practically implemented to TOVS data because of there is insuffiecient number of data point in a TOVS scan to determine the matrix with acceptable accuracy. This solution may be useful with larger channeled instruments which can provide more information as to the functional variation of the $\lambda$ coefficients.

The integral equation is then solved bye the general differential inversion formula

$$B(z) = I(z) + \sum_{n=1}^{N} \lambda_n(z) \nabla^n I(z) \tag{42}$$

# A Connection Machine Application of DI

## A.1 Introduction

Future instruments used for the remote sensing of vertical atmospheric profiles will have much larger numbers of channels, providing higher resolution. The current instrument used, HIRS, has approximately 20 channels available for remote sensing. The High-resolution Interferometer Sounder (HIS) and the AIRS instrument will have over 2000 channels available. This represents a significant increase in the amount of operations that will have to be performed by an inversion algorithm. Also, the accuracy of the computations will have to be greater to account for the higher resolution. New methods will have to be developed to accommodate the drastic increase in the number of channels, which will demand faster and more accurate computation. The Differential Inversion algorithm provides a physical, efficient way of determining vertical atmospheric temperature profiles. The Connection Machine is a data parallel system. Data parallel computing associates one processor with each data element. The operations involved in the Differential Inversion technique can especially be used to take advantage of a data parallel system by associating each channel with a series of processors. Each channel will then be able to simultaneously perform the necessary inversion operations at any desired accuracy.

## A.2 The Problem

The equation for the upwelling radiance measured by an instrument can be expressed for each channel $i$ at frequency $\nu_i$ as

$$R_{\nu_i} = \int_{-\infty}^{\infty} W_{\nu_i}(z) B(z)\, dz \qquad i = 1 \ldots P \tag{43}$$

where $W_{\nu_i}(z)$ denotes the atmospheric weighting functions and $B(z)$ is the Planck function which relates to the atmospheric temperature. The series of equations produced can generally be expressed as the integral equation

$$R(\bar{z}) = \int_{-\infty}^{\infty} W(z, \bar{z}) B(z)\, dz \tag{44}$$

by associating the frequency, $\nu_i$, with the variable $\bar{z}$, which represents the peak height of the weighting function $W_{\nu_i}(z)$.

Differential Inversion(DI) provides the solution for the Planck function

$$B(z) = R(z) + \sum_{n=1}^{N} \nabla^n \left[\lambda_n(z) R(z)\right] \tag{45}$$

where the $\lambda$-coefficients are related to the moments of the weighting functions.

The inversion process can now be carried out at each channel

$$B(z_i) = R(z_i) + \sum_{n=1}^{N} \nabla^n \left[\lambda_n(z_i) R(z_i)\right] \qquad i = 1 \ldots P \tag{46}$$

We now have $P$ equations with $N + 1$ terms. Also, the expansion contains $N$ $\lambda$-coefficients at $P$ levels, which must to be determined prior to the inversion.

## A.3 Parallel Applications

Equation (4) suggests several ways the problem can be parallelized using Differential Inversion(DI). The Connection Machine is suited to multi dimensional parallelization, which allows us to optimize so that the fewest number of serial operations are performed.

- **Number of Channels, P**

  Each channel of the instrument can be handled separately. This allows the machine to do the inversion at $P$ levels simultaneously. The number of channels used for a high resolution instrument would be about 2000. ($P = 2000$)

- **Number of Terms, N**

  Each term in the DI expansion can be handled separately. This allows the machine to calculate each term in the series simultaneously. The number of terms to achieve 2K accuracy may be around 32. ($N = 32$)

- **Weight Function calculations**

  The first step in the DI technique is the reduction of the weighting functions to the $\lambda$ coefficients. This a seperate operation, done prior to the DI expansion. This process involves calculating $N$ moments at each of the $P$ levels. Then the conversion of the moments to $\lambda$-coefficients must be performed. This involves a complicated relation between the moments and the $\lambda$-coefficients which also lend them selves to parallel operations.

## A.4 Conclusions

If the $\lambda$-coefficient calculations can be done to necessary accuracy prior to the reduction of the scan then the operations involved in each scan are represented by the expansion in equation (4) only. Given the previous estimates of the number of channels and the number of terms we would have 64,000 ($N \times P$) possible operation performed simultaneously. The Connection Machine has 64K processors. Each processor would be assigned to perform an operation. The types of operations for each of the processors are

- *Determining Finite Derivatives* This involves looking at the values of neighboring processors. This type of communication is very fast on the Connection Machine and would be performed at each processor simultaneously.

- *Multiplication of Coefficients* This involves multiply two values at each processor. This operation would be performed at every processor simultaneously.

- *Summing Terms in the Series* This involves adding all the values in the processors along one dimension. This operation is very basic to the Connection Machine

The operations involved in the DI technique can take advantage of a data parallel system in a number ways by associating each channel with a series of processors, so that many of the operations can then be done simultaneously. The Connection Machine and Differential Inversion may provide the most efficient means of reducing data from high resolution instruments in the future.

# References

[1] S. Bochner and W. Martin. *Several Complex Variables.* Princeton University Press, Princeton, 1948.

[2] M. T. Chahine. Inverse problems in radiative transfer: Determination of atmospheric parameters. *Journal of Atmospheric Sciences*, 27:960–967, 1970.

[3] M. T. Chahine. A general relaxation method for inverse solution of the full radiative transfer equation. *Journal of Atmospheric Sciences*, 29:741–747, 1972.

[4] Eddington. *Mon. Not. R. Astron. Soc.*, 73:359, 1913.

[5] Jean I. F.King, Robert G. Hohlfeld, and James C. Killian. Application and evaluation of a differnetial inverion technique for remote temperature sensing. *Meteorology and Atmospheric Physics*, 41:115–126, 1989.

[6] Jean I. F. King. Theory and application of differential inversion to remote temperature sensing. In A. Deepak, H. E. Fleming, and M. T. Chahine, editors, *Advances in Remote Sensing.* A. Deepak Publishing Company, 1985.

[7] C. Konstantopoulos, Larry Mittag, Guido v. H.Sandri, and R. Beland. Deconvolution of gaussian filters and antidiffusion. *Journal of Applied Physics*, 68:1415–1420, 1990.

[8] W. L. Smith. Iterative solution of the radiative transfer equation for temperature and absorbing gas profile of an atmosphrere. *Applied Optics*, 9:515–518, 1970.

1991 USAF-RDL SUMMER FACULTY RESEARCH PROGRAM

GRADUATE STUDENT RESEARCH PROGRAM

Sponsored by the

AIR FORCE OFFICE OF SCIENTIFIC RESEARCH

Conducted by the

Research and Development Laboratory

FINAL REPORT

# Large Scale Stellar Winds Effects from a Luminous Embedded Star


| | |
|---|---|
| Prepared by: | Kimberly A. Engle |
| Academic Rank: | Graduate Student |
| Department and | Department of Astronomy and Astrophysics |
| University: | The Pennsylvania State University |
| Research Location: | Geophysics Laboratory |
| | Hanscom AFB, MA 01731 |
| USAF Researcher: | Dr. Frank O. Clark |
| Date: | 9 August 1991 |

# LARGE SCALE STELLAR WINDS EFFECTS FROM A LUMINOUS EMBEDDED STAR

**Kimberly A. Engle**

## ABSTRACT

In order to obtain an infrared model of the celestial background that is applicable to Department of Defense goals, astronomical objects that emit infrared radiation must be well understood and modeled. This objective not only satisfies The United States Air Force's goals of obtaining an infrared model of the sky background, it also provides significant contributions to astronomy.

IRAS 05553+1631 was studied at many different wavelengths, including the four IRAS (Infrared Astronomical Satellite) of 12, 25, 60, and 100 microns. IRAS 05553+1631 is believed to be a deeply embedded young star with a bipolar outflow that heats the local molecular cloud. The outflow causes local heating that produces detectable emission in all four IRAS bands. This source is the second known object of this type, the first being well-studied L1551.

# I. INTRODUCTION

The Department of Defense is very interested in obtaining a model of the celestial background. To formulate an accurate model, astronomical objects that emit infrared radiation must be well understood. Information obtained regarding the astronomical objects will not only satisfy the goals of the United States Air Force, but will at the same time provide significant contributions to the astronomical community.

The Infrared Astronomical Satellite (IRAS) flew in 1983. The IRAS Point Source Catalog source IRAS 05553+1631 and surrounding region was studied in detail at many different wavelengths, including the four IRAS bands of 12, 25, 60, and 100 microns.

The area surrounding IRAS 05553+1631 was first noticed as being slightly unusual on the Palomar Optical Sky Survey (POSS), where the object exhibited nearly symmetrical extended luminosity. This region contains the Herbig Ae/Be star HD 250550, which was initially thought to be responsible for the extended infrared emission detected by IRAS since it was located within close proximity to the nebulous object. Further observations showed, however, that a bipolar flow emanating from IRAS 05553+1631 is responsible for the infrared emission. This suggested that IRAS 05553+1631 is a young embedded star. This object is the second such bipolar flow with associated extended far-infrared emission to be observed, the first being well-studied L1551. Even though IRAS 05553+1631 and L1551 are similar in many ways, they each have very different bolometric luminosities and therefore different spectral types. Also, IRAS 05553+1631 exhibits clear IRAS associated emission at 12 and 25 microns while L1551 does not. IRAS 05553+1631 beckons for further study.

# II. OBSERVATIONS

In order to understand the physical processes that cause the infrared emission in the region of IRAS 05553+1631, this area must be studied at many wavelengths.

Optical data for IRAS 05553+1631 is contained on the POSS blue and red prints, while information at one micron was obtained from a similar atlas. IRAS 05553+1631 appears only on the one micron image and not the Palomar prints because of optical extinction from the surrounding dark molecular cloud. The object on the Palomar Prints is seen on close inspection to be a companion.

Contour maps for the 12, 25, 60, and 100 micron data are presented in Figure 1. Extended infrared emission can be clearly seen at 60 and 100 $\mu$m, and some excess emission is seen at 12 or 25 $\mu$m. Bigmaps done by F.O. Clark and R.J. Laureijs at IPAC (NASA Infrared Processing and Analysis Center) using the IRAS data are presented in Figure 2. The data presented in Figure 1 are a simple destriped "regird" (a standard IPAC product) while the bigmap routine (another standard IPAC product) utilizes a different destriping algorithm. The bigmaps do not show the bipolar flow at all four IRAS wavelengths due to striping in the data.

An image resolution enhancer called Yoric was used to improve the resolution of the IRAS data. This procedure was done (at IPAC) for the 12, 25, 60 and 100 $\mu$m data. The 100 $\mu$m data will be enhanced again at a later date because the initial run did not produce good results. These enhanced images are shown in Figure 3.

The CO spectrum at 3mm was observed by Clark and Laureijs on the Gornergrat on the University of Cologne three meter submillimeter telescope using a beam size of $4'$. The temperature peaks, CO velocity, the width of the CO line, and the integral of the CO line are presented in Figure 4 in contour format. A representative CO spectrum is also shown. (See Figure 5, lower spectrum.)

Kinematic properties of this region have been probed using OH data gathered with the 25 meter telescope near Dwingeloo, The Netherlands. An OH spectrum for the region of excess far-infrared emission is shown in Figure 5 (upper spectrum). The OH spectral features are very unusual and very broad.

The MPIfR Bonn 100 meter telescope near Effelsberg, Germany, was used by F.O. Clark and R.J. Laureijs to obtain $NH_3$ observations of the region.

Small scale molecular observations were made using the 3 mm CO J=1→0 line at the University of Texas Millimeter Wave Observatory 5 meter telescope. Figure 6 is a contour map of the line wings of this object. The contour map was produced by first removing a Gaussian profile from the stronger parts of the line, then integrating the remaining red and blue wings.

Published optical photometric and spectroscopic data for stars in the field of IRAS 05553+1631 were used to estimate its distance by deriving the extinction as a function of distance. The results of this derivation are given in Figure 7. These data suggest that there may be a local thin cloud with an extinction of about 0.3 magnitudes, with an appreciable jump in extinction at approximately one kiloparsec. The extinction curve thus provides a distance for IRAS 05553+1631 of one kiloparsec.

## III. PHYSICAL QUANTITIES

The extended infrared emission detected around IRAS 05553+1631 can provide a wealth of information concerning the source and the surrounding region. The emission can reveal estimates of the mass of the warm dust, the luminosity of the stellar wind (if the dust is shock heated), and the apparent color temperature of the emitting region (Clark et al. 1987).

The mass of the region is estimated using Hildebrand's (1983) analysis and the 60 $\mu$m data from IRAS. Hildebrand's equation for the mass calculation is

$$Mc = \left[\frac{F(\nu)}{B(\nu,T)}\right] * C(\nu) * D^2$$

where $F$ is the flux, $B$ is the Planck function, $C$ represents the dust emissivity characteristics (size, emissivity, particle mass density, gas-to-dust ratio), and $D$ is the distance to the source.

Using the extinction curve of stars in the field of IRAS 05553+1631, a distance of one kiloparsec to this object is adopted. The extinction in magnitudes of all the stars within three degrees of IRAS 05553+1631 was measured and plotted. The result, displayed in Figure 7, suggests that a local obscuring cloud with an extinction of 0.3 magnitudes lies between us and the source at about one kiloparsec. Therefore the distance to the source is taken to be one kiloparsec. This value is consistent with both the nearby Herbig Ae/Be star, HL 250550 (a B6-9 V star with little extinction) and with the nearby open cluster NGC 2169.

F.O. Clark et al. (1987) published some of the physical quantities describing IRAS 05553+1631 and the surrounding region. The spectral class for this object was estimated as approximately B3, with an associated bolometric luminosity of greater than $900L_\odot$. The infrared luminosity was determined to be approximately $450L_\odot$. The velocity of the shock heating gas is 43 km/s, and the velocity of the OH emitting gas is about 32 km/s. This rapidly-moving gas produces very broad OH and CO spectral lines that can been seen in Figure 5. The temperature of the dust was determined to be 26K.

## IV. ANALYSIS

IRAS 05553+1631 has all the characteristics of a deeply embedded young star. It is a very bright infrared source and has no optical counterpart. The presence of CO wings in the immediate vicinity of the star indicate the presence of winds, which is also consistent with a deeply embedded young star.

The small-scale structure of the region surrounding IRAS 05553+1631 can be discerned from the CO data. Observations from the University of Texas' Millimeter Wavelength Observatory (shown in Figure 6) exhibit a bipolar flow emanating from this infrared object.

The large-scale structure defined by the CO and the OH lines indicate the presence of shocks. The broad CO line region outlines a triangular region with one apex on IRAS 05553+1631. The so-called "hot spots" seen on the 60 (and 100) $\mu$m images (Figure 1) reveal that the shocks from the bipolar flow are heating the surrounding gas and dust. Initially it was thought that the material is being heated by the nearby star HD 250550, but the infrared luminosity of the extended infrared emission indicates that HD 250550 is unimportant as a heating source to this region. Figures 1 and 6 clearly shows the flow emanating from the IRAS source and interacting with the molecular cloud. The flow from the opposing jet is invisible because IRAS 05553+1631 is located on the edge of the molecular cloud, and the opposing jet is flowing into a region of negligible density. There is no material present for the shocks to heat, so no emission is seen in that region.

The mass estimated from both the IR and CO data suggests that the triangular region associated with the IRAS 05553+1631 bipolar outflow is physical. This region contains shocks and dust with an elevated color temperature, suggesting shock heating of the dust.

The bigmaps done at IPAC (Figure 2) show a great deal of striping in all four IRAS bands despite the implementation of a destriping algorithm. The striping degrades much of the data, so the outflow from IRAS 05553+1631 is not visible on the bigmaps.

The four bands of IRAS were also analyzed using the resolution-enhancing software package called Yoric. (These reductions were done at IPAC also.)

Yoric regrids the data, then attempts to extract all of the point sources present. Yoric, like the bigmap routine, also contains a destriping algorithm. Yoric however was much more successful in removing the striping than bigmap because the destriping logic is more sophisticated. The 12 $\mu$m image of IRAS 05553+1631 shows only extended emission (Figure 3). The 25 $\mu$m image, however, returns three point spread functions for IRAS 05553+1631 and no extended emission. IRAS 05553+1631 seems to be a multiple source at 25 $\mu$m, where one object is the main IRAS source, another is located just north and the third is situated directly south of the IRAS source. The 60 $\mu$m image displays the three sources also. The 100 $\mu$m image seems to exhibit multiple sources also, but Yoric must be performed again on the 100 $\mu$m IRAS data to obtain better results since the first attempt to run Yoric on the 100 $\mu$m data was not very successful. The outflow that is visible on all the contours is also seen in the 60 and 100 $\mu$m Yoric reductions.

There are two main interpretations of these results. The 12 $\mu$m data suggests that one source only is present, IRAS 05553+1631, along with extended infrared emission. The data from the other three IRAS bands indicate that IRAS 05553+1631 is a multiple source with no extended emission. One explanation is that the source may be a cluster of young embedded stars, with one star producing the outflow that is clearly seen on all four bands of the contoured IRAS data. None of these possible multiple sources are seen in the optical region of the spectrum (i.e. on the POSS prints), including IRAS 05553+1631.

## V. CONCLUSIONS

IRAS 05553+1631 is a young embedded star possessing a bipolar outflow that shock-heats the local molecular cloud. The flow is clearly visible on the contours done on the four IRAS bands and on the Yoric reductions. The

Yoric reductions reveal that either IRAS 05553+1631 is a source of multiple young embedded stars (with one possessing the bipolar outflow), or that the source is a single object with extended infrared emission. It is unclear at this point which interpretation is correct. I believe that the data at this point supports the former conclusion, and it is known that stars can be and usually are formed in clusters (commonly called a stellar nursery). Once more data is gathered on this object, a precise model can be made describing the emission, and consequently IRAS 05553+1631 and similar objects can be included in the Air Force model of the infrared sky background.

## VI. FUTURE STUDIES

As stated previously, it is unknown whether or not IRAS 05553+1631 is a multiple infrared sources with one young star producing the bipolar outflow, or a single source with extended infrared emission. One future study could include a high-resolution study of IRAS 05553+1631 to determine if the source is indeed multiple. Also, the Yoric resolution-enhancer algorithm must be redone for the 100 micron IRAS data to determine the number of infrared sources present at tl wavelength. Using the reduced 60 $\mu$m data from IRAS, more precise mass estimates of the region surrounding IRAS 05553+1631 can be obtained.

Before these young stars such as IRAS 05553+1631 and L1551 can be incorporated into the Air Force model of the infrared sky background, the true nature of these sources must be understood.

**ACKNOWLEDGEMENTS**

I would like to thank the Air Force Office of Scientific Research and the Phillips Laboratory Geophysics Directorate for allowing me to participate in this wonderful program. I would especially like to thank Drs. Steven Price, Frank Clark, and Paul LeVan, and the other of the employees of the Optical Physics division for providing a very pleasant and educational working environment.

I would like to thank Dr. Frank Clark for providing me with ideas for a future thesis topic that would benefit not only my career, but also the Air Force and Astronomy community in general.

I would especially like to thank Dr. Paul LeVan for allowing me to accompany him on an infrared observing run at Wyoming's Infrared Observatory (WIRO). This experience was extremely educational and invaluable for my future studies. I would like to thank Dr. Frank Clark for providing me with ideas for a future thesis topic that would benefit not only my career, but also the Air Force and astronomy in general.

## REFERENCES


Clark, F.O. et al., 1986a, "Space-Bourne Submillimeter Astronomy Mission" ESA SP-260, 173.

Clark, F.O. et al., 1986b, *Astro. and Astrophys. Letters*, **168**, L1.

Clark, F.O. et al., 1987, *Lecture Notes in Physics*, **297**, 140.

Clark, F.O. and Turner, B.E., 1987, *Astro. and Astrophys.*, **176**, 114.

Hildebrand, R.H., 1983, *Quarterly Journal of the Royal Astro. Soc.*, **24**, 267.

Laureijs, R. Infrared Properties of Dust in Interstellar Clouds, Groningen, Netherlands, University of Groningen, 1989.

Figure 1

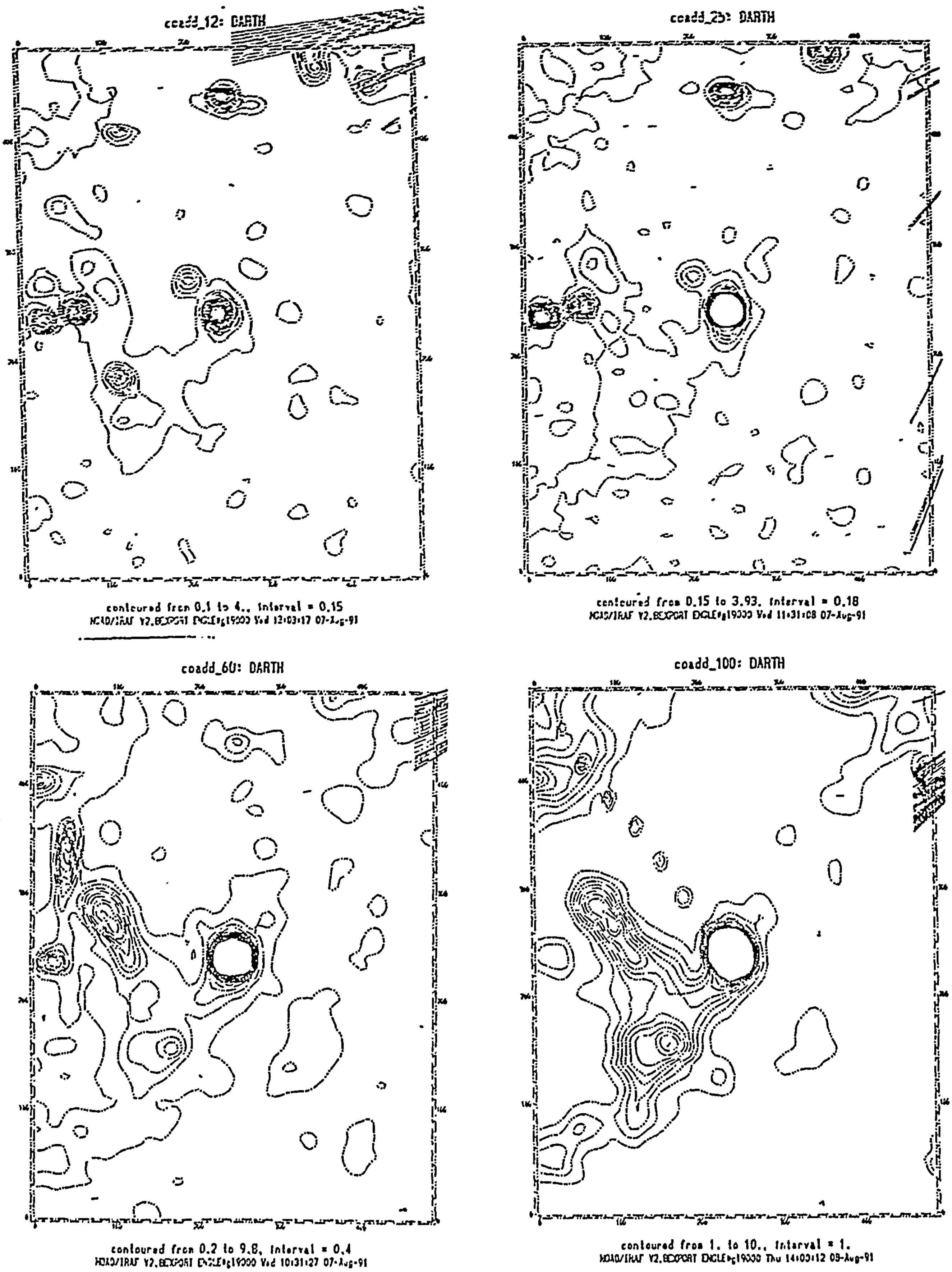

coadd_12: DARTH
contoured from 0.1 to 4., interval = 0.15
coadd_25: DARTH
contoured from 0.15 to 3.93, interval = 0.18
coadd_60: DARTH
contoured from 0.2 to 9.8, interval = 0.4
coadd_100: DARTH
contoured from 1. to 10., interval = 1.

Figure 2

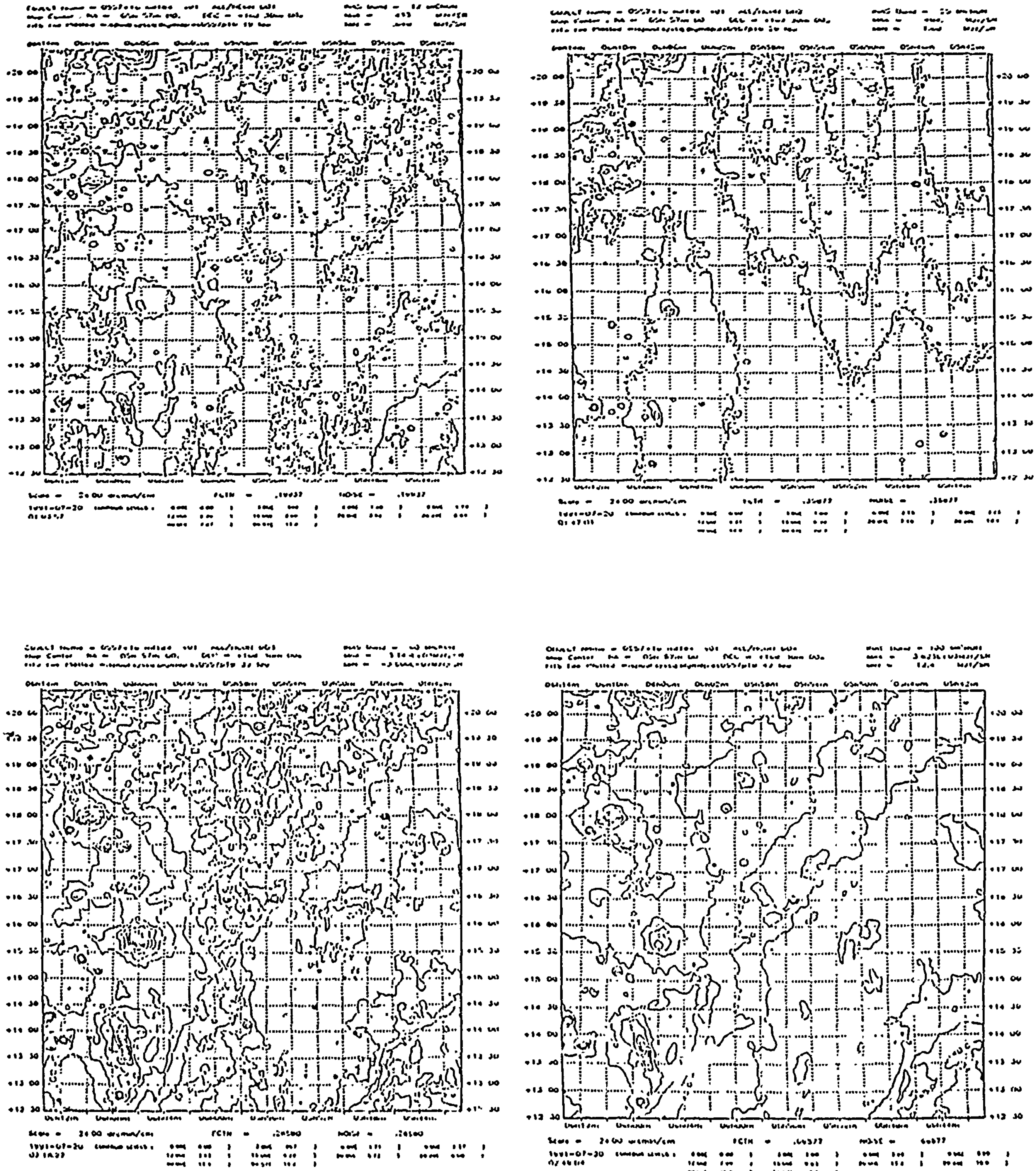

Figure 3

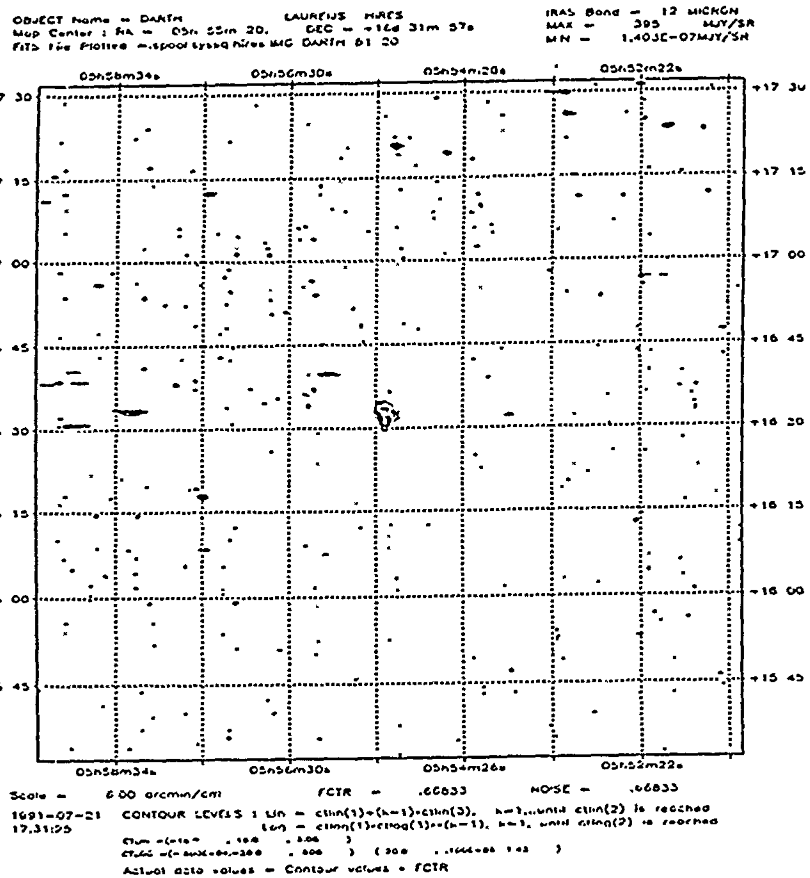
OBJECT Name = DARTH
LAURENS HIRES
IRAS Band = 12 MICRON
MAX = 395 MJY/SR
05h58m34s
05h56m30s
05h54m26s
05h52m22s
+17 30
+17 15
+17 00
+16 45
+16 30
+16 15
+16 00
+15 45
Scale = 6.00 arcmin/cm
FCTR = .66833
NOISE = .66833
1991-07-21
17.31.25
CONTOUR LEVELS
Actual data values = Contour values * FCTR

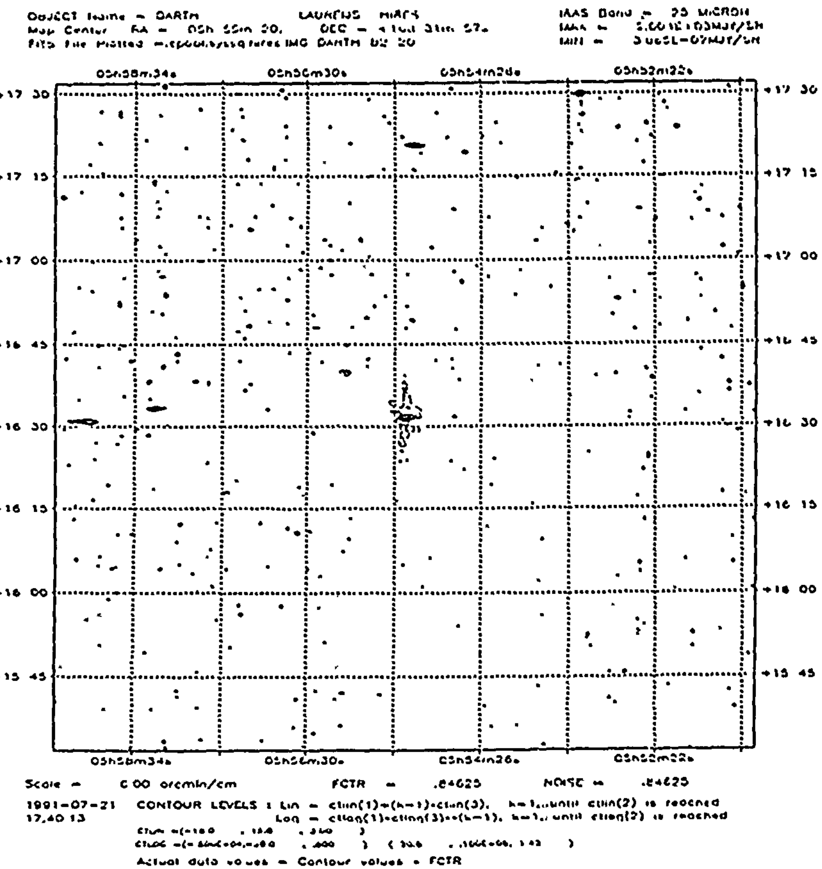
OBJECT Name = DARTH
LAURENS HIRES
IRAS Band = 25 MICRON
05h58m34s
05h56m30s
05h54m26s
05h52m22s
+17 30
+17 15
+17 00
+16 45
+16 30
+16 15
+16 00
+15 45
Scale = 6.00 arcmin/cm
FCTR = .84625
NOISE = .84625
1991-07-21
17.40.13
CONTOUR LEVELS
Actual data values = Contour values * FCTR

Figure 3 cont.

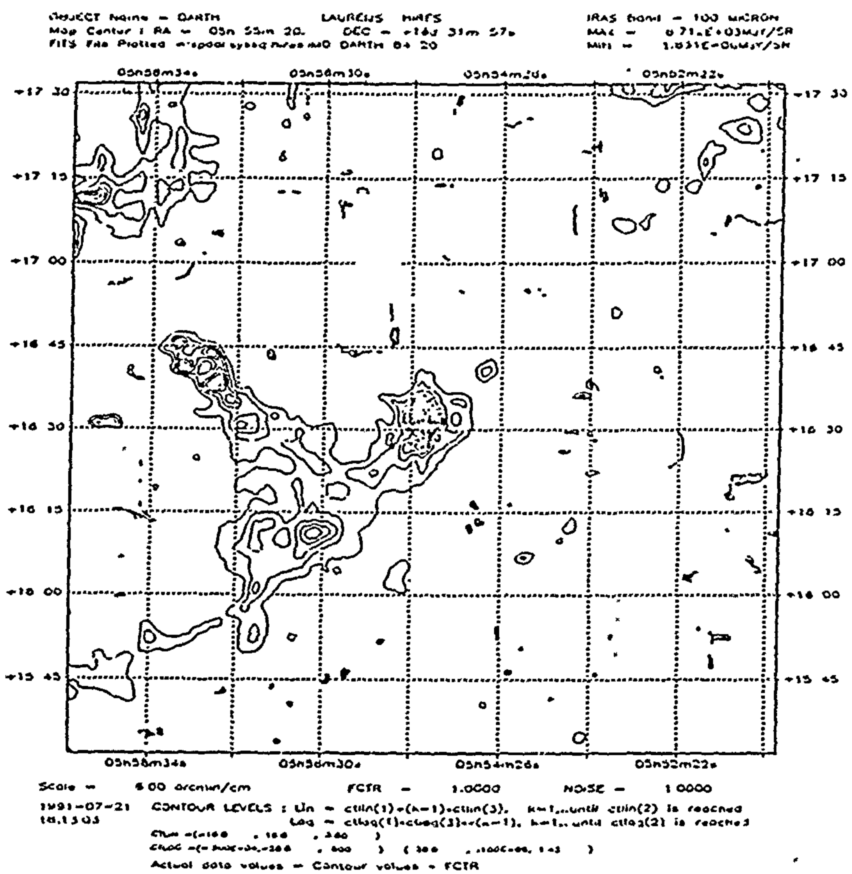


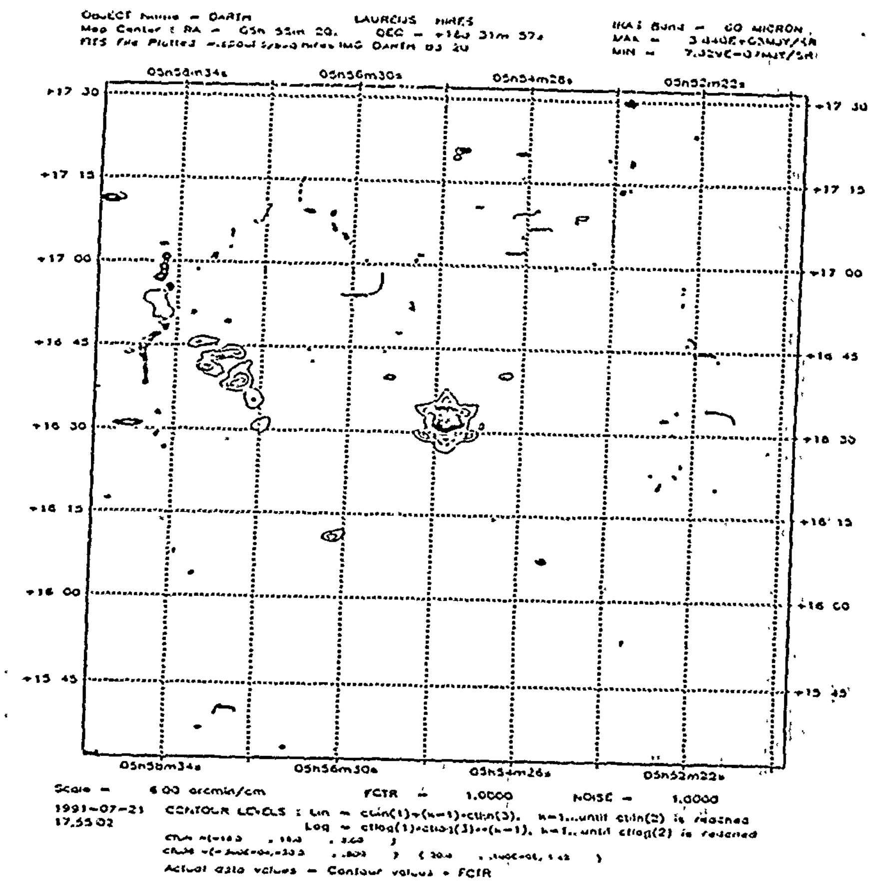

Figure 4

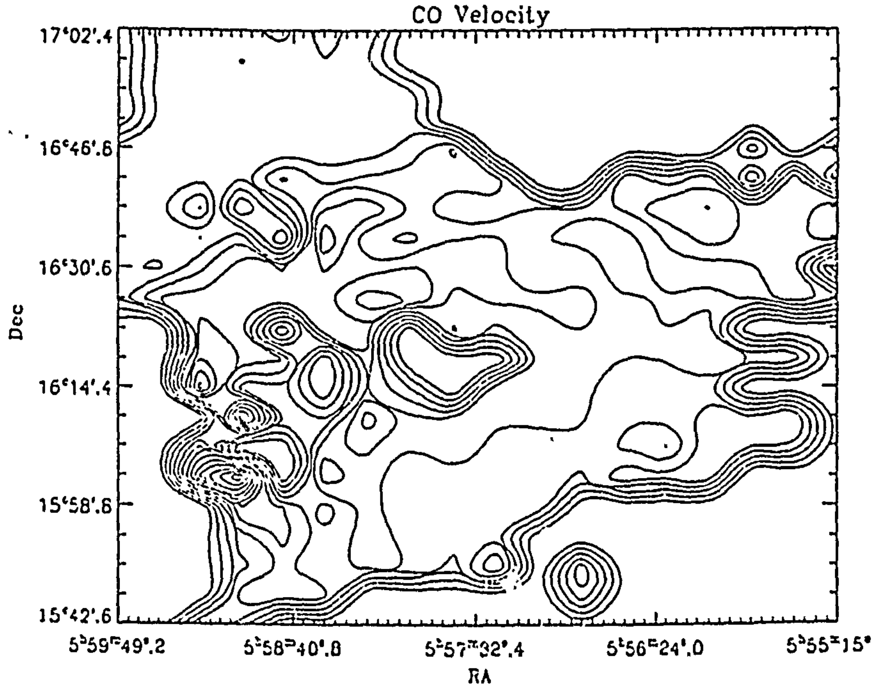

CO Velocity
17°02'.4
16°46'.6
16°30'.6
16°14'.4
15°58'.6
15°42'.6
Dec
5h59m49s.2
5h58m40s.8
5h57m32s.4
5h56m24s.0
5h55m15s
RA


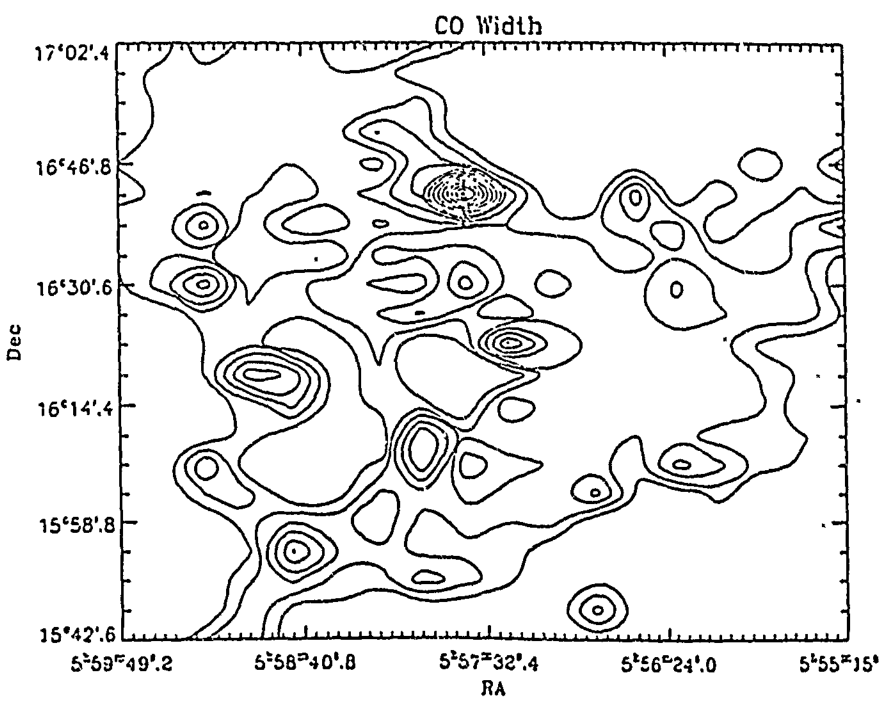

CO Width
17°02'.4
16°46'.8
16°30'.6
16°14'.4
15°58'.8
15°42'.6
Dec
5h59m49s.2
5h58m40s.8
5h57m32s.4
5h56m24s.0
5h55m15s
RA

Figure 4 cont.

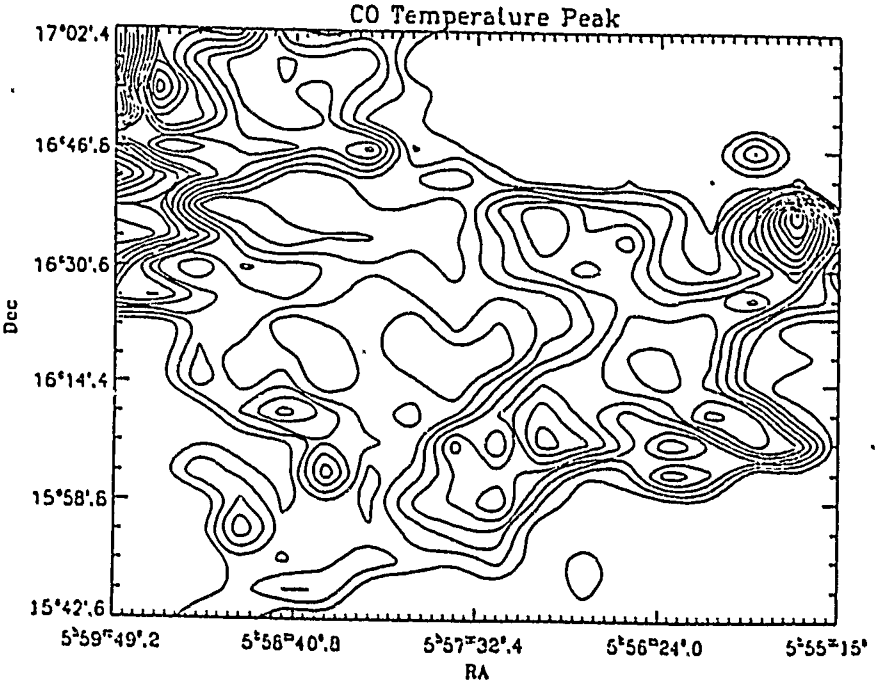


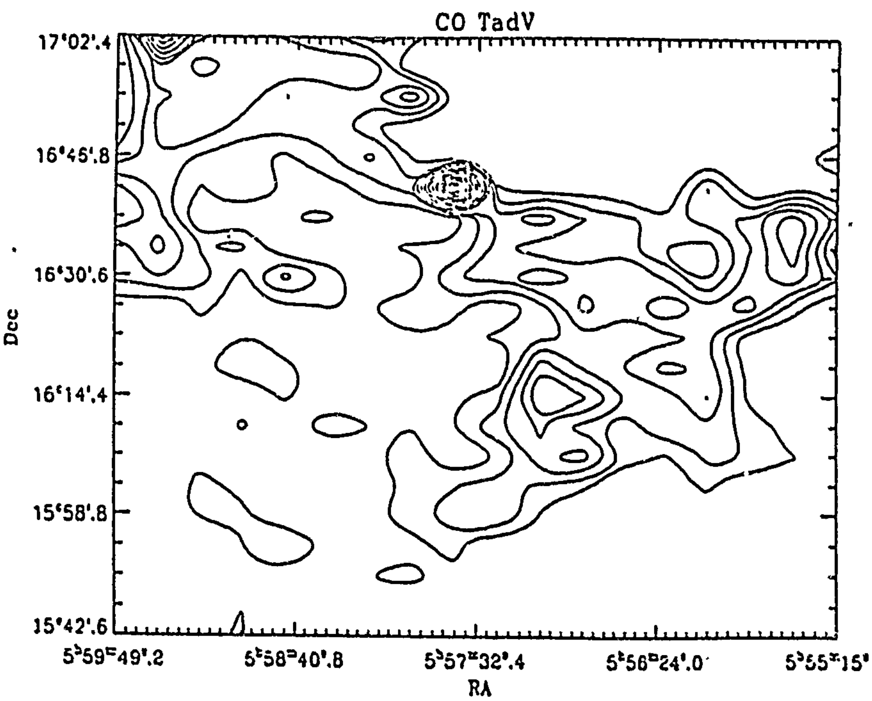

Figure 5

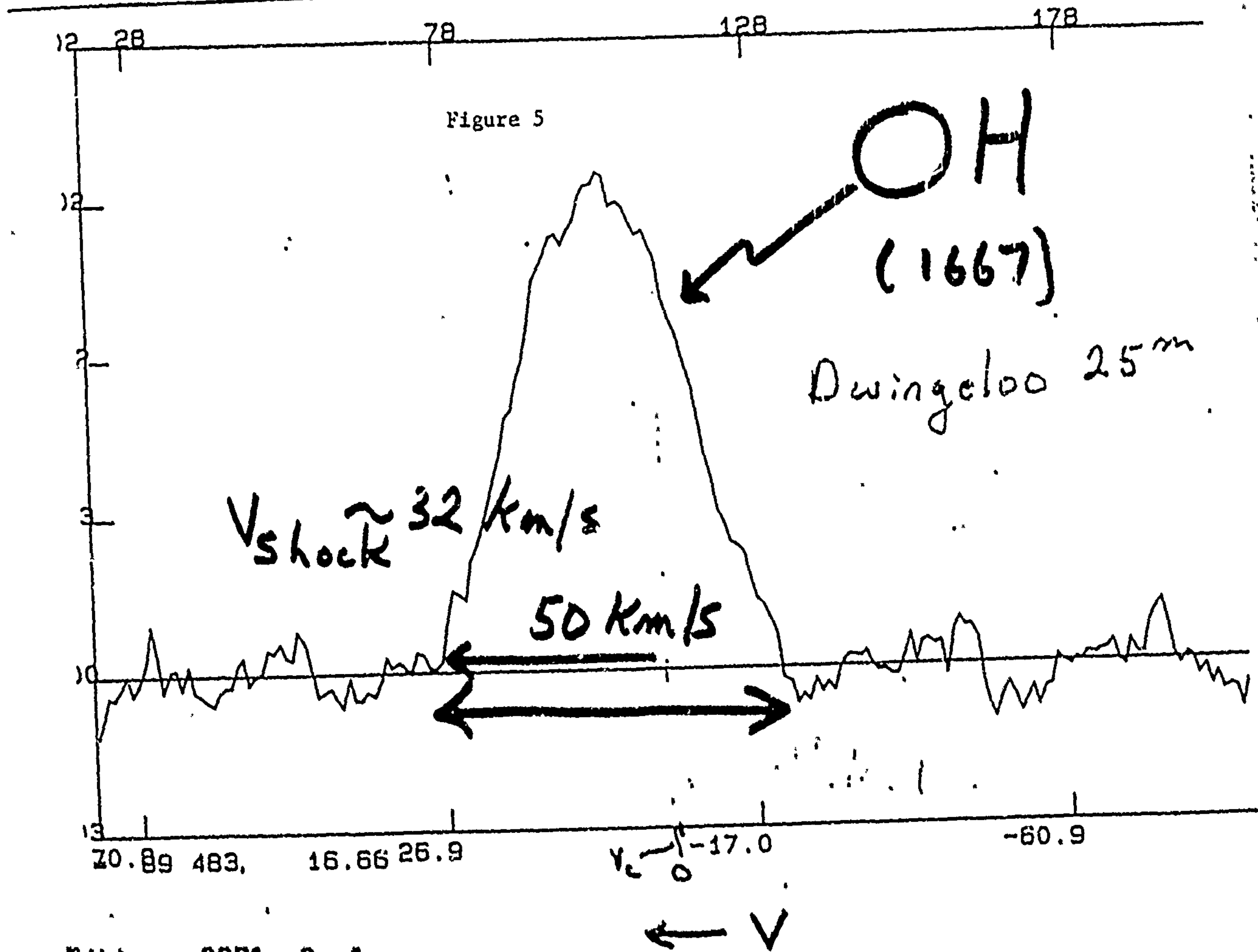

OH
(1667)
Dwingeloo 25 m
Vshock ~ 32 km/s
50 km/s
-17.0
-60.9
← V


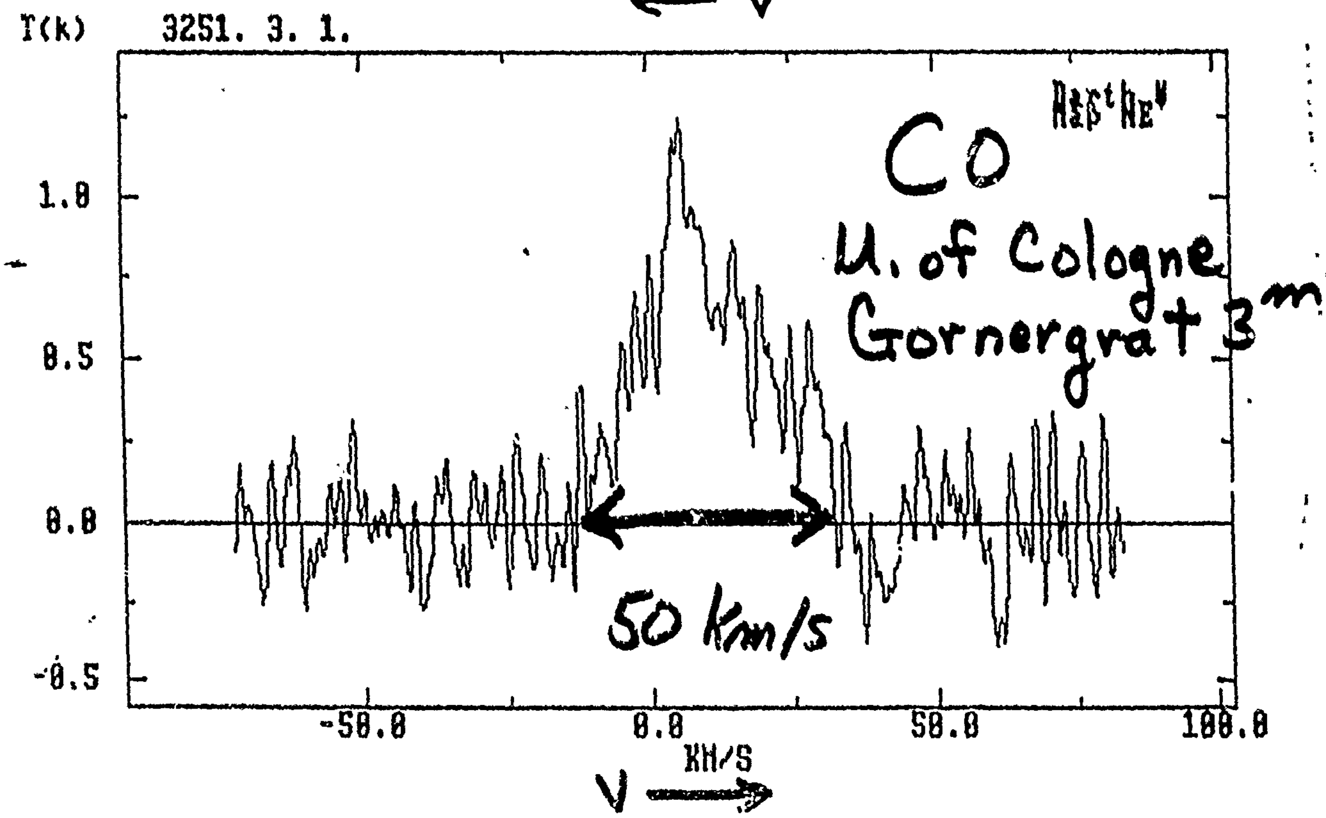

T(K) 3251. 3. 1.
CO
U. of Cologne
Gornergrat 3 m
50 km/s
1.0
0.5
0.0
-0.5
-50.0
0.0
50.0
100.0
KM/S
V →

IRAS 05553+1631

Figure 6

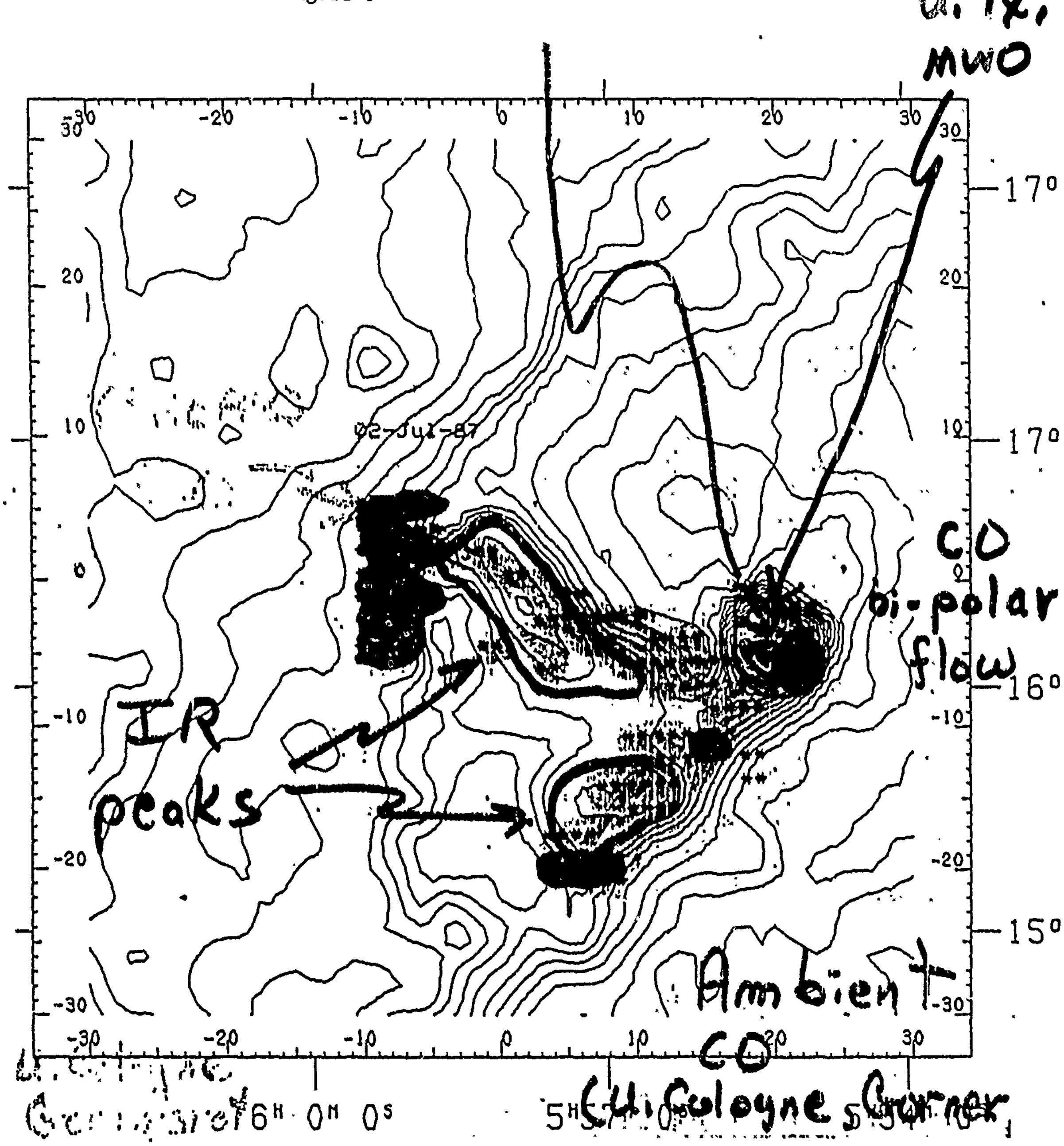

Figure 7

All Stars Within 3 Degrees of IRAS 05553+1631

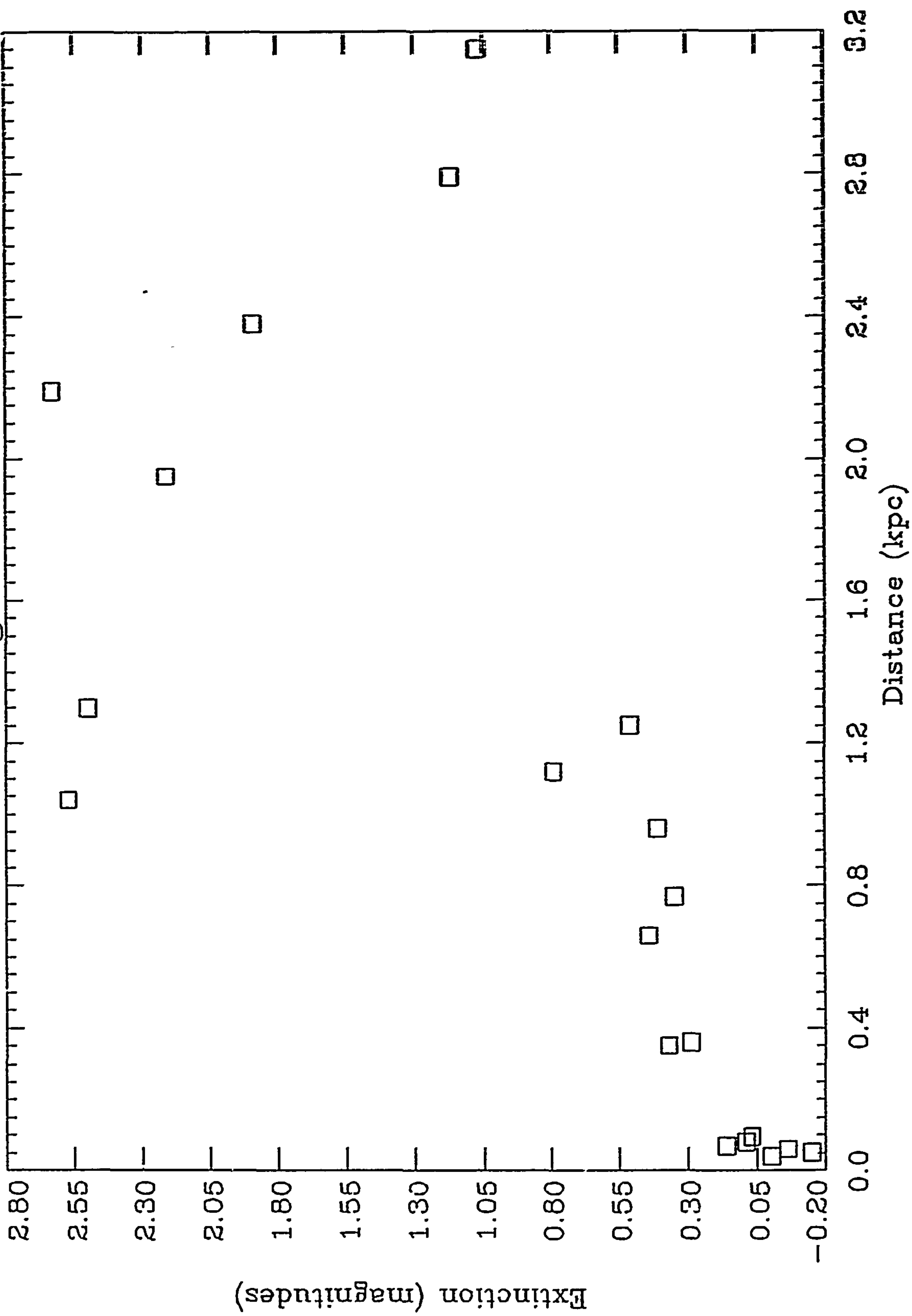

# INFRARED AND RADIO CORRELATIONS WITH GALACTIC H II REGIONS

Thomas A. Kuchar

Department of Astronomy

Boston University

## ABSTRACT

Infrared emission from galactic H II regions as revealed by IRAS (Infrared Astronomy Satellite) images was compared to radio continuum emission. H II regions are a major source of infrared emission in the Galactic plane, the brightest part of which is not yet well characterized. Three methods were employed to correlate IR with the radio. The most successful of these found a linear relation between each of the four IRAS wavebands and 11cm continuum flux. H II regions emit strongly in the infrared and thus provide background clutter for target detection and tracking in the infrared. The IR–radio correlations can be used to characterize this emission and thus improve celestial background models.

## I. INTRODUCTION

Target detection and tracking in the infrared (IR) must deal with clutter that can be caused by celestial backgrounds such as the galactic plane. Since dust in the Galaxy is optically thin at IR wavelengths, the galactic plane shines brightly in the infrared. Therefore targets which cross the galactic plane may be totally lost if an allowance is not made for this bright emission. Thus it is worthwhile to characterize this infrared emission with a variety of scale sizes and spectral components.

The brightest part of the galactic plane is the central region. This area is not yet well characterized observationally, and therefore models of this component of the celestial background are not yet ideal. The brightest IR emission from the galactic plane originates in H II regions, areas of ionized gas which surround young, hot stars (mainly spectral types O and B). Thus probing the central environment of the galactic plane with H II regions can improve models of the galactic plane.

Large scale IR surveys of the galactic plane at several wavelengths can be used to characterize the gross IR properties of H II regions. The most recent large scale survey of the infrared sky was conducted by the Infrared Astronomy Satellite (IRAS) (Neugebauer *et al.*, 1984, Beichman *et al.* 1985). IRAS surveyed the sky at 12, 25, 60, and 100$\mu$m with spatial resolutions ranging from 2 to 5 arcminutes (depending on the spectral band). This research effort uses data provided by IRAS in the form of sky flux images and source catalogs to examine the IR emission from galactic H II regions. The Celestial Backgrounds Division of the Geophysics Laboratory at Hanscom AFB has a continuing interest in modeling and interpreting the infrared sky. Thus methods already developed at the Geophysics Lab can be readily applied to infrared data provided by the 'RAS mission.

Several authors (*e.g.* de Jong *et al.* 1985, Helou *et al.* 1985, Haslam and Osborne 1987, Beck and Golla 1988) have demonstrated that there exist correlations between the radio continuum and infrared emission in spiral galaxies. These correlation have been made primarily with IRAS 60 and 100 $\mu$m emission, which was measured over the disk of external galaxies. This research effort seeks to extend this work by searching for correlations between radio continuum and IRAS 25 $\mu$m emission.

Cox *et al.* 1986 have done extensive modelling of infrared emission arising from heated dust. A major component of the modelled emission is from warm dust with color temperatures $T_C \sim$ 30–40 K. This dust component is heated by O and B type stars associated with H II regions. These stars are also responsible for ionizing the surrounding gas. The emission from free electrons thus produce the radio continuum associated with the H II regions. Haslam and Osborne compared 11cm radio continuum with the 60$\mu$m IRAS emission over a 1 degree strip centered on the galactic plane. They discovered that each 60$\mu$m peak had a corresponding 11cm peak. It is this type of correlation that this effort investigated.

## II. OBJECTIVES

Part of the goal of this research effort was to characterize the spectral emission of H II regions in the infrared. Specifically, this effort sought to find correlations between the IR and radio continuum emission for H II regions. Through these types of correlations, a broad set of IR properties of H II regions should be definable. This study took three broad approaches:

1. identify H II regions in the IRAS Small Scale Structure Catalog (SSSC, see Beichman *et al.* 1985) and compare their fluxes in the four IRAS bands to their published radio continuum fluxes;
2. compare the IRAS 25$\mu$m and radio continuum emission for a large, extended ($\sim$ 1°) H II region on a pixel–by–pixel basis; and
3. follow the procedure of Haslam and Osborne (1987) and compare the IRAS 25$\mu$m emission with the radio continuum over a strip of the galactic plane.

The results of each of these approaches are discussed in §III.

## III. ANALYSIS AND RESULTS

### a. *H* II *Region Fluxes*

Most H II regions that are within 1 kpc of the sun are easily identified in the optical. However, beyond that distance the dust opacity in the galactic plane becomes large enough to obscure all of the optical emission from H II regions. However at IR wavelengths this same dust has a low opacity. Thus the IRAS mission would have mapped many more H II regions than those which are only optically identifiable. Therefore to identify the IR emission associated with H II regions for celestial background models, it is necessary to use catalogs of H II regions which are not solely optically selected. Most H II regions can be identified over trans-galactic paths through the radio emission from recombination lines. A search of the astronomical literature was performed in order to make a comprehensive list of H II region recombination line surveys. The references for these surveys are listed in the Table 1. The last reference of the table contains a list of optically identified H II regions. This was included in the list, since most of the recombination line surveys did not include H II regions that had been optically identified.

For the radio–IR flux correlations the 11cm continuum survey of Reich *et al.* (1984) and the recombination line survey of Lockman (1989) were used. These two surveys were chosen because they covered nearly the same area in the galactic plane ($0° \lesssim \ell \lesssim 75°$, $| b | \lesssim 1\overset{\circ}{.}5$). Also Lockman's survey of the first galactic quadrant examined most of the continuum peaks in this area for recombination lines, and thus is one of the more complete surveys of this region of the Galaxy.

IR fluxes of the H II regions were obtained from the IRAS Small Scale Structure Catalog (SSSC). The SSSC lists objects in uncomplicated areas (*i.e.* areas where the emission from objects is easily distinguishable from the emission of other structures) of the IR sky which have angular sizes smaller than 8 arcminutes but larger than a point source. Of the 460 entries in Lockman's catalog, 48 H II regions had fluxes listed in the SSSC for at least one of the IRAS bands. The search for H II regions in the SSSC was limited to sources that were within five arcminutes (the largest resolution element of the IRAS survey) of the position listed by Lockman. Although this limit was chosen somewhat arbitrarily, most of the H II regions in the SSSC were quite close to the positions listed by Lockman. The average difference between the position of the recombination line and the position listed in the SSSC is 1.3±1.0 arcminutes. The maximum difference is 4 arcminutes. Of the 48 H II regions identified in the IR, Reich *et al.* list the fluxes for 23 of them.

Figure 1 shows the radio flux plotted against the IR flux for each of the four IRAS wavebands. The line in each plot represents a linear, least-squares fit to the data. The fits are summarized in Table 2: column 1 lists the IRAS waveband, columns 2 and 3 the coefficients of the fit, column 4 the $\chi^2$ of the fit, column 5 the number of points in the fit, and column 6 the RMS scatter of the data about the fit.

Each of the four plots in Figure 1 shows a linear correlation between IR flux and 11cm flux. Although these correlations seem promising, some cautionary notes are needed. First, the figure is plotted on a log-log scale. The RMS deviations are small, but since this is a logarithmic scale, they are multiplicative factors and not additive. Also Reich *et al.* and the SSSC quote different source sizes for the H II regions. Since the radio and IR fluxes were integrated over different source sizes, this could have the tendency to increase the scatter in the plots. Also the fluxes quoted in the SSSC were used without regard to flux quality or corrections for assumed spectral shape (*i.e.* color correction, see IRAS Explanatory Supplement). These, too, will have a tendency to increase the scatter in the plots of Figure 1.

*b. The Rosette Nebula and S252*

The previous section showed that correlations can be made between the radio and infrared fluxes of H II regions. These fluxes, however, were integrated over the size of the H II region. Most of these H II regions are just a few arcminutes across, and therefore only cover several pixels in both the radio and IR surveys. It is possible that a correlation between the IR and radio may exist over th- face of the H II region, on a pixel-by-pixel basis. Two extended ($\sim 1°$) were chosen to determine if such a correlation exists.

For this comparison the Rosette Nebula, $(\alpha, \delta)_{1950} = (6^h29^m, +5°01')$, and S252, $(\alpha, \delta)_{1950} = (6^h07^m, +20°32')$, were chosen. The IRAS 25$\mu$m data of these two objects were compared to the 6cm radio continuum survey of Condon *et al.* (1989).

The IRAS super skyflux images have a resolution of 5 arcminutes, whereas the the radio continuum data has a much finer resolution of 40 arcseconds. This higher resolution can increase the scatter of a pixel-to-pixel plot, since the IR data did not resolve the finer details of the radio data. To compensate for this, the radio data was smoothed to a 5 arcminute resolution. The scatter plots are constructed by taking the pixels in a designated area of the IRAS map and searching the radio map for the corresponding pixels nearest to the IR position. Since the sampling intervals of the two surveys are different (IRAS = 1 arcminute, 6cm = 40 arcseconds), it is possible that most of the IR and radio pixels will not be at the same position. Since positional errors of as much as 40 arcseconds are likely, this indicates that the radio data may not smoothed over the same area corresponding to the IRAS pixel. This, too, will increase the scatter of the pixel-to-pixel plot. The discrepancy in the sampling intervals was not corrected in this investigation.

Figure 2 shows the 25$\mu$m map of the Rosette Nebula. The contours start at 10 MJy/sr and are spaced every 5 MJy/sr. The three boxes in this figure outline the areas from which the pixels for the scatter diagrams were drawn. The larger area (box 1) outlines the maximum extent of the Rosette's 6cm continuum. The other boxes mark areas that contain (2) and are devoid (3) of IRAS point sources. These latter two areas were chosen since areas containing embedded sources (as exhibited by emission from point sources) may complicate the form of the correlation. Figure 3, which is divided into three frames, shows the scatter diagrams for each of these regions. (The top frame, 3a, corresponds to box 1 data, the bottom frame, 3c, to box 3 data.) No clear linear correlation is really seen in any of these figures. Figure 3a shows a concentration of points near the center of the plot. It can be seen that this concentration can be attributed to an overlap of the plots in Figures 3b and 3c.

Figure 4 shows the scatter diagram for S252. The area from which the pixels are plotted encompasses the full extent of the IR emission. As such this area is comparable to box 1 of Figure 2. Like Figure 3, this figure does not show a clear linear correlation.

The lower envelope of points that appears in both Figures 3a and 4 is not due to the arbitrary size of the regions chosen for the scatter plots. Increasing the size of the area of the plotted pixels does not significantly add any points below the envelope. This lower limit in the 25$\mu$m emission is due to the diffuse emission surrounding these H II regions. Thus the minimum intensity of the diffuse background emission is determining the the boundary of this lower envelope.

*c. The Galactic Plane*

The procedures outlined in Haslam and Osborne were applied to the IRAS 25$\mu$m and 6cm data. Haslam and Osborne originally compared the IRAS 60$\mu$m data to the Reich *et al.* 11cm data in a one degree wide strip centered on the galactic plane. Their procedure was used to separate thermal from non-thermal er. ' sion. However, since the technique compares radio and IR data, it is applicable here. The method is outlined as followed:

1. remove the background zodiacal emission from the IRAS data;
2. remove the diffuse IR emission associated with H I gas; and
3. plot the radio data against the IR data.

Their final scatter plot showed a well defined lower envelope, which is the type of correlation sought here. Since the data sets used here are sufficiently different from those of Haslam and Osborne, some modifications to the above procedures were made. These are detailed below.

IRAS Super Skyflux images at 25$\mu$m were obtained for the galactic plane. These images covered a 60 square degree strip in the plane: $30° < \ell < 60°$, $| b | < 0\overset{\circ}{.}5$. The Super Skyflux images are superior to the first IRAS skyflux products since they have improved calibration, positional reconstruction, de-striping, and zodiacal emission subtraction. Thus these higher quality images were already corrected for zodiacal emission.

However, these images needed to be corrected for diffuse galactic IR emission. It has been shown for high galactic latitudes that diffuse emission at 60 and 100 $\mu$m is well correlated with neutral hydrogen column density. It is thought that this emission is due to dust associated with this gas. Haslam and Osborne used this correlation to remove the diffuse emission at 60$\mu$m. However no such correlation has been demonstrated to exist at 25$\mu$m.

Since the 25$\mu$m diffuse emission need only be removed, it was not necessary to find a correlation similar to that of the 60 and 100$\mu$m data. Therefore previously published techniques were used to remove this emission. Such algorithms have been applied to data at high galactic latitudes for removing zodiacal emission ($| b | \gtrsim 30°$, Laureijs, 1989) and have been adapted for this work. The general algorithm basically removes the contribution of point and extended sources from the images and smooths the resulting data. The resulting image is thus an estimate of the background. The algorithm was adapted so that the background images have no structures smaller than $\sim 1°$. These images were then subtracted from the IRAS galactic plane images.

The third step of the above procedure was somewhat modified. Again, the 6cm data of Condon *et al.* was used for the correlation and was smoothed to the resolution of the IR data. However, the intensity were averaged over $\pm 0\overset{\circ}{.}5$ latitude range to form a single profile for both the IR and the radio. Figure 5, which is divided into three frames, shows these profiles. The top frame (5a) shows the IR profile and the middle frame (5b) shows the radio profile. Most of the peaks in the top frame are due to H II regions. The bottom frame (5c) shows the ratio of IR to radio intensities. The hash marks at the top of 5c indicate the longitudes of H II regions in Lockman's survey (with $| b | \leq 0\overset{\circ}{.}5$).

Figure 6 shows the IR–radio scatter plot of the first two frames of Figure 5. The top plot of Figure 6 shows all of the data. In the second plot (6b), however, an attempt was made to eliminate the background emission in the radio and IR by plotting only the data with a ratio IR/radio $\geq 0.005$. As can be seen in Figure 5c, this ratio is indicative the low level background. As a result of this imposed cutoff, Figure 6b has an artificial upper limit. From examining both plots of Figure 6, there does appear to be a lower envelope to the scatter. This is the type of correlation reported by Haslam and Osborne. The lower envelope in the second plot (6b) is somewhat more readily apparent, since the clutter of the low radio flux was eliminated from the plot. The line drawn in Figure 6b is not a fit to the data but is merely there to highlight the lower envelope. The equation for this line is:

$$\log(F_{6\mathrm{cm}}) = 0.42\log(F_{25/\mu\mathrm{m}}) + 1.15$$

Although the full equation of the line is not important, the slope of the line indicates the relationship between the IR and the radio. Also, since this line was fit by eye, it is not a precise relation. Thus the slope may have a range within ± 0.05 of the slope in the above equation.

## IV. CONCLUSIONS

Of the three correlation techniques investigated here, the flux correlations between the the four IRAS bands and the 11cm continuum seem the most promising. The linear relations derived in §IIIa for H II regions can generally be used to predict the IR brightness of these objects in the galactic plane. However, the scatter in the fits is large. All of the IR and radio fluxes for these correlations had been previously published. Thus the fluxes for the IR and radio were not calculated over the same angular extent. The scatter can most likely be reduced by calculating the fluxes for a large set of H II regions over a consistent set of angular sizes. Too, it would be worthwhile to compare the IR fluxes to the radio fluxes derived from a number of different continuum surveys. This may provide some insight into the processes and physical state of the matter that produces the observed emission.

The other two methods searched for correlations by comparing IR and radio continuum intensities over extended areas of the sky. The first method compared IR and radio emission over the face of the H II region. The second compared the average emission of both the IR and radio over an extended region in the galactic plane. The scatter diagrams produced by these approaches showed weak correlations at best.

The comparison over the face of two H II regions, The Rosette Nebula and S252, showed no apparent correlations. The galactic plane correlation did have a lower envelope in the scatter diagram. This envelope did appear to show a linear relation. However, it was not clear that this correlation is as strong as the IR-11cm correlations. Since the 11cm data appeared to correlate well with the IRAS data, it may be worthwhile to repeat this procedure with 11cm data.

REFERENCES

Beck, R. and Golla, G. 1988, *Astr. Ap.*, Vol. 191, L9.

Beichman, C.A., Neugebauer, G., Habing, H.J., Clegg, P.E., and Chester, T.J. (eds.), IRAS Catalogs and Atlases Explanatory Supplement, Washington, D.C. U.S. Government Printing Office. 1985.

Caswell, J. L. and R. F. Haynes 1987, *Astr. Ap.*, Vol. 171, 261.

Condon, J., Broderick, and Seielstad, G. 1989, *A.J.*, Vol. 97, 1064.

Cox, P., Krügel, and P. G. Mezger 1986 *Astr. Ap.*, Vol. 155, 380.

de Jong, T. Klein, U., Wielebinski, R., and Wunderlich, E. 1985, *Astr. Ap.*, Vol. 147, L6.

Downes, D., Wilson, T. L., Bieging, J., and Wink, J. 1980, *Astr. Ap. Suppl.*, Vol. 40, 379.

Fich, M. and Blitz L. 1984, *Ap. J.*, Vol. 279, 125.

Haslam, C. G. T. and Osborne, J. L. 1987 Nature, Vol. 327, 211.

Helou, G., Soifer, B. T., and Rowan-Robinson, M. 1985, *Ap. J. (Letters)*, Vol. 289, L7.

Laureijs, R. Infrared Properties of Dust in Interstellar Clouds, Groningen, Netherlands, University of Groningen, 1989.

Lockman, F.J. 1989, *Ap. J. Suppl.*, Vol. 71, 469.

Neugebauer, G. *et al.* 1984, *Ap. J. (Letters)*, Vol. 278, L1.

Reich, W. Fürst, E., Steffen, P., Reif, K., and Haslam, C. G. T. 1984. *Astr. Ap. Suppl.*, Vol. 58, 197.

Reifenstein, E. C., Wilson, T. L., Burke, B. F., Mezger, P. G., and Altenhoff, W. J. 1970, *Astr. Ap.*, Vol. 4, 357.

Wilson, T. L., Mezger, P. G., Gardner, F. F. and Milne, D. K. 1970, *Astr. Ap.*, Vol. 6, 364.

Wink, J. E., Altenhoff, W. J., and Mezger, P. G. 1982, *Astr. Ap.*, Vol. 108, 227.

TABLE 1
H II REGION SURVEYS

| Reference | No. of Sources |
|---|---|
| Caswell and Haynes *Astr. Ap.*, Vol. 171, p. 261 | 316 |
| Downes *et al. Astr. Ap. Suppl.*, Vol. 40, p. 379 | 262 |
| Reifenstein *et al. Astr. Ap.*, Vol. 4, p. 357 | 82 |
| Lockman *Ap. J. Suppl.*, Vol. 71, p. 469 | 462 |
| Wilson *et al. Astr. Ap.*, Vol. 6, p. 364 | 130 |
| Wink *et al. Astr. Ap.*, Vol. 108, p. 227 | 90 |
| Fich and Blitz *Ap. J.*, Vol. 279, p. 129 | 205 |

TABLE 2

LEAST SQUARES FITS OF THE FORM
$\log(F_{11cm}) = A \log(F_{IRAS}) + B$

| IRAS band | A | B | $\chi^2$ | N | RMS |
|---|---|---|---|---|---|
| 12$\mu$m | 0.88 | 1.54 | 0.066 | 14 | 0.25 |
| 25$\mu$m | 1.02 | 2.00 | 0.062 | 20 | 0.24 |
| 60$\mu$m | 1.10 | 2.80 | 0.043 | 11 | 0.20 |
| 100$\mu$m | 0.85 | 3.18 | 0.040 | 15 | 0.19 |

FIGURE 1

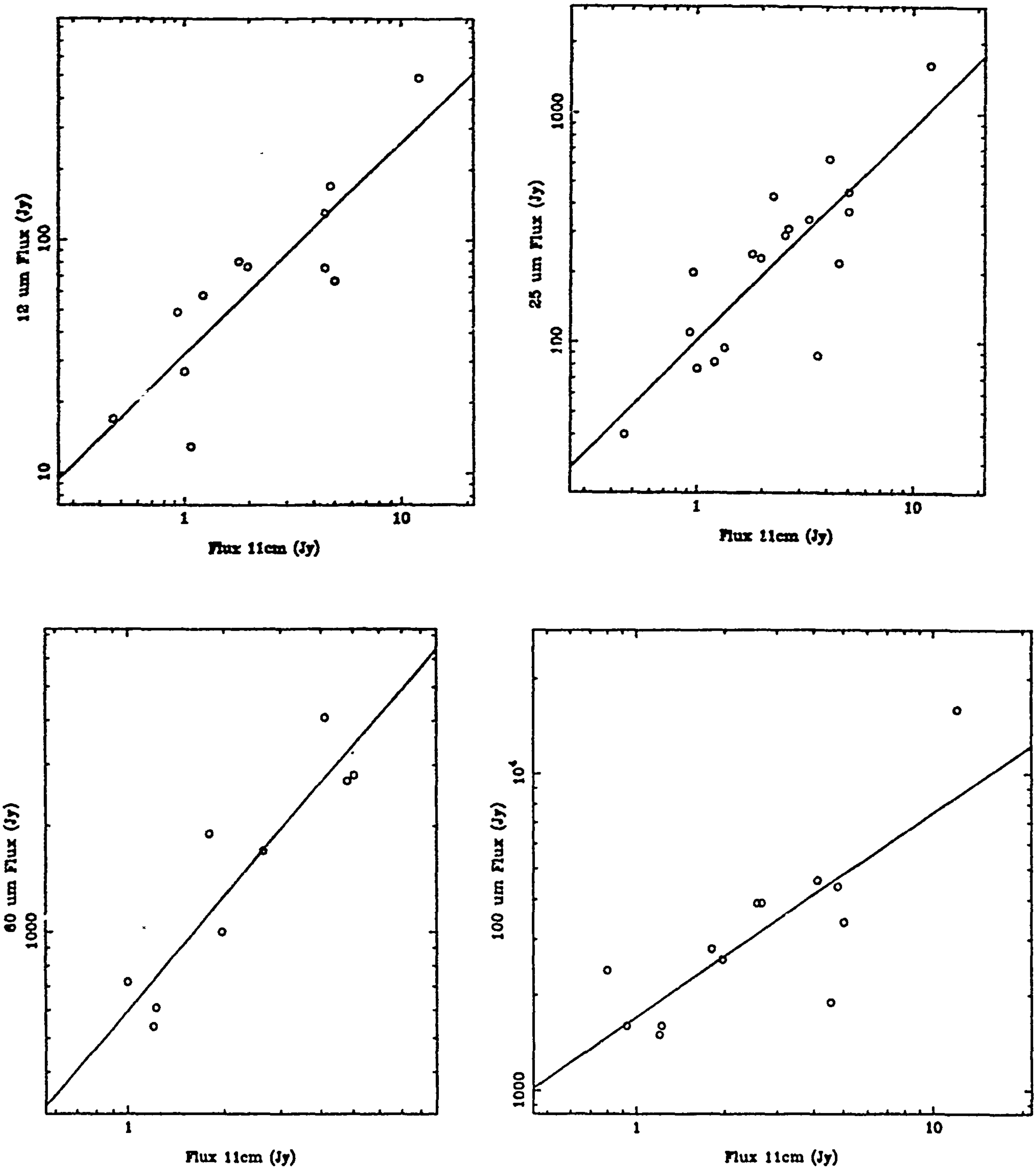

12 um Flux (Jy)
10
100
1
10
Flux 11cm (Jy)
25 um Flux (Jy)
100
1000
1
10
Flux 11cm (Jy)
60 um Flux (Jy)
1000
1
Flux 11cm (Jy)
100 um Flux (Jy)
1000
$10^4$
1
10
Flux 11cm (Jy)

FIGURE 2

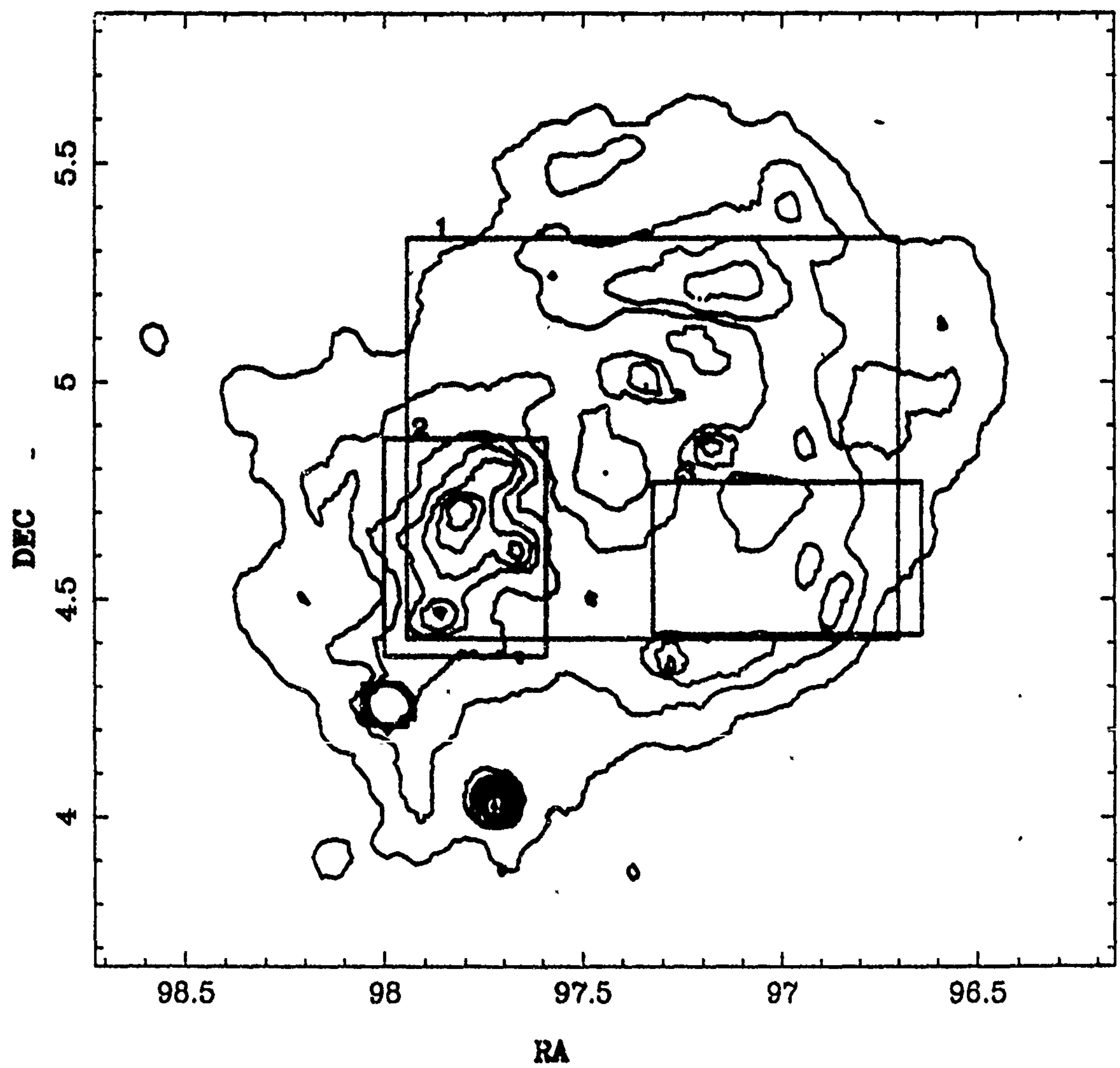

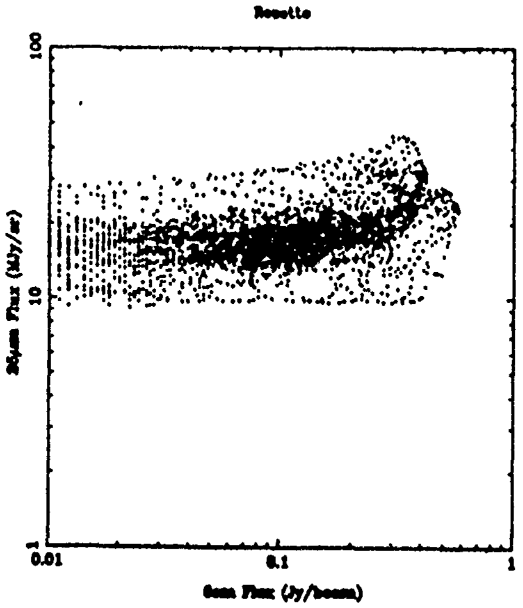
Rosette
100
10
1
25μm Flux (MJy/sr)
0.01
0.1
1
6cm Flux (Jy/beam)

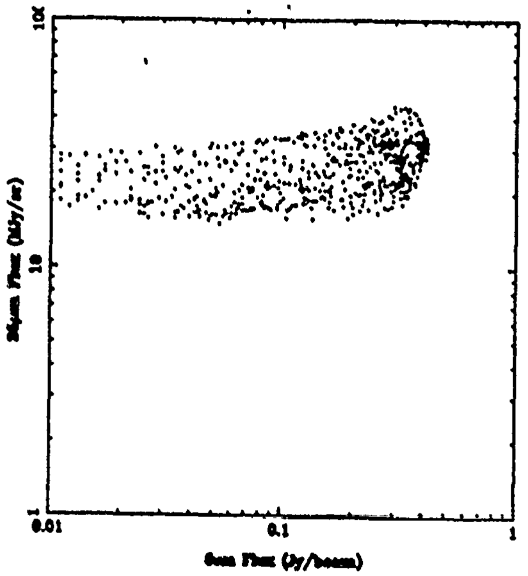
10
1
25μm Flux (MJy/sr)
0.01
0.1
1
6cm Flux (Jy/beam)

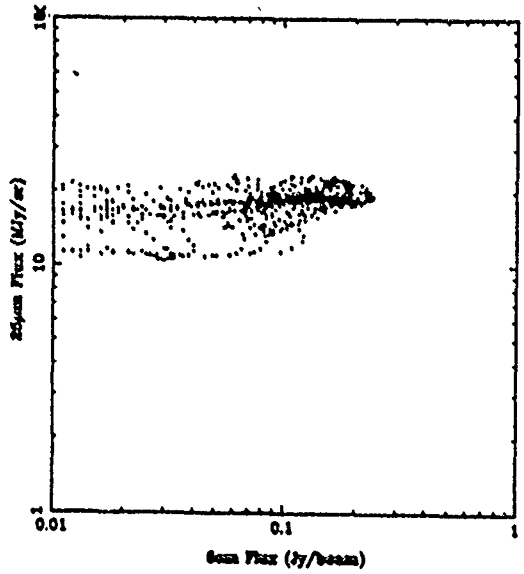
10
1
25μm Flux (MJy/sr)
0.01
0.1
1
6cm Flux (Jy/beam)

FIGURE 4

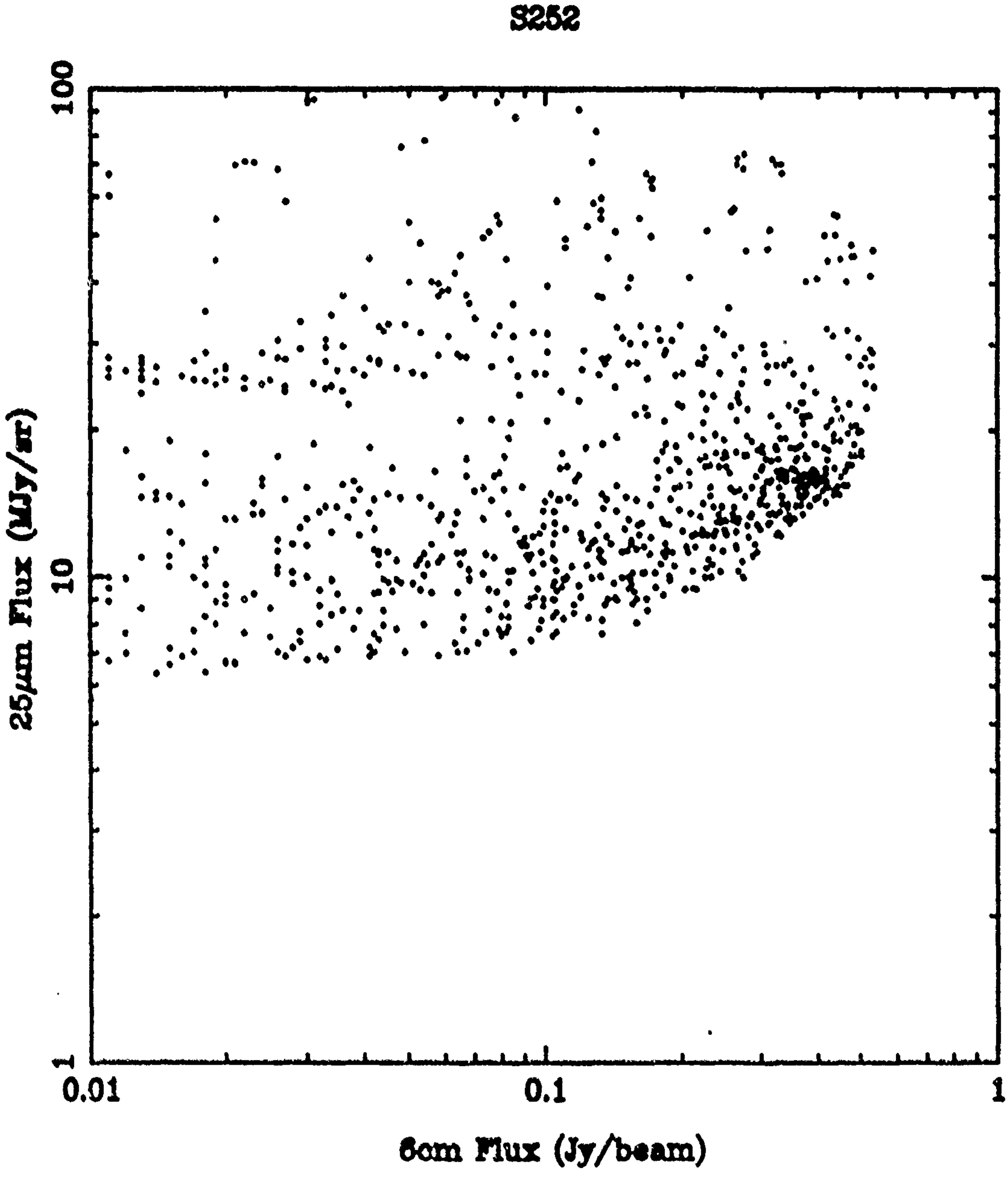

FIGURE 5

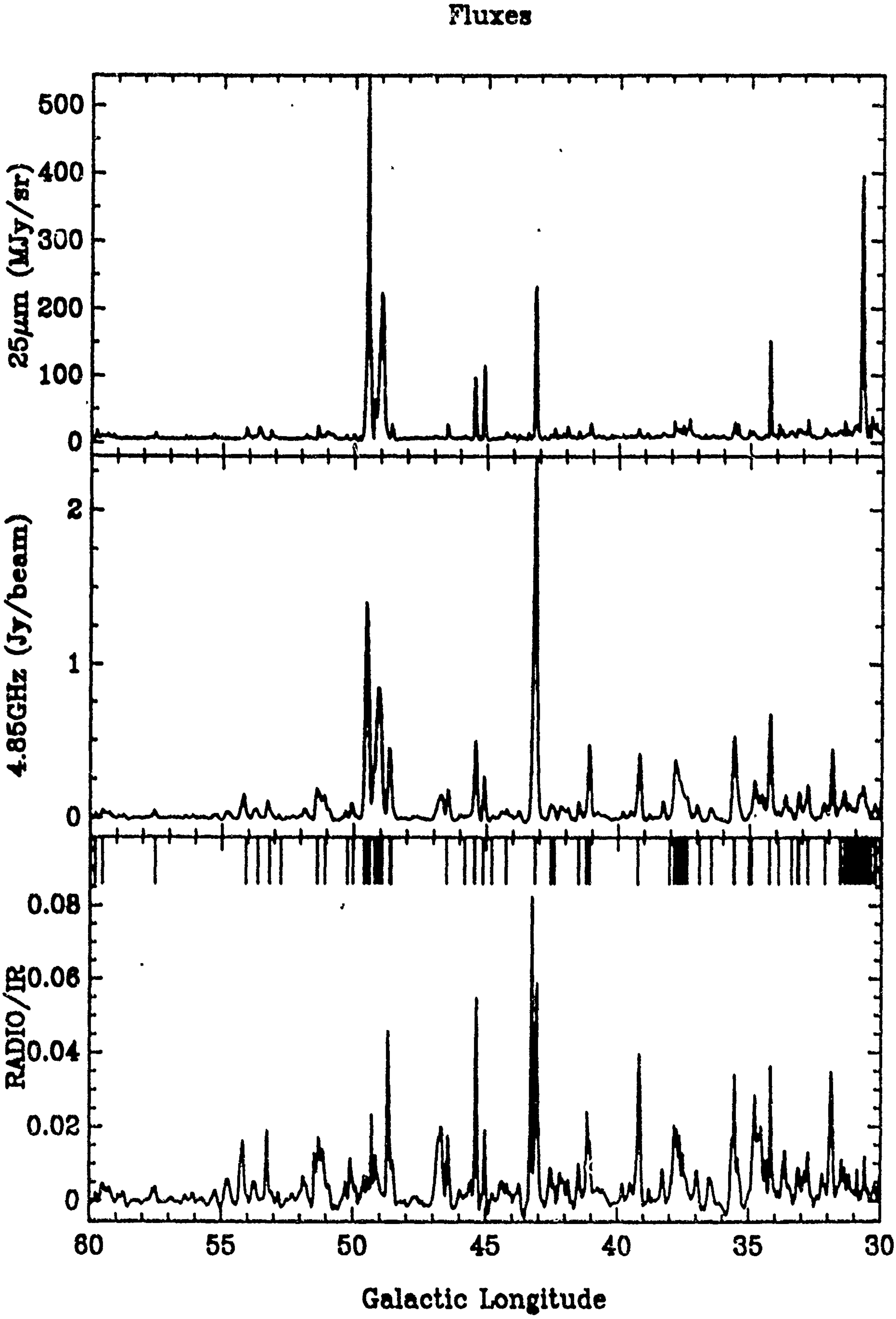
Fluxes
25μm (MJy/sr)
0
100
200
300
400
500
4.85GHz (Jy/beam)
0
1
2
RADIO/IR
0
0.02
0.04
0.06
0.08
60
55
50
45
40
35
30
Galactic Longitude

FIGURE 6

Ratio Limit = 0.000

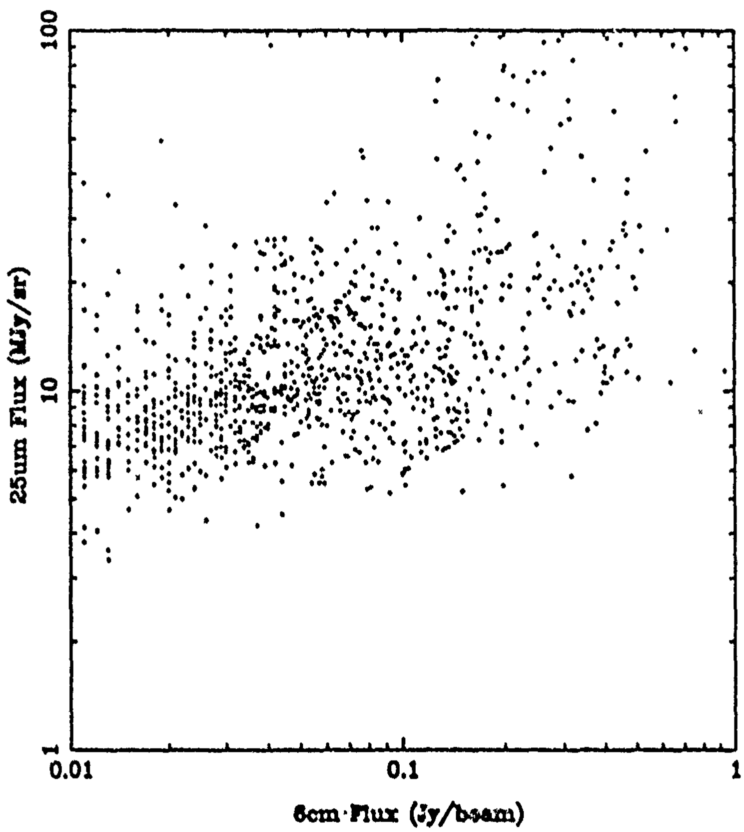


Ratio Limit = 0.005

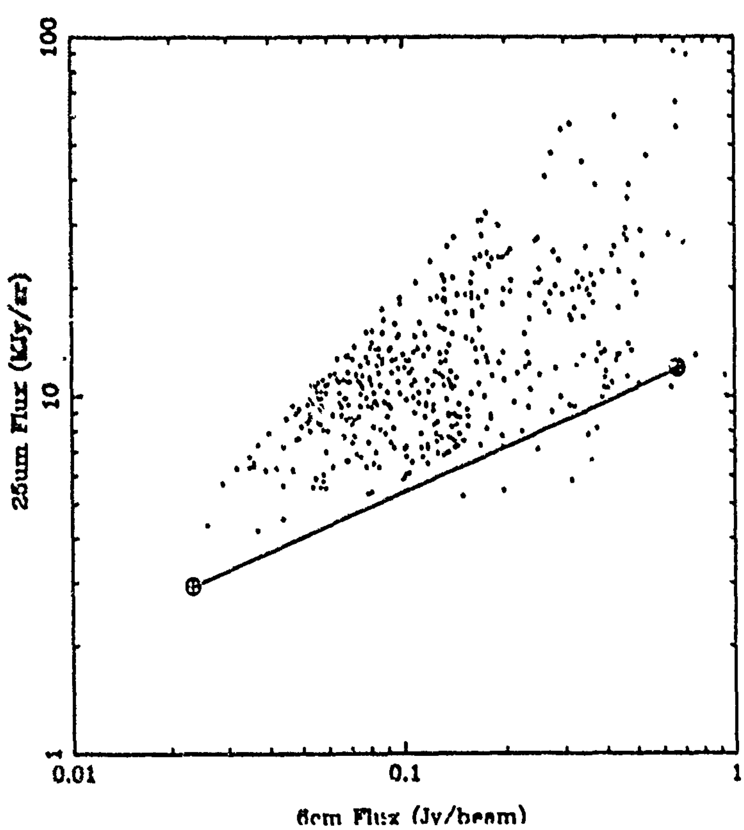

**1991 SUMMER RESEARCH PROGRAM**
**FOR**
**FACULTY AND GRADUATE STUDENTS**

Sponsored by the
UNITED STATES AIR FORCE OFFICE OF SCIENTIFIC RESEARCH

Conducted by the
RESEARCH & DEVELOPMENT LABORATORIES

FINAL REPORT

# STRUCTURAL AND VIBRATIONAL ANALYSES OF THE WAKE SIDE PLASMA SENSOR FOR THE WAKE SHIELD FACILITY


| | |
|---|---|
| Prepared by: | Dr. Joseph J. Rencis, Associate Professor, P.E.<br>Timothy J. Urekew, Ph.D. Candidate<br>Christopher Scarpino, M.S. Student |
| Academic Department: | Mechanical Engineering |
| University: | Worcester Polytechnic Institute<br>100 Institute Road<br>Worcester, Massachusetts 01609 |
| Research Location: | Phillips Laboratory<br>Geophysics Directorate<br>Space Systems Technology Branch<br>Hanscom Air Force Base, Massachusetts 01731 |
| USAF Research Contact: | Dr. David Hardy |
| Date: | August 31, 1991 |

# ACKNOWLEDGEMENT

The authors would like to thank the USAF Office of Scientific Research, and the Research and Development Laboratories for extending them the opportunity to participate in the 1991 Summer Research Program at the Phillips Laboratory, Geophysics Directorate, Hanscom Air Force Base, Massachusetts. The authors would also like to acknowledge the contribution of Dr. David Hardy, Dr. Lon Enloe, Al Locker, Paul Hartnett, Martha Woodward and the staff of the Space Systems Technology Branch. In addition, the authors would like to thank Dr. Adolph Jursa for his efforts during the course of the project.

# I. SCOPE

This report serves as supporting documentation in certifying the Wake Side Plasma Sensor (WSPS) for flight as a secondary structure on the Wake Shield Facility. The WSPS is an experiment package that mounts on the free-flying Wake Shield Facility (WSF). A sectional view of the WSPS is shown in Fig. 1.

# II. APPLICABLE DOCUMENTS

The following documents were used in defining the scope and analysis procedure used in this report.

<u>NASA</u>

| | |
|---|---|
| JSC-20545 (July 1985) | Simplified Design Options for STS Payloads |
| SED Engineering Handbook EHB-2 (November 1990) | Systems Engineering Division Bolted Joint Handbook |

# III. ANALYSIS METHODOLOGY

A static, margin-of-safety based analysis was carried out for critical areas of the WSPS structure. The analysis was performed using the IMAGES-3D personal computer based finite element package [1]. The numerical results were checked against hand calculations when possible. In the Finite Element analyses, inertial loadings are distributed uniformly, throughout the model. In the hand calculations, inertial loadings are applied as point loads acting at the center of gravity of the WSPS. Reactions in critical areas of the structure were determined using Newton's Laws for static equilibrium. Stresses are calculated from the reactions and the structural response is reported as a margin of safety. A finite element modal analysis was also performed to obtain the first three natural frequencies and corresponding mode shapes.

## 3.1 Applied Loads

The WSPS is an experiment package which is attached to the Wake Shield Facility and is therefore classified as a secondary structure. The approximate weight of the WSPS is 25.0 lbs. This is the weight of the mass simulator used in dynamic testing of the Wake Shield Facility at Space Industries Incorporated (SII). The actual weight of the WSPS is not expected to deviate significantly from 25.0 lbs. In

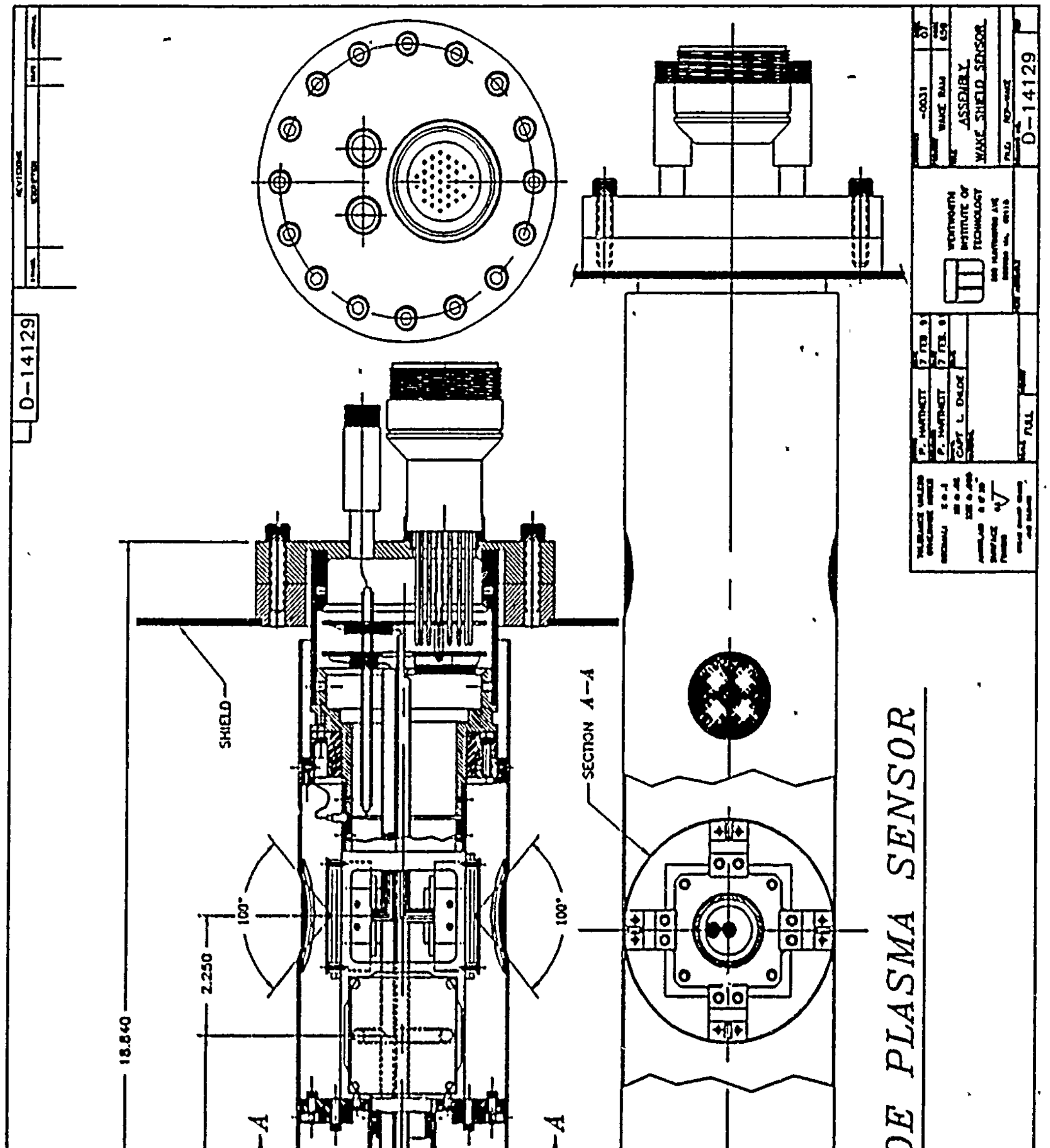


Figure 1 - Sectional View of WSPS

accordance with p.6 of NASA document JSC-20545, a load factor of 31.0 g was applied to the WSPS since its weight is in the 20-50 lb. range. This load factor is intended to represent mechanically and acoustically induced random vibration as well as excitation from low frequency transients. A primary load factor of 31.0 g is applied along each of three coordinate axes with a load factor of 25% of the primary load applied to each of the remaining two orthogonal axes. The three resulting load cases, as required in JSC-20545, are listed in Table 3.1.1. The coordinate system used for applying the required load factors is shown in Fig. 3.1.1 and is parallel to the coordinate system for the WSF. All analyses are carried out relative to the coordinate system shown in Fig. 3.1.1.

Table 3.1.1 - Load Cases for Secondary Structure

| Load Case | Load Factors, g | | |
|---|---|---|---|
| | X | Y | Z |
| 1 | 31.0 | 7.75 | 7.75 |
| 2 | 7.75 | 31.0 | 7.75 |
| 3 | 7.75 | 7.75 | 31.0 |

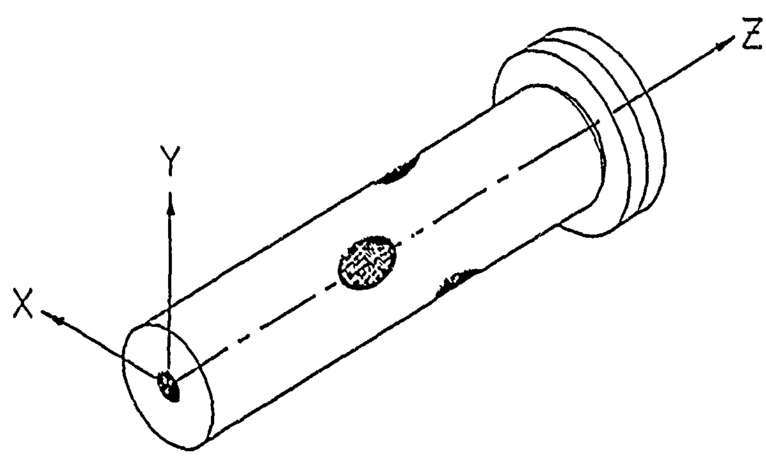


Figure 3.1.1 - WSPS Coordinate System

### 3.2 Critical Structures.

The critical structural items on the WSPS are labeled in Fig. 3.2.1 and are listed in Table 3.2.1. The critical structures are fabricated from AISI 304 stainless steel, A-286 alloy, and from 99% aluminum oxide ceramic. Material properties for the AISI 304 stainless steel and A-286 alloy are taken from [2] and [3], respectively.

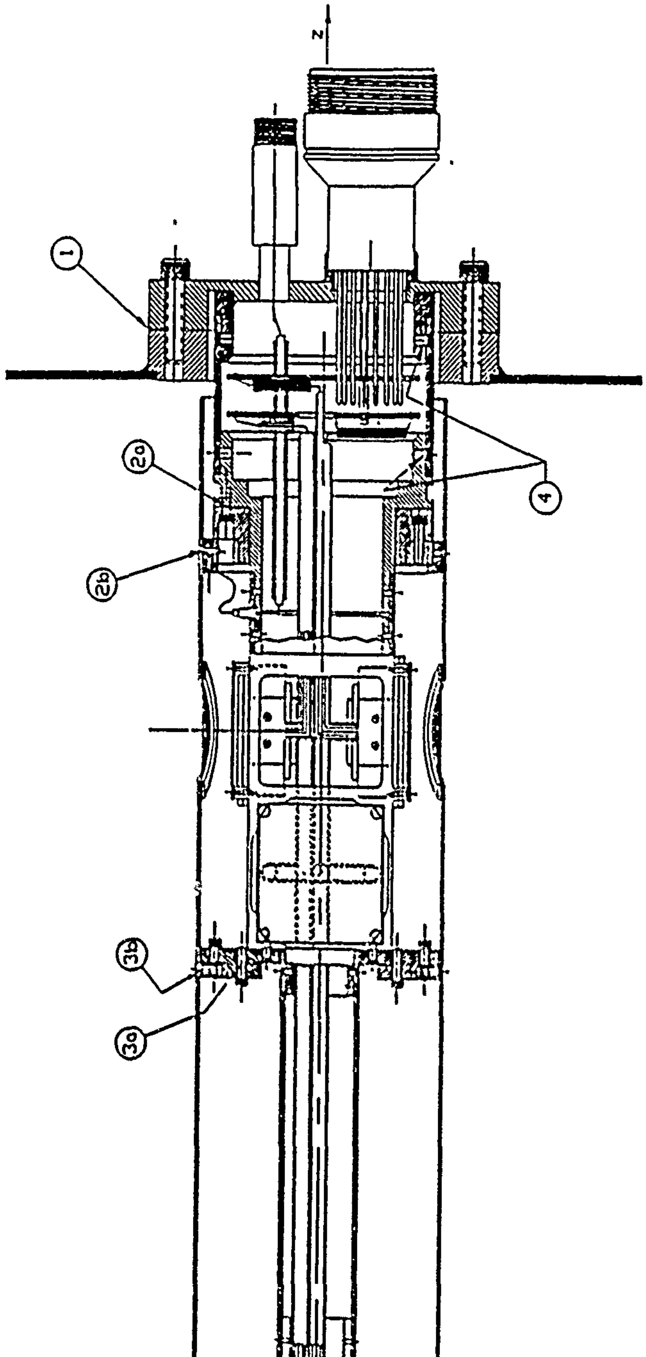


Figure 3.2.1. - Safety Critical Structures

Material properties for the ceramic are taken from [4] and are included in Appendix A.

Table 3.2.1 - Critical Structural Items on WSPS

| Item No. | Description |
|---|---|
| 1 | Joint between conflat flange. |
| 2a | Joint between ceramic ring, probe, and cover |
| 2b | Joint between sensor cover and stainless steel ring |
| 3a | Joint between ceramic tab, stainless steel bracket and cover |
| 3b | Joint between sensor cover and stainless steel ring |
| 4 | Inner cylinder probe joints |

Critical items 1, 2b, 3b, and 4 are analyzed for ductile failures modes since these items are constructed of stainless steel. Items 2a and 3a are analyzed for fracture and ductile failures since these items are constructed of ceramic and stainless steel. The ceramic material in items 2a and 3a is used as an electrical insulator between the WSPS cover and probe.

### 3.3 Analysis Steps.

The critical structural items of the Wake Side Plasma Sensor are the parts and hardware found in the six joints described in Table 3.2.1. The general procedure used to analyze these joints are listed below:

1. Determine fastener forces reacting secondary structure load factors.
2. Determine the minimum required fastener preload for the joint.
3. Determine the maximum allowable fastener preload for the joint.
4. Determine the margin of safety for the joint fasteners using minimum preload.
5. Determine the margins of safety for applicable failure modes of the joint components.
6. Perform a fail-safe analysis by removing the most severely stressed fastener and repeating steps 1 through 5.
7. Determine the minimum and maximum torque values for the joint fasteners using the minimum and maximum preload values from steps 2. and 3., respectively.

The above analysis procedure is based upon theory presented in the Systems Engineering Division Bolted Joint Handbook, NASA Langley Research Center, and in Mechanical Engineering Design by Joseph Shigley [5]. A detailed description of the analysis procedure can be found in Appendix B. A description of the finite element model used for the inertial loading and vibration analyses is included in Appendix C. The detailed analyses for critical items 1, 2a, 2b, 3a, 3b, and 4 can be found in Appendices D, E, F, G, H, and I, respectively.

A vibration analysis of the Wake Side Plasma Sensor is performed using the finite element model to obtain the first three natural frequencies and corresponding mode shapes. Details of the vibration analysis are included in Appendix J.

## IV. ANALYSIS SUMMARY

The results are presented as margins of safety for the structural analysis and as natural frequencies for the vibrational analysis.

### 4.1 Structural Analysis

The parts and hardware associated with each critical structural item listed in Table 3.2.1 were analyzed for appropriate modes of failure (i.e. ductile failure, fracture). Factors of safety of 2.0 and 4.0 were applied on the margin of safety for ductile and fracture critical items, respectively, as required for non-tested structures in JSC-20545. A fail-safe analysis was performed for each critical structural item by removing the most severely stressed fastener in the joint and reanalyzing the WSPS subjected to the load cases shown in Table 3.1.1. A summary of the structural and fail-safe analyses results are included in Table 4.1.1. In addition, assembly torques were calculated for the minimum required and maximum allowable preloads, and are listed in Table 4.1.2. All of the critical structural items satisfy the non-negative margin of safety requirement in JSC-20545. Detailed structural analyses are included in Appendices D, E, F, G, H, and I for critical structural items 1, 2a, 2b, 3a, 3b, and 4, respectively.

Table 4.1.1 - Structural Analysis Results

| Critical Item No. | WSPS Part | Margins of Safety | | Fail - Safe Margins of Safety | |
|---|---|---|---|---|---|
| | | Yield | Ultimate | Yield | Ultimate |
| 1 | 5/16-24 A-286 Soc. Head Cap Scr. | 5.6 | 8.3 | 5.3 | 7.9 |
| | AISI 304 SS Conflat Flange | 1.9 | 6.3 | 2.2 | 7.0 |
| | AISI 304 SS Flange Weldment | 2.9 | 3.7 | 2.9 | 3.7 |
| 2a | #8-32 A-286 Soc. Head Cap Scr. | 2.7 | 3.3 | 2.6 | 3.3 |
| | AP35 99% $Al_2O_3$ Ceramic Ring | - | 7.4 | - | 7.8 |
| | AISI 304 SS Receiving Cylinder | 7.9 | 21.2 | 8.9 | 23.7 |
| 2b | #8-32 A-286 Flat Head Soc. Scr. | 3.4 | 4.5 | 4.9 | 6.5 |
| | AISI 304 SS Ring Screwed to Cover | 13.1 | 34.2 | 19.9 | 51.3 |
| | AISI 304 SS Cover | 0.8 | 3.5 | 0.3 | 2.2 |
| | AISI 304 SS Spacer Ring | 21.7 | 55.8 | 5.2 | 14.4 |
| 3a | #8-32 A-286 Flat Head Soc. Scr. | 4.5 | 6.1 | 0.4 | 0.8 |
| | AP 35 99% $Al_2O_3$ Ceramic Tabs | - | 20.6 | - | 5.4 |
| | AISI 304 SS Tab on Sensor Housing | 6.1 | 16.9 | 1.0 | 4.1 |
| 3b | #8-32 A-286 Flat Head Soc. Scr. | 6.6 | 7.6 | 5.3 | 6.3 |
| | AISI 304 SS Steel Ring | 40.2 | 102.1 | 20.2 | 52.0 |
| | AISI 304 SS Steel Cover | 0.8 | 3.5 | 0.3 | 2.2 |
| 4 | #10-24 A-286 Flat Head Soc. Scr. | 0.5 | 0.9 | 0.1 | 0.4 |
| | AISI 304 SS Quarter Panels | 1.4 | 5.1 | 2.1 | 6.8 |
| | AISI 304 SS Conflat Flg. Weldment | 1.5 | 5.1 | 1.6 | 5.6 |
| | AISI 304 SS Cyl. to Qrt. Panels | 8.5 | 22.8 | 9.0 | 24.0 |

Table 4.1.2 - Assembly Torque Specifications

| Critical Item No. | WSPS Fasteners | Assembly Torques (in-lbf) | |
|---|---|---|---|
| | | Minimum | Maximum |
| 1 | 5/16-24 A-286 Socket Head Cap Screw | 23 | 224 |
| 2a | #8-32 A-286 Socket Head Cap Screw | 8 | 36 |
| 2b | #8-32 A-286 Flat Head Socket Screw | 4 | 36 |
| 3a | #8-32 A-286 Flat Head Socket Screw | 7 | 20 |
| 3b | #8-32 A-286 Flat Head Socket Screw | 2 | 20 |
| 4 | #10-24 A-286 Flat head Socket Screw | 24 | 52 |

**4.2 Vibrational Analysis**

A modal analysis of the WSPS was performed using the finite element model to obtain the first three natural frequencies. These frequencies are listed in Table 4.2.1. The fundamental frequency of 85.3 Hz is more than fourteen times the 6.0 Hz limit specified in JSC-20545. Detailed vibrational results are included in Appendix J.

Table 4.2.1 - Vibrational Analysis Results

| Mode | Frequency (Hz) |
|---|---|
| 1 | 85.3 |
| 2 | 85.3 |
| 3 | 155.0 |

## V. REFERENCES

1. IMAGES-3D User's Manual, Version 2.0, Celestial Software, Inc., 125 University Ave., Berkeley, CA 94710, 1990.

2. MIL HDBK-5E, "Metallic Materials and Elements for Aerospace Vehicle Structures."

3. Unbrako Socket Screws, (Personal Communication: John Buda), Highland Avenue, Jenkintown, PA, 1991.

4. McDanel Refractory Co.,"Catalog of Standard Products", 1991, 510 Ninth Avenue, P.O. Box 560-s, Beaver Falls, PA 15010.

5. Shigley J. E., Mechanical Engineering Design, 3rd edition, McGraw-Hill, 1977.

INFRARED EMISSION OF DIFFUSE HII REGIONS

Russell F. Shipman

Abstract

A one grain infrared emission model was created to reproduce the IR emission of the Rosette Nebula. The temperature gradient, which reproduces the IRAS 60/100 ratio as well as the 60 and 100 micron surface brightnesses, cannot reproduce the 12 and 25 micron surface brightnesses. Therefore, more than one grain component is necessary to explain the 12 and 25 micron surface brightnesses. The temperature gradient, which reproduces the 60/100 ratio, has a very shallow slope suggesting that the dust is heated largely by the ionized gas.

## INTRODUCTION

The purpose of this summer project is to explore the physics of dust grains in large, diffuse HII regions. Historically, the questions raised by this project have been limited to small, compact HII regions. The large HII regions, although well studied at optical and radio wavelengths, are too large for modern telescopes and detectors to map efficiently. It was not until the Infrared Astronomical Satellite (IRAS) that infrared data was available on HII regions on the order of a degree across. These regions, however, offer detailed information concerning the dust they contain. The IRAS data were taken at four wavelengths: 12, 25, 60, and 100 microns. Therefore, not only do the data supply information about the amount of infrared radiation but also the relative amounts at different wavelengths (i.e. a four point spectrum). For HII regions with a diameter around a degree, the IRAS data also present details of the IR emission from different parts of the cloud.

This project concentrates on modeling the IR emission from the Rosette Nebula. At infrared wavelengths, the Rosette is about two degrees in diameter and fairly circular. The hydrogen has been ionized by the stellar cluster NGC 2244. Outside of the ionized region there is an envelope of neutral atomic hydrogen.

## DISCUSSION

The dust in and around the HII region is heated to an equilibrium temperature T by the central stellar cluster as well as by the ultraviolet photons from the ionized gas. The grains then emit the energy as black bodies with peak emission determined by the temperature T. The infrared emission seen by a far-off observer would then be the sum of all the emission from the grains along the line of sight.

Observations of compact HII regions have shown that the spectra are much too broad for simple, one temperature, black body emission (Herter et al. 1979). These observations suggest directly that grains at different temperatures must be present in the HII region. Since grains of different sizes reach different equilibrium temperatures, grains of varying size may account for the broad spectrum (Natta and Panagia 1976, Zeilik 1977). Another possibility is that only a single grain component exists in the HII region. This component gets significantly hotter closer to the center of the region, therefore producing the observed broad spectrum (Aannestad 1978). Since the latter model offers a simpler explanation for the broad spectrum, it is the model adopted for this project.

For a cloud that is optically thin in the infrared, the IR dust emission at one point in the HII region is given by equation 1.

$$dF_\lambda = n(R)\,C_\lambda B_\lambda(T(R)) \tag{1}$$

Here n(R) is the dust grain density at the radius R. The emissivity, $C_\lambda$, of the dust grains determines the extent to which each grain emits as a true black body at a given wavelength. The Planck curve is given by $B_\lambda(T)$ where T(R) is the temperature of the dust at the radius R. To reproduce the observations, equation 1 must be integrated along the line of sight. Therefore, the observed flux at the indicated wavelength is given by equation 2:

$$F_\lambda = \int n(s)\,C_\lambda B_\lambda(T(s))\,ds \tag{2}$$

## MODEL

In order to perform the integration of equation 2, a few assumptions must be made. As seen from radio and optical images, the Rosette nebula appears circular. The model, therefore, assumes spherical symmetry. For one grain component, the choice of emissivity is not very important. The emissivity chosen is the one used by P. Aannestad (1978). One important parameter is the density at a radius R. From the radio emission of the free electrons, one gets a good measure of the electron density throughout the nebula (Bottinelli and Gouguenheim 1964, Menon 1962). If most of the hydrogen is ionized, the hydrogen density is the same as the electron density. The model then assumes a constant ratio of hydrogen density to dust density.

The temperature as a function of radius is the only free parameter of the model. The temperature gradient which best fits the IRAS 60/100 ratio is shown in figure 1. Figure 2 shows the adopted density gradient which is basically a constant density with a ten arc minute hole of zero density at the center of the HII region. Figures 3, 4, and 5 plot the 60/100 ratio, the 100 micron flux and the 60 micron flux, respectively, as functions of the radius. The solid lines are the results of the model while the dotted lines are the IRAS data for the Rosette Nebula. The IRAS data shown are the sums of ten radial cuts through the center of the HII region. The cuts span a range of ten degrees around the center.

The 12 and 25 micron surface briqhtness curves are omitted since the model produces fluxes that are up to 10 orders of magnitude too small. The model is unable to reproduce the 12 and 25 micron fluxes because the temperature gradient is both too low and has too shallow a slope. To produce the observed 12 micron surface brightness, the dust grains must reach temperatures around 200 Kelvin.

CONCLUSION

The temperature gradient of figure 1 is surprisingly flat. The gradient proposed by P. Aannestad (1978) is much steeper indicating that the central stellar cluster performs most of the heating of the dust. The flat gradient of this model seems to indicate that the dust is heated mostly by the ionized gas.

The problem in modeling the 12 and 25 micron fluxes suggests that there is more than one grain size inside the HII region. Thus, one obvious improvement to the model is to add a second, smaller grain component reaching equilibrium at a higher temperature. It should also be possible to match the 100 micron surface brightness better in the central region by adopting a density gradient that reflects better the density of the neutral hydrogen outside of the ionized region. The 21cm line emission of the neutral hydrogen is one way to get this density. Lastly, to make this project more meaningful, the model must be applied to more HII regions.

In conclusion, a simple one grain model can reproduce parts of the IRAS data. In particular, a dust component of large grains can explain the 60/100 ratio, and the 60 and 100 micron surface brightnesses. While the model cannot reproduce the 12 and 25 micron data, it provides a pointer for future adjustments and improvements. It can, in effect, teach by omission.

I would like to thank Dr. Frank O. Clark for his support and insights.

REFERENCES

Aannestad, P. A. 1978, Ap. J., 220, 538.
Bottinelli, L., and Gouguenheim, L. 1964, Ann Astrophy, 27, 685
Herter, T., Duthie, J. G., Pipher, J.L., and Savedoff, M.P. 1979, Ap.J., 234, 897
Menon, T.K., 1962, Ap.J.., 135, 394
Natta, A., and Panagia, N., 1976, Astr. Ap., 50, 191
Zeilik, Michael II, 1977, Ap. J., 213, 58

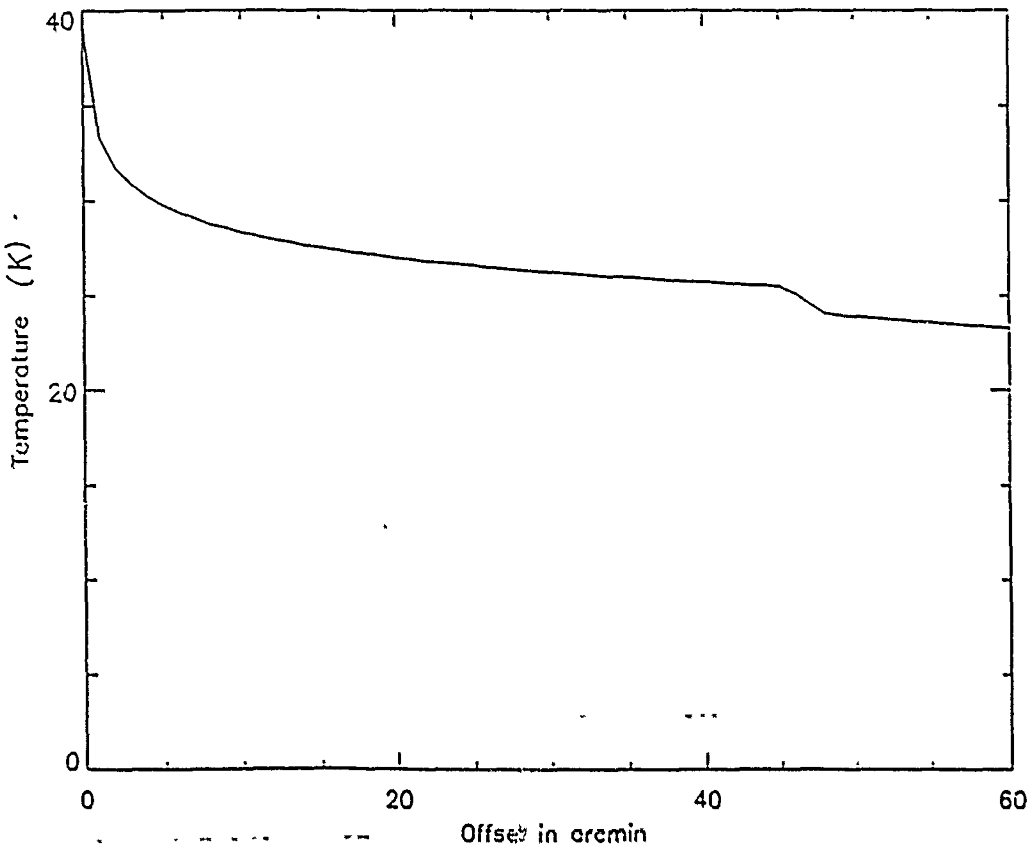


Figure 1. Temperature g..adient for best fit model.

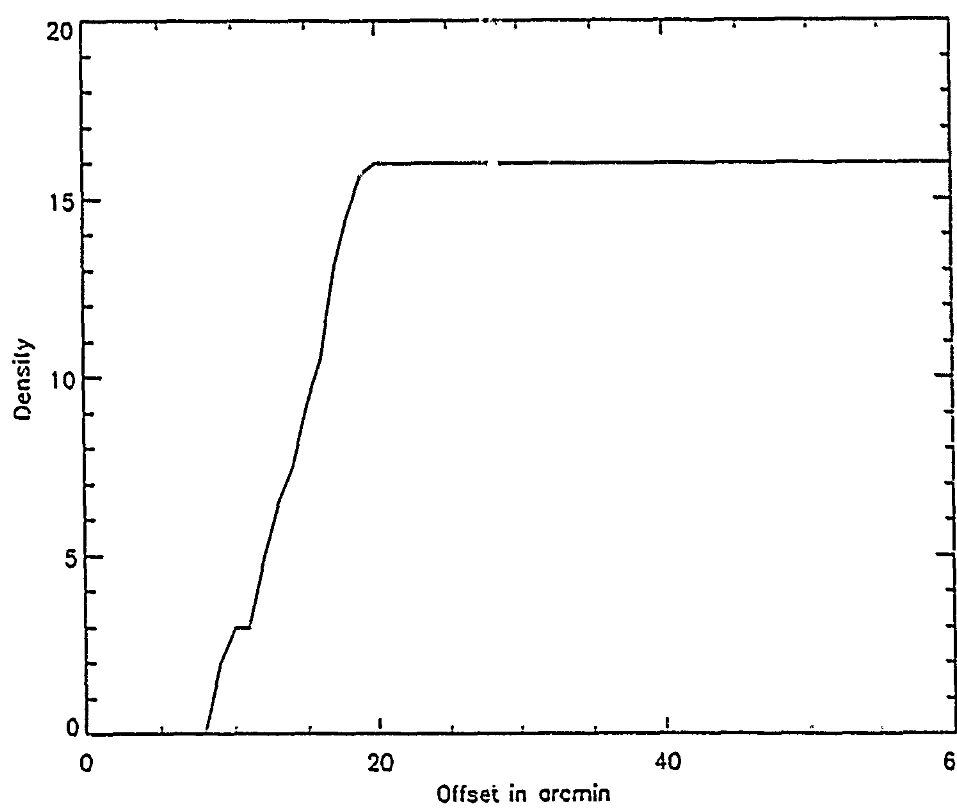


Figure 2. Electron density gradient for the Rosette.

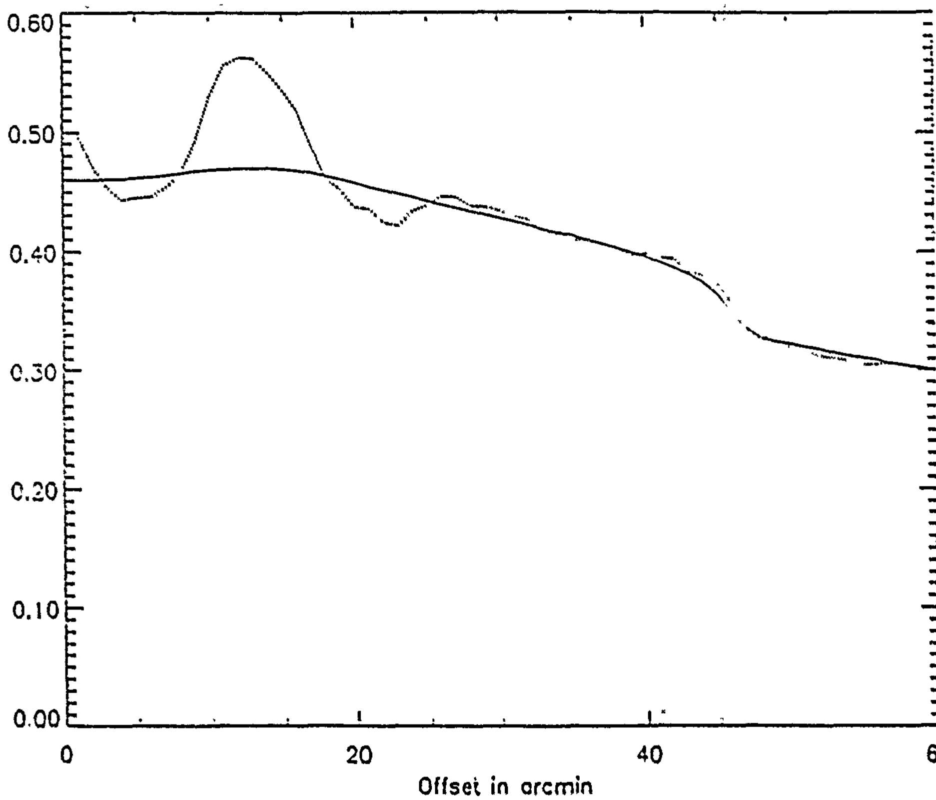


Figure 3. 60/100 ratio. Dotted line - data, solid line - model.

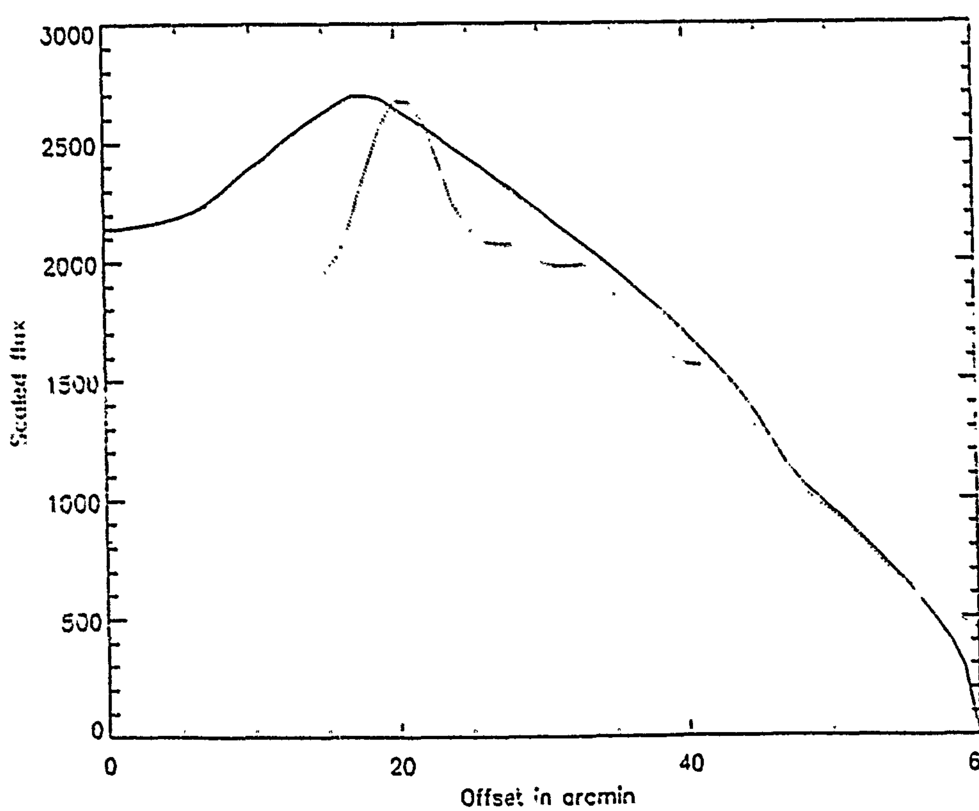


Figure 4. 100 micron surface brightness. Dotted line data, solid line - model.

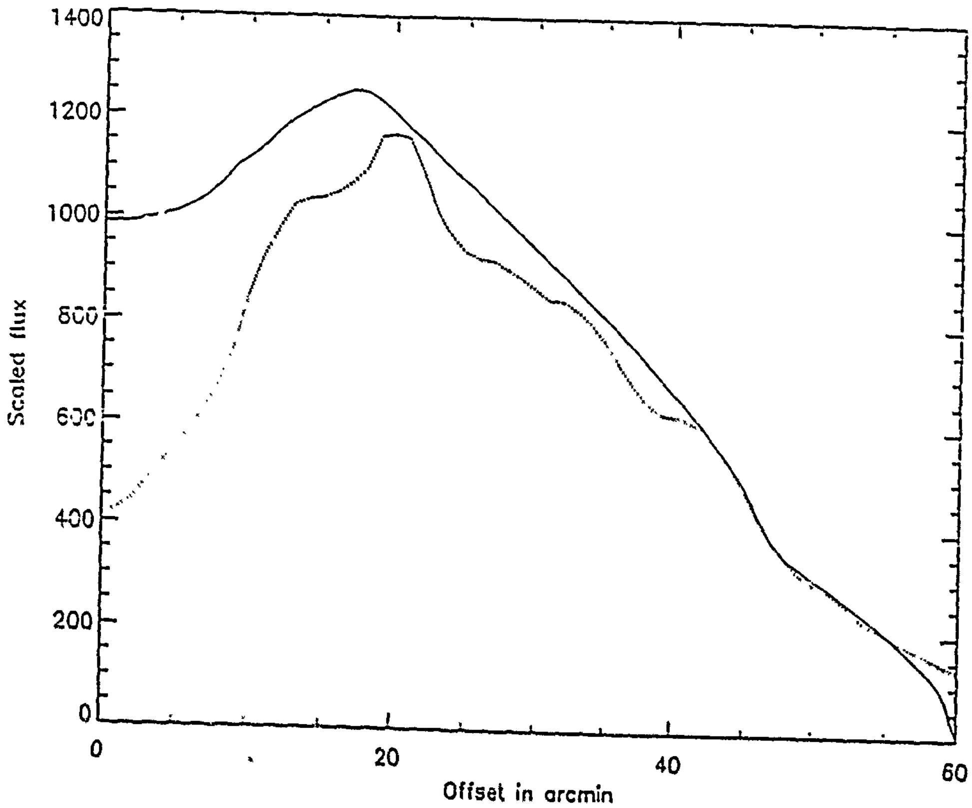


Figure 5. 60 micron surface brightness. Dotted line - data, solid line - model.

# STRUCTURAL AND VIBRATIONAL ANALYSES OF THE WAKE SIDE PLASMA SENSOR FOR THE WAKE SHIELD FACILITY

BY

Timothy J. Urekew
Christopher Scarpino
Dr. Joseph J. Rencis

SEE: CHRISTOPHER SCARPINO

# Two-Dimensional Finite Element Source Code Using Four-Noded Quadrilateral Elements, Truss Elements, and Frame Elements

BY

Richard Castillo

## ABSTRACT

A finite element source code was written in response to a need for a method of numerical analysis which would enable an engineer to model both continuum and frame structures in conjunction with one another or separately. This source code contains the following three elements.

1) Four-noded Quadrilateral Elements
2) Truss Elements
3) Frame Elements

This program was written in the Fortran 77 language. The advantage of this source code is that it can handle both continuum and frame structures. The disadvantage, however, is that as the model becomes more complicated the creation of the input file becomes very cumbersome. A solution to this problem would be to marry this source code to an interactive - graphical - menu - driven program for rapid model definition and generation of the input - file. This would significantly reduce the time required to define a mathematical model of a structure.

# INTRODUCTION

## Description and Background

Scientists and Engineers are often faced with practical physical problems whose solution by conventional analytical methods are either too difficult or even impossible. Faced with this the Scientist or Engineer seeks a so-called "numerical" solution to the problem. There are a number of numerical procedures available with which to attack an otherwise insoluble problem. The "Finite Element" method is one such method.

In this method the body (i.e. continuum or structure) is broken up into a number of elements of finite dimensions. These finite elements representing the body will be interconnected by means of nodes. Nodes can be thought of as "nut-and-bolt" devices which secure adjacent finite elements through their ends or corners and hold them together. The next step in this method of analysis is to determine the element stiffness matrix of the individual elements representing the body. This will then be assembled to form the overall stiffness matrix for the entire discretized body. This will lead to the matrix equation

$$[K]\{\delta\} = \{P\} \qquad 1.0$$

in which [K] denotes the 'overall stiffness matrix'. The 'overall force vector' {P} lists all the externally applied forces at all the nodes, while $\{\delta\}$ lists all the displacements of all the nodes.

For a given set of prescribed boundary conditions and external forces acting on the body, equation 1.0 can be solved uniquely for nodal displacements, $\{\delta\}$, from which the stresses, strains and forces within the model can be subsequently computed.

## Purpose of Report

The purpose of this report will be as follows:

1) Explain the concept of stiffness and compute the stiffness coefficient of a Truss Element. The stiffness coefficients for a frame and four noded quadrilateral element are also discussed.

2) Establish the stiffness matrix for a single truss element.

3) Explain the concept of assembling the element stiffness matrices into the Global Matrix and certain procedures in the assembling process which will save storage memory and computing time.

4) Give a detailed description of the input file and an example.

5) Give a listing of the subroutines in the main program LIN_FEM and a short description of their purpose.

## Sources of Information

In writing this finite element code my two main sources were:

1) Concepts and Applications of Finite Element Analysis Third Edition. Robert D Cook. John Wiley and Sons.

2) Matrix Structural Analysis William McGuire John Wiley and Sons.

The first source was used mainly to determine how to assemble the overall global stiffness matrix and consequently the solution of that matrix which would yield the nodal displacements. The second source was used to compute the element stiffness coefficients for the truss and frame elements. The derivation of the Four-Noded Quadrilateral was taken from class notes in finite element course taken at the University of New Mexico.

This finite element code was instigated primarily for a Two-Dimensional analysis. The possibility, however, for expansion in the Third-Dimension would not be very difficult.

## The Concept of Stiffness

Stiffness is defined as the ratio of force to displacement and is by custom given the symbol K.

$$K = F/\Delta \qquad 2.0$$

The stiffness coefficient for a Truss member can be defined in terms of its cross-sectional properties. This is accomplished as follows:

$$F = \sigma A \qquad 3.0$$

$$\sigma = E\varepsilon \qquad 4.0$$

Substituting 4.0 into 3.0 yields:

$$F = E\varepsilon A \qquad 5.0$$

but

$$\varepsilon = \Delta/L \qquad 6.0$$

Substituting 6.0 into 5.0 yields

$$F = E\Delta A/L \qquad 7.0$$

Substituting 7.0 into 1.0 yields the stiffness coefficient of a truss element in terms of its cross-sectional properties:

$$K = EA/L \qquad 8.0$$

This result indicates that the stiffness coefficient remains constant for a given truss member.

The process of developing all the stiffness coefficients for a frame and a four noded quadrilateral element are somewhat more involved.

For a frame element the well known 'principle of superposition' is used. Using this, the total 'effect' due to the simultaneous action of several 'causes' (i.e. effects due to each cause acting separately.) The explicit expressions for all the coefficients can be seen in the second reference "Matrix Structural Analysis".

For a Four-noded Quadrilateral element the element stiffness matrix is defined as

$$[K] - \int_{-b}^{b} \int_{-a}^{a} [B] \ [E][B] \ t \ dx \ dy$$

where t = element thickness

[B] = strain - displacement matrix

[E] = Matrix of elastic stiffness

For this finite element source code Gauss Quadrature was used to evaluate the integral.

Truss Member Element Stiffness matrix

If a positive displacement $\delta_1$ is imposed on the near end of the member of figure 1.0a, while the far end is held pinned, the forces developed at the ends of the member are:

$$q_1' = (AE/L)\delta_1 \qquad q_2' = (-AE/L)\delta_1$$

Note that $q_2'$ is negative since for equilibrium it acts in the negative x' direction. Likewise, a displacement of $\delta_2$ at the far end, keeping the near end pinned as in figure 1.0b results in member forces of

$$q_1'' = (-AE/L)/\delta_2 \qquad q_2'' = (AE/L)/\delta_2$$

By superposition, figure 1.0c, the resultant effect of both $\delta_1$ and $\delta_2$ is: $q_1 = (AE/L)(\delta_1 - \delta_2) \qquad q2 = (AE/L)(\delta_2 - \delta_1)$

Both of these equations may be written in matrix for as:

$$\begin{bmatrix} q_1 \\ q_2 \end{bmatrix} = \begin{bmatrix} \frac{AE}{L} \end{bmatrix} \begin{bmatrix} 1 & -1 \\ -1 & 1 \end{bmatrix} \begin{bmatrix} \delta_1 \\ \delta_2 \end{bmatrix} \qquad 9.0$$

where

$$K' = \frac{AE}{L} \begin{bmatrix} 1 & -1 \\ -1 & 1 \end{bmatrix} \qquad 10.0$$

The matrix k' defined by equation 10.0 is called the element stiffness matrix. It should be noted that in the development of equation 9.0 both equilibrium and compatibility of deformation of the member have been satisfied. The element stiffness matrix is always symmetric owing to the reciprocity of causes and effects in linear systems. This will be of great value in the assembly process discussed in the next section.

## Assembly of the Overall Stiffness Matrix

Having calculated the [K]'s of individual elements into which the body is subdivided, the next step is to assemble these to form what is called the 'overall stiffness matrix' for the entire discretized body. This is done by ensuring that the equilibrium and compatibility conditions are satisfied at all the nodes within the discretized body.

This process is accomplished by starting with a null structure stiffness matrix [K], then adding to it the [K] of each element. When the last element has been added, the structure stiffness matrix is complete and [K] is complete. The physical meaning of [K] is as follows: The jth column of [K] is the vector of loads that must be applied to nodal D.O.F. j while all other nodal D.O.F. are zero.

If the structure has n D.O.F. this means that the global matrix is an nxn matrix. The resulting global matrix is also symmetric with many zeros away from the main diagonal.

As the number of D.O.F grows for a more complicated structure the global matrix also becomes very large. This would of course lead to larger storage requirements and more expensive computing time. Because the assembled matrix is symmetric it makes sense to store only the upper half-band of the assembled matrix. general purpose equation solvers are available for such banded systems of equations.

## Description of the Input file 'Input.Dat'

The following is a description of the input file used by lin_fem. The input file is in free format. It is broken down into 7 parts. Each part is described below. A example of an input file is included at the end of the description.

### 1.0 Title

The title of the problem is written in the beginning of the input file. It should be limited to two lines.

### 2.0 Global Parameters

The global parameters are written, on the same line, in the following order:

1) Global number of nodes
2) Global number of elements
3) global number of Domains
4) Global number of cracks
5) Dimensionality of the problem
6) Thermal Flag
7) Acceleration flag
8) Number of degrees of freedom per node of the structure

### 3.0 Domain

For each domain there is a line in the input file. Each line consists of the following:

1) The domain number
2) The domain type (1: FE domain)
3) The domain analysis code 1: Plane Stress
   2: Plane Strain
   3: Axisymmetry)

### 4.0 Elements

For each element there is a line in the input file. Each line consists of the following:

1) The element number
2) The number of the domain that contains this element
3) The number of nodes N that belong to this element
4) The element code (3: 4 Noded Quadrilateral Element
   4: Frame Element
   5: Truss Element)
5) Node number 1...node number N

Remarks:

The element-node connectivity list is written in a given order for a 4-noded quadrilateral element. The nodes associated with that particular element are listed in a counterclockwise order.

### 5.0 Nodes

For each node there is a line in the input file. Each line consists of the following:

1) The node number
2) x-coordinate
3) y-coordinate
4) Boundary Condition set in the x-direction
5) Boundary Condition set in the y-direction
6) Boundary Condition set in the ⊘-direction
   Note: If a node is connected to a truss or a 4-noded quadrilateral, only the Boundary Condition set in the 0-direction should be fixed.

### 6.0 Boundary Condition Sets

For each different boundary condition set there is a line in the input file. Each line consists of the following:

1) Boundary Condition set number
2) Boundary Condition Code
   (1: if displacement is specified
   0: if force is specified)
3) Boundary Condition Value

### 7.0 Material Sets

For each different material set there is a line in the input file.

Each line consists of the following:

1) Material Set number
2) material model code (1: for isotropic linear elasticity)
3) Youngs Modulus
4) Poissons Ration/Moment of Inertia
5) Thickness/Area
6) Coefficient of Thermal Expansion
7) Density
8) Temperature
9) Gauss order of integration

Descriptions of Subroutines used in 'LIN_FEM'

INPUT:

this subroutine reads the input data to the finite element program from a file called INPUT.DAT. The information read is echoed to an output file called OUTPUT.DAT.

STIFF_ELEM:

This subroutine calculates the element stiffness matrices and stores them in STIFF.DAT.

STIFF_Q4:

This subroutine computes the element stiffness matrix for a beam element.

STIFF_TRUSS:

This subroutine computes the element stiffness matrix for a truss element.

ASSIGN_EQ_NUM:

This subroutine assigns consecutive numbers to DOF which have not been fixed. Those DOF which have been fixed are assigned the value zero.

BANDWIDTH:

This subroutine calculates the semibandwidth of the structure stiffness matrix.

ASSEMBLE:

This subroutine assembles the structure stiffness matrix [Kff] and the forcing vector {{Fs} - [Kfs]{Ds}}

SOLVER:

This subroutine solves a symmetric system of banded simultaneous linear equations using the method of Banachiewicz (Cholesky decomposition for symmetric matrices).

DISPL_OUTPUT:

This subroutine outputs the displacements and nodel coordinates for each node in a Q4 element in the model.

RECOVER_STRAIN_STRESS:

This subroutine computes the stresses and strains for each Q4 element in the model.

DISPL_FORCES_OUTPUT_FRAME:

This subroutine outputs the displacements, forces and nodel coordinates for each frame element in the model.

DISPL_FORCES_OUTPUT_TRUSS:

This subroutine outputs the displacements, forces and nodel coordinates for each truss element in the model.

## CONCLUSION

This was a very general Two-Dimensional Finite Element Source Code which will enable engineers to analyze continuum and frame structures in conjunction with one another or separately.

The disadvantage of using this Finite Element Program is that as the model becomes more complicated the creation of the input file becomes very cumbersome. A solution to this problem would be to marry this source code to an interactive-graphical-menu driven program for rapid model definition and generation of the input file. This would significantly reduce the time required to define a mathematical model of a structure.

This finite element code as mentioned above is only capable of analyzing two-dimensional problems. This will naturally limit the modeling of realistic problems. The possibility for expansion into the third-dimension would not be very difficult.

In terms of this summer program I learned a tremendous amount. In the beginning weeks I was primarily concerned with learning the computer system. Namely the UNIX operating system, the VI editor, the DBX debugger and the Sun Spark Station. In the middle portion of the program I studied and became very familiar with the "Finite Element Method" and with the remaining time I had left programmed and debugged my source code.

Portal Frame with Shear Wall and Diagonal Bracing

| | | | | | | | | | | |
|---|---|---|---|---|---|---|---|---|---|---|
| 4 | 5 | 1 | 0 | 2 | 0 | 0 | 3 | | | |
| 1 | 1 | 1 | | | | | | | | |
| 1 | 1 | 2 | 4 | 1 | 1 | 2 | | | | |
| 2 | 1 | 2 | 4 | 1 | 2 | 3 | | | | |
| 3 | 1 | 2 | 4 | 1 | 3 | 4 | | | | |
| 4 | 1 | 4 | 3 | 2 | 1 | 2 | 3 | 4 | | |
| 5 | 1 | 2 | 5 | 3 | 2 | 4 | | | | |
| 1 | 0.0 | | 0.0 | | 1 | 1 | | | | |
| 2 | 0.0 | 120.0 | | | 3 | 2 | | | | |
| 3 | 120.0 | | 120.0 | | 2 | 2 | | | | |
| 4 | 120.0 | | 0.0 | | 1 | 1 | | | | |
| 1 | 1 | | 0.0 | | | | | | | |
| 2 | 1 | | 0.0 | | | | | | | |
| 3 | 0 | | 10.0 | | | | | | | |
| 1 | 1 | 0.2900E+05 | | 1800.0 | | 50.0 | 0 | 0 | 0 | 0 |
| 2 | 1 | 0.2900E+05 | | 0.3 | | 1.0 | 0 | 1.0 | 0 | 2 |
| 3 | 1 | 0.2900E+05 | | 900.0 | | 25.0 | 0 | 0 | 0 | 0 |

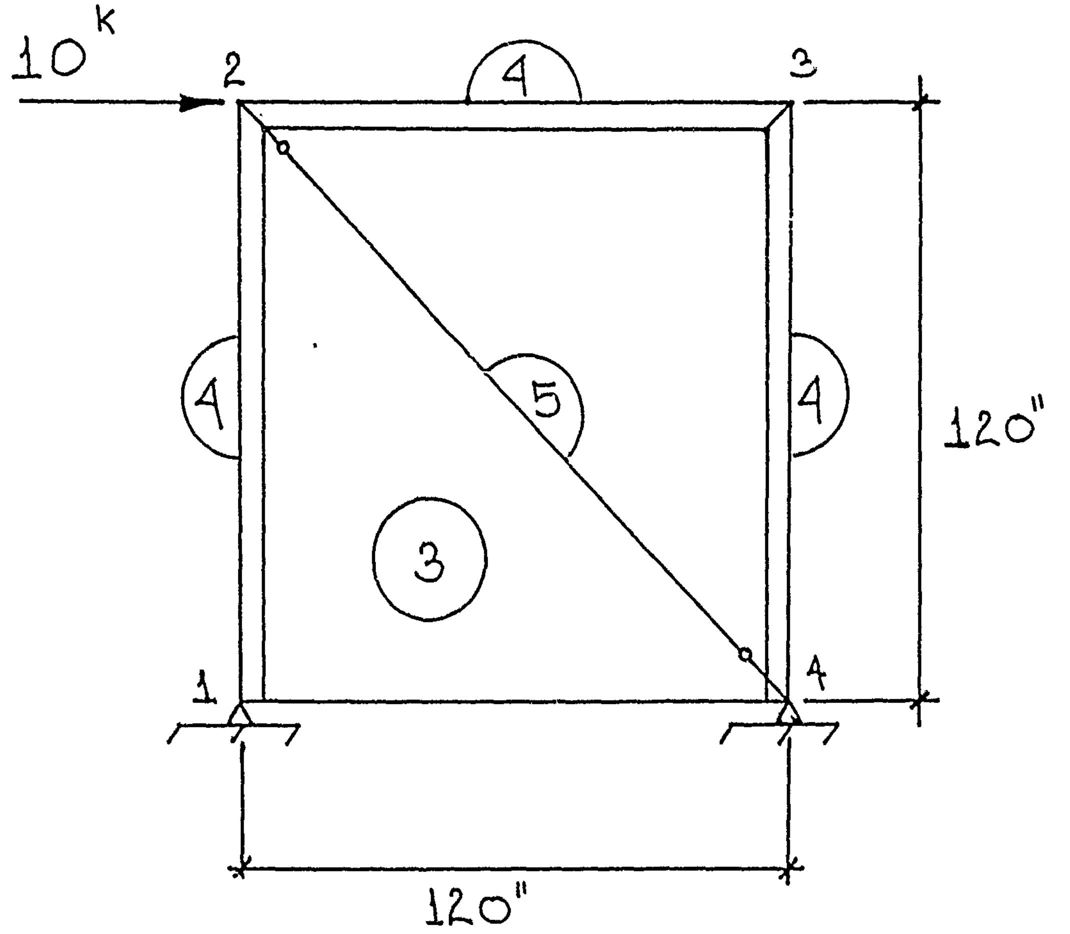

10 k
2
3
4
4
5
4
3
1
4
120"
120"

--------------OUTPUT OF PROGRAM LIN_FEM--------------------

PORTAL FRAME WITH SHEAR WALL AND DIAGONAL BRACING

| | | |
|---|---|---|
| NUMBER OF NODAL POINTS | - | 4 |
| NUMBER OF ELEMENTS | - | 5 |
| NUMBER OF DOMAINS | - | 1 |
| NUMBER OF CRACKS | - | 0 |
| DIMENSIONALITY OF PROBLEM | - | 2 |
| THERMAL STRESS FLAG | - | 0 |
| ACCELERATION FLAG | - | 0 |
| NUMBER OF DOF PER NODE | - | 3 |

ELEMENT CONNECTIVITY:

ELEMENT TYPE:

3 - Four Noded Quadrilateral Element
4 - 2 Dimensional Frame Element
5 - 2 Dimensional Truss Element

| ELEM | DOMAIN | NUM_NOD | CODE | MAT_SET | -----------CONNECTIVITY--------- | | | |
|---|---|---|---|---|---|---|---|---|
| 1 | 1 | 2 | 4 | 1 | 1 | 2 | | |
| 2 | 1 | 2 | 4 | 1 | 2 | 3 | | |
| 3 | 1 | 2 | 4 | 1 | 3 | 4 | | |
| 4 | 1 | 4 | 3 | 2 | 1 | 2 | 3 | 4 |
| 5 | 1 | 2 | 5 | 3 | 2 | 4 | | |

NODE INFORMATION:

| NODE | COORDINATES X | COORDINATES Y | BC SET X | BC SET Y |
|---|---|---|---|---|
| 1 | 0.0000 | 0.0000 | 1 | 1 |
| 2 | 0.0000 | 120.0000 | 3 | 2 |
| 3 | 120.0000 | 120.0000 | 2 | 2 |
| 4 | 120.0000 | 0.0000 | 1 | 1 |

NODAL BOUNDARY VALUE SETS:

BC CODES: 0:FREE; 1:FIXED

| SET # | CODE | VALUE |
|---|---|---|
| 1 | 1 | 0. |
| 2 | 0 | 0. |
| 3 | 0 | 10.00 |

MATERIAL PROPERTY SETS:

```
MATERIAL MODELS: ISOTROPIC LINEAR ELASTICITY - 1

MAT =  MODEL  YOUNGS MOD.   MOMENT OF     AREA      COEFF. EXP.
                            INERTIA
  1      1    0.2900E+05     1800.        50.00          0.

        DENSITY      TEMPERATURE      GAUSS ORDER
           0.             0.               0

MAT =  MODEL  YOUNGS MOD.   POISS RATIO   THICK     COEFF. EXP.
  2      1    0.2900E+05    0.3000        1.000          0.

        DENSITY      TEMPERATURE      GAUSS ORDER
         1.000            0.               2

MAT =  MODEL  YOUNGS MOD.   MOMENT OF     AREA      COEFF. EXP.
                            INERTIA
  3      1    0.2900E+05     900.0        25.00          0.

        DENSITY      TEMPERATURE      GAUSS ORDER
           0.             0.               0


-------------END OF INPUT PHASE--------------

ELEMENT FORCES FOR A FRAME ELEMENT IN THE LOCAL COORDINATE SYSTEM

ELEMENT #1
      NODE 1:
     AXIAL FORCE         SHEARING FORCE      MOMENT
  -10.0000000000000    0.264966648435229    0.
      NODE 2:
     AXIAL FORCE         SHEARING FORCE      MOMENT
   10.0000000000000   -0.264966648435229    31.795978122275

ELEMENT #2
      NODE 2:
     AXIAL FORCE         SHEARING FORCE      MOMENT
   0.26417396246489   -0.82897378015052    -31.795978122275
      NODE 3:
     AXIAL FORCE         SHEARING FORCE      MOMENT
  -0.26417396246489    0.52914044681718    -31.700875495787

ELEMENT #3
      NODE 3:
     AXIAL FORCE         SHEARING FORCE      MOMENT
   0.5291.044681718    0.26417396246489     31.700875495787
      NODE 4:
     AXIAL FORCE         SHEARING FORCE      MOMENT
  -0.52914044681718   -0.26417396246489     1.4210854715202D-14


 STRAINS STRESSES AND DISPLACEMENTS IN THE Q4 ELEMENTS:
------------------------------------------------------

 COORDINATE DISPLACEMENTS

 NODE   X_COORD      Y-COORD      X_DISPL     Y-DISPL
```

| | | | | |
|---|---|---|---|---|
| 1 | 0.0000E+00 | 0.0000E+00 | 0.0000E+00 | 0.0000E+00 |
| 2 | 0.0000E+00 | 0.1200E+03 | 0.5261E-02 | 0.8276E-03 |
| 3 | 0.1200E+03 | 0.1200E+03 | 0.5240E-02 | -0.4379E-04 |
| 4 | 0.1200E+03 | 0.0000E+00 | 0.0000E+00 | 0.0000E+00 |

ELEMENT NO. - 4

| NODE_LOC. | STRAIN(X) | STRAIN(Y) | STRAIN(XY) | STRESS(X) | STRESS(Y) | STRESS(XY) |
|---|---|---|---|---|---|---|
| 1 | 0.0000E+00 | 0.6897E-05 | 0.4385E-04 | 0.1154E+00 | 0.2692E+00 | 0.4890E+00 |
| 2 | -0.1822E-06 | 0.6897E-05 | 0.3658E-04 | 0.1083E+00 | 0.2662E+00 | 0.4080E+00 |
| 3 | -0.1822E-06 | -0.3649E-06 | 0.3640E-04 | -0.1322E-01 | -0.1729E-01 | 0.4060E+00 |
| 4 | 0.0000E+00 | -0.3649E-06 | 0.4366E-04 | -0.6105E-02 | -0.1425E-01 | 0.4870E+00 |
| 0 | -0.9109E-07 | 0.3266E-05 | 0.4012E-04 | 0.5108E-01 | 0.1260E+00 | 0.4475E+00 |

ELEMENT FORCES FOR A TRUSS ELEMENT IN THE LOCAL COORDINATE SYSTEM

ELEMENT #5
NODE 2:
AXIAL FORCE
13.393818027442

ELEMENT #5
NODE 4:
AXIAL FORCE
-13.393818027442

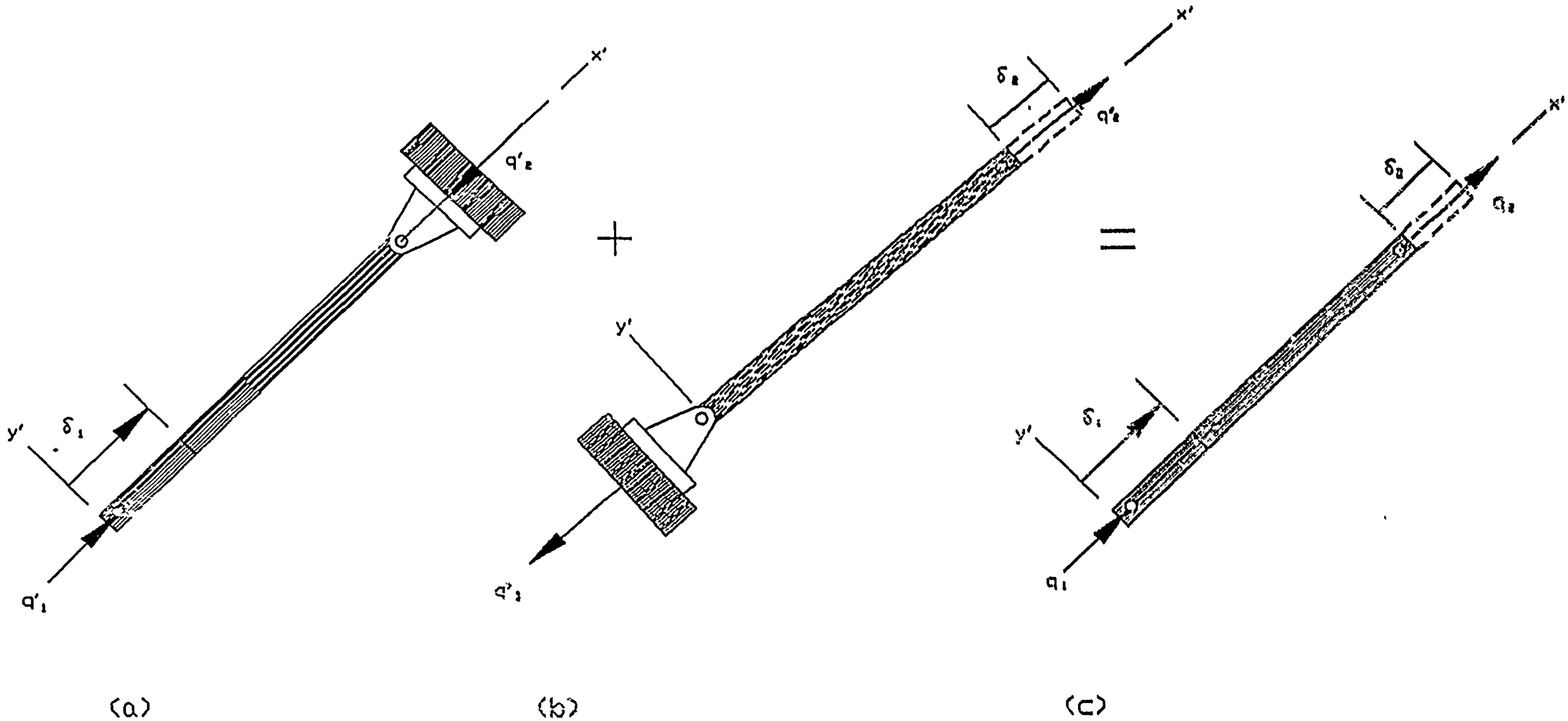


Fig. 1.0

# Assembly and Operation of the Working Fluid Experiment

John F. Crawford, University of New Mexico

## Abstract

A 1-5 eV plasma is desired to be used as a working fluid for shockless compressions which have densities on the order of $10^{19}/cm^3$. This report describes the successful assembly and testing of the working fluid experiment (WFX).

## Introduction

Applications involving projectile acceleration require a medium with very high sound speed. Since the speed of a projectile is limited by the accelerating medium, a high density, low temperature plasma would be useful for this and other applications.

This report describes the assembly, operation, and initial data collected on this WFX plasma source. This work was achieved by myself, Professor John Gahl, and a variety of Phillips Laboratory personnel, who were largely responsible for securing a location for the experiment and all of the necessary equipment to carry out this research project.

## Experiment

The WFX consists of a coaxial plasma gun operated in the snowplow mode [1,2]. The WFX can be operated at a variety of fill pressures to achieve the desired densities, and gun voltages can be varied to produce a variety of plasmas. The snowplow mode of operation is desired because the moving plasma front can be used to compress the remaining chamber gas to high densities. This results in lower directed energy and high densities. The gun was typically operated with a fill pressure of 20 torr.

The gun consists of s 30 cm long inner conductor and a set of rods make up the outer conductor. Figure 1 is a schematic of the gun design. Figure 2 displays the assembly of the inner conductor and the power feed connection. The voltage on the inner conductor is held off from the outer conductor by a glass sleeve. The "doorknob" is connected to the inner conductor against a copper washer as seen in Fig 2.

The WFX is powered by a 55 kJ, 60 kV capacitor bank and is fed by a parallel plate transmission line. To fire the experiment, the WFX is filled the the desired pressure, and the capacitor bank is switched onto the experiment through a rail gap switch. This applies a pulse to the gun between the conductors. Initially the gun breaks down along the glass sleeve . The glass sleeve is installed to protect the inner conductor and keep contaminants to a minimum.

The working fluid is created by the discharge which ionizes the fill gas. As the discharge moves towards the doorknob, the J x B forces cause the discharge to lift off the insulator and travel past the doorknob region of the chamber to the enclosed end of the gun which I will call the "bucket". This is where the working fluid is be created.

The WFX can be operated in two different configurations. In the first, the conductors are electrically isolated for their entire length (no doorknob installed). However, in this setup, it was predicted that magnetic flux would enter the bucket region of the experiment. In the second configuration, the doorknob is installed with a "mixing plate" (see figure 3). The mixing plate has holes in it to allow plasma into the bucket while excluding the magnetic flux. It was speculated that the gun driving circuit would see enough inductance to keep the discharge at the breech of the gun even though the gun is electrically shorted at the doorknob.

The diagnostics at this stage of the experiment consisted of voltage monitors for bank voltage, current monitors for both bank current and plasma current. The metal endplate of the bucket was replaced with a Lexan endplate to allow for open shutter photography which was used to determine plasma fill characteristics in the bucket region of the experiment. B dot probes were installed in the WFX bucket region to determine sheath velocity, flux intensity, plasma sheath duration, and plasma sheath symmetry.
There were three probes installed in various locations along the

bucket, and they were oriented along the bucket wall. They were placed with one at the midplane of the bucket and the others 6 cm and 10 cm closer the the breech.

## Results

The WFX was operated in several different experimental configurations. The bank voltage was varied, the mixing plate was installed and removed, and different fill gases at different fill pressures were used to obtain data. The bank voltage ranged from 40 - 50 kV. These voltages were chosen to protect the capacitor bank voltage from reversing too severely. There were restrikes evident in the pulse traces, but typical pulse lengths were 5μs in duration. Fill pressures ranged from 5-100 torr to get a variation in plasma density.

The shots compared are for different gases under the same experimental conditions. With Hydrogen and Helium at 20 torr and no mixing plate installed, the Hydrogen shots seem to have a more symmetric plasma sheath especially closer to the bucket. When Hydrogen was used as the fill gas, approximately 30% of the magnetic flux enters the bucket whereas with Helium, only about 5% of the flux reaches the bucket. Both of these gases produced a second sheath (due to restrikes) which appears at the B dot probes on the third half cycle, but the second Hydrogen sheath did not reach the bucket whereas the Helium plasma did. The plasma sheath arrived at the first B dot (b1) and second B dot (b2) at the same amount of time. There was a 2 μs delay between b2 and the probe in the bucket, b3. B3 is separated from b2 by 6 cm. The sheaths for both of these feed gases reached the bucket, but the Helium plasma seemed to be more symmetric.

Next, the mixing plate was installed and the experiment was performed again with the same chamber parameters. The Hydrogen plasma was very symmetric and had only one plasma sheath. The Helium plasma produces two non-symmetric plasma sheath. No flux from either plasma entered the bucket. The B dot signals for the Helium plasma are approximately three times the magnitude of the Hydrogen plasma signals. This was unexpected since the Rogowski signals were the same for both of the plasmas. Open shutter photography suggested that the Helium plasma was uniform in the bucket, but this photo may be showing reflections of plasma light on the other side of the mixing plate through the holes in the plate.

For fill pressures of 50 torr, the Helium plasma gave much smaller B dot signals. The open shutter photography suggests that this plasma may not be driven into the bucket. It may be that the plasma is not being lifted from the glass insulator and therefore no plasma is seen in the bucket. For Hydrogen at 50 torr without the mixing plate, b1 and b2 see a very symmetric plasma front, but b3 doesn't indicates flux in the bucket although it has a very noisy signal. There is an initial plasma sheath followed by a second much smaller sheath. This may indicate a better initial conduction path for the power supply and therefore more plasma was formed for the initial current sheath. With the mixing plate installed, the B dot signals were 30% smaller, but they showed a very symmetric current sheath except in the bucket. In the bucket, b3 indicated no plasma was present and open shutter photography indicated an asymmetric plasma sheath. This may be due to the plasma not mixing after it enters the bucket.

At 75 torr, with the mixing plate installed, the plasma front was symmetric but there was no plasma or flux in the bucket. The plasma pulse in the gun prior to the mixing plate did however lengthen to 10$\mu$s with a flatter peak. Without the mixing plate installed, the WFX shorted.

At 100 torr, with the mixing plate installed, the WFX shorted.

## Conclusions

More sophisticated diagnostics are necessary if the physics of the working fluid are to be better understood. The diagnostics available gave information describing the general parameters of the plasma. There were plans to use spectroscopy and other diagnostics as we were finishing this project. Knowledge of temperature and density in addition to how and when the plasma is formed would be of great value.

This project went extremely well from start to finish. We had little or no problems with any aspect of the project. This was due mainly to the team assembled to assist our work on this project. The work conducted established an excellent foundation for future work on this experiment.

References


1.) Cheng D. Y., "Plasma Deflagration and the Properties of a Coaxial Plasma Gun," Nuclear Fusion, 10, 305, (1970)

2.) Len, L. K., "The Snowplow and Deflagration Modes of Operation in a Coaxial Plasma Gun, Ph.D Thesis, University of New Mexico (1984)

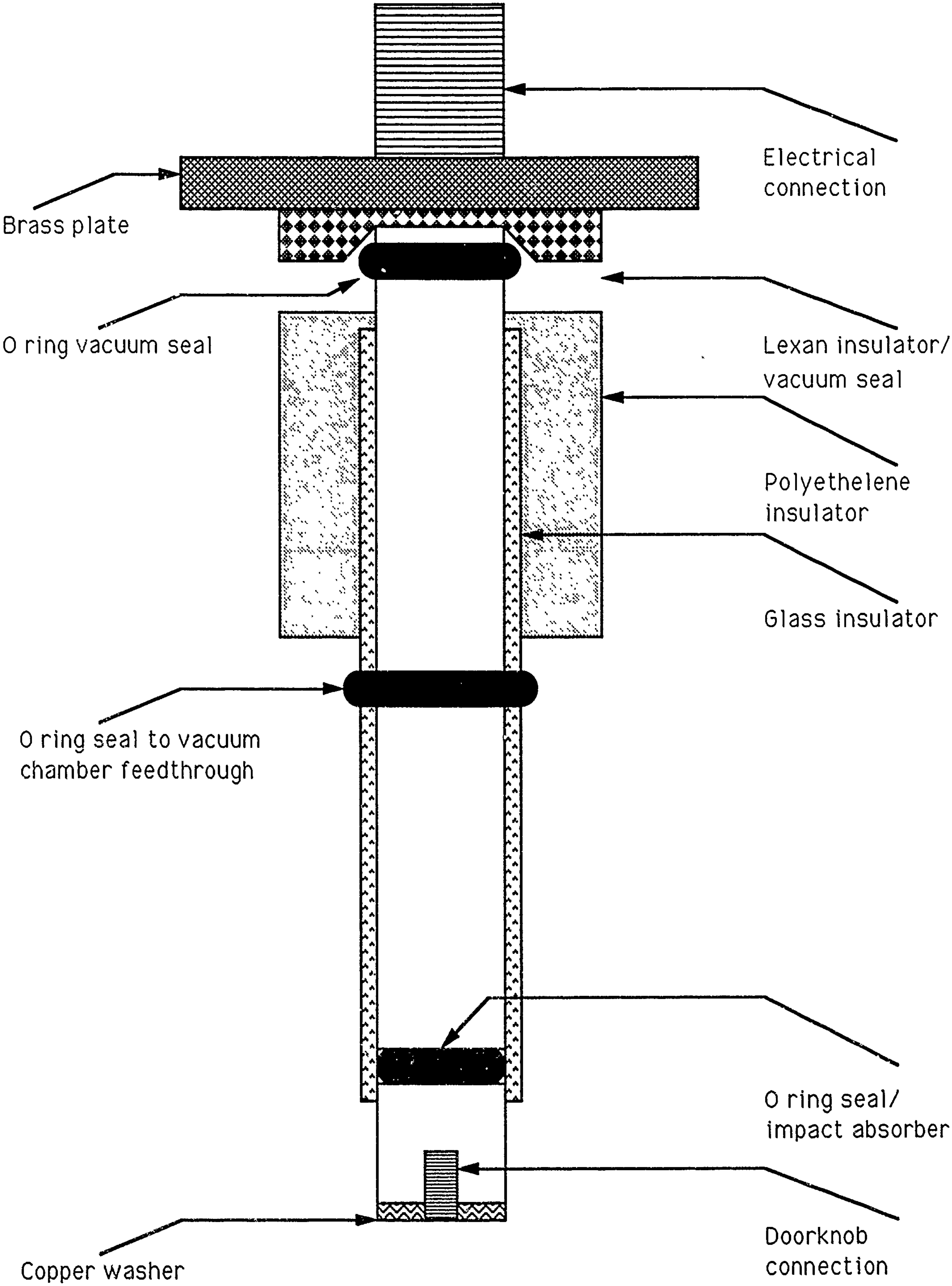

Electrical connection
Brass plate
O ring vacuum seal
Lexan insulator/ vacuum seal
Polyethelene insulator
Glass insulator
O ring seal to vacuum chamber feedthrough
O ring seal/ impact absorber
Doorknob connection
Copper washer


Figure 1

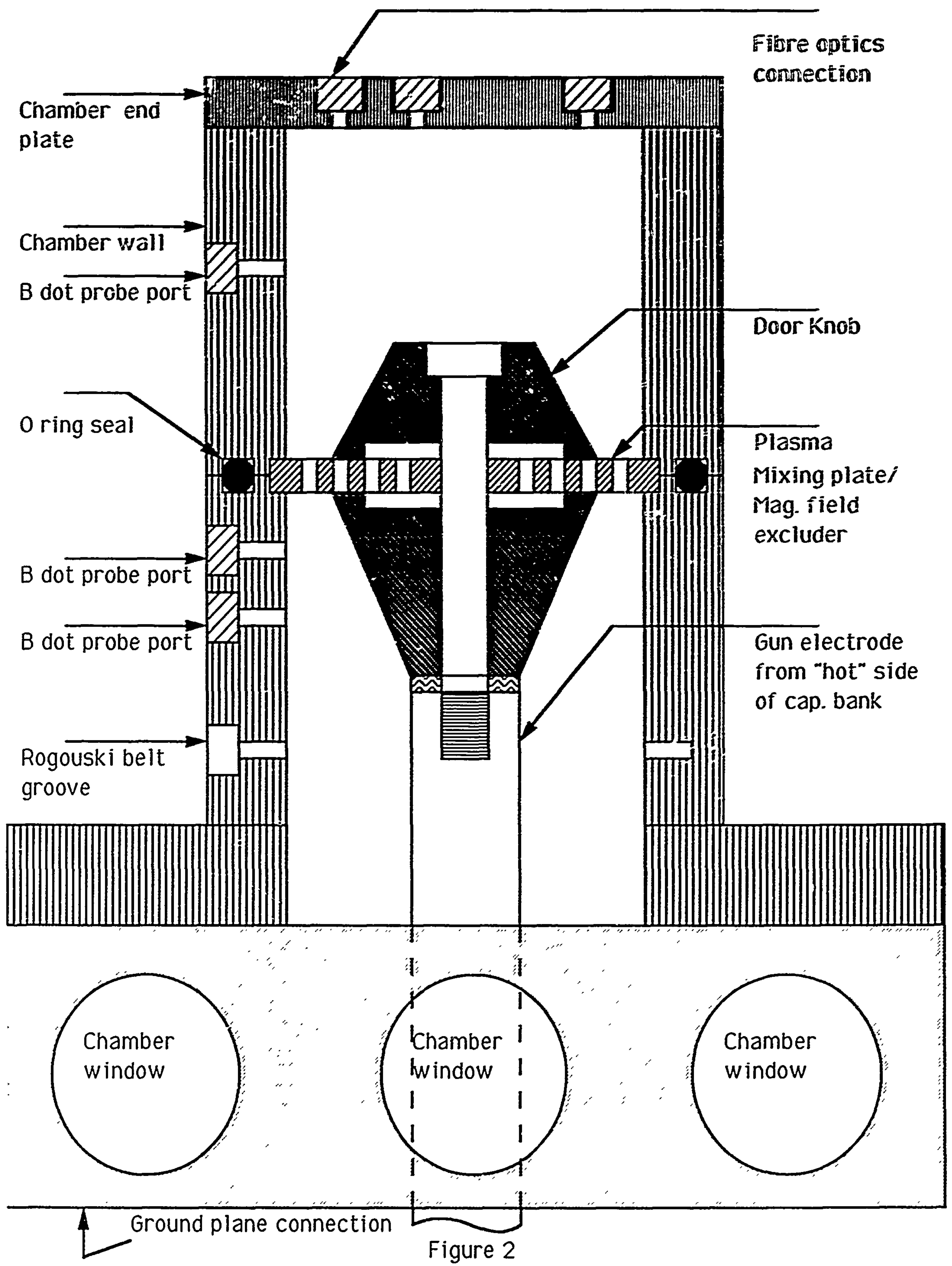
Fibre optics connection
Chamber end plate
Chamber wall
B dot probe port
Door Knob
O ring seal
Plasma Mixing plate/ Mag. field excluder
B dot probe port
B dot probe port
Gun electrode from "hot" side of cap. bank
Rogouski belt groove
Chamber window
Chamber window
Chamber window
Ground plane connection

Figure 2

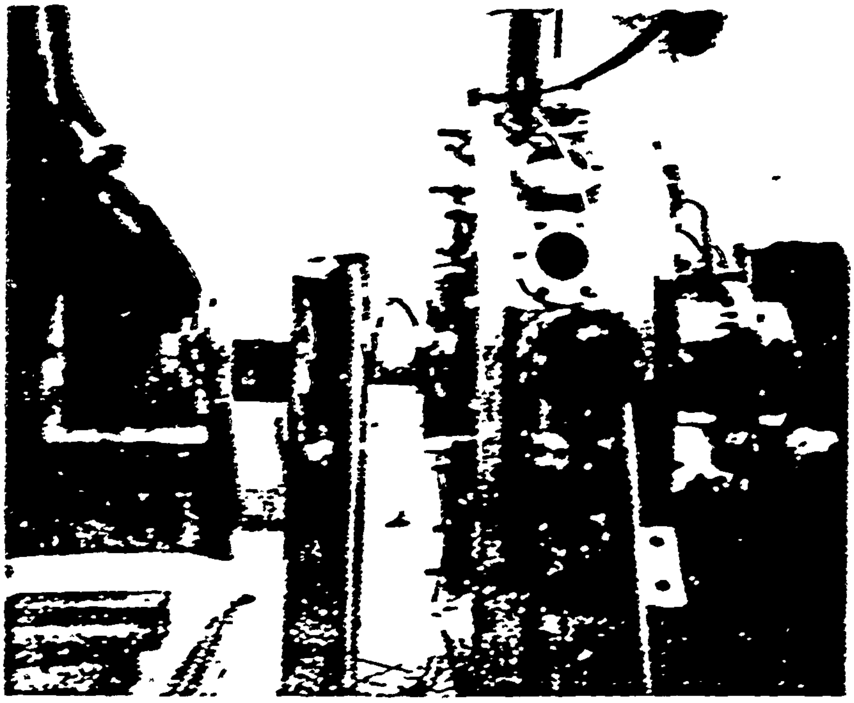

Photograph of WFX

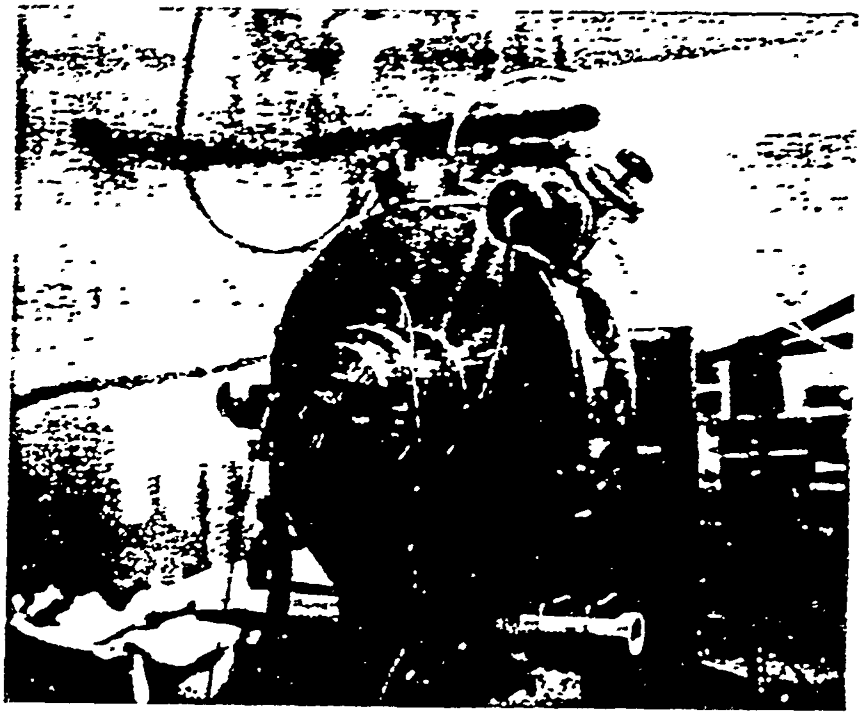

Photograph of WFX

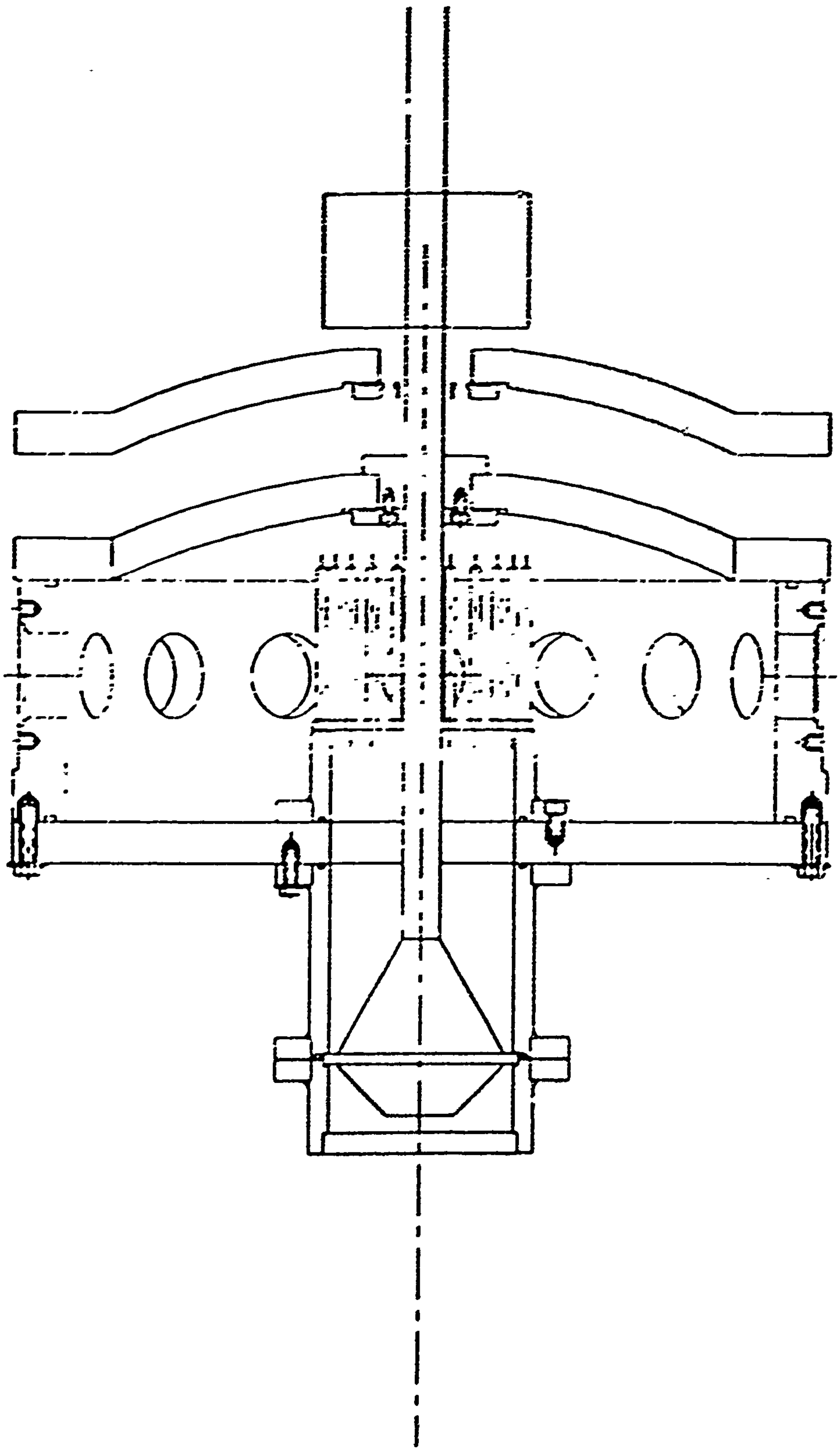

Schematic of WFX

AN EXPERIMENT TO DETERMINE ANGULAR DISTRIBUTION OF BACKSCATTERED ELECTRONS AS A FUNCTION OF ENERGY & MATERIAL: A STATUS REPORT

ROBERT DAVIES

## 1. Introduction

Accumulation of electrical charge on orbiting spacecraft surfaces is a phenomenon receiving an increasing amount of attention. Such charge build-up is known to have produced operational anomalies of varying severity, ranging from insignificant to complete vehicle failure. Understanding the underlying mechanisms of this phenomena is logically the first step toward minimizing its effects.

Recent studies have revealed a strong link between the most significant charging events and precipitating high energy electrons originating in the earth's magnetotail. Additionally, a strong correlation exists between the energy of the incident electrons and the severity of the surface charging. Other variables, such as angle of incidence of the precipitating electrons and surface composition are less understood. This report summarizes progress of an on-going experiment probing the importance of these variables. Following a brief discussion of the project's goals and planned method, descriptions of experimental apparatus design, construction and testing are given.

## 2. Project Goals and Method

Surfaces impacted by high energy electrons are subject to a variety of effects, as illustrated in Figure 1. Three of these effects in particular - the absorption of electrons, the

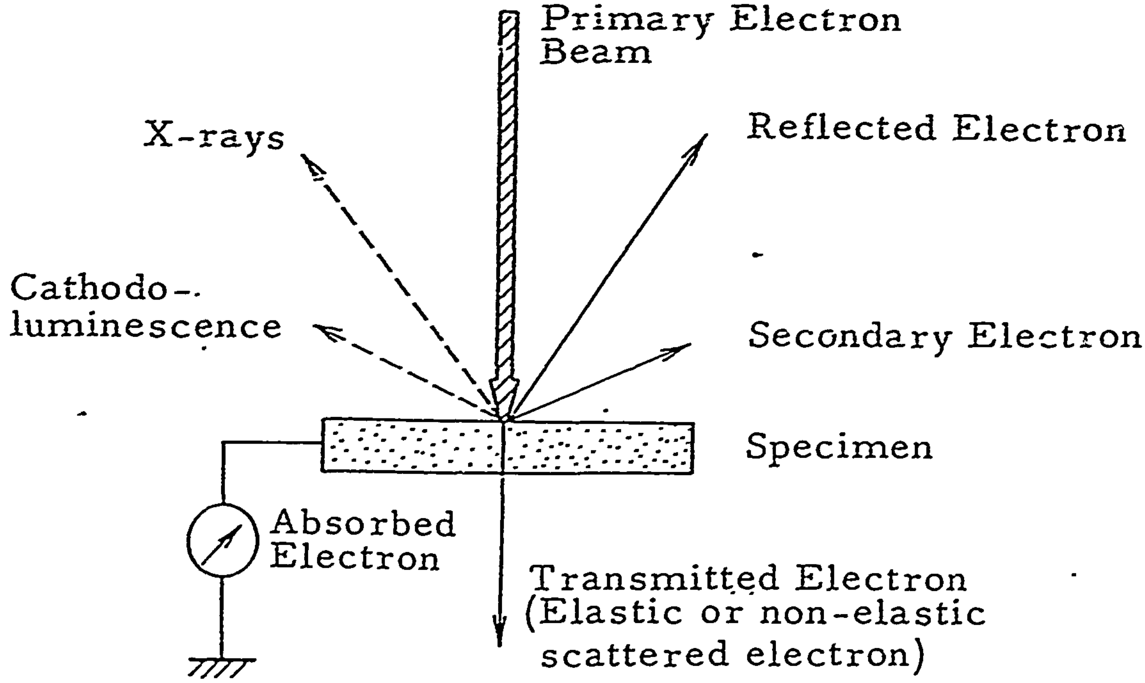


Fig. 1 Various Effects of Bombarding a Specimen with an Electron Beam

production of reflected or *backscattered electrons* (BSEs), and the production of *secondary electrons* (SEs) - are particularly relevant to the issue of spacecraft charging.

The absorption of electrons, quite logically, constitutes negative charging. Backscattered electrons are incident electrons which have merely bounced off the surface and, therefore, constitute no charging. Secondary electrons originate on the surface of the spacecraft itself, but are ejected as a result of the incident high energy electrons. SEs, therefore, constitute positive charging.

Precise determination, then, of BSE and SE coefficients is of prime importance to accurate prediction of current balance. The former, determination of BSE coefficients and energies as a function of incident beam energy, reflected angle, and material, is the primary goal of this project, to be accomplished by illuminating various materials with a beam of high energy electrons while orienting a detector at various angles around the sample to collect and measure BSEs.

A Hitachi S-500 30 KeV Scanning electron Microscope (SEM), depicted in Figure 2, was modified to accommodate the BSE detection apparatus and served as a high energy electron source. Design and construction of the detecting apparatus comprised the bulk of my effort at Phillips Laboratory and will be discussed next.

## 3. Choosing a Detecting Device

Choice of an electron detector appropriate for this project centered primarily around size and an ability to operate in the SEM environment. Three devices were initially considered - they were the channeltron, a solid state detector (a digital photodiode array), and the Faraday cup. All of these are proven electron detectors, registering collected electrons as current displayed on an attached electrometer. Additionally, each can easily be constructed to fit inside the SEM chamber.

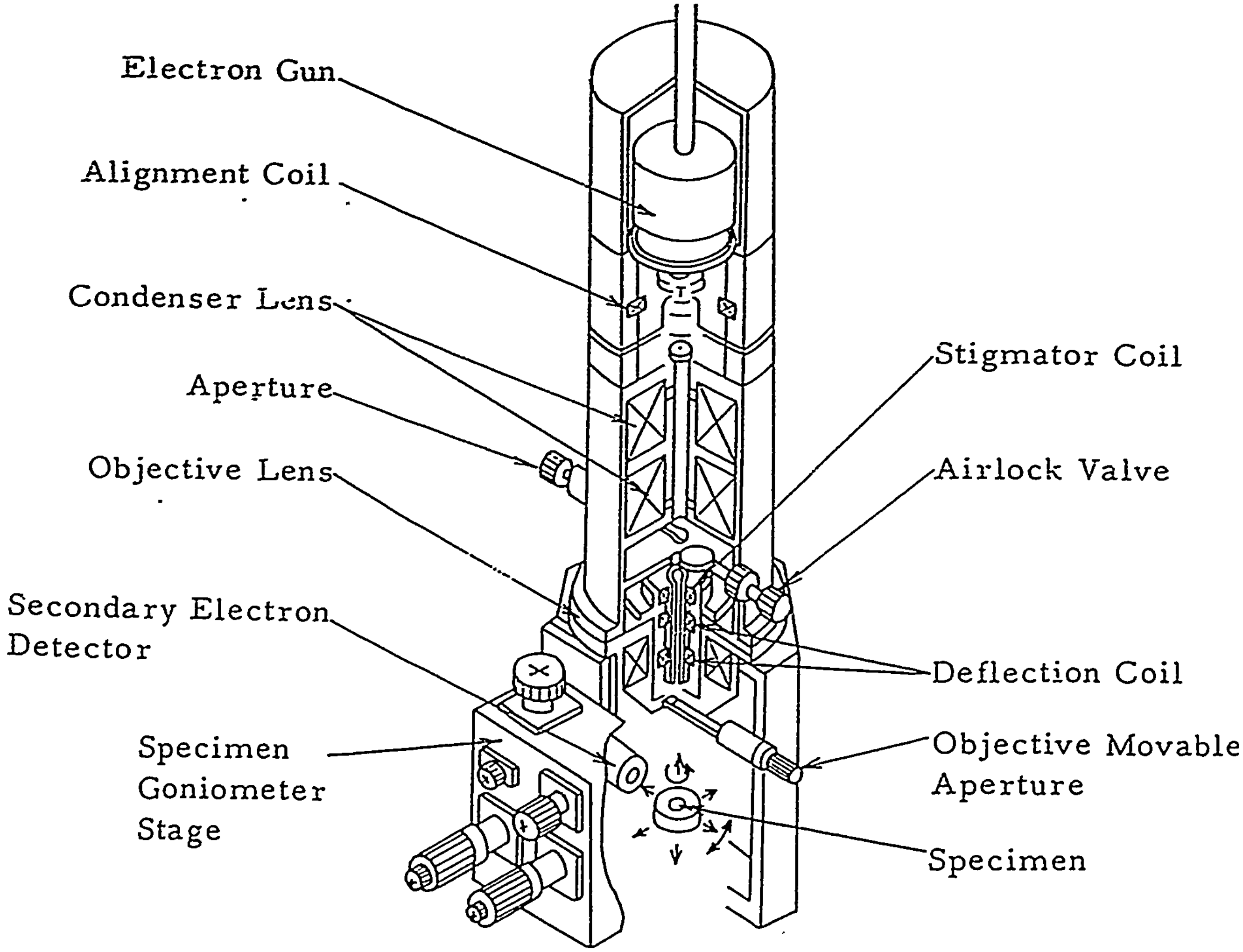


Fig. 2 Hitachi S-500 SEM Column

The channeltron and solid state device were both rejected on the basis of their inability to distinguish x-rays from electrons. This problem is potentially solvable in the case of the solid state detector, though time and expense proved prohibitive. No such flaw exists for the Faraday cup. It registers only electrons and ions, the latter being relatively rare in the SEM chamber. Furthermore, the Faraday cup is by far the simplest of the three devices to design and construct.

By itself, this detector cannot determine the range of energies of the electrons collected, a prime objective of this experiment. Consequently, the concept of an electrostatic filter was added to the basic Faraday cup idea. This is discussed further in the next section.

## 4. Detection Apparatus Design

Having settled on a method of detection, design of the detection apparatus proved to be four separate design problems: 1) detector (Faraday cup) design, 2) electrostatic filter design, 3) integration of detector and filter, and 4) design of a mounting apparatus. Primary consideration in all cases was the size restriction imposed by the SEM chamber, measuring roughly 4" x 4" x 5 1/2".

### *Faraday Cup*

Design of the Faraday cup centers on field-of-view (FOV) and overall dimensions. The FOV needs to be large enough to collect a measurable number of electrons, and small enough such that maintaining a minimum length/aperture (aspect) ratio of 10:1 is still possible given overall size limitations. This aspect ratio is required in order to prevent significant loss of collected electrons and any SEs they might produce. With is in mind, a 3/32" aperture and 1" overall length was determined. The device was constructed with aluminum and the interior given a graphite coating to reduce interior SE production.

Performing an order of magnitude calculation with the following assumptions:

r = distance to target = 2"

$\eta$ = backscattering coefficient = .3

$I_B$ = beam current = 200$\mu$A,

field of view is found to be

$$FOV(\Omega) = \frac{A}{r^2}[SR] = \frac{\pi(\frac{1}{32})^2}{4} = 7.67 \times 10^{-4}\ Sr,$$

and

$$I_{FC} = \eta\ I_B \frac{\Omega}{2\pi} = .3(200 \times 10^{-6}A)\ (\frac{7.67 \times 10^{-4}\ Sr}{2\pi\ Sr}) = 7 \times 10^{-9}\ A,$$

where $I_{FC}$ is the current collected by the Faraday cup. This calculation, while assuming (almost certainly incorrectly) $\eta$ to be independent of direction, and an optimistic value of .3, nevertheless indicates an unfiltered measurement ~nA, a current certainly measurable with acceptable accuracy.

*Electrostatic filter*

Determination of an accurate BSE energy profile will be accomplished through the use of an electrostatic filter - essentially a small washer placed in front of the Faraday cup and given a negative bias. Ideally, electrons with an energy greater than this bias should penetrate the aperture and be collected, while those with less energy are deflected away. This, of course, applies only to electrons approaching along the aperture center line. Electrons approaching off axis and at various angles, edge effects on the electric field surrounding the filter, and the geometry of the filter itself will all affect which electrons penetrate and which do not. With this in mind, parametric studies using a computer simulation were performed to aid in designing an effective electrostatic filter.

Figures 3a and 3b illustrate the importance of filter length. Depicted is the top half of a filter cross-section. The lines surrounding the filter are equipotentials, while the lines approaching from the left are electrons attempting to penetrate the filter. As electrons approach from further off axis, more energy is required to penetrate. These figures illustrate that this excess energy is reduced simply by shortening the filter. Figures 3c through 3e introduce increased angles of incidence (representing electrons originating from a point source at a closer distance) and depict further resolution improvement through increased aperture size, a grooved interior, and an increased filter housing aperture to filter aperture distance. Of the myriad of parameters tested, these were found to be the most critical. Finally, Figure 3f indicates further refinement by increasing target distance, represented by a slight decrease in the angle of incidence of the approaching electrons. These computer simulations resulted in a final filter design of 9/64" aperture diameter, grooved to 15/64", and an overall length of 7/32". The device was constructed with aluminum.

Concurrent to serving as a design aid, accurate computer modeling of the filter is crucial to this experiment from a data standpoint. Without such modeling, we cannot be certain to a fair degree of accuracy which electrons are being counted and which are not. Nor can energy resolution, and therefore experimental error, be calculated. Present configuration predicts a 2.3% error in energy resolution.

*Detector/Filter Integration*

Combining both the Faraday cup and electrostatic filter was accomplished by first mounting each in a stainless steel housing of its own, then mounting the two housings together.

Housing the filter was necessary to contain the strong electric field produced by its large negative potential. The concern here is to prevent any stray field from affecting the path of either the primary or backscattered electron beams. The filter was then fitted into a

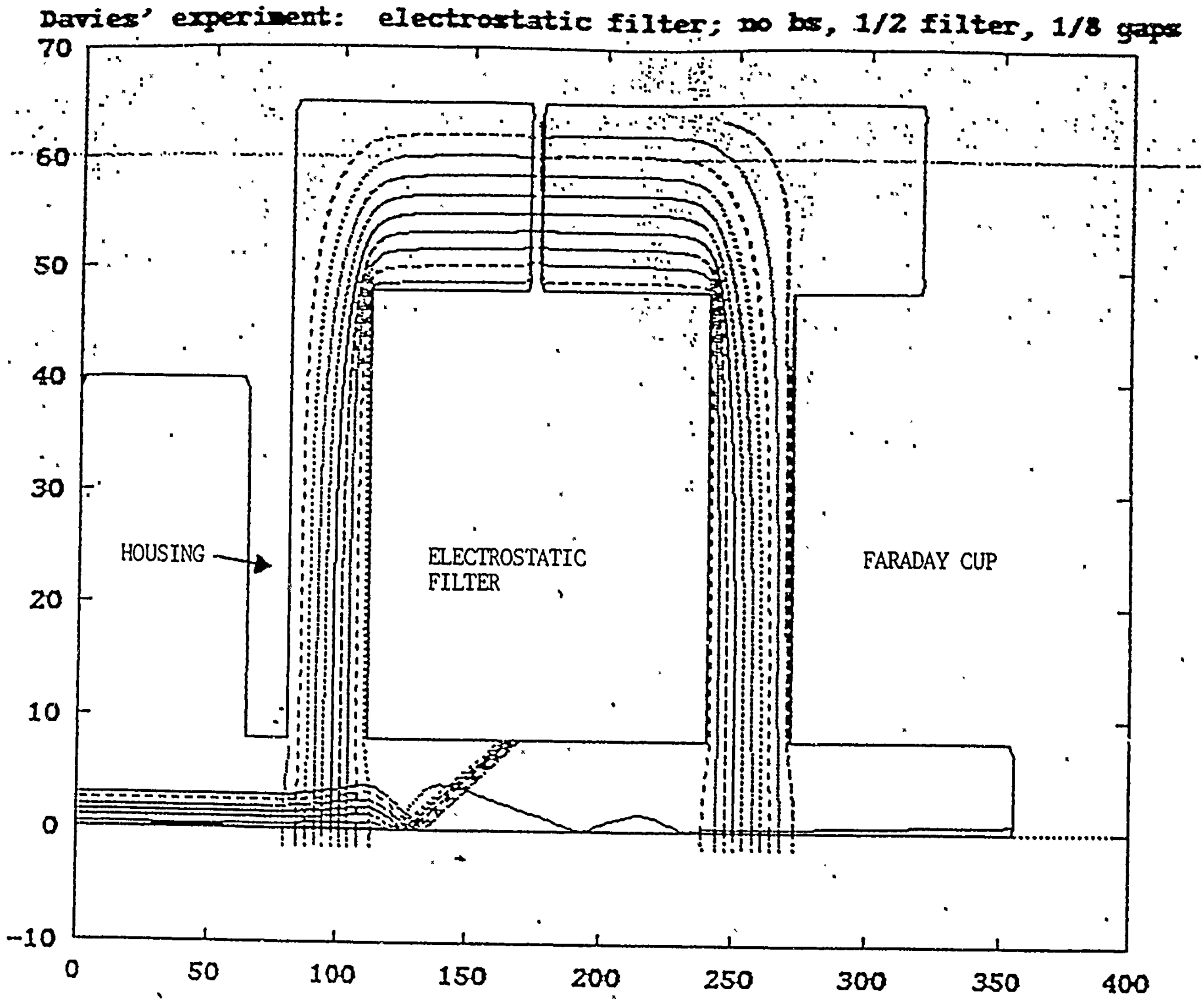


Fig. 3a Computer Simulation of Electrostatic Filter - Basic Design

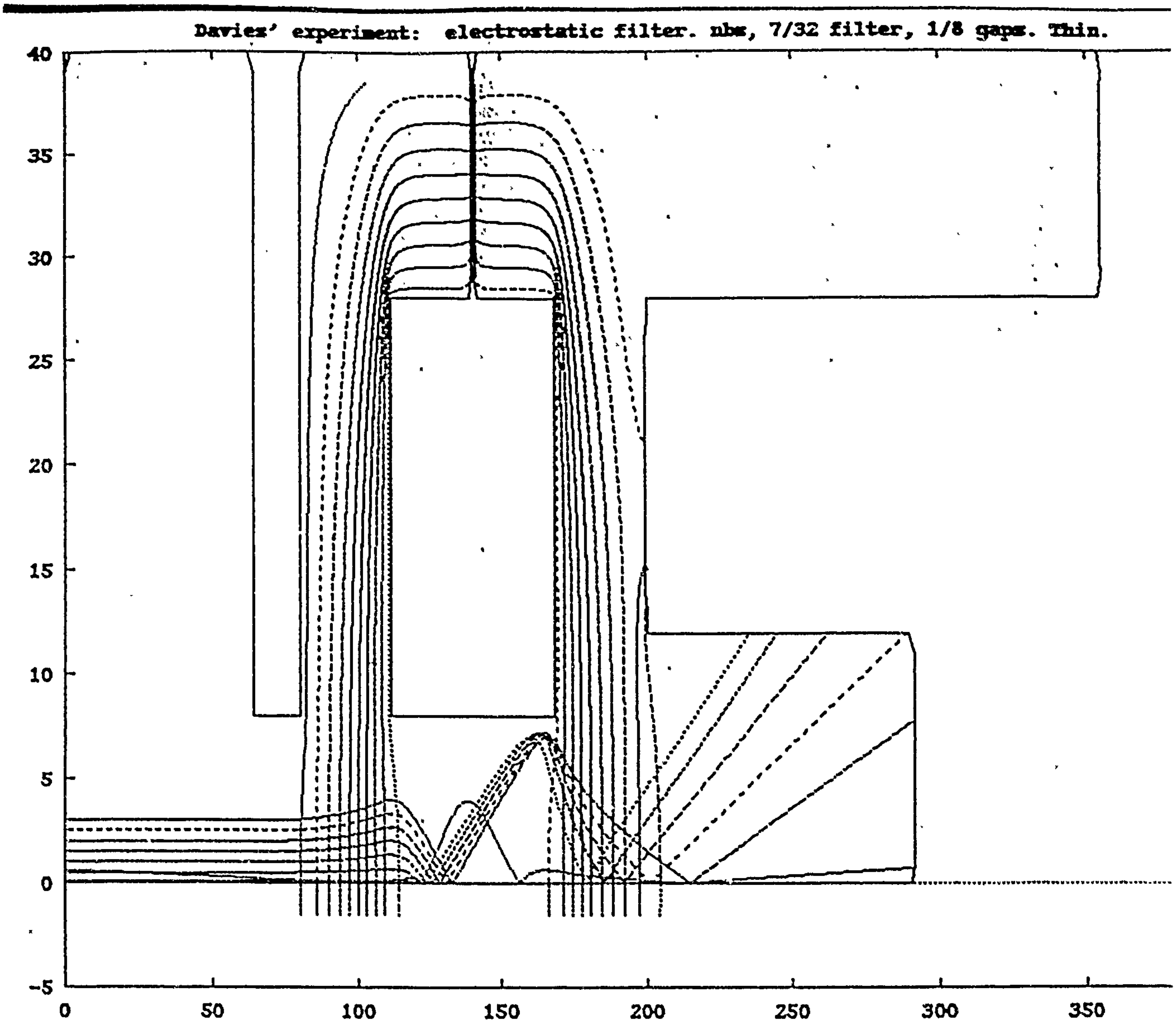


Fig. 3b Shortening the Filter

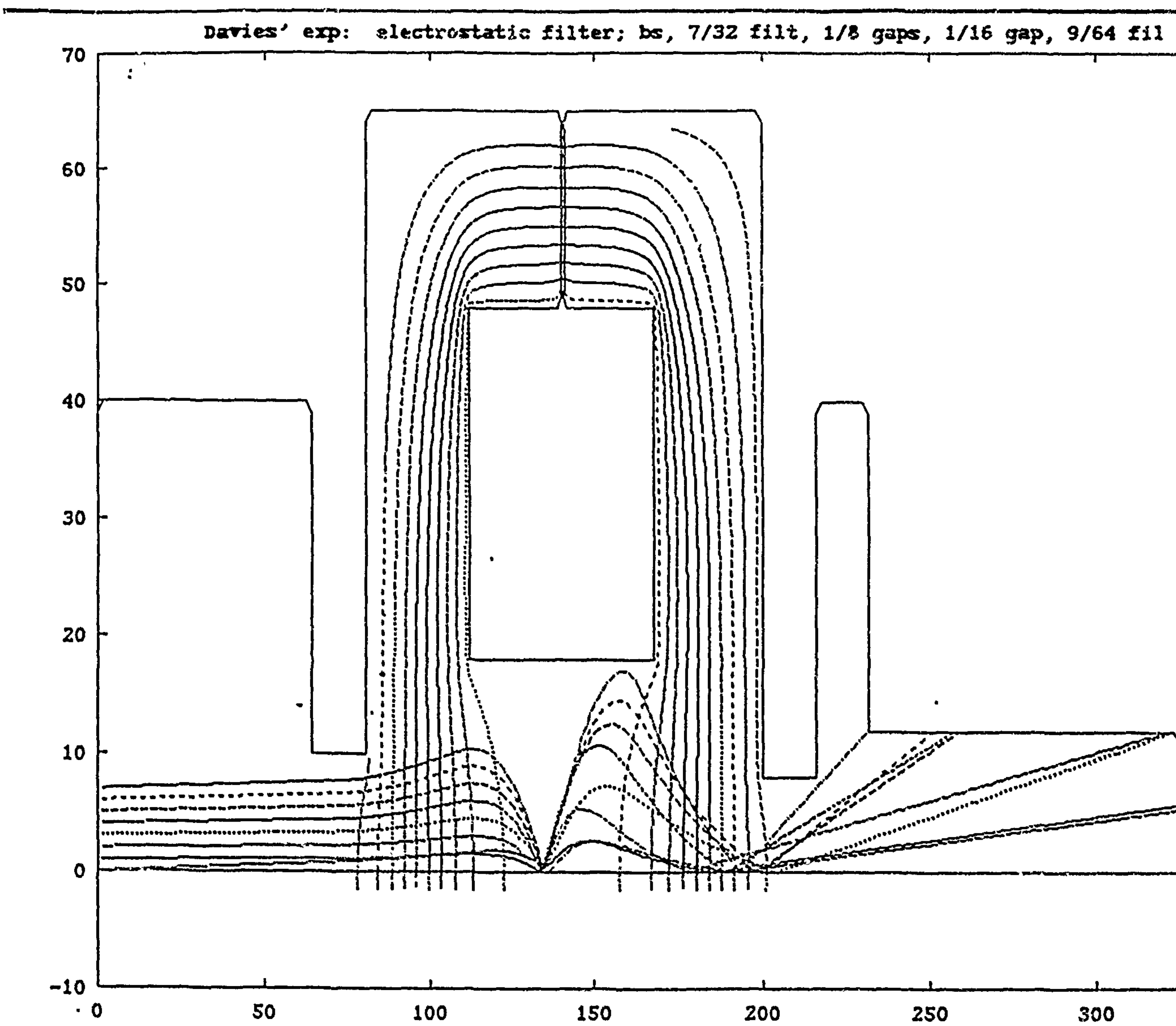


Fig. 3c Increasing Aperture Size

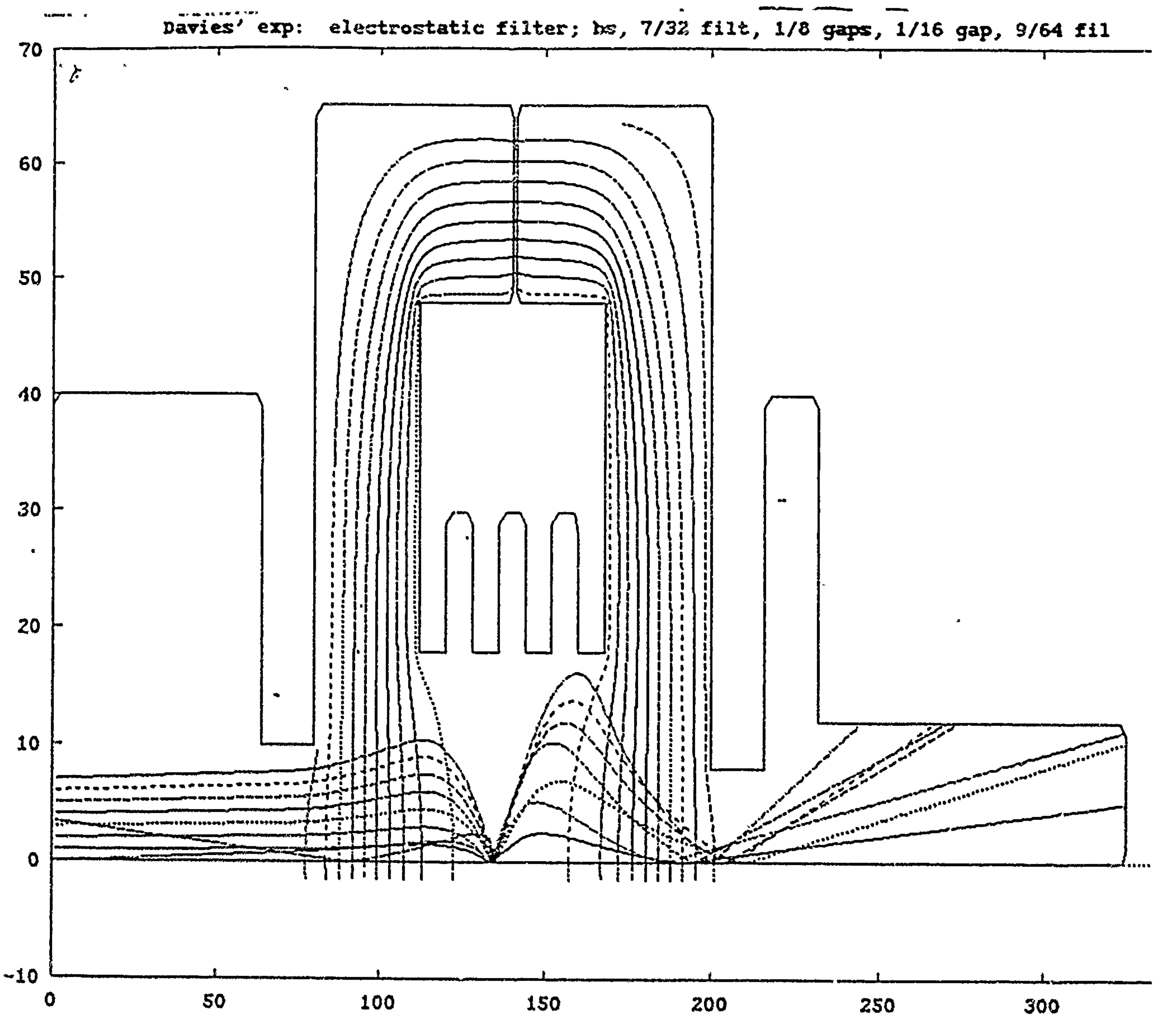


Fig. 3d Grooving Filter Interior

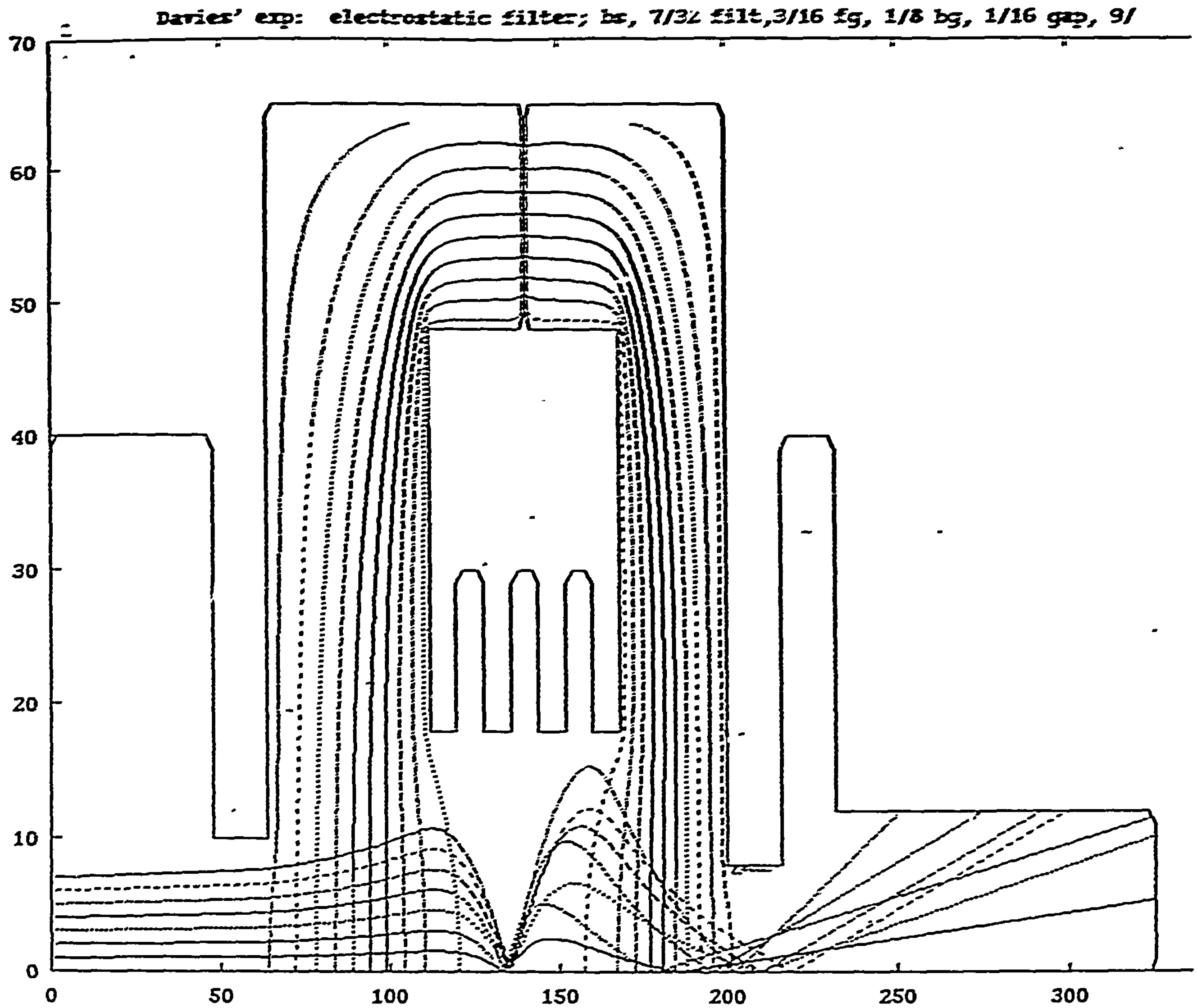


Fig. 3e Widening Front Housing-to-Filter Gap

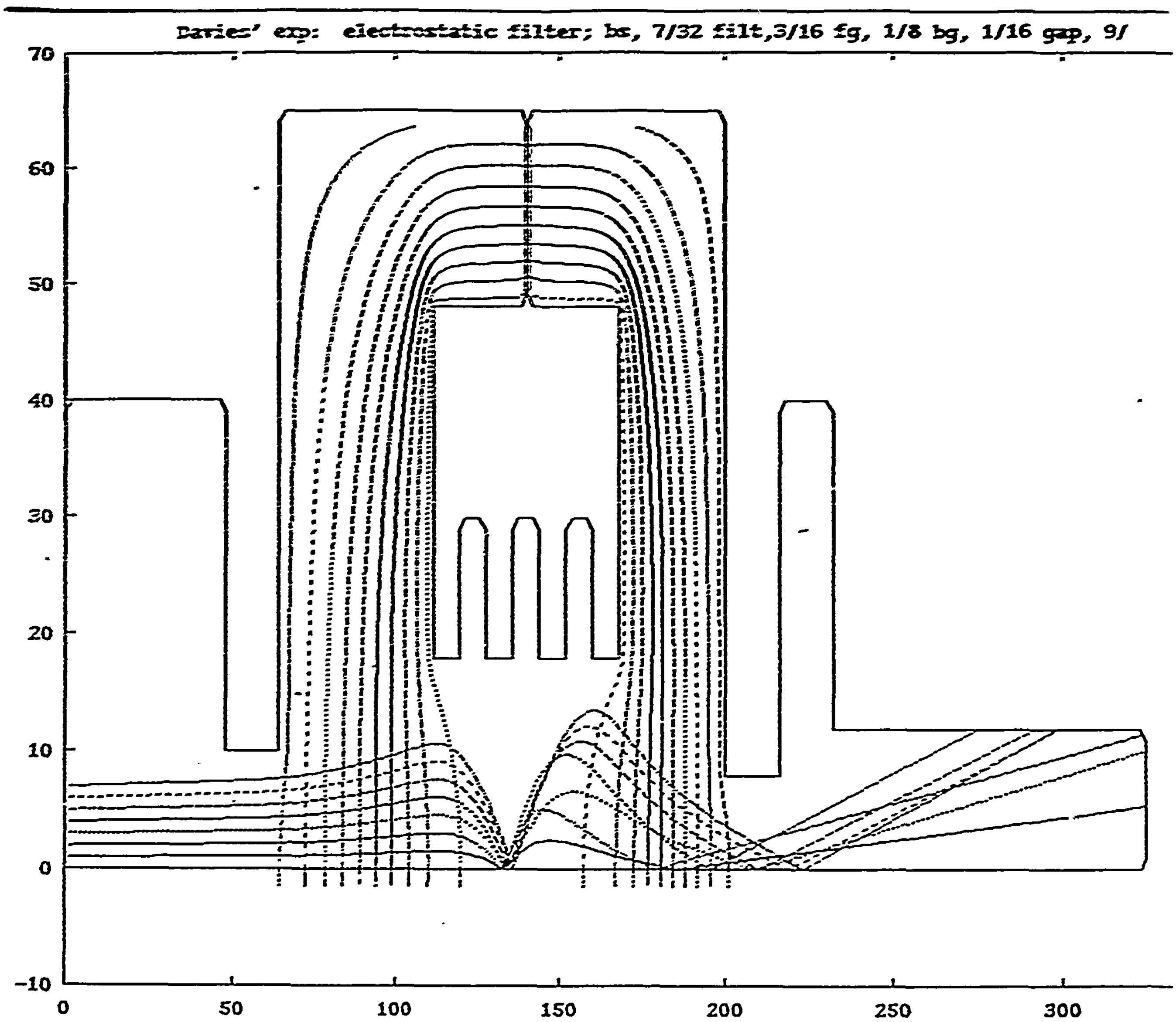


Fig. 3f Increasing Target Distance

teflon sleeve to isolate it from the housing, the sleeve then being fitted into the housing as illustrated in Figure 4. The design prevents the teflon insulation from "seeing" the incoming electron beam directly, preventing any unwanted charging of the insulator. Set screws hold the filter a precise 3/16" from the housing aperture.

Also addressed was the issue of an electrical breakdown occurring between the filter and the housing. Studies previously performed at a pressure of $1 \times 10^{-5}$ torr (comparable to that attained in the SEM) with a stainless steel anode and aluminum cathode separated by a 1mm gap, gave a first spark at 36 KV and a final breakdown of 44 KV. Minimum separation between the filter and housing is 4.7 mm, indicating that arcing should not pose a problem.

The Faraday cup housing was designed to isolate the device from all unwanted electrical influences; specifically, any charge bleed-off from the filter. As depicted in Figure 5, the detector is first mounted in a teflon sleeve, this assembly then being mounted in an aluminum isolating sleeve to be separately grounded. A second teflon sleeve is added, and the entire assembly is then fitted into the detector housing. Set screws hold the device a precise 1/16" from the housing aperture. Additionally, this aperture is coated with graphite to minimize SE production here. Finally, the front of the detector housing is inserted into the rear of the filter housing and secured with set screws. The detector housing aperture remains a fixed 1/8" from the rear of the filter. All apertures line up precisely. The entire assembly measures approximately 1 7/8" in length and 1 1/8" in diameter.

*Mounting Assembly*

The detector/filter assembly is mounted to a pivot arm and stage as depicted in Figure 6. The stage is designed to fit snugly into the SEM chamber, with the beam striking the center of the stage. The pivot arm is positioned such that the detector always views the stage center regardless of the viewing angle. Additionally, the detector assembly may be

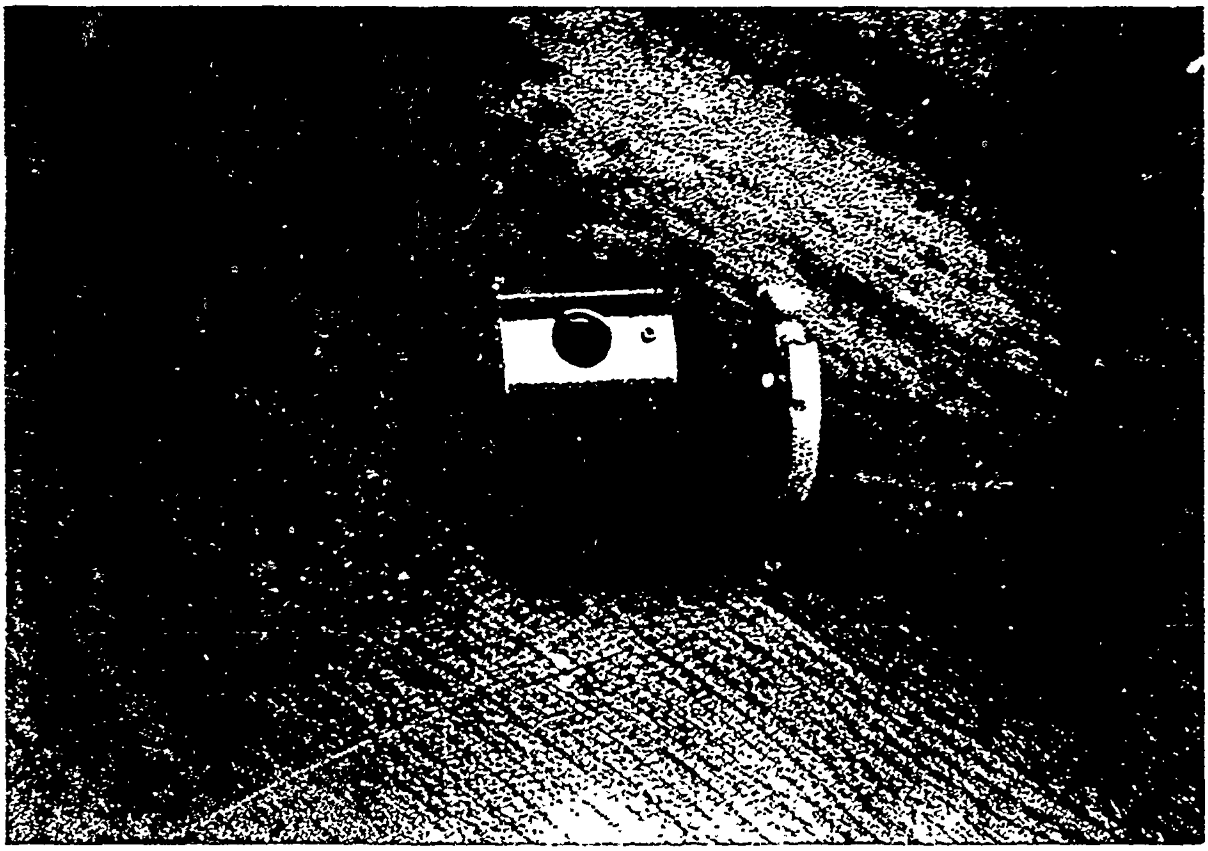

Fig. 4 Electrostatic Filter Assembly

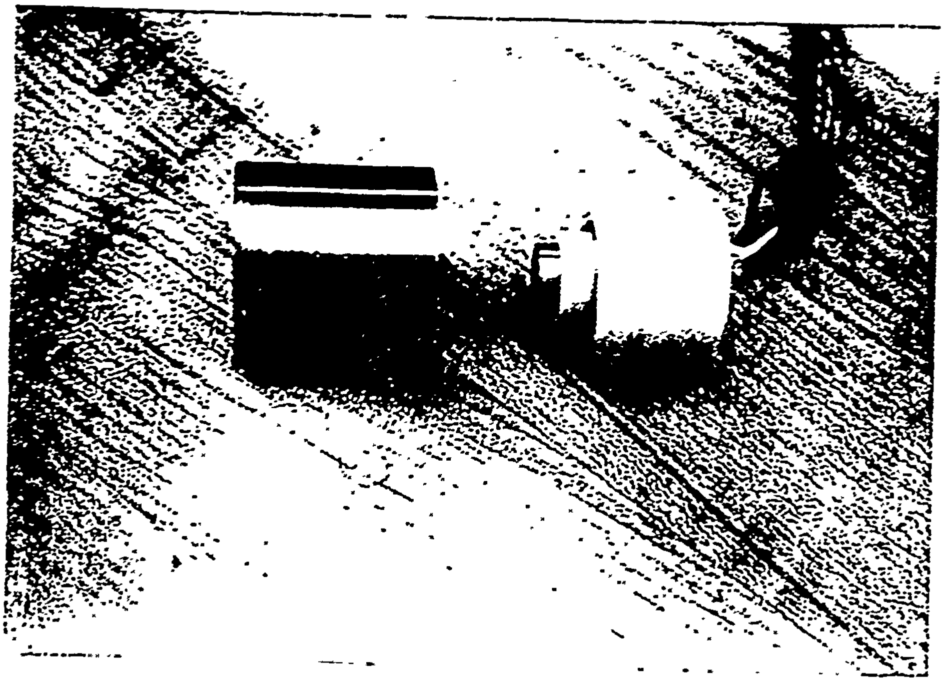

Fig. 5a Detector Assembly

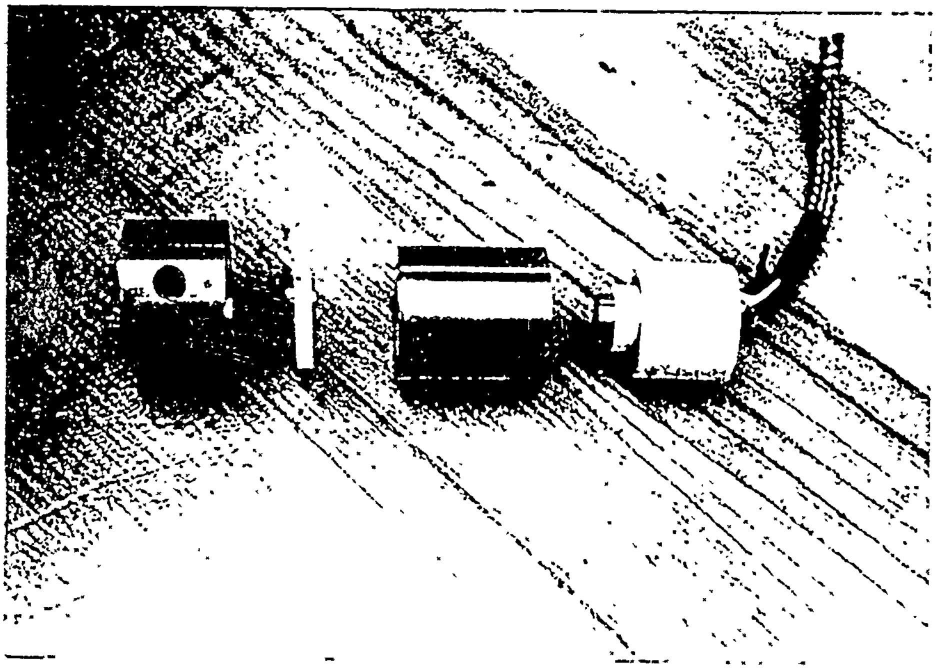

Fig. 5b Integrated Filter and Detector Assembly

Fig. 6 Detector/Filter Mounting Assembly

shifted on the arm, allowing target distance to vary from 2 1/2" to 3 1/4". Owing to the interior chamber geometry, this arrangement gives an angular detection range of 0 - 78°.

## 5. Wiring and Connections

Wiring requirements for this project consist of a high voltage (HV) cable from the power source to the filter, measurement of both sample current and detector current, and grounding.

*High Voltage*

Power is supplied by a Spellman 20 KV power supply. Coaxial cable transfers the power to a high voltage feedthrough mounted on the side of the SEM. Inside the chamber, power is transferred from the feedthrough to the filter with high voltage wire wrapped in braided shielding. Connection to the filter is achieved via pressure contact with a spring mounted at the end of the wire.

*Electrometer Measurements*

Since a constant beam current is critical to the experiment, sample current is monitored along with detector current. Both connections are with pins. Insulated wires wrapped in braided shielding separately connect the sample and the Faraday cup to a multi-pin vacuum feedthrough. Wires on the outside then connect the pins to a set of Kiethely picoammeters.

*Grounding*

The HV coaxial cable is grounded to the SEM column, as are both electrometers. Within the chamber, the shielding covering the HV wire and sample and detector wires is grounded to the stage, which is, in turn, grounded to the column. Both the detector and filter housing are grounded to the SEM as well through direct contact with the stage. Finally, a wire/pin connection to the isolation plate surrounding the Faraday cup is used to ground this plate to the SEM as well.

## 6. Initial Test Results

Design and construction of the apparatus described in Section 3 required nine weeks of this ten week program. While meaningful data collection was not possible in my one remaining week, I was able to accomplish valuable testing of the design and method. As a safety precaution, the imager and x-ray analyzer were removed from the SEM column for all tests involving the use of high voltage.

Tests to 20 KV were successfully conducted on the HV feedthrough both with and without the filter connected. Initial arcing problems from the spring/wire connection to the detector housing were solved by eliminating the use of solder. As expected, no arcing was detected between the filter and filter housing. Chamber pressure was maintained at roughly $1 \times 10^{-5}$ torr.

Problems were encountered, however, in attaining the expected 200μA sample current. Repeated tests confirmed a value of only 1-2μA. Additionally, my detector current registered roughly 60 pA, irregardless of an open or closed aperture, indicating the wires were picking this up as a noise level. Removal of the lower columnater aperture in the SEM increased sample current to 27.7μA, however the beam was diffuse and highly uncontrollable. Under these conditions, the noise in the detector wires remained at approximately 60pA.

## 7. Recommendations and Conclusion

Shielding the wiring delivering signal from the multi-pin vacuum feedthrough to the electrometers should eliminate noise contamination. All indications are that this noise is associated with fields created by the SEM electronics outside the chamber. The problem remains, however, that sample current is two orders of magnitude below that expected. It now appears a femto ammeter will be required to make the measurements.

Time restrictions did not allow me to complete this experiment while at Phillips Laboratory, though the project certainly merits completion. Once perfected, this technique will provide a tremendous amount of data regarding BSE coefficients of various materials. Additionally, a minor modification to the experiment should allow accurate determination of SE coefficients as well. Accurate energy and directional profiles of these coefficients, as well as dependence on material are not currently available. If completed, data from this project will almost certainly prove a useful tool in understanding and minimizing spacecraft charging.

## Acknowledgements

I would like to acknowledge the tremendous amount of technical assistance provided by members of Phillips Laboratory, specifically Dr. Charles Stein, Dr. Warren Wilson, Mr. Charles Miglionico, Mr. Robert Roybal, and SSgt. Robert Robertson. The success of this program as an educational experience is largely due to their patience, time, and effort.

**MITIGATION TECHNIQUES TO MINIMIZE**

**DAMAGE RESULTING FROM EXPLOSIVE LOADING**

**ON STRUCTURES FOUNDED ON PILES**

**IN SATURATED SOILS**

Prepared by
Nathan A. Dowden
for
Phillips Laboratory, USAF
Kirtland AFB, NM

August 1991

**Abstract**

The Phillips Laboratory of the United States Air Force is currently examining the survivability of critical structures founded on piles in saturated soils subjected to explosive loading. The "typical" threat to structures has been established as a 500 Kg general purpose bomb of conventional munitions. T' [illegible]us of this paper is to identify and investigate available methods of mitigating damage to the pile foundation in the event of an attack. Various methods, such as structural isolation, ground modification, and energy absorption/dissipation are reviewed within.

**Mitigation Techniques to Minimize Damage Resulting From Explosive Loading on Structures Founded on Piles in Saturated Soils**

## I. Introduction

The United States Air Force is currently investigating the potential vulnerability of deep foundations to blast-induced failure. It has been demonstrated that traditional design practices for structures founded on piles may not be adequate to assure survivability of the structure in the event of a sub-surface detonation of conventional munitions. Catastrophic failure of a foundation system due to explosive loading of the soil was observed during the Hayman Igloo test of November 1988 (Ref. 1). Extreme liquefied conditions in the soil were observed resulting in approximately 20 feet of subsidence of a nearby structure. The ASCE Committee on Soil Dynamics of the Geotechnical Engineering Division defines liquefaction as "...the transformation of a soil from a solid state to a liquefied state as a consequence of increased pore pressure and reduced effective stress." (Ref. 8) In addition to the possibility of failure due to liquefaction, failure of piles due to crushing, buckling, or shearing are of major concern.

A large number of vital Air Force structures in the Pacific Theater are constructed on hollow core, spun-cast, concrete piles. At the present time, the Air Force is preparing a full-scale test, to be conducted in 1992 to examine the blast effects of a sub-surface detonation on vertically loaded piles. The test scenario will be representative of the site configurations currently in use throughout the U. S. installations in Korea and Japan. The testing will quantify the types and amount of damage that an unprotected pile-supported foundation will experience.

A parallel aspect of the investigative process is the identification and evaluation of the "state-of-the-art" in mitigation techniques. The purpose of this paper is to present options currently available to protect the pile supported foundations currently in existence and to offer alternatives to design concepts for future structures. At this point in time, there is a scarcity of research into protective measures for large magnitude lateral loads on pile foundations. Some techniques from seismic engineering may offer viable solutions to the problem, however the lateral loads commonly associated with earthquakes are usually 2 to 3 orders of magnitude lower than those experienced in blast loading. Current plans anticipate scaled testing to validate proposed designs once possible alternatives have been characterized.

## II. Background

### Site Characterization

The utilization of piles as a foundation support is dictated by a soil with inadequate bearing capacity for the proposed structure, where the bearing capacity is a function of soil type and its associated properties, presence of water, and the degree of saturation. Furthermore, the possibility of liquefaction occurring is greatest in a fully saturated soil. A survey was conducted in April 1990 of bases in the Pacific Air Force (PACAF) and United States Air Forces of Europe (USAFE) to determine the number and location of structures founded on piles in saturated soils. In the Pacific area the Air Force identified 281 facilities in Korea (Osan and Kunsan AB) and Japan (Misawa and Kadena AB) that were constructed on pile foundations. Only one such structure in the USAFE, at Lakenheath AB in England, was found to be constructed on piles (Ref. 2).

The focus of the Air Force research has, therefore, been largely on the conditions existing at the PACAF bases in

Korea and Japan. Table 1 summarizes the typical soil profiles while Table 2 shows the sub-surface rock and water conditions at the 4 PACAF bases (Ref. 2). The soil conditions combined with high water tables create an environment in which the threat of liquefaction is high.

Table 1. Summary of Soil Profiles at PACAF Bases

| Base | Type of Soil | Depth of Layer (ft) |
|---|---|---|
| Osan | Clayey Sand | 0 to 14 |
| | Clay/Sandy Clay | 4 to 12 |
| | Silty Sand/Silt | 12 to 30 |
| Kunsan | Clayey Sand | 0 to 20 |
| | Sandy Clay | 20 to 50 |
| Misawa | Clay | 0 to 7 |
| | Sandy Clay | 7 to 20 |
| | Sand | 20 to 44 |
| Kadena | Clay | 0 to 40 |

Table 2. Summary of Subsurface Rock and Water Table Conditions at PACAF Bases

| Base | Type of Bedrock | Depth to Bedrock (ft) | Depth to Water Table (ft) |
|---|---|---|---|
| Osan | Gneiss | 30 ft | 5-16 ft |
| Kunsan | Shale/Breccia | 50 | 2-4 |
| Kadena | Limestone | 40 | 90 |
| Misawa | Sandstone | 44 | 30 |

Threat

In order to develop protective measures, the threat to the structure must first be established. Corson, et al state that,

> "As a result of extensive research at the Weapons Laboratory through July 1990, the "typical" conventional weapon threat to Korean aircraft shelter pile foundations was determined to be a 500 Kg general purpose (GP) bomb with an explosive weight of approximately 210 Kg." (Ref 2,3)

The current practice in conventional munitions deliverance is to implement delayed fuzing on weapons targeted for hardened structures. (Ref. 4) Therefore, if the GP bomb misses the aircraft shelter and strikes the ground, it can be assumed that penetration beneath the ground surface will occur. The depth of penetration is a function of bomb shape, height and angle of delivery, fuse delay, and soil conditions. (Ref. 2,5) It has been shown that the "typical" GP bomb of concern is capable of achieving depths of penetration of 9 meters given conditions such as those at Osan AB, Korea. (Ref. 6,7) Corson, et al say, however, that "...based on recent research, a "typical" 500 Kg GP bomb penetration depth of 4.5 to 6.0 meters (15 to 20 feet) was determined for Osan and Kunsan." (Ref. 2)

Structure

At the PACAF airbases, 171 aircraft shelters comprise 77% of the facilities considered critical and are 60% of the total 281 facilities founded on piles. For the purpose of analysis, the typical foundation design of a third-generation aircraft shelter will be examined.

The aircraft shelters in Korea typically utilize a single row of piles beneath the arch walls while in Japan double rows of piles support the shelter arch walls.

The piles used are end-bearing resting on bedrock. The vast majority of the piles used throughout the PACAF bases are hollow core, spun-cast, pretensioned concrete piles manufactured by the Dae Lim Corporation of Korea. These piles are of uniform cross section with outside diameters ranging from 250 to 550 mm (10 - 22 inches). The average pile outer diameter is approximately 400 mm (16 in) with an average hollow inner diameter of 200 mm (8 in).

The piles support grade beams which are constructed directly on top of the piles The arched walls of the structure rest immediately upon the grade beams. Tie beams running laterally across the shelter are tied into the grade beams. A course of approximately 1 foot of gravel is then placed in the floor slab area, covering the tie beams, providing a surface upon which the floor slab is then constructed. A vapor barrier is first placed over the base material and expansion joints are constructed along all wall contacts before the concrete is placed. Thus, the floor slab is typically free-floating from the remainder of the structure.

## III. Blast Effects

The scenario of concern is that of a sub-surface detonation of a 500 Kg GP bomb. Upon detonation, peak accelaerations and pressures of up to 99,000 G's and 34,000 psi respectively may be experienced close in to the point of detonation. The expansion of gases generates a compressive wave that propagates outward in a spherical manner. If the point of detonation is close enough to the piles, some may experience crushing, shearing spalling, or buckling of the pile. The degree of damage will be dependent on range to effect and the occurrence of liquefaction. If the soil achieves a liquefied state, a loss of lateral support will result, thus the chance of failure due to buckling is increased. For further discussion of blast effects numerous texts and papers have have been written on the subject. One excellant text in particular, The Dynamics of Explosion and Its Use, by Josef He.rych is especially informative. Additional informtion is left to the reader's discretion.

## IV. Mitigation Techniques

### Ground Isolation

The objective of this research is to identify viable methods of alleviating damage to pile foundation systems. The immediate focus is on the protection of existing structures at PACAF bases in Korea and Japan. Parallel to this research is the recommendation of pre-construction foundation preparation techniques for future structures to enhance their survivability. The overwhelming majority of the research to date has been concerned with earthquake-induced ground motions as opposed to the high levels of loading experienced in an explosive event. Thus, uncertainty exists as to the applicability of each technique of pile protection from blast effects. Mitigation techniques for the minimization of destructive effects generated by the detonation of high explosives fall into three general categories: 1) Isolation of the foundation from the weapon effects, 2) Modification of the soil structure to increase strength characteristics, 3) Implementation of energy absorbing/dissipating materials. It is questionable whether any individual technique can independently provide adequate protection, thus, the possibility of combining methods is foreseen.

The most obvious solution to the problem at hand is to prevent the penetration of a weapon into the soil surrounding a structure.

Interception of an incoming GP bomb at the ground surface would prevent the threat of a sub-surface detonation. If the bomb manages to penetrate the ground, then the task is to prevent the bomb form "J-hooking" underneath the structure.

Prevention of ground penetration may be achieved by the construction of a reinforced concrete "burster" slab adjacent to the footing of the structure. Based on calculated overpressures, the slab would have to extend at least 10 - 15 feet outward from the edge of the structure to ensure maximum overpressures felt by the piles did not exceed the compressive strength of the pile. Alternatively, other options to prevent ground penetration include steel netting or high-tensile strength geosynthetic fabric placed in a horizontal manner directly on the ground surface. Either of these techniques would provide a high-strength pseudo-skin encapsulating the soil itself.

In addition to a horizontal burster slab, it is recommended that a vertical concrete curtain wall be installed. A curtain wall extending approximately 20 feet beneath the ground surface would prevent the bomb from "J-hooking" beneath the structure. Drake, et al. has observed that the trajectory of an earth penetrating weapon will often curve away from its normal path after intersection of the ground surface before detonation occurs, thus, the possibility of the weapon exploding directly beneath a structure exists. (Ref. 5)

It is desirable to ensure that a bomb does not detonate in the immediate vicinity beneath a structure, therefore, the combination of a concrete curtain wall and burster slabs may offer a functional degree or protection.

Soil Improvement

A relatively new aspect of geotechnical engineering, soil improvement techniques (modification of strength parameters such as permeability, relative density, and cohesion) have been utilized in seismic engineering as an effective method of structural protection from earthquake loading. Although application of this technology is not yet extensive, an increasing number of projects throughout the United States, Canada, and Japan have benefitted from its use. Much of the information available is the result of applications in private industry by such firms as GKN - Hayward Baker of North America, Nippon Kokan K.K. of Japan, and Konoike Construction Co., Ltd, also of Japan.

Soil improvement techniques that appear to offer positive results as mitigation methods for blast-loading are grouting, the placement of gravel drains, or stone columns, by vibrocompaction or vibroflotation, or de-watering the site. By grouting the soil, the relative density of the soil is increased, and if chemically grouted, the soil can actually be transformed into a sandstone-like material. Gravel drains also increase the relative density of a soil as well as providing a highly-permeable pathway for the dissipation of the increased pore-pressures that arise in the soil. De-watering the site will increase the effective stress acting on the soil and decrease the level of saturation, both factors reducing the probability of liquefaction in the soil.

Grouting

According to Welsh, "Grouting is the injection of pumpable materials into a soil or rock formation to change the physical characteristics of the formation." (Ref. 13) Four basic types of grouting are currently utilized in geotechnical engineering today. These are compaction, slurry, chemical, and jet grouting.

Compaction grouting utilizes a low slump, high viscosity cementitious grout pumped at high pressures into the formation. As the grout is pumped into the formation, the soil or rock matrix is compressed, thus decreasing the void ratio accompanied by an increase in relative density if the formation is a soil. A drawback to compaction grouting is the high pressures asssociated with the procedure have a propensity to initiate formation hydrofracturing. Thus, it is imperative to implement a riqorous QC/QA program to monitor grout flow rates ensuring uniform grout distribution.

Slurry grouting employs the pumping of an ultrafine ground cement as a grout mixture and is probably the most widespread form of grouting used in the United States today. According to Mitchell (Ref 9), the permissable soil types in which slurry grouting is feasible are confined to those with a "groutability ratio" , **N**, where:

$$N = (D_{15})soil/(D_{85})grout$$

$N > 24$ : grouting consistently possible

$N < 11$ : grouting not possible

Jet grouting utilizes rotating water jets affixed to the auger bit of a rotary drilling rig. After the bit has reached the desired depth, high pressure jets of water compact the surrounding soil as the bit is being removed. Simultaneously, a low viscosity cementitious grout is being pumped through a grout tube in the auger assembly filling the voids created by the jets. Thus, the relative density of the soil in the area is increased, decreasing the chances of liquefaction.

The last method of grouting is chemical grouting. This process utilizes specially formulated chemical mixtures that combine with sands, with less than 20 percent passing a U.S. sieve No. 200, to form a sandstone-like substance. These compounds can develop unconfined strengths of well over 4100 KN per square meter. Sodium silicate grouts are commonly employed throughout the United States as they offer low viscosity, controllable set time of the grout, and moderate cost as well as being non-toxic (as opposed to acrylamides, which were previously used as a grouting compound, that exhibited problems with toxicity). The most renowned application of chemical grouting is the Pittsburgh Subway project by GKN Hayward-Baker in 1983 (Ref. 10). This project entailed the placement of over 3,785,000 liters of sodium silicate grout for underpinning purposes.

Stone Columns

The advancement and implementation of stone columns as a ground modification technique has predominantly been motivated by the research in seismic engineering examining processes capable of mitigating earthquake effects. Two basic principles govern the design and application of stone columns: the densification of surrounding soils upon placement of the stone columns, and the dissipation of the increased pore water pressures through the higher permeability of the gravel used in stone column as opposed to that of the surrounding soil.

Stone columns are constructed through the principle of "vibro-compaction/vibro-replacement". A vibrator is suspended from a mobile crane or rig and is lowered into the ground. The vibrator induces liquefaction in a confined region immediately surrounding the tip of the jig, thus as the vibator advances, it is clearing a pathway ahead of itself. Once the vibrator has reached the desired depth, the process is repeated in reverse as the mechanism is removed from the soil. As the vibrator is being extracted from the ground, crushed stone is poured down the hollow core of the vibratory jig. The stone is compacted by either the effects of the vibrating jig being raised and lowered, or through the use of a power mandrel or rotary hammer. The compaction of the stone at the bottom of the augered hole causes a densification of the soil matrix in which the pile is founded by forcing a decrease in the void ratio, similar to the results derived by compaction grouting.

The increased permeability of the stone column allows for rapid dissipation of increased pore pressures developed by either seismic events or blast loading. Nippon Kokan, K. K. of Japan conducted a full-scale test of a prototype pile, during land reclamation operations in the Bay of Tokyo, in which super-seismic lateral loads of the order of 1000 G's were developed. Stone columns effectively prevented liquefaction of the surrounding soils by alleviating the increased pore pressures experienced as a result of the lateral loading.

De-Watering

Charlie, et al. (Ref 11) have noted that the likelihood of liquefaction in a soil is a function of the degree of saturation. Thus, by draining the soil, the percent saturation is decreased. If a soil is less than 100 percent saturated, it is extremely difficult to induce liquefaction. The obvious method to lower the degree of saturation is by de-watering the soil in the area. This can be achieved by installing sub-surface horizontal drains linked together to form a drainage field. Utilizing a common sump, the water may then be removed from the drainage system by a submersible pump. A foreseeable problem at the PACAF bases is the presence of high water tables. At the Korean bases, it is not uncommon for the entire area to be submerged during the moonson season, therefore, de-watering the sites may be difficult, if not impossible. This is due to the fact that as water is pumped from the drainage field, the recharge rate may be such that no significant drop is noted in the piezometric surface of the water table, therefore, no drop in the degree of saturation is realized.

Energy Absorbing/Dissipating Materials

A promising area of research is in the use of materials with damping characteristics that would minimize the energy transmission to the foundation region such that any damage that might occur to the pile system would be negligible. Techniques that have demonstrated potential as a means of mitigating the damage to piles are dynamic isolation systems, viscoelastic gels, and hollow, glass micro-spheres.

Dynamic isolation systems have been successfully utilized in seismic engineering to protect structures from earthquake effects through the use of springs to isolate the building from anticipated damage. The placement of springs "disconnects" the structure from the driving force (i.e. ground motion resulting from the earthquake) which effectively creates an uncoupled system. Additionally, the material damping properties inherit to the spring further reduce the degree of motion experienced by the structure.

The use of viscoelastic gels as a protective measure for structures is, as of yet, an untried technology. The prospects, however, are promising as gels have been utilized as a damping material in applications ranging from isolation tables for laser stabilization to energy absorption in running shoes. A problem that bears consideration is the question of toxicity of gels that might be considered for injection into the soil matrix.

The concept of hollow, glass microspheres as a means of energy dissipation has been forwarded by Johnson. (Ref. 12) The premise is to inject hollow, boro-silicate into the soil matrix; the compressive strength of the spheres is such that the extreme overpressures generated by a blast would crush the spheres as the compressive wave propagated through the soil. As the spheres successively fail, the amount of energy that is propagated is reduced as well as reducing pore fluid pressures

Discussion

While all the techniques offer some degree of protection against the blast effects of the proposed threat, the ability to mitigate the damage is not unifor throughout. The concept of installing concrete burster slabs could guarantee high levels of protection, however, the amount of concrete necessary are enormous. If we consider a vertical wall of dimensions 1 foot thick by 20 feet tall extending around a perimeter approximately 70 yards by 115 yards, approximately 822 cubic yards of concrete would be required for construction of the cutoff wall alone. Besides the obvious expense involved, drainage problems are likely as the placement of a cutoff wall would interrupt the flow patterns of groundwater.

Grouting methods seem to offer good possibilities, however, the technology, as of yet, has not been applied as a protective measure against blast effects. Therefore, no reliable data is available on the effectiveness of this application. Again, cost is a paramount issue, as injection grouting is expensive, especially when dealing with the volume in question.

The advantage of grouting is the increase in relative density which decreases the probability of liquefaction. These techniques do not appreciably decrease the magnitude of the energy being propagated through the soil. Thus, the threat of crushing or shearing are still present in the pile, however, the likelihood of failure due to flexure is reduced as the lateral support provided by the soil is still present if liquefaction does not occur.

The use of stone columns offers promising possibilities as a mititgation method. A ring-like pattern of stone columns could be placed around the structure, creating a zone of densified soils in which liquefaction would not occur. Additionally, a degradation of energy propagation would be realized as the compressive wave passed through successive density interfaces of compacted and non-compacted soils. The degree of reduction is unknown, however it is hoped that future field tests and research will be able to quantify this phenomena.

## V. Conclusions

The two techniques offering the greatest possibilities of being cost effective mitigation techniques are stone columns and the injection of hollow microspheres. The stone columns have proven effective for **some** super-seismic loading conditions and can be constructed with locally available gravels. Furthermore, the use of stone columns is becoming more widespread in earthquake engineering thus there are companies familiar with installation techniques. If an affordable source of hollow microspheres is available this concept bears further investigation. The microspheres offer both increased resistance to liquefaction through the densification of surrounding soils during the injection process as well as decreased levels of overpressure at the pile. The decrease in energy results from the change in momentum upon collapse of the microspheres.

At this point it appears that the emphasis of future research should examine the application of mitigation techniques for proposed structures. An advantage of pre-construction ground modification is the ability to ensure uniform improvement of the site and reduced cost of application. Techniques such as dynamic deep compaction, a process of dropping a large weight on the order of 20 - 40 tons from heights of 50 to 100 feet in a grid pattern, and explosive compaction can be employed without risk of damage to existing structures.

The problem posed involves the analysis of both the ability to provide protection to the piles as well as being economical to implement. The various techniques proposed to mitigate blast effects offer some degree of increased protection to the structure, however, some may be prohibitively expensive. Testing, scaled or full-scale, is needed to quantify the feasibility of the proposed mitigation techniques.

## References


1) Gill, J.J., Interpretation of the Initial Results of the 500,000 lb (TNT Equivalent) Hayman Igloo Test, Proceedings of the 60th Shock and Vibration Symposium, Norfolk, VA, 1989

2) Corson, W.M., Gill, J.J., Maxwell, K.H., Thomas, J.N., Jackson, P.J., Survivability of Structures Founded On Piles in Saturated Soil, Proceedings of Test Technology Symposium IV, John Hopkins University, Laurel, MD, April 1991

3) Red-on-Blue Manual (Effectiveness Estimates for Soviet/ Warsaw Pact Nonnuclear Munitions) (U), 61 JTCG/ME-77-15, October 1982 (SECRET-NOFORN-WNINTEL)

4) Vulnerability Assessment of the NATO Third-Generation Aircraft Shelter (U), 61 JTCG/ME-89-7, January 1990, (SECRET-NOFORN)

5) Drake, J.L., Twisdale, L.A., Frank, R.A., Dass, W.C., Rochefort, M.A., Walker, R.E., Britt, J.R., Murphy, C.E., Slawson, T.R., Sueg, R.H., Protective Construction Design Manual, Section V, ESL-TR--87-57, AFESC, Tyndall AFB, FL, 1989

6) Crawford, R.E., et al., Protection from Nonnuclear Weapons (U), AFWL-TR-70-127, Air Force Systems Command, Kirtland AFB, NM, 1971

7) Effects of Impact and Explosion, Volume I (U), (AD 221586), National Defense Research Committee, Washington , D.C., 1946

8) ASCE, Journal of the Geotechnical Divisio;n, 104:GT9, 1978

9) Mitchell, J.K., "Soil Improvement - State-of-the-Art Report," Proceedings of the Tenth International Conference on Soil Mechanics and Foundation Engineering, Stockholm, June 1981

10) Parish, W.C., Baker, W.H., Rubright, R.M., "Underpinning with Chemical Grout," Civil Engineering, ASCE, August 1983

11) Charlie, W.A., Veyera, G.E., Doehring, D.O., Abt, S.R., Blast Induced Liquefaction Potential and Transient Porewater Pressure Response of Saturated Sands, Colorado State University, Ft. Collins, CO, October 1985

12) Johnson, C.F., Hollow Glass Microspheres as a Countermeasure to Blast Induced Liquefaction, Thesis, Colorado State University, Ft. Collins, CO, 1989

13) Welsh, J., "Insitu Testing For Ground Modification Techniques," Use of Insitu Tests in Geotechnical Engineering, ASCE Geotechnical Special Publication No. 6, New York, June 1986

1991 USAF-RDL SUMMER FACULTY RESEARCH PROGRAM/

GRADUATE STUDENT RESEARCH PROGRAM

Sponsored by the

AIR FORCE OFFICE OF SCIENTIFIC RESEARCH

Conducted by

Research and Development Laboratories, Inc.

# FINAL REPORT

## Stimulated Emission Pump Spectroscopy of Iodine


| | |
|---|---|
| Prepared by: | Shawn J. Gaffney |
| Academic Rank: | Graduate Student |
| Department and | Electrical Engineering |
| University: | Notre Dame |
| Research Location: | USAF PL/LIDC<br>Kirtland AFB, NM 87117 |
| USAF Researcher: | Capt. Mel Nowlin |
| Date: | 30 Aug 91 |

Stimulated Emission Pump Spectroscopy of Iodine

by

Shawn J. Gaffney

## ABSTRACT

Work was completed on an experimental station to perform stimulated emission pumping of ground state iodine and data was collected under a variety conditions. Two optical tables were prepared with the proper optical equipment to simultaneously converge the beams of two pulse dye lasers and one argon ion laser onto a reaction point . The appropriate optics and monitoring equipment was added to observe the wavelength of all beams as well as beam absorption at the reaction site. The fabrication of a pressure controlled iodine cell allowed studies of relaxation rates in vacuum and partial pressures of various chosen ambients.

## Acknowledgements

I wish to express my appreciation to the Air Force Systems Command and the Air Force Office of Scientific Research for providing the opportunity to participate in the research efforts of the Philips' Lab's Chemical Laser division. The cooperation and encouragement among the lab's personnel made the working environment very enjoyable. In particular, Capt. Bob Cranich, Dr. Dan Johnson, and Marty Vias were always willing to lend both a helping hand and discuss technical matters. Dr. Mike Heaven kept things running smoothly and could be counted on for expertise in all areas. In addition, Dr. Heaven both a sense of unity among the researchers and the leadership necessary for technical excellence.

Capt. Mel Nowlin is leader of the SEPS experiment and is an excellent engineer. His combination of managerial and engineering skills, as well as, the support and encouragement he provided to myself and my family, made the research period very rewarding.

# I. INTRODUCTION:

The stimulated emission process occurs when an excited atom is induced by an outside source to emit its excited state energy. In the case of SEPS, this outside influence is a laser pulse, and the energy emission is in the form of a photon. By tuning this laser pulse so its photons have energy exactly equal to the energy difference between the excited state of the atom and a desired lower energy state, the atom is stimulated into emitting a photon. This photon is identical to the stimulating photon in energy, direction of travel, frequency and phase; thus light produced through this process appears as a laser beam.

The Chemical Laser Facility at Kirtland AFB is particularly concerned with using the stimulated emission process in the analysis of the C.O.I.L. chemical laser. The efficiency of this laser and other chemically pumped halogen lasers is controlled by the collision dynamics of the rotational and vibrational levels of ground states. Iodine was chosen to be the first investigated due to its relevance to the C.O.I.L. laser, but the experimental apparatus design allows flexibility in investigation other gaseous substances.

## II. OBJECTIVES:

The principal goal of the summer research was to determine the rate of vibrational energy transfer in ground state iodine. Because these values are not available in the existing literature, this data serves as a guide for optimizing the C.O.I.L. laser and as indication of performance for theoretical models.

The experimental station consists of one argon-ion laser, two pulse dye lasers (PDL), two Nd:Yag pulse lasers, assorted optics, two wave meters, and a monocrometer. Data acquisition is accomplished via a National Instruments A/D conversion board which reads the output of a photomultiplier tube used with the monocrometer and assorted signal processing equipment. The argon-ion laser serves as a pumping source for the iodine and the Nd:Yag lasers pump the pulse dye lasers. The output beams from the three dye lasers converge onto a controlled low pressure iodine cell. The iodine is placed into a vibrationally excited state by a pulse from the first PDL. This is followed by a pulse from the second PDL which causes stimulated emission. Finally, the monochrometer is used in conjunction with the signal processing/data acquisition equipment to measure differences in absorption of the probe laser beam as it passes through the reaction cell. Simply holding all conditions equal while varying the probe time yields information on the energy relaxation rates of the ground state being probed.

III.

In completing the assembly of the experimental station, the following requirements were necessary and constituted my main assignment as a participant in the 1991 Summer Graduate Student Research Program (GSRP). A pressure tune control was modified for controlling a pulse dye laser etalon. A pressure monitoring and control system was fabricated for the iodine cell and various tuning and electronic problems with the Nd:Yag lasers were corrected. Finally, a large volume of data was collected, and its analysis is continuing. Because this would be the only opportunity to collect such data, all effort was concentrated upon collecting as much information as possible. Publication of the data analysis is to follow shortly.

# FINITE-DIFFERENCE TIME-DOMAIN SOLUTIONS TO MAXWELL'S EQUATIONS FOR COMPLEX GEOMETRIES.

Michael C. Governale

Abstract

The Finite-Difference Time-Domain (FD-TD) method for solving Maxwell's equations for complex geometry using the stair-step method at the boundary may be improved by using interpolative methods. It has been found that the interpolation method improves resolution at the boundary by closer approximations to the amplitude and frequency domains. Various solutions in 2-D using this technique are presented, including scattering and coupling of objects in the interior.

## Introduction

The essence of this paper is to derive a solution to Maxwell's equation in finite difference form. This problem has been solved for the case of a rectangular grid but is still in the developmental stages for curved and complex geometry. In this paper I develop the theory leading up to the finite difference method, then solve the problem for a perfect conductor in a square or rectangular box. Then the problem is formalized in the case of curved geometry and applied to a circular region. Finally I compare the technique developed for the curved geometry with the current stair-step technique.

Discussion

Finite-Difference Time-Domain (FDTD) codes have become very popular in the modeling of electromagnetic fields and their behavior in complex geometries. The greatest limitation being their inability to handle the behavior near the boundary with accuracy without the reduction of the cell size. An improvement has been made in coping with irregular boundaries such as curves, and sharp corners, as well as barriers, and thin slots. The improvement eliminates the need to use very small cell sizes in order to retain resolution of the field near these boundaries.

An example of a problem that would benefit from this method, is the modeling of a field inside a container which is composed of irregular shapes at it's boundary, and scattering objects in it's interior. This method is especially effective for the modeling of high frequency waves in a body of such geometries. The technique is an improvement of the FDTD code which was carried out in two-dimensions for circular, elliptic, and more complex geometries using microwave sources varying sinusoidally in the interior of the container. Several variations of the code were then compared with the simplest techniques currently being used in order to evaluate the improvement at the boundary.

Since the initial development of the FDTD method by Yee, and Taflove, the computer hardware has made it possible to model 3-D codes for complex scattering and coupling, primarily done by Kunz, Holland, and Merewether. At the present time, FDTD has been applied to a wide variety of problems such as to improve memory efficiency and management. These issues were influenced by the need to model features smaller than a FDTD cell such as for thin-slots, and wires.

Probably the main limitation of the original FDTD code is it's inaccurate depiction of curved boundaries. These boundaries are modeled using the 'staircase' method, an approximation which has been recognized as a "probable source of error", by Ray. As a result, several new methods have been developed in the past following the footsteps of Madsen, Mei, Yee, and Taflove such as finite-elements, and modified volume techniques. The problem however, is that such techniques require more computer memory, run-time, and smaller cell sizes than the original FDTD method.

The reason for holding onto the FDTD methods are for it's simplicity, speed of execution, and it's fixed memory requirements. It has been found that improvements in the memory storage can be made to the FDTD method which will enable the use to be transferred to large objects at high frequencies using parallel computing, or supercomputers.

Maxwell's equations in their most general form are given as:

$$\nabla \cdot D = \rho_f \qquad \nabla \cdot B = 0$$

$$\nabla \times E = -\frac{\partial B}{\partial t} \qquad \nabla \times H = J_f + e\frac{\partial D}{\partial t}$$

When the constituent equations, $E = eD,\ \ B = \mu H,\ \ J_f = \sigma E + J'$ are applied to this set of equations for a perfect conductor with no extraneous currents, where propagation occurs in a vacuum, Maxwell's equations are written as:

$$\nabla \cdot E = \frac{\rho_f}{e_o} \qquad \nabla \cdot H = 0$$

$$\nabla \times E = -\mu_o \frac{\partial H}{\partial t} \qquad \nabla \times H = J' + e \frac{\partial E}{\partial t}$$

For the FDTD method used here, only the curl equations are of interest. When the curl operations are performed for the case of $H_z$ perpendicular to the direction of the propagation and a current source emanating in the y-direction, we obtain:

$$\frac{\partial H_z}{\partial x} = e_o \frac{\partial E_x}{\partial t} \qquad \frac{\partial H_z}{\partial y} = J_y + \epsilon_o \frac{\partial E_y}{\partial t}$$

$$\mu_o \frac{\partial H_z}{\partial t} = \frac{\partial E_x}{\partial y} - \frac{\partial E_y}{\partial x}$$

These are the essential equations needed to develop the PDE method which approximates the fields. A mesh is defined which encompasses the scattering object for which the local field points are used to define the spatial location for the approximating equations. The temporal development is then incorporated into these equations and after a given time has elapsed, this set of solutions is used to develop a picture of the field in space and time.

Now that the general equations in differential form have been found, the next step is to put them into a form suitable for the computer code. In order to do this the finite difference method is used. This method relies on Taylor's Theorem in the following manner:

$$U_p \approx U_o + h\frac{\partial U_o}{\partial x} + h^2\frac{\partial^2 U_o}{\partial x^2} + \ldots$$

When this equation is applied to two field points, either ahead of or behind the point to be evaluated, we may solve for the approximate derivative and retain the error terms for error evaluation. In this case, the first partial is of interest, leaving to second order the error term written as:

$$\frac{\partial U_o}{\partial x} \approx \frac{U_p - U_o}{h} + (1/2)h\frac{\partial^2 U_o}{\partial x^2} + \ldots \; ; \quad where \quad U(\xi) = (1/2)h\frac{\partial^2 U_o}{\partial x^2}$$

Applying this theorem to both the spatial and temporal derivatives, we arrive at the following set of working equations:

$$E^n{}_x(i,j) = \frac{\Delta t}{e_o}\left[\frac{H^{n-1/2}{}_z(i,j) - H^{n-1/2}{}_z(i,j-1)}{\Delta y}\right] + E^{n-1}{}_x(i,j)$$

$$E^n{}_y(i,j) = -\frac{\Delta t}{e_o}\left[\frac{H^{n-1/2}{}_z(i,j) - H^{n-1/2}{}_z(i-1,j)}{\Delta x}\right] - \Delta t J^{n-1/2}{}_y(i,j)$$

$$+E^{n-1/2}{}_y(i,j)$$

$$H^{n+1/2}{}_z(i,j) = \frac{\Delta t}{\mu_o}\left[\frac{E^n{}_x(i,j+1) - E^n{}_x(i,j)}{\Delta y}\right] - \frac{\Delta t}{\mu_o}\left[\frac{E^n{}_y(i+1,j) - E^n{}_y(i}{\Delta x}\right.$$

where, the $\Delta t$ is the timesize, $\Delta x$, and $\Delta y$ are the stepsize in each direction, and i,j are the spatial location relative to the cell being used. The stepsize is incremented in lengths governed by the Courant condition, and the time is incremented using the leap-from method. The Courant condition in 2-D is needed in order to insure stability of convergence. he equation which is used in 2-D is:

$$c\Delta t \le \frac{1}{\sqrt{\frac{1}{\Delta x^2} + \frac{1}{\Delta y^2}}}$$

When this condition is met, stability is insured, and numerical dispersion is held to the error given by the error terms in the Taylor series approximation. The temporal descretization is denoted by n-1, n-1/2, n, and n+1/2. In the leap-frog method, the spatial and time derivatives are staggered by increments of 1/2. This implies that when the Courant condition is met by choosing the appropriate stepsize, then the timesize is chosen to be 1/2 of this value.

With the general equations set up, and the method of spatial and temporal descretization known, it is left to describe the computers job. The general method is to start in the lower left hand side of the grid, look to see if the cell is inside or outside of the boundary, and then to use the equations to calculate the values at this location. If this cell is outside of the boundary, the computer assigns the value of zero to this cell. If it is on the boundary, then the computer must invoke the boundary condition previously prescribed. If the cell is within the boundary but not lying on the boundary then the equations are used as normal. The computer then works it's way upward until it reaches the top of the grid. then goes back to the lower left hand corner but one cell to the right. This process is repeated until all of the grid is finished, where the timestep is incremented.

In the case of the square mesh, where all the cells lie either parallel to the boundary, or inside of the boundary, the above method works well and converges nicely. For example, figure 1 is a picture of the Magnetic field in a square box with a current source located at it's center propagating in the y-direction.

The initial field is a dipole, as it has not yet reached the boundary. Once the field reaches the boundary, for the case of a perfect conductor, (boundary condition set to zero), scattering occurs and the field starts to diffuse. It is essential at this point to explain the effect of scattering on the numerical process. In an actual field propagating in space, the dispersion relationship, is exact, but in the case of numerical analysis becomes:

$$\sin^2[(\frac{v_p}{c})\alpha\pi(\frac{\Delta x}{\lambda})]=\alpha^2\sin^2[\pi(\frac{\Delta x}{\lambda})] \quad where \quad \alpha=\frac{c\Delta t}{\Delta x}, \quad v_p=\frac{\omega}{k}, \quad k=\frac{\cdot}{\cdot}$$

where the phase speed, $v_p$ , as a function of the grid resolution alters as time is incremented. In free space, all waves propagate at the same speed, however in computer simulation this is not true and is caused by the finite choice for the stepsize. This is known as numerical diffusion. Although this is a problem, the actual errors made by the computer by adding, and subtracting, i.e. round off error, will exceed the rate of numerical diffusion. This is known as numerical dispersion, and increases as the code is run a significantly long time. So it is safe to assume, that as long as the code is run short enough time periods to control numerical dispersion, the effects of numerical diffusion will not be of concern. Once the scattering process has started, it will continue until a resonant condition arises. The condition in theory will then be a repeating process in which the field oscillates in time. As this is not theory, but practice, we then must be concerned with the effects of unnatural decay of the oscillating field.

In the treatment of complex geometry, i.e. geometric configurations other than objects with square and rectangular sides, several approaches may be used. One approach, is to simply zero all cells that have boundary crossings. This is known as the stair-step method and is the current method being used in practice. In this section, I start with the stair-step method, then move on to the interpolation method. The differences and significance of the differences are then discussed in the next section.

The method may be applied to nonlinear or anisotropic dispersive materials, (see Luebbers, Hunsberger, Kunz), but in order to simplify matters, a perfect grounded conductor is assumed for materials at or inside the boundaries. The general procedure used for interior points is the same as for FDTD, the formal difference being in defining the boundaries and the calculations for cells which lie on the boundary.

In this technique, a series of functions which define the boundary are used. There is no limit to the complexity of the geometry, as piecewise definition of several functions may be employed to define the object. The method uses simple logical-code to determine when a cell lies on the boundary. When a cell is found to lie on the boundary, the code determines which sides of the cell are affected, then uses the appropriate boundary equations for that particular cell.

The stair-step method is affectionately known as the lego block technique. It simply takes the cell which is affected by the boundary crossing and sets it equal to the boundary value prescribed by the initial condition. In doing this, the shape is approximated by small squares, and hence the name lego block. This method works pretty good as long as the cell size is taken to be very small. However, this may be impractical as a smaller cell size means more computer storage space, and this becomes a problem for large objects. Most importantly, it decreases the resolution of the field near the boundary, as it does not give exact simulation from the true distance to the boundary.

The method of interpolation takes the distance to the boundary, and then uses the previous inner field data to interpolate the value at the boundary cell. This method greatly improves the resolution at the boundary at the lowest cost in computer time. The method used here is Newton's Forward and or Backward Divided Difference Interpolation. The general form of this equation for the case in the x-direction is:

$$U_p \approx f_0 + (x-x_0)\, f[x_0, x_1] + (x-x_0)\,(x-x_1)\, f[x_0, x_1, x_2] + \ldots +$$

$$(x-x_0)\ldots(x-x_{n-1})\, f[x_0, \ldots, x_n]$$

In the case of linear interpolation of the electric field we have:

$$f[x_0, x_1] = \frac{E(i+a,j) - E(i-1,j)}{h+ah}$$

These equations then yield;

$$E(i,j) \approx E(i-1,j) + h\left[\frac{E(i+a,j) - E(i-1,j)}{h+ah}\right]$$

The denotation being used for the x-component on a top side boundary. The letter h is the stepsize, and ah is the actual distance from the cell center to the boundary point. When this equation is used for a perfect conductor, it simplifies to:

$$E(i,j) \approx \left(\frac{a}{1+a}\right) E(i-1,j)$$

Note that in lattice units defined as unity, the distance 'a' must be multiplied by the stepsize to retain the proper value needed in the interpolation. The beauty lies in the simplicity of the method. Since the function defining the boundary is in lattice units, the values of a, and b are easily obtained by subtracting the value at the lattice point from the function value at the boundary. The FDTD method being used is a combined difference method which uses forward differencing for the magnetic fields, and backward differencing for the electric fields in order to homogeneously distribute the boundary effects to the entire grid. Since the linear interpolation is only accurate to first order, I have decided to use a quadratic interpolation which is accurate to second order, so that the interpolation maintains accuracy below the order of the finite difference approximation. When the calculations for the quadratic interpolation are done in 2-D, the following interpolation equations are used:

$$f_1=\frac{E_x(i,j+1)-E_x(i,j+2)}{h},\qquad f_2=\frac{-E_x(i,j+1)}{h+bh},\qquad f_3=\frac{f_2-f_1}{2h+bh}$$

$$E_x(i,j)=E_x(i,j+2)+(2h)f_1+(2h^2)f_3$$

$$f_1=\frac{E_y(i+1,j)-E_y(i+2,j)}{h},\qquad f_2=\frac{-E_y(i+1,j)}{h+ah},\qquad f_3=\frac{f_2-f_1}{2h+ah}$$

$$E_y(i,j)=E_y(i+2,j)+(2h)f_1+(2h^2)f_3$$

$$f_{1a}=\frac{H_z(i-1,j)-H_z(i-2,j)}{h},\qquad f_{2a}\ \frac{-H_z(i-1,j)}{h+ah},\qquad f_{3a}=\frac{f_{2a}-f_{1a}}{2h+ah}$$

$$H_z(i,j)=H_z(i-2,j)+(2h)f_{1a}+(2h^2)f_{3a}$$

when the boundary lies on the right, and:

$$f_{1b}=\frac{H_z(i,j-1)-H_z(i,j-2)}{h},\qquad f_{2b}=\frac{-H_z(i,j-1)}{h+bh},\qquad f_{3b}=\frac{f_{2b}-f_{1b}}{2h+bh}$$

$$H_z(i,j) = H_z(i,j-2) + (2h)\,f_{1b} + (2h^2)\,f_{3b}$$

when the boundary lies on the top. Note that the electric field components are interpolated in the opposite direction, i.e. the x-component of the electric field is interpolated from the value of the x-component behind in the y-direction. This enables the use of the closest component inside the boundary, as the equations for the interior points are stepping in this same direction. For example, the FDTD equation for the x-component of the electric field is:

$$E^n{}_x(i,j) = \frac{\Delta t}{e_o}\left[\frac{H^{n-1/2}{}_z(i,j) - H^{n-1/2}{}_z(i,j-1)}{\Delta y}\right] + E^{n-1}{}_x(i,j)$$

When the st p to (i,j-1) occurs outside of the boundary, the value is taken by interpolating from (i,j-1) and (i,j-2). This further simplifies the coding procedure by eliminating complex multi-field point equations such as is used in finite-difference formulae approximating derivatives on the boundary, in terms of internal pivotal values, (see Fox,L). This does not occur for the magnetic field, as both left and right pivotal values are available, however when the boundary cuts both sides of a cell, an average value is used for the magnetic field.

Results

In order to maintain simplicity and accuracy with the lowest cost in computer time, the method chosen for the remainder of this paper is the quadratic interpolation. In this section, discussion is made while presenting the graphic results of the progression of several fields. First the basic fields are introduced, then the time progression of the magnetic field in a circle is given. Next, the comparison of the stair-step method for the circle is made. Then I shift to the scattering problem by displacing the current in the circle. The final step is to locate a barrier and a slot in the circle, to study the effects of scattering and coupling over a few periods of time.

The following general fields were created inside a circle of radius 64 cells, or 6 wavelengths, where the frequency is taken to be in the microwave region. Shown in figure 1 are the x and y components of the electric fields after a time progression of one period, or 32 iterations with a stepsize of 1/32 seconds. Note the symmetry in all cases.

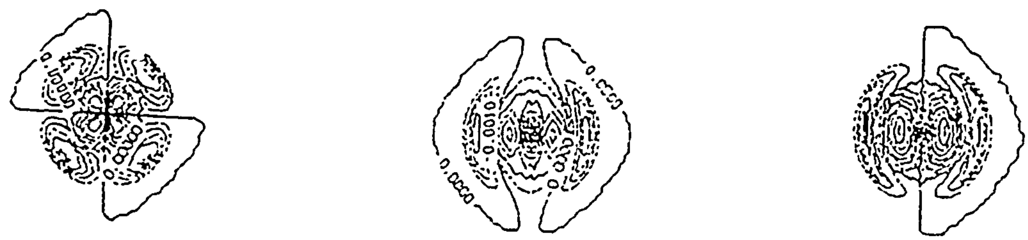

**fig. 1.** The x, and y components of the electric fields, from left to right, and the magnetic field on the right after 32 time iterations in the microwave region.

In figure 2 is the same configuration of the circle as given above. The magnetic field is shown as it progresses in time. It is notable that the initial field configuration at three periods gives the most information, as it is a convergent solution to the temporal and spatial domains. The maximum of information regarding the field strength, frequency and phase are found here. After the field begins scattering off the boundary as shown for periods four through eight, the disfiguration of the field is accompanied by the same frequencies bı ɔscillating amplitudes. It is interesting to note that periods six through eight do not change much, owing to the fact that these fields are resonating in a steady state situation. Most of the change in the fields are due to numerical dispersion and diffusion.

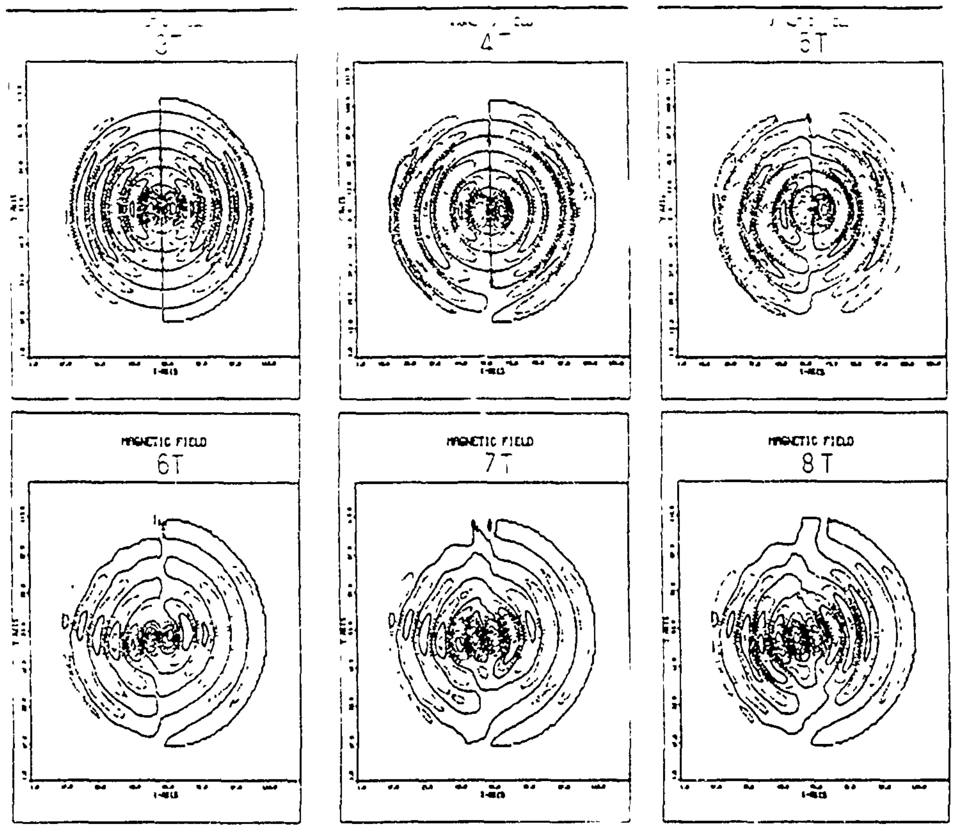


fig. 2. The time progression of the magnetic ıeld in a circle.

When a comparison in made with the stair-step method graphically, one cannot see the difference until several periods has elapsed. The greatest difference was found to exist at the boundaries in the amplitude and frequency domains. When the stair-step method is compared to the interpolation method with identical parameters, the error at three periods is found to exist primarily at the boundary. Even though the error is small, the difference being about 0.00034 on the average with a deviation of 0.0038, over a data range of -0.003358 to 0.00358. Since the deviation at the boundary is approximately 50% of the data range it is conclusive that the interpolation method greatly improves the technique. Figure 3 shows the difference graphically after three periods.

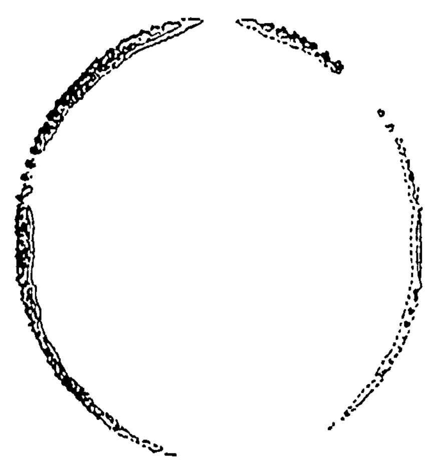

fig. 3. The difference between the stair-step method and the interpolation method after coupling.

In order to show the effects of scattering and coupling, the current was displaced to the bottom half of the circle. In figure 4, you can see the effect of having the current source very close to the boundary. The boundary couples to the field quickly where after a single period it acts as a scatterer for the rest of the progression. Note how the field 'creeps' up the sides of the boundary. Without accuracy at the boundary, this effect is distorted and cannot be modeled effectively. When the same circle with the same placement of the current source has a conducting barrier placed inside, the confinement becomes even greater. The field is broken up in two separate sections of eddies. The barrier acts as a coupling and scatterer as the field again 'creeps' up and around the barrier.

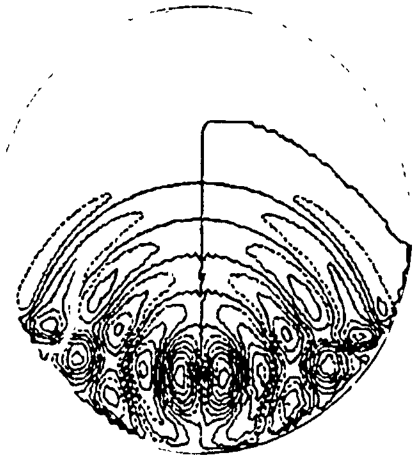

**fig. 4.** The magnetic field inside a circle with the current source displaced to show the effect of coupling and scattering.

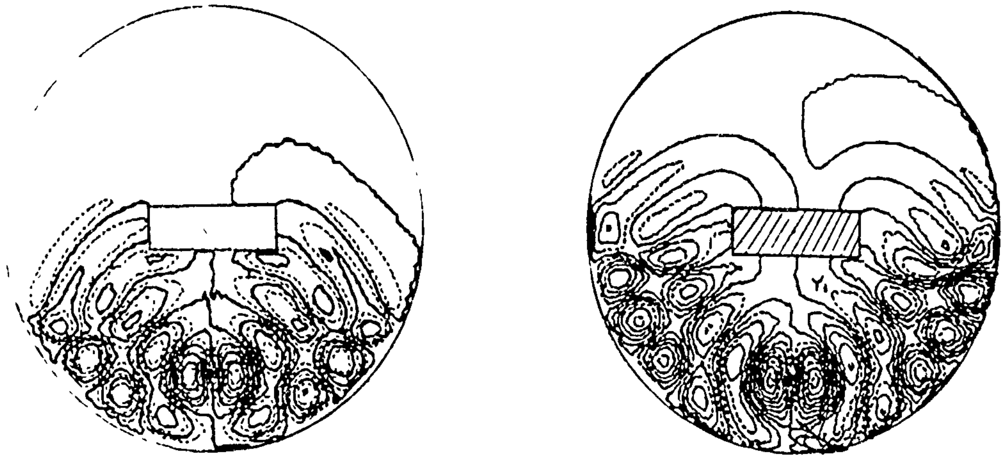

**fig. 5.** A conducting barrier is placed inside the circle.

The effects of scattering and coupling were also studied for the propagation of the field through a slot. This slot is taken to be ten cells wide, which is about 5/8 of a wavelength of the source frequency. The slot is twenty cells long or about 5/4 of a wavelength. Note how the field has to build up on the left hand side before it couples to the walls of the slot and propagates through. It took three periods to get the field out of the slot, and the field coupled to the right boundary after five periods. It is interesting to note here that the slot size can be halved without loss of resolution. This corresponds to a width of about 5/16 wavelengths. It is also interesting to note that a integral multiple of the cellsize is not required in choosing the slot width, as the interpolation makes up for this discrepancy. Also note the antennae-like dipole field that builds up near the entrance to the slot.

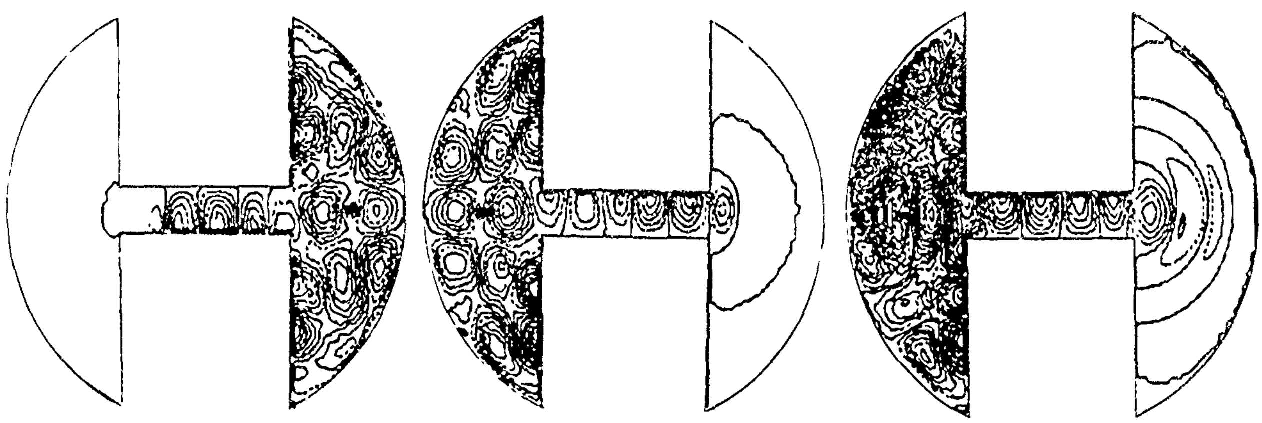

fig. 7. The propagation of the magnetic field through a slot of width 5/8 of a wavelength.

## Conclusion

The FDTD codes using the stair-step method have difficulty in the treatment of complex geometry, whereas the method of interpolation allows for finer resolution at the boundary in modeling objects, barriers, and slots. The major advantage of this technique being that the maximum cell size may be used over the entire grid thereby minimizing the amount of computer storage needed as well as maintaining maximum resolution of the boundary. Subsequently it has been found that larger objects with high frequency sources can be modeled without the common reduction of the cell size.

**Parallelization of a Two Dimensional Vlasov code**

James Koga

Graduate Student Research Associate

**Abstract**

A connection machine SIMD Vlasov code [4] is implemented on the MIMD Intel i860. Two versions of the code are implemented. A test problem is run and relative speed of the code is compared with the Cray YMP. A version of the code with 32 nodes achieves speeds faster than a comparable serial code on the Cray YMP. In this report the numerical scheme, timings, and test problem results will be presented.

# 1 Introduction

This paper describes the implementation of a 2-D Vlasov-Maxwell code on a MIMD parallel computer (i860). Vlasov-Maxwell codes can be used to simulate various electromagnetic phenomena which occur in plasmas [3, 1]. It is one of two popular methods for simulating this type of phenomena. The other method is the so-called particle-in-cell (PIC) technique [2]. In the PIC method individual particles are tracked and followed and the fields from these particles are calculated self consistently (Eulerian method). In the Vlasov-Maxwell technique the evolution of various quantities are calculated at fixed grid points (Lagrangian method). Each scheme has its advantages and disadvantages. The main advantage of the Vlasov-Maxwell scheme is that it lends itself to parallelization whereas the PIC technique is not as easily parallelized. The Vlasov-Maxwell scheme, however, requires more computation, more memory, and has more numerical stability constraints than the PIC scheme. It is the purpose of this study to determine the ease of parallelization of the Vlasov-Maxwell system for MIMD machines.

A Vlasov-Maxwell code which is already running in parallel on the Connection machine [4] is chosen as an initial code platform. Two implementations of the code are described. One implementation involves decomposing the grid into slabs and the other into squares.

In the following sections the specifics of the numerical method and the particular implementation of this method on the Intel i860 is presented. Numerical tests, and speed results will also be presented.

## 2 Numerical Method

In this simulation technique a plasma is represented by a discretized version of the Vlasov-Maxwell system of equations. The Vlasov equation is a continuity equation for phase space representing a system of particles. It is written in the form [3]:

$$\frac{\partial f_s}{\partial t} + \frac{\vec{p}_s}{m} \cdot \frac{\partial f_s}{\partial \vec{x}} + \vec{F}_s \cdot \frac{\partial f_s}{\partial \vec{p}} = 0 \tag{1}$$

where the subscript $s$ refers to the individual species ( background electrons, beam electrons, ions, etc...) used and the Lorentz force $\vec{F}_s$ is obtained from the equation:

$$\vec{F}_s = q_s(\vec{E} + \vec{v}_s \times \vec{B}/c). \tag{2}$$

The fields $(\vec{E}, \vec{B})$ in the Lorentz force equation are obtained from the set of Maxwell's equations:

$$\nabla \cdot \vec{E} = 4\pi\rho \tag{3}$$

$$\nabla \times \vec{E} = -\frac{1}{c}\frac{\partial \vec{B}}{\partial t} \tag{4}$$

$$\nabla \cdot \vec{B} = 0 \tag{5}$$

$$\nabla \times \vec{B} = 4\pi\vec{J} + \frac{1}{c}\frac{\partial \vec{E}}{\partial t} \tag{6}$$

The density $\rho$ and current $\vec{J}$ are calculated from:

$$\rho(\vec{x}) = \sum_s q_s \int d\vec{p}\; f_s(\vec{x}, \vec{p}, t) \tag{7}$$

$$\vec{J}(\vec{x}) = \sum_s q_s \int d\vec{p}\; \vec{v}_s\; f_s(\vec{x}, \vec{p}, t) \tag{8}$$

In the current formulation the electrostatic field calculated from equation 3 is neglected. This approximation assumes that the charge density $\rho$ is 0 everywhere at all times and therefore the electrostatic component of the field is 0.

The Vlasov equation is discretized in two dimensions using a "splitting" technique [3]. In this technique the distribution function $f = f(v_{x_i}, v_{z_j}, x_k, z_l)$ is advanced forward in time in a four step process for each species $s$ [3, 5]:

$$\begin{aligned}
f^{n+1/4}_{ijkl} = f^{n}_{ijkl} &- \frac{\Delta t}{2\Delta x}\frac{p_{x_i}}{\gamma_{ij}} \cdot (f^{n}_{k+1} - f^{n}_{k-1})_{ijl} && (9)\\
&+ (\frac{\Delta t}{2\Delta x}\frac{p_{x_i}}{\gamma_{ij}})^2 \cdot (f^{n}_{k+1} - 2f^{n}_{k} + f^{n}_{k-1})_{ijl} &&\\
f^{n+1/2}_{ijkl} = f^{n+1/4}_{ijkl} &- \frac{\Delta t}{2\Delta z}\frac{p_{z_j}}{\gamma_{ij}} \cdot (f^{n+1/4}_{l+1} - f^{n+1/4}_{l-1})_{ijk} && (10)\\
&+ (\frac{\Delta t}{2\Delta z}\frac{p_{z_j}}{\gamma_{ij}})^2 \cdot (f^{n+1/4}_{l+1} - 2f^{n+1/4}_{l} + f^{n+1/4}_{l-1})_{ijk} &&\\
f^{n+3/4}_{ijkl} = f^{n+1/2}_{ijkl} &- \frac{\Delta t}{2\Delta p_x} F_{xjkl} \cdot (f^{n+1/2}_{i+1} - f^{n+1/2}_{i-1})_{jkl} && (11)\\
&+ (\frac{\Delta t}{2\Delta p_x} F_{xjkl})^2 \cdot (f^{n+1/2}_{i+1} - 2f^{n+1/2}_{i} + f^{n+1/2}_{i-1})_{jkl} &&\\
f^{n+1}_{ijkl} = f^{n+3/4}_{ijkl} &- \frac{\Delta t}{2\Delta p_z} F_{zikl} \cdot (f^{n+3/4}_{j+1} - f^{n+3/4}_{j-1})_{ikl} && (12)\\
&+ (\frac{\Delta t}{2\Delta p_z} F_{zikl})^2 \cdot (f^{n+3/4}_{j+1} - 2f^{n+3/4}_{j} + f^{n+3/4}_{j-1})_{ikl} &&
\end{aligned}$$

where

$$F_{xjkl} = q_s(E_{xkl} + \frac{v_{zl}}{c} B_{ykl})^{n+\frac{1}{2}} \tag{13}$$

$$F_{zikl} = q_s(E_{zkl} - \frac{v_{xl}}{c} B_{ykl})^{n+\frac{1}{2}} \tag{14}$$

and

$$E_{x\,kl}^{\,n+\frac{1}{2}} = \frac{1}{2}(E_{x\,l+\frac{1}{2}} + E_{x\,l-l+\frac{1}{2}})_k \tag{15}$$

$$E_{z\,kl}^{\,n+\frac{1}{2}} = \frac{1}{2}(E_{z\,k+\frac{1}{2}} + E_{z\,k-\frac{1}{2}})_l \tag{16}$$

$$B_{y\,kl}^{\,n+\frac{1}{2}} = \frac{1}{2}(B_{y\,kl}^{\,n+1} + B_{y\,kl}^{\,n}) \tag{17}$$

In each step the distribution function is advanced a full time step using only one term at a time in the Vlasov equation. The fractional time indicies for the distribution function $f$ at each step are used for notational purposes only. This discretization scheme is numerically stable when the following conditions are met [3, 5]:

$$\frac{p_x \Delta t}{m \Delta x} < 1 \quad \frac{p_z \Delta t}{m \Delta z} < 1 \tag{18}$$

$$\frac{F_x \Delta t}{\Delta p_x} < 1 \quad \frac{F_z \Delta t}{\Delta p_z} < 1 \tag{19}$$

Maxwell's equations are written in a left handed cartesian system for convenience:

$$\frac{\partial E_x}{\partial t} = c\frac{\partial B_y}{\partial z} - J_x \tag{20}$$

$$\frac{\partial E_z}{\partial t} = -c\frac{\partial B_y}{\partial x} - J_z \tag{21}$$

$$\frac{\partial B_y}{\partial t} = c[\frac{\partial E_x}{\partial z} - \frac{\partial E_z}{\partial x}] \tag{22}$$

These equations are discretized in the following manner:

$$\begin{aligned} E_{x\,k+\frac{1}{2}\,l}^{\,n+\frac{1}{2}} &= E_{x\,k+\frac{1}{2}\,l}^{\,n-\frac{1}{2}} - \Delta t J_{x\,k+\frac{1}{2}l}^{\,n} \\ &+ \frac{c\Delta t}{\Delta z_l}(B_{y\,k+\frac{1}{2}\,l+\frac{1}{2}}^{\,n} - B_{y\,k+\frac{1}{2}\,l-\frac{1}{2}}^{\,n}) \end{aligned} \tag{23}$$

$$\begin{aligned} E_{z\,k\,l+\frac{1}{2}}^{\,n+\frac{1}{2}} &= E_{z\,k\,l+\frac{1}{2}}^{\,n-\frac{1}{2}} - \Delta t J_{z\,k\,l+\frac{1}{2}}^{\,n} \\ &- \frac{c\Delta t}{\Delta x_k}(B_{y\,k+\frac{1}{2}\,l+\frac{1}{2}}^{\,n} - B_{y\,k-\frac{1}{2}\,l+\frac{1}{2}}^{\,n}) \end{aligned} \tag{24}$$

$$\begin{aligned} B_{y\,k+\frac{1}{2}\,l+\frac{1}{2}}^{\,n+1} &= B_{y\,k+\frac{1}{2}\,l+\frac{1}{2}}^{\,n} - \frac{c\Delta t}{\Delta x_k}(E_{z\,k+1\,l+\frac{1}{2}}^{\,n+\frac{1}{2}} - E_{z\,k\,l+\frac{1}{2}}^{\,n+\frac{1}{2}}) \\ &- \frac{c\Delta t}{\Delta z_l}(E_{x\,k+\frac{1}{2}\,l+1}^{\,n+\frac{1}{2}} - E_{x\,k+\frac{1}{2}\,l}^{\,n+\frac{1}{2}}) \end{aligned} \tag{25}$$

The currents $J_x$ and $J_z$ are calculated from:

$$J_{x\,kl}^{\,n} = \sum_s q_s \sum_i \sum_j A_{ij} f_{sijkl}^{\,n} (\frac{p_{x_i}}{m_0 \gamma_{ij}}) \Delta v_x \Delta v_z \tag{26}$$

$$J_{z\,kl}^{\,n} = \sum_s q_s \sum_i \sum_j A_{ij} f_{sijkl}^{\,n} (\frac{p_{z_j}}{m_0 \gamma_{ij}}) \Delta v_x \Delta v_z \tag{27}$$

where $A_{ij}$ is a normalization constant, and then

$$J_{x\,k+\frac{1}{2}\,l}^{\,n} = \frac{1}{2}(J_{x\,k+1\,l}^{\,n} + J_{x\,k\,l}^{\,n}) \tag{28}$$

$$J_{z\,k\,l+\frac{1}{2}}^{\,n} = \frac{1}{2}(J_{z\,k\,l+1}^{\,n} + J_{z\,k\,l}^{\,n}) \tag{29}$$

A similar set of finite difference equations for the Vlasov equation and Maxwell's equations can be written in cylindrical coordinates.

## 2.1 Boundary Conditions

The boundary conditions used are dependent on whether cartesian or cylindrical coordinates are used for the test problem.

In both geometries the boundary conditions are periodic in the $z$ direction. That is, all the field quantities, currents, and distribution function values are periodic beyond the simulation boundaries in $z$. In the case of cartesian coordinates periodic boundary conditions are employed in the two spatial directions $(x, z)$. Also the distribution functions are 0 beyond the momentum coordinate boundaries $(p_x, p_z)$ for the cartesian case and $(p_r, p_z)$ for the cylindrical case.

In the case of cylindrical coordinates conducting wall boundary conditions are employed at $r = R$ where $R$ is the maximum radius of the domain. For conducting wall boundary conditions all field quantites, currents, and distribution function values are equal to 0. Handling the field, currents and distribution function at $r = 0$ is a little trickier. The field quantity which needs special care is the $E_{z\,1\,l+\frac{1}{2}}$ field component. It's calculation requires the knowledge of $B_{\theta\,\frac{1}{2}\,l+1}$ for $r = 0$. By symmetry arguments the field $B_{\theta\,\frac{1}{2}\,l+1}$ can be said to be equal to $-B_{\theta\,\frac{3}{2}\,l+1}$ so the time advance equation becomes:

$$E_{z\,1\,l+\frac{1}{2}}^{\,n+\frac{1}{2}} = E_{z\,1\,l+\frac{1}{2}}^{\,n-\frac{1}{2}} - \Delta t J_{z\,1\,l+\frac{1}{2}}^{\,n} - 2\frac{c\Delta t}{\Delta r_1}(B_{\theta\,\frac{3}{2}\,l+\frac{1}{2}}^{\,n}) \tag{30}$$

All other field quantities can be calculated once this field component is determined. The distribution function $f_{ijkl}$ at the $r = 0$ boundary is calculated using the symmetry argument also. In this case $f_{ij2l}$ is chosen equal to $f_{ij0l}$ due to the fact that the distribution function is symmetric about $r = 0$. The time advance equation becomes:

$$f_{ij1l}^{n+1/4} = f_{ij1l}^{n} \quad + \quad (\frac{\Delta t}{2\Delta x}\frac{p_{xi}}{\gamma_{ij}})^2 \cdot 2(f_2^n - f_1^n)_{ijl} \tag{31}$$

# 3 Parallel Implementation

In this section the specific hypercube implementations of the set of finite difference equations from the previous section are described.

## 3.1 Slab Decomposition

The first implementation of the code on the hypercube involves decomposing the spatial grid of the simulation into slabs. Each slab is assigned to one node. Each node communicates with two other nodes. The advantage of this method is that communication is either north and south or east and west depending on how the slab is oriented. In the current implementation the communication occurrs in the north and south directions. The slabs extend across the entire simulation grid length either in $x$ or $r$ depending on the geometry used. Decomposition of the simulation grid is along the $z$ direction for either geometry. This is shown in figure 1.

The grid is decomposed in the following manner. First the number of nodes $nd$ is determined. To determine the number of cells in the $z$ direction per node:

$$nc_z = n_z/nd \tag{32}$$

where $n_z$ is the size of the total grid in the $z$ direction respectively and $nc_z$ is the number of grid cells in the the $z$ direction for each node. To determine north and south nodes the node numbers are calculated in the following manner:

$$North = menod + 1 \tag{33}$$

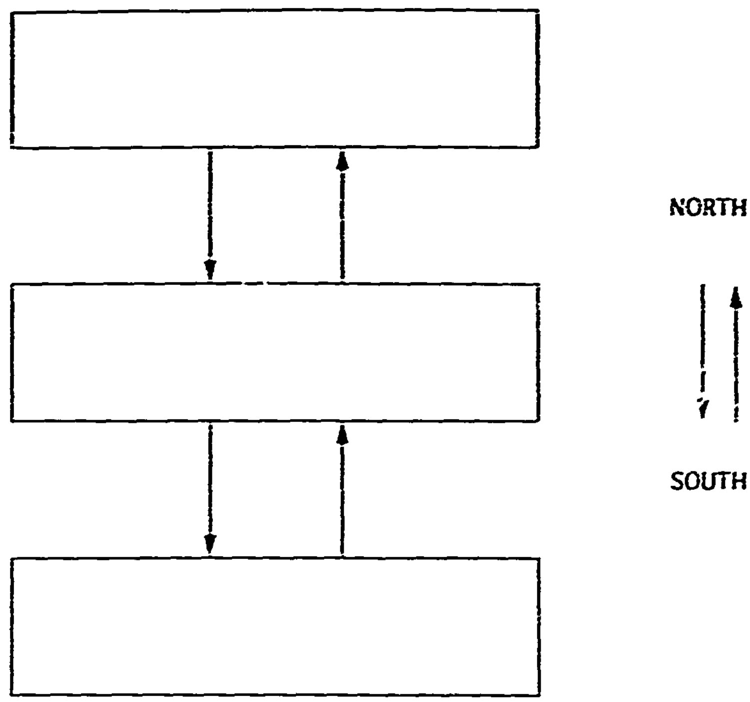


Figure 1: This figure shows the communication path for north and south communication in the slab geometry.

$$South = menod - 1 \tag{34}$$

where $menod$ is the node number of the specific node and $North$ and $South$, are the node numbers of the north and south nodes respectively. This implemation is chosen because of its simplicity and the speed of communication between i860 nodes. Grey coding to find the nearest physical nodes made little difference in the speed of the code.

The types of quantities which are transferred are fields, currents, and distribution functions. They are needed to update the boundary cells of each slab block assigned to each node. This is done at every time step. The quantity which requires the most amount of data transfer is the distribution function. Although only boundary cells need to be transferred, each boundary cell for the distribution function contains a real numbers where:

$$n = n_{p_x} \cdot n_{p_z} \cdot n_s \tag{35}$$

where $n_{p_x}$ and $n_{p_z}$ are the number of grid cells in the $p_x$ and $p_z$ momentum coordinates respectively, and $n_s$ is the number of species. In the slab decomposition the distribution function needs to be transferred once per time step. Although the "time splitting" scheme [3] used requires updates to the distribution function in four stages for two dimensional problems, updated boundary cell distribution function values are only needed at the $z$ boundaries.

Data transfer between the nodes is carried out asynchronously. This is to done to overlap communication with computation.

Boundary conditions in $x$ or $r$ depending on the geometry are handled in each slab block as described in section 2.1. Boundary conditions in the $z$ direction are handled in the transfer of data between neighboring slabs. The top and bottom slab boundary conditions are handled by noting that in both the cartesian and cylindrical geometries the boundary conditions are periodic in $z$. Therefore, the top and bottom slabs only need to transfer data in a wrap around fashion. The disadvantage of this implementation is the amount of communication is not optimized for this type of geometry. This will be described in section 4.

### 3.2 Square Geometry

The second implementation of the code involved decomposing the spatial grid of the simulation into square blocks and assigning one node to each block. Each node communicates with four other nodes as shown in figure 2. As opposed to the slab geometry communication must occur in four directions $(North, South, East, and West)$.

The grid is decomposed in the following manner. First the number of nodes is

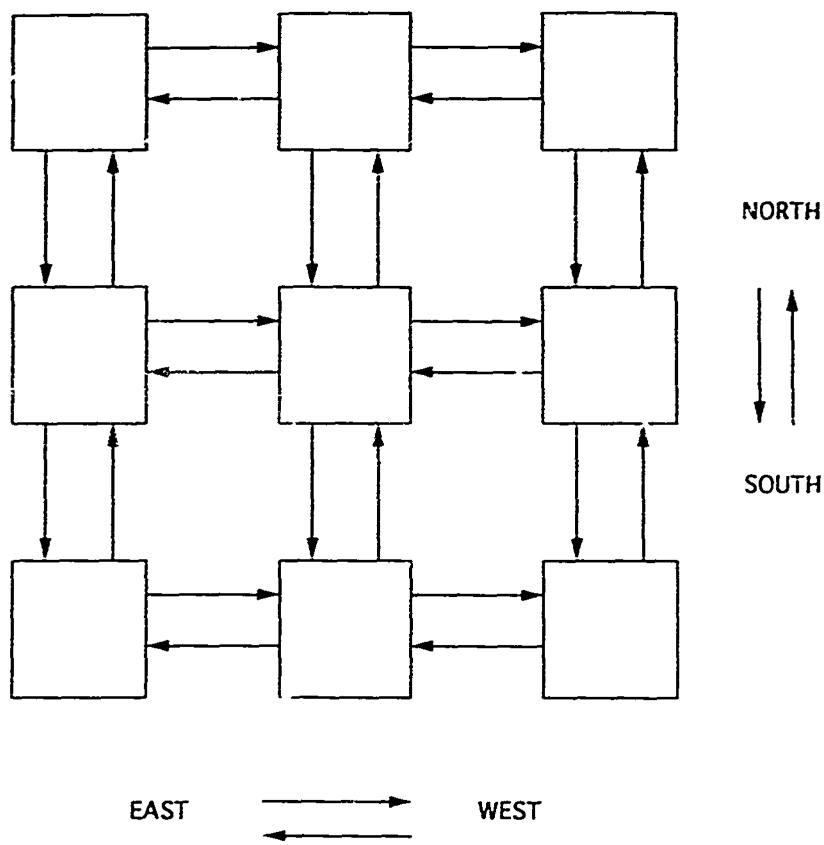


Figure 2: This figure shows the communication path for north, south, east, and west communication in the square geometry.

determined in the program. To determine the number of cells in the $x$ direction and the $z$ direction in cartesian coordinates the dimension of the nodes used is used. The dimension $n$ is defined as $nodes = 2^n$ where $nodes$ is the number of nodes used. The number of blocks in the respective directions is determined from:

$$r = n_x/(n_x + n_z) \tag{36}$$

$$nb_x = 2^{n \times r} \tag{37}$$

$$nb_z = 2^{n - n \times r} \tag{38}$$

where $n_x$ and $n_z$ are the size of the total grid in the $x$ and $z$ directions respectively and $nb_x$ and $nb_z$ are the number of blocks in the $x$ and $z$ directions respectively. The number of cells per node is determined from :

$$nxm = n_x/nb_x \tag{39}$$

$$nzm = n_z/nb_z \tag{40}$$

To determine north,south,east, and west nodes the node numbers are calculated in the following manner:

$$ix = menod/nb_z + 1 \tag{41}$$

$$iz = (menod + 1) - (ix - 1) * nb_z \tag{42}$$

$$izp = iz + 1 \tag{43}$$

$$izm = iz - 1 \tag{44}$$

$$ixp = ix + 1 \tag{45}$$

$$ixm = ix - 1 \tag{46}$$

$$North = (ix - 1) * nb_z + izp - 1 \tag{47}$$

$$South = (ix - 1) * nb_z + izm - 1 \tag{48}$$

$$East = (ixp - 1) * nb_z + iz - 1 \tag{49}$$

$$West = (ixm - 1) * nb_z + iz - 1 \tag{50}$$

where *menod* is the node number of the specific node and *North*,*South*, *East*, and *West* are the node numbers of the north, south, east, and west nodes respectively.

As in the case of the slab decomposition, the types of quantities which are transfered are fields, currents, and distribution functions. They are needed to update the boundary cells of each square block assigned to each node. This is done at every time step. As in the slab geometry case the dominant data transfer is done with the distribution function. It is more complex in this case since the boundaries need to be updated at both the $x$ and $z$ boundaries in cartesian coordinates or the $r$ and $z$ boundaries in cylindrical coordinates. So in the square decomposition scheme the distribution function needs to be transferred twice.

Boundary conditions are handled in the transfer of the data to the respective boundary cells. In the case of cartesian coordinates periodic boundary conditions are imposed on all quantities. Blocks at either end of the grid transfer data in a wrap around fashion. Blocks at the west end transfer data to the east blocks and blocks at the east end transfer to blocks at the west end. A similar situation occurs for blocks at the north and south ends. In the case of cylindrical coordinates the north and south block data are handled in the same manner since the boundary conditions are periodic in this direction. Blocks at the east end have all quantities at their eastern boundaries set equal to 0. This is to handle the conducting wall boundary conditions there. The western blocks are at the $r = 0$ boundary. The west end of these blocks handle the fields, distribution function, and currents as descibed in section 2.1.

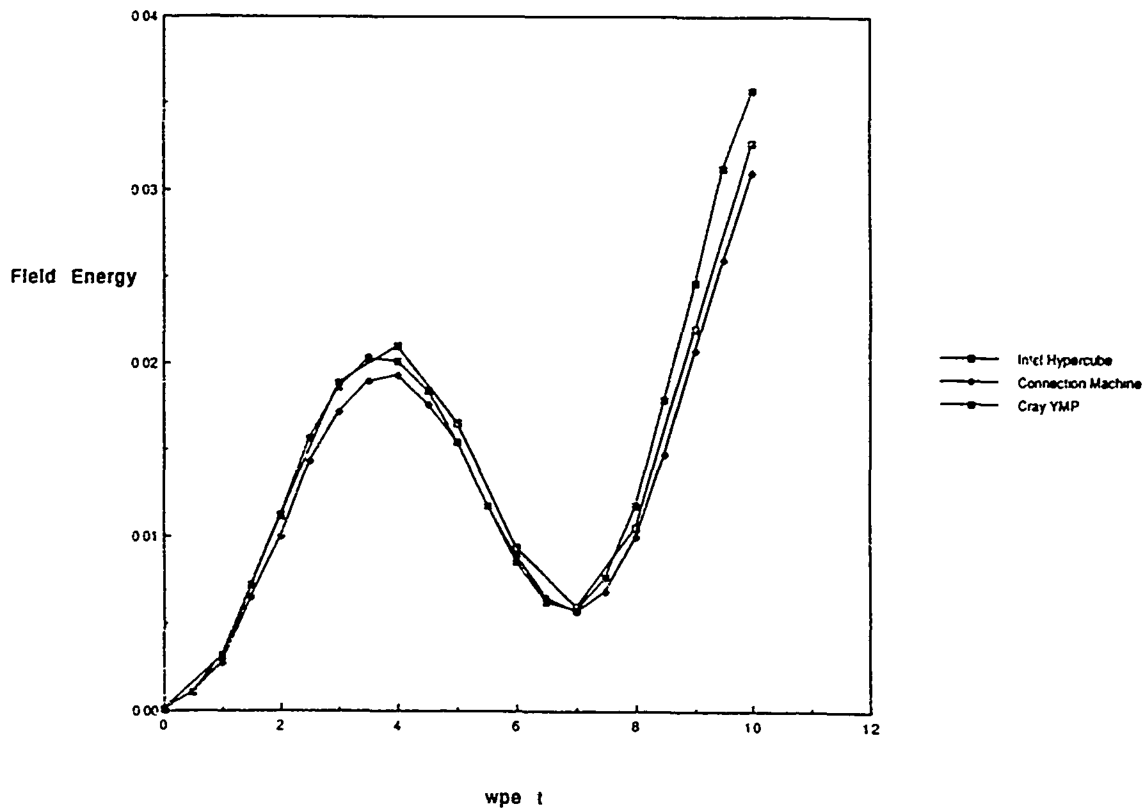


Figure 3: This figure shows a comparison between the intel hypercube, the connection machine and the Cray YMP on a test problem. The growth in field energy as a function of time ($\omega_{pe}t$) is shown.

# 4 Results

To test the code a problem involving two couterstreaming electron beams is run. The beams are unstable to the two stream instabity which has a well known maximum growth rate [6]. The code is timed for various problem sizes and performance is compared with the Cray YMP. The results presented here are only for the cartesian geometry case.

## 4.1 Two Stream Instability

Figure 3 shows the growth in the field energy as a function of time in units of plasma frequency. The field energies are plotted for the three machines on which the problem was run (Intel i860, , a Connection Machine, and a Cray YMP). Note that the results agree very well over the length of the run. The slight differences can be attributed to the differences in precision and random number generators used for the initialization of the fields. The maximum growth rate for the two stream instability is:

$$\gamma_{max} = \frac{\omega_{pe}}{\sqrt{8}} \tag{51}$$

This predicts a maximum growth time of 400 simulation timesteps. It is evident that the first maximum in the field energy measured in the simulation closely corresponds to that of the two-stream instability [5, 6].

The integrated distributions functions of one of the beams at various time steps are shown in figures 4 and 5. The other beam evolves in a similar manner.

Note that the $z - p_z$ distribution function becomes negative (figure 4). This is an inherent problem with Vlasov simulation techniques. Since only two points are chosen to represent the distribution function of the two beams in $p_z$ space, truncation errors result which cause the distribution function to become negative. A solution to this problem may be in higher resolution in $p_z$ which translates into a larger number of grid cells and more memory. Another approach may be to use transform methods in the momentum directions [1]. This is something which still needs to be resolved.

The evolution of the $x - z$ distribution function is shown in figure 5. The beam starts out as a finite width beam in $x$ with an initial small perturbation in $z$ ( the oscillations can be seen along the beam at the top ). As the beam evolves it begins to spread in $x$. By the end of a 1000 timestep run the beam has spread to the point where the multiple beams are beginning to overlap due to the periodic boundary conditions. By the end of the run the results are no longer valid for a single beam since overlap has occurred. Results before this point are valid.

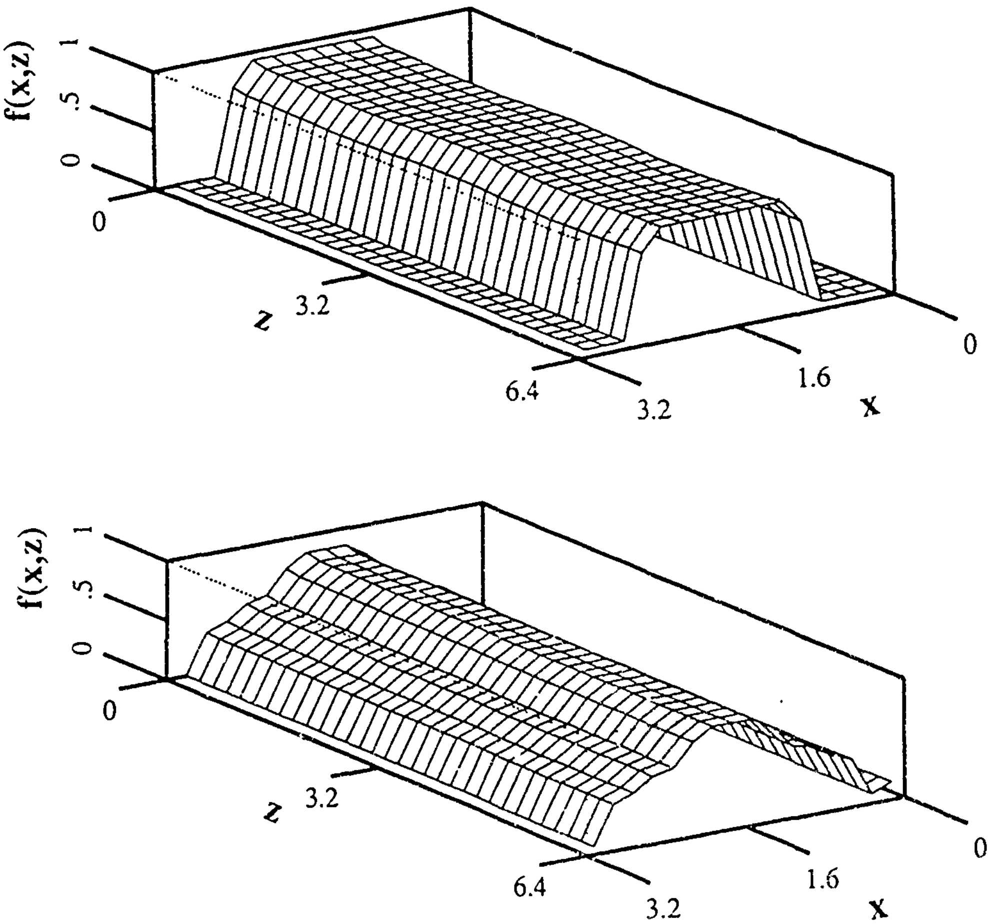


Figure 4: The integrated distribution function $f(z, p_z)$ at 0 and 400 timesteps from the top to the bottom

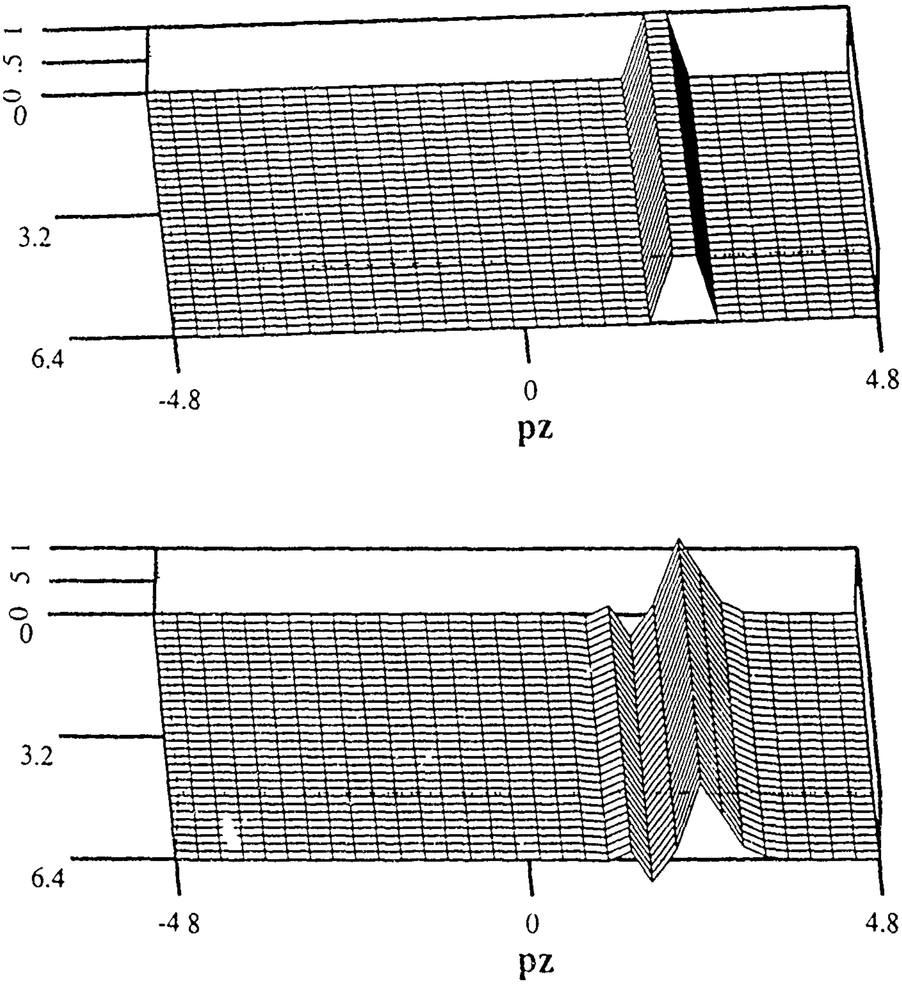


Figure 5: The integratea distribution function $f(x, z)$ at 0 and 400 timesteps from the top to the bottom

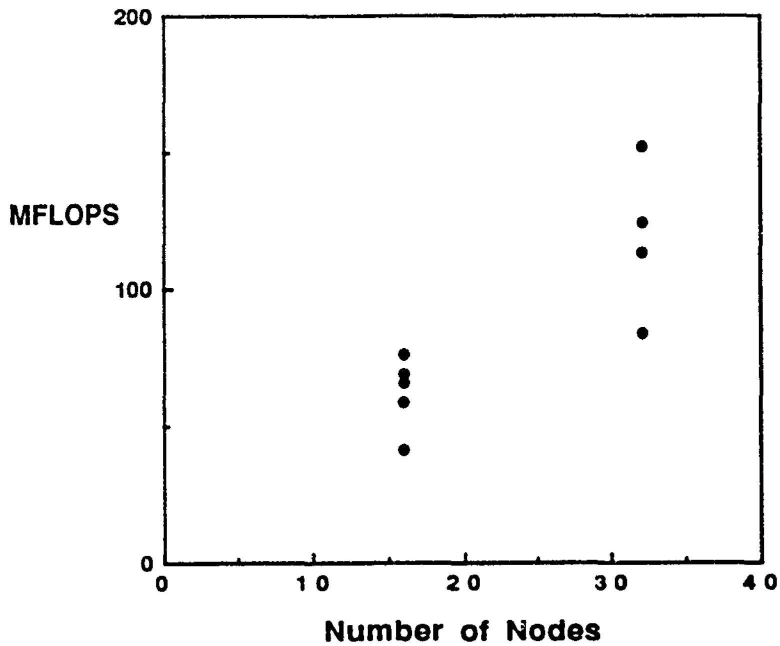


Figure 6: This figure shows the number of MFLOPS versus nodes

### 4.2 Speed

Figure 6 shows MFLOPS (million floating point operations per second) of the code for various size problems run on the Intel i860. Both the slab and square implementation were run in a few cases. Most of the cases are done in the square geometry. It is evident that the speed of the code is not linearly dependent on the number of nodes based on the scatter of the data points. The maximum speed is approximately 152 MFLOPS for 32 nodes. The efficiency of the code is dependent on the ratio of the number of floating point operations per node to the number of transfers per node (figure 7). The figure indicates a nearly linear dependence. It is obvious that reduction in communication increases efficiency. In the extreme case of no communication the number of MFLOPS would be linearly dependent on the number of nodes. This is assuming exclusion of speedup due to vectorization which would depend on problem

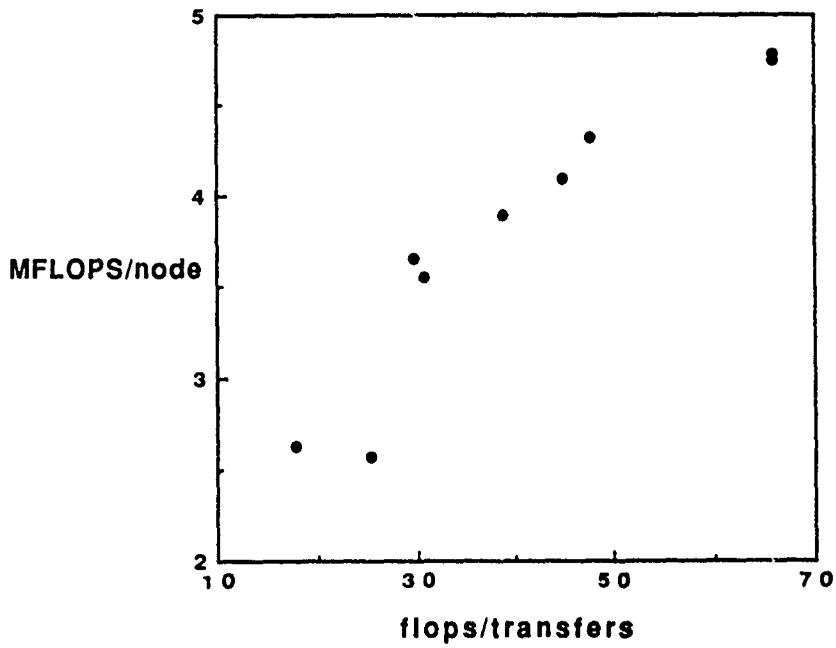


Figure 7: This figure shows the number of MFLOPS per node versus the ratio of the number of floating point operations to the number of data transfers per node

sizes. The amount of communication per node can be minimized by considering the shape of the region computed for each node. Two quantities which give an indication of the shape are the perimeter of the region which is $2(nc_x + nc_z)$ and the area of the region which is $nc_x \cdot nc_z$ where $nc_x$ and $nc_z$ are the number of cells per node in the $x$ and $z$ direction respectively. The ratio of the perimeter to the area of the region is in proportion to the amount of communication per computation for each node. The ratio can be represented by the formula:

$$\frac{p}{a} = \left(\frac{2(r+1)}{\sqrt{r}}\right)\frac{1}{\sqrt{N}} \tag{52}$$

where

$$r = \frac{nc_x}{nc_z} \tag{53}$$

$$N = nc_x \cdot nc_z. \tag{54}$$

Minimizing $p/a$ reduces the amount of communication per computation for each node. The smallest value is achieved by chosing $r = 1$ for a fixed number of cells per node $N$. At this point it can be seen why the slab geometry is not optimal for communication. Although the slab geometry needs only two directions of communication, the ratio $r$ is generally far from 1. Also as the number of nodes is increased the ratio $r$ increases. Equation 52 also shows that the larger the total problem size the larger $N$ is for a fixed number of nodes. So efficiency is also enhanced when the problem size is large. The problems with the highest efficiency or MFLOPS per node are the problems with the largest number of grid points per node.

As a comparison for outright speed a serial version of the code was also run on the Cray YMP at NASA Ames. No effort was made to optimize the code for vectorization. Tests are performed on the code with 32 nodes on the Ames hypercube. The speed was 2.3 times faster than the Cray YMP for the largest problems run. Although this may not be a fair test, it does give rough idea of the size of the parallel machine necessary to achieve speeds comparable to a Cray YMP. Obviously a more rigorous test needs to be performed where both codes are optimized for each specific machine.

## 5 Conclusions

It is found that the Vlasov-Maxwell system of equations does lend itself to parallelization on MIMD machines. The decomposition of the domain of the problem is static and the load is balanced among the processors. This is in contrast to PIC implementations where the decomposition can be dynamic and the load is not balanced. As with any implementation of the Vlasov technique memory requirements are high. MIMD machines aid in this area. For fixed problem sizes the amount of memory needed per processor decreases with the increase in the number of processors. A two stream instability test problem running on three different machines shows close agreement between the codes. It is found that the 32-processor Intel hypercube can achieve speeds faster than the Cray YMP for unoptimized codes.

However, to achieve high effiecieny some care must be taken in the decomposition of the the domain and in the time advance algorithm. The shape of the region determines the relation between the amount of communication between nodes and the amount of floating point operations performed on each node. This communication can be minimized by chosing square regions for each node.

There are a few improvements which can be made. Obviously the codes need to be optimized for both the hypercube and the Cray YMP to obtain an accurate comparison between the machines. One way to increase the speed of the code would be to take more advantage of the vectorization and pipelining capabilities of both machines. Another improvement in the speed of the hypercube version of the code would be reduction in the amount of communication which is occuring between the nodes. Due to the lack of time transfer of the distribution function $f$ was not fully optimized. Also there is the problem with the distribution function going negative after a few hundred timesteps. A solution may be to increase the resolution of the velocity distribution or going to some type of transform method [1].

## References


[1] Armstrong, T. P., Harding, R. C., Knorr, G., and Montgomery, D., "Solution of Vlasov's Equation by Transform Methods" in "Methods in Computational Physics", Volume 9, B. Alder, ed.(Acedemic Press, 1970), p. 29.

[2] Birdsall, C. K., and Langdon, A. B., "Plasma Physics via Computer Simulation", (McGraw-Hill, 1985).

[3] Byers, J. A., and Killeen, J., "Collisionless Plasma Models" in "Methods in Computational Physics", Volume 9, B. Alder, ed.(Acedemic Press, 1970), p. 259.

[4] Campbell, P. M., and von Laven, S. A., "Vlasov Maxwell Alogorithm for Electromagnetic Plasma Simulation on Distributed Architectures", submitted to "Fourteenth International Conference on the Numerical Simulation of Plasmas", September 3-6, 1991.

[5] Campbell, P. M., private communication

[6] Krall, N. A., and Trivelpiece, A. W., "Principles of Plasma Physics", (McGraw-Hill, 1973), p. 457.

## ABSTRACT

# TROUBLESHOOTING THE SPECTRA PHYSICS 5800 TUNABLE DIODE LASER

by

John E. McCord
1991 RDL Graduate Summer Fellow

A Spectra Physics 5800 series high-resolution tunable lead-salt diode laser was reassembled and checked for proper operation as part of the introductory work for a planned transient study of NO ro-vibrational transfer with bromine radical. During this procedure, several technical problems and equipment failures were discoverd on the laser system. The details of these problems and recommended steps for bringing the diode laser back to factory specifications are presented in this report.

## TROUBLESHOOTING THE SPECTRA PHYSICS 5800 TUNABLE DIODE LASER

by
John McCord
RDL Graduate Summer Fellow

### I. INTRODUCTION:

Tunable diode laser high-resolution infrared spectroscopy provides information necessary for fundamental studies of the molecular transitions involved in the absorption of gases. In 1988, a Spectra Physics 5800 series tunable lead-salt diode laser was assembled and calibrated at the Phillips Lab's Chemical Laser Facility as part of the introductory work for a transient study of SO ro-vibrational energy transfer. The high-resolution diode laser was calibrated with $SO_2$ and $NH_3$ gases, and the first diode laser line positions were observed for sulfur dioxide in the 1075 to 1160 $cm^{-1}$ region. Further information on this work can be found in the 1988 UES final report by Dr. David A. Dolson (UES Faculty Fellow, 1988).

Presently, the Chemical Laser Facility is interested in a transient study of the ro-vibrational energy transfer from Br* to NO gas. The energy transfer from bromine radical to NO induces a population inversion in the nitrous oxide energy levels and thus generates a gas phase chemical laser. An important precursor to this study would be the recording of high-resolution absorption spectra for NO in the 5.3 micron region. The mapping out of the NO ro-vibrational lines in this region would be useful in future NO kinetic studies.

Since 1988, though, the diode laser itself had been disassembled and moved into various laboratories at the laser facility. Therefore, my first objective as a 1991 RDL Summer Fellow was to reassemble the diode laser into my lab area in building 625. My second objective for the research effort was to check the operation of the diode laser by reproducing ammonia reference spectra that had been recorded in previous 1988 diode work. My third goal for the summer was to record the high-resolution NO absorption spectra for use in further NO transient studies.

## II. PROBLEM DISCUSSION

After a few weeks of gathering parts and accesories, the 5800 diode laser was assembled and ready for computer-controlled data acquisition. Laser diodes in diode cold-head ports 1 and 3 were used to record ammonia spectra in the 1160 to 1090 $cm^{-1}$ region. Since I was working on a limited time scale, and since these lines are well-documented in previous summer efforts by Dolson and Nickels, I was not concerned with the quality of these spectral scans. Thus, these scans are not as resolved as the earlier scans due to pressure broadening. Also, a ground-loop problem resulted in some of the ammonia scans having a slight sinusoidal appearance. One of the better reperesentative ammonia absorption line and etalon scans is included in this report (Figures 1a and 1b).

At this point, I began to work towards the recording of quality, resolved NO absorption spectra and passive etalon scans in the 5.3 micron region (a known pressure of NO would be used in the reference cell to provide better resolution, and time would be taken to address the ground-loop problem). A cylinder of NO gas was found and a laser diode operating in the 1910 to 1925 $cm^{-1}$ region was borrowed from McDonnell-Douglas corporation in St. Louis, MO.

Installation of the new diode into port 4 of the diode cold-head was performed, but no apparent laser emision from the new diode could be detected (detection of laser output from a diode is a relatively minor procedure). After re-installing the dic 'nto port 1 (a "tried and true" position), lasing from the diode was still not seen by the system's cold-head detector. An indium-arsenide ir detector was then placed directly in front of port 1, and again there was no sign of infrared emission from the diode. A test outlined in the cold-head manual for detection of diode lasing based on the output of the diode cold-heat heating element was then performed on the NO diode. The diode also failed this diagnostic. As a result of these efforts, I concluded the 1900 $cm^{-1}$ diode did not work, and I returned it to Spectra Physics for final testing.

Not having a 5.3 micron diode, and not being able to get one in before my summer research period was over, did put a premature end to my NO absorption work. The moving around and disassembly of the 5800 series diode laser system, though, has left it in a condition far from being up to factory specifications. Since the alignment, operation, equipment interconnecion, and computer-controlled data acquisition procedures are well documented in previous reports by Mary Nickels (1989 UES Graduate Summer Fellow) and by this author (1988 UES Graduate Summer Fellow), I feel it is very important to document other existing equipment and technical problems that it will be important to correct before further experimental usage of the diode laser system.

As of my departure from the Chemical Lasers Facility, the main "showstopper" for the system was the fact that the three channel preamplifier had completely stopped working. Its correct operation had been intermittant before that. The output signals from the preamp were electrically "noisy" on a day-to-day basis, with the output commonly appearing sinusoidal in nature (its output intensity varied over time, but it was not 60 Hz cycling). This varying output was especially problematic when bringing the preamp outputs into the lock-in amplifiers, as the variance made it impossible to choose the best possible sensitivy setting on the lock-in. Without an operational preamplifier for the detector outputs, it will be virtually impossible to view absorption lines or etalon fringes on an oscilloscope.

As for the detector cold-head, the detector element in port 2 never gave any output to the scope using any of the three amplifier channels. The fact that this detector did not work was later confirmed by checking its output line with a pico-ammeter. The operation of the thermocouple guage attached to the detector cold-head is also suspect since it never gave an output reading below 25 mtorr; even though the diffusion pump used to evacuate the cold head would show pressures between $10^{-6}$ and $10^{-8}$ mtorr. Also, the maximum detector cold-head refrigeration temperature was between 20 and 25 K, although temperatures below 10 K should be possible. Mary Nickels, in her 1989 summer report, discusses a similar problem and mentions that the detector was sent back to Spectra Physics for repair (and that the compressor for this cold-head was rebuilt). I would conclude that there are still problems with the detector cold-head refrigeration system.

The diode cold-head also has a problem in that it leaks in a signifigant amount of atmosphere over the time-span of several days. I believe this leak exists either at the o-ring seal around the removable end-plate or at the vacuum valve used when pumping out the cold-head. This leak over time eventually causes problems when trying to operate a particular diode at a higher temperature (i.e. above 60 K). As the diode cold-head temperature is increased, the outgassing of the condensed atmospheric molecules leads to a conduction effect inside the cooling jacket, which in turn leads to a condesation occuring on the outside of the laser emission window. This makes the detection of the diode lasing almost impossible.

The compressor for the diode cold-head leaks helium at a very signifigant rate. To maintain the maximum refrigeration temperature on the diode cold-head (below 10 K), it is reccomended that the helium pressure in the compressor be kept between 250 and 260 psi. To do this would require recharging the compressor at least once a week, a procedure that normally should only be necessary ever 2 to 3 months.

Also of interest is the fact that I never detected any laser emission from the diodes originally in ports 2 and 4 (serial numbers 8123-12 and 8123-18 respectively). It is now known that port 4 is a functional port, and therefore I have to question the integrity of the diodes themselves. It is my understanding that being shipped non-operational diodes directly from the company is not that uncommon.

III. RESULTS

Figure 1a represents the diode laser absorption scan for ammonia line 11, page 167, in the Handbook of Infrared Standards by Rao. In this book, the line appears as a single, broad absorption feature. The diode scan resolves this feature into three absorption lines, and better resolution would be possible if these lines were not pressure broadened due to an excess of ammonia in the reference cell. (The narrowline diode laser from an average diode has a spectral resolution of $3 \times 10^{-4}$ $cm^{-1}$). I also reproduced several of the other ammonia reference line scans previously recorded by this author and Dr. David A. Dolson in 1988.

I must stress that I was concerned only in reproducing similar features to the previous work and not with matching or improving the quality of the existing scans. The reproductions were only meant as a diagnostic to determine if the diode laser was current and temperature scanning properly; if the passive etalon still generated fringes (Figure 1b); and if the monochromator drum was still reasonably calibrated.

The parameters from the existing scans did lead directly to reasonable reproductions of the previously recorded ammonia absorption features. So despite the existing technical problems with the equipment, up until the point that the preamplifier quit working, the diode laser system could have been used to record NO absorption lines around 5.3 micron.

IV. CONCLUSIONS AND RECOMMENDATIONS

At this point, I would recommend buying a new three channel preamplifier and a detector element for detector cold-head port two. The system could be used to record preliminary absorption spectrum at this time. At present, a 5.3 micron diode is on order from Spectra Physics for the planned NO work.

I also agree with the plan to have a factory representative from Spectra Physics check out the problems with the diode system that I have outlined here and in other writings at the laser facility. As stated, the system could be used if a new preamp is obtained, but I feel it would be worth the time and money to bring the system and equipment up to factory specifications. Quality spectra can be recorded with this device, as proven by the Dolson/McCord data notebook already in existence at the facility.

In the interim before the factory representative arrives, I suggest that the diode cold-head evacuation procedures I outlined before my departure be performed on a regular basis. I would also suggest that the

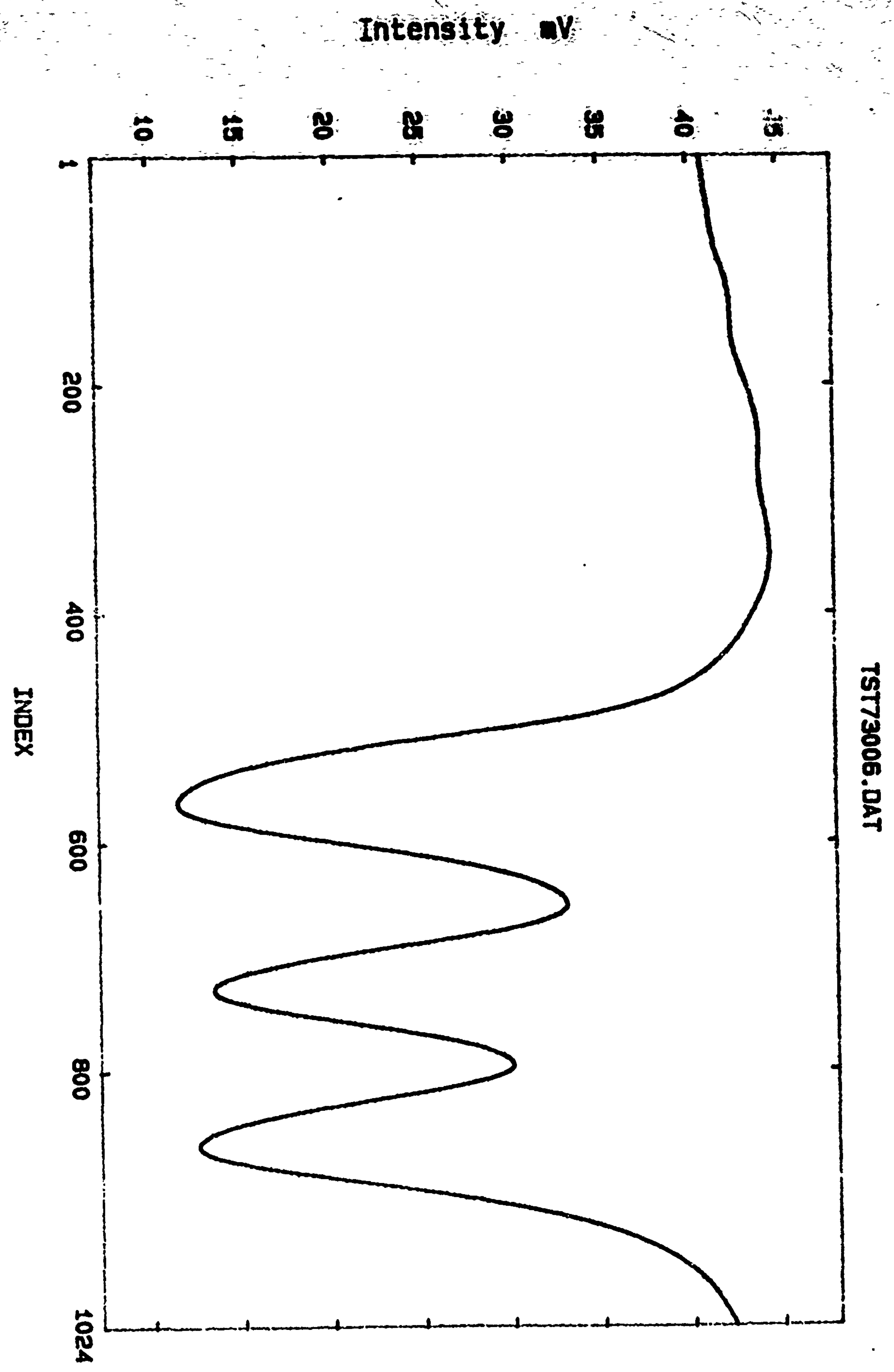


Figure 1a: Ammonia Absorption Line 11, Page 167, Rao.

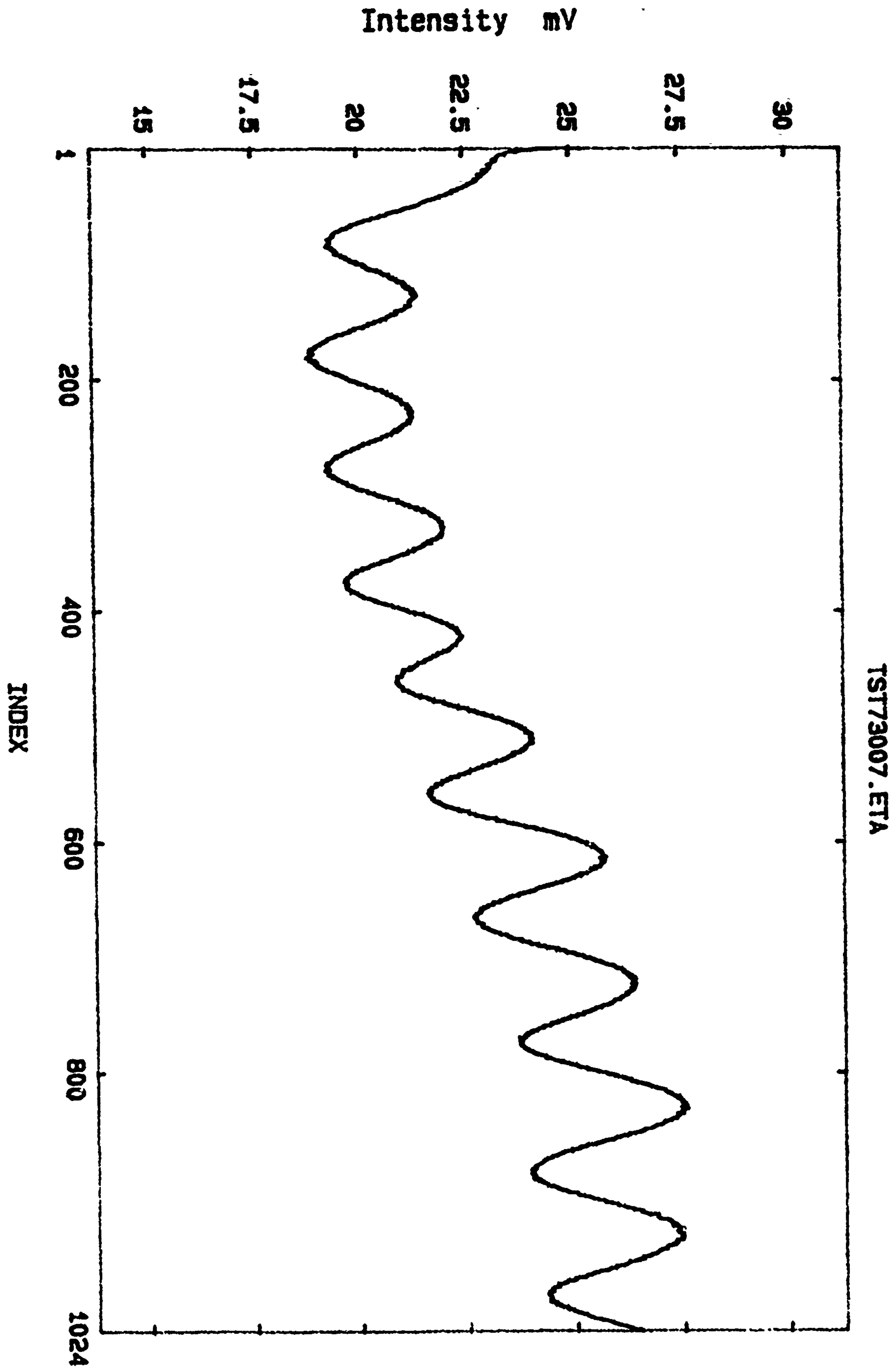


Figure 1b: Representative Etalon Scan

diode cold-head compressor be recharged with helium on a bi-weekly basis. At some point, it might also be a good idea to find a functional helium leak detector and to check the diode cold-head for the aforementioned leak. Adhering to a regular maintenance schedule for the equipment and keeping the system stationary should allow for continued nominal operation until a plan (and a price!) for complete technical repair can be established.

Summer Research Activity
June 3, 1991 through August 9, 1991

Scott M. Peterson

Graduate Student, EECE Department
University of New Mexico

August 19, 1991

# 1.0 Introduction

The purpose of this report is to outline research conducted during the 1991 AFOSR Summer Research Program by Scott Peterson (associate number 434) at the LMI branch of the Phillips laboratory Kirtland AFB, New Mexico. During the course of this effort, Mr. Peterson was under the direction of Capt. Micheal Roggemann, Phillips Laboratory and Dr. Mohammed Jamshidi, professor of Electrical and Computer Engineering at the University of New Mexico.

The goal of the research activity was to formulate an understanding and investigate the problem of implementing a closed loop adaptive optics system using the phase reconstruction law known as minimum variance. The type of system that was considered is a general adaptive optics system consisting of a Hartmann type wavefront sensor and a continuous plate deformable mirror. The optical wavefront is propagated through the wavefront sensor where phase differences in the form of wavefront slopes across the telescope aperture are measured. These values are input to the minimum variance reconstructor matrix and the output of the reconstructor is a set of deformable mirror actuator commands that apply a conjugate phase correction to the wavefront.

Minimum variance is obtained by minimizing the mean-square residual phase error between the measured and actual wavefront. In this manner the reconstructor takes into account the correlation between atmospheric phase statistics and slope measurements from the wavefront sensor. The desired result is to design a deformable mirror controller using minimum variance reconstruction which is stable and highly responsive. Since there has been no previous work in which minimum variance has been applied to a closed loop system, it is hoped that this research and subsequent efforts can serve as the basis for a masters degree thesis and a technical article.

The first four weeks of this effort were used to investigate the dynamics and stability characteristics of a generic adaptive optics system under a closed loop (feedback) configuration and integrate a model of the dynamical system into an existing computer simulation. The results of this preliminary investigation and computer models are outlined in section 2.1. Three weeks were spent in an attempt to adapt the theoretical derivation of the minimum variance control law to the closed-loop configuration. The difficulties and restrictions encountered in this attempt are given in section 2.2. Further consideration indicated the need for a more detailed second order model which would account for interactuator coupling in the temporal response of the deformable mirror. Two weeks were used to develop the differential equations for the mirror dynamics, state space equation formulation and computer simulation of a decoupled second order system and the effort is outlined in section 2.3. The last week of the summer research effort was used to consider the effects of noise and model uncertainty on closed loop stability and is discussed in section 2.4.

# 2.0 Research Activity

## 2.1 Deformable Mirror Dynamics

The first step in examining the problem of applying closed loop control to an adaptive optics system is to gain an understanding of the system's mechanical and temporal dynamics. Initially we assume wavefront sensor measurements are represented by pure gain (assumed to be unity) and a time delay.

The preliminary block diagram for a simple closed loop adaptive optics system is shown in figure 2.1.1. Here $\phi(\bar{x},t)$ is the incoming wavefront containing optical aberrations due to atmospheric turbulence, $\mu(\bar{x},t)$ is the wavefront corrections applied by the deformable mirror and $\varepsilon(\bar{x},t)$ is the resulting corrected wavefront.

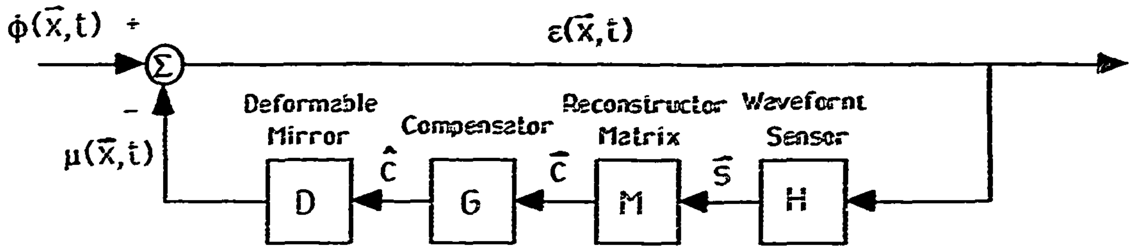


Figure 2.1.1
Closed Loop Adaptive Optics System

Wavefront phase slopes, $\bar{s}$, are measured by the wavefront sensor and are input to the minimum variance reconstructor, M, which generates deformable mirror actuator commands, c. These commands are propagated through a compensator, G, such that the resulting compensated actuator commands, $\hat{c}$, position the mirror in a manner consistent with desired system operational characteristics. This block configuration, however is not in canonical form when the deformable mirror actuator displacements are used as the controllable states. This implies the addition of a higher frequency inner loop containing the deformable mirror (DM loop) as shown in figure 2.1.2.

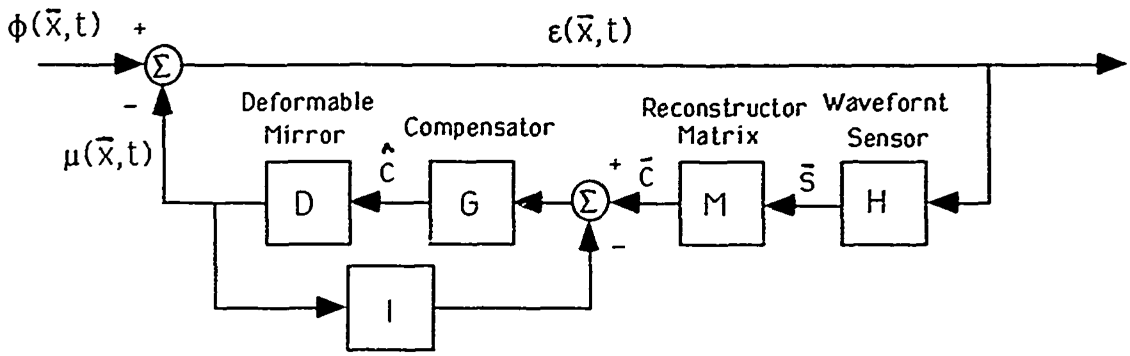


Figure 2.1.2
Closed Loop System With Added Loop for Actuator Position Feedback

Since the displacement states are not readily available, state estimation was briefly considered and a state estimator was designed. It was determined however, that the displacement states could be directly measured at the deformable mirror using an interferometer.

Previous analysis has treated deformable mirror dynamics as a completely decoupled, first order model. Thus the relationship between the ith actuator response and its generated input command is given by the first order differential equation

$$\dot{x}_i(t) = -\frac{1}{\tau_i} x_i(t) + \frac{1}{\tau_i} c_i(t) \tag{1}$$

where $x_i(t)$ is the linear displacement of the $i^{th}$ actuator as a function of time, $\tau_i$ is the actuator time constant, k is a proportional input gain and $c_i(t)$ is the actuator command assumed to be a product of a constant amplitude and the unit step function. The entire system can be written as the state equation

$$\mu(\bar{x},t) = [\ e_1(\bar{x})\ \ e_2(\bar{x})\ \ \ldots\ \ e_N(\bar{x})\ ]\ x(t) \tag{2}$$

where $e_i(\bar{x})$ are the influence functions associated with each actuator. The open loop transfer function for each actuator is given by

$$D(s) = \frac{k e_i(x)}{1 + \tau_i s} \tag{3}$$

The closed loop transfer function for the compensated DM loop is given by

$$T_{ci}(s) = \frac{G(s)D(s)}{1 + G(s)D(s)} \tag{4}$$

For this system a Proportional plus Integrator (PI) type compensator was chosen so that transient response would increase while eliminating steady state error for step input commands. The transfer function for a PI compensator is given by

$$G(s) = K_P + \frac{K_I}{s} = \frac{K_P s + K_I}{s} \tag{5}$$

where $K_P$ and $K_I$ are the proportion and integration gains respectively. Substitution of the deformable mirror plant and compensator into the closed loop transfer function gives

$$T_{ci}(s) = \frac{K_P s + K_I}{\tau_i s^2 + (1+K_P)s + K_I} \tag{6}$$

where the gain k is assumed unity and the actuator influence functions are ignored since the required solution is for actuator displacement. Taking the Z-transform of this function gives

$$T_{ci}(z) = \frac{K_D E(z - z_0)}{z^2 + (K_D E - F - 1)z + (F - K_D E z_0)} \tag{7}$$

where the constants E and F are a result of the discrete time system

$$\begin{aligned} E &= 1 - e^{-T/\tau_i} \\ F &= e^{-T/\tau_i} \end{aligned} \tag{8}$$

T is the discrete time-step. $K_D$ is a constant dependent upon the PI gains

$$K_D = K_P + K_I T \tag{9}$$

and thus can be chosen to produce the desired transient and steady state responses. The open loop function for the compensated system is given by

$$D(z)G(z) = \frac{EK_D(z - z_0)}{(z - 1)(z - F)} \tag{10}$$

To improve the transient response we place a dominant pole at

$$z_1 = e^{-T/\tau_i} \tag{11}$$

where it is assumed that $\tau_c$ can be chosen small enough to accommodate the desired response. For the point $z_1$ to be on the root locus we must have $D(z_1)G(z_1) = -1$, thus we have

$$K_D = \frac{(1 - e^{-T/\tau_c})(e^{-T/\tau_c} - e^{-T/\tau_i})}{E(e^{-T/\tau_c} - z_0)} \qquad (12)$$

For phase lag compensation the zero of the open loop function is placed close to the pole at z=1, we choose $z_0$=0.9. Writing the input-output relationsnip as

$$\frac{X(z)}{C(z)} = T(z) \qquad (13)$$

and taking the inverse Z-transform we obtain the difference equation for each actuator displacement

$$x_k = K_D E(c_{k-1} - z_0 c_{k-2}) - \alpha x_{k-1} - \beta x_{k-2} \qquad (14)$$

where $c_k$ is the input command at the $k^{th}$ time-step and $\alpha$ and $\beta$ are given as

$$\alpha = K_D E - F - 1$$

$$\beta = F - K_D E z_0 \qquad (15)$$

This difference equation was programmed into an off-line simulation of the deformable mirror actuator response and later into an existing optical beam train simulation called OTFSIM. The results of the off-line indicate an optimal vale of $\tau_c$=2.0E-6 seconds for transient response of about 7.0E-6 seconds and an overshoot value of approximately 1% with a deformable mirror time constant of $\tau_i$=1.0E-5 seconds. A plot of the uncompensated and compensated time responses are shown in figure 2.1.3.

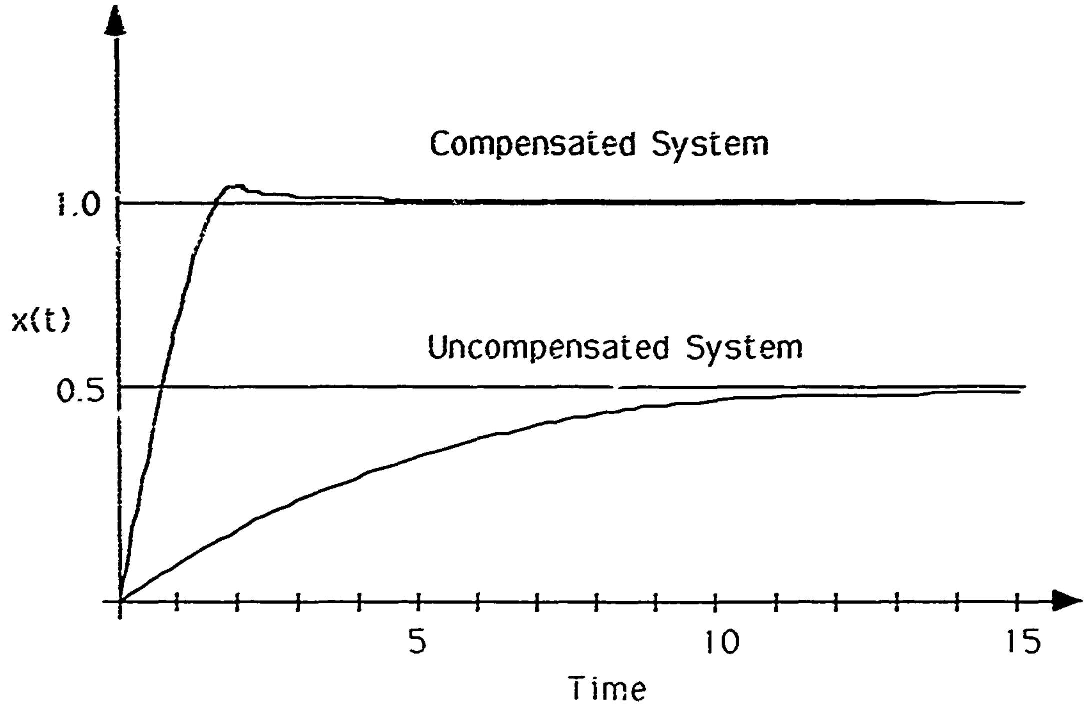


Figure 2.1.3
Step Response for Compensated and Uncompensated System

Note the relatively slow rise time and large steady-state error in the uncompensated case.

An identical model was integrated into OTFSIM and was tested using a least squares type reconstruction law and a spherical wavefront aberration. The results, as expected, showed nearly complete removal of the aberration within the limits of the adaptive optical system's capability in one imaging time-step (1.0E-4 seconds). A randomized "moving" phase screen was then implemented in the OTFSIM simulation to model the effects of typical atmospheric turbulence. Again the system was tested using the least squares control law and was found to satisfactorily remove the disturbance aberrations.

At this point we have implemented a PI type compensator based on a first order model of the deformable mirror dynamics. The first order model is inherently stable and the PI compensator has produced a more responsive wavefront sensor-deformable mirror adaptive optics system that will allow image sampling at higher frequencies.

## 2.2 Adaptation of Minimum Variance to Closed Loop System

As previously mentioned, the minimum variance control law takes into account correlations between atmospheric phase statistics and slope measurements from the wavefront sensor. This control law however has been derived and applied only to open loop systems as shown in figure 2.2.1.

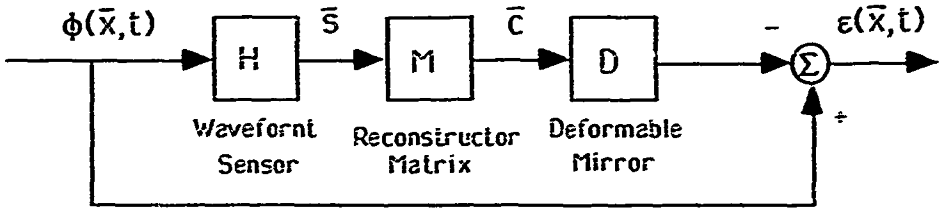


Figure 2.2.1
Open Loop Configuration

It was determined that the control law should be rederived for the closed loop configuration (if possible) so that any loop instability resulting from previous deformable mirror corrections as well as atmospheric statistics and sensor measurement correlation could be eliminated by means of compensation. Substitution of the feedback portion of the wavefront sensor measurements into the expressions for the average mean square error over the aperture lead to a control matrix expression for which we found no closed form solution. It was determined however, that using an interferometer device to measure the current deformable mirror shape directly, one could subtract off these contributions from the output of the wavefront sensor in the feedback path. In this manner we are essentially dealing with open loop input to the control law and a closed loop derivation is not necessary. This loop configuration is shown in figure 2.2.2.

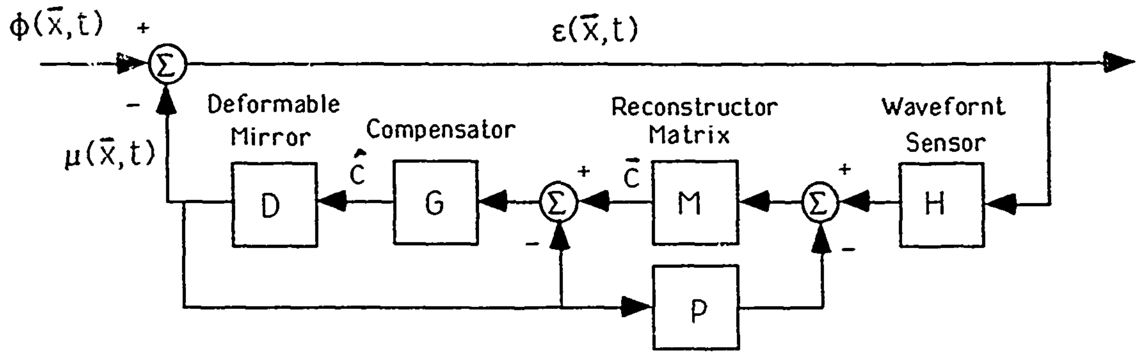


Figure 2.2.2
Closed Loop Configuration

2.3 Second Order Coupled System

To account for interactuator temporal coupling, a second order model was developed. This model is derived by considering the effect on the response of a single actuator due to motions of all other surrounding actuators. We assume the deformable mirror at a single actuator position behaves dynamically as a spring-mass system. This situation can be illustrated schematically as shown in figure 2.3.1.

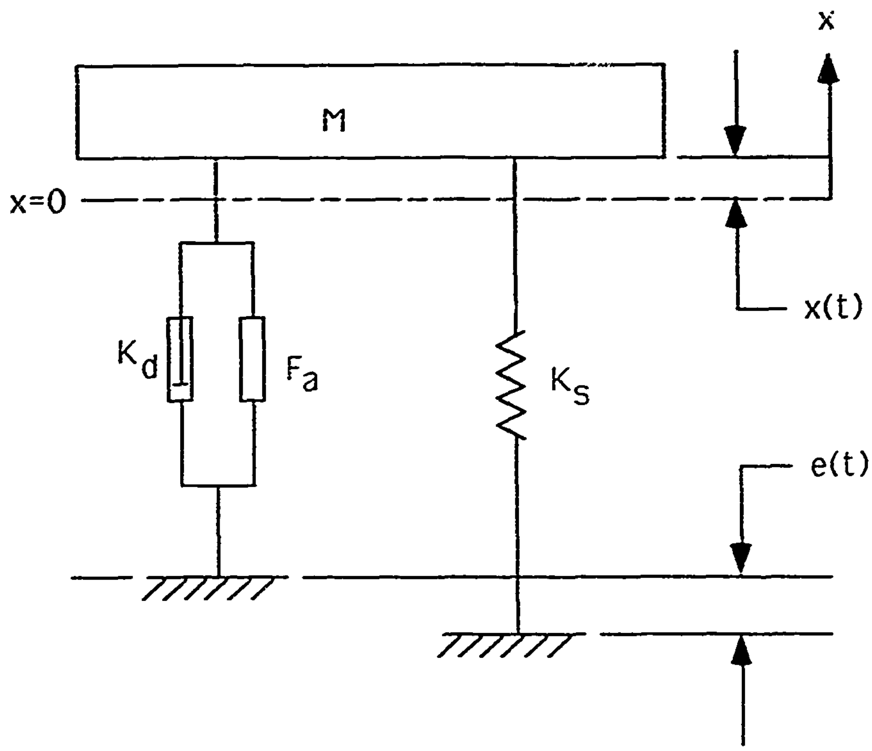


Figure 2.3.1
Deformable Mirror and Actuator as a Spring-Mass System

The forces acting on the mirror are due to the piezoelectric expansion of the actuator, $F_a$, inherent damping, $K_d$, and a force associated with the current mirror deflection tension. The tension force is proportional to the actuator displacement relative to some time-varying equilibrium position and is given by

$$F_t = K_s(x - e) \tag{16}$$

where $K_s$ is a tension (spring) constant, x is the current actuator displacement and e is the position of the equilibrium point due to the relative displacements of all other actuators. Figure 2.3.2 shows the relative positions of a single ($j^{th}$) actuator, and its equilibrium point due to the surrounding actuators.

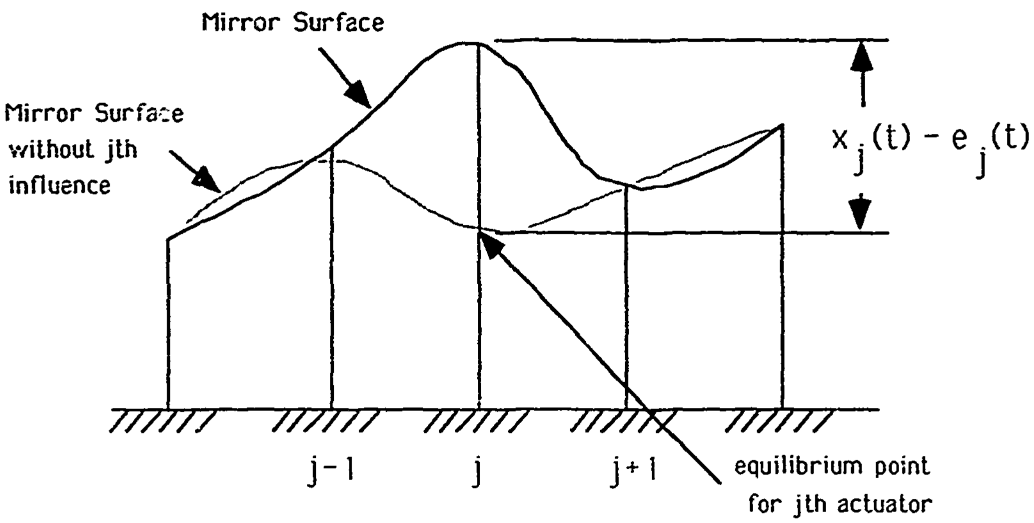


Figure 2.3.2
Equilibrium Point for a Particular Actuator

The deformable mirror model at the $j^{th}$ actuator results from the differential equation for forced spring-mass motion

$$\ddot{x}_j(t) + k_1\dot{x}_j(t) + k_2(x_j(t) - e_j(t)) = F_j(t) \quad (17)$$

where

$$k1 = \frac{K_d}{K_s} \quad \text{- Damping ratio}$$

$$k2 = \frac{K_s}{M} \quad \text{- Tension (spring) constant}$$

$$F_j(t) = \frac{F_a(t)}{M} \quad \text{- Actuator forcing function}$$

The time-varying equilibrium position of the $j^{th}$ actuator is given as a linear combination of the actuator influence functions

$$e_j(t) = \sum_{i \neq j} x_i(t) r_i(j) \quad (19)$$

where $r_i(j)$ denotes the value of the $i^{th}$ influence function at the location of the $j^{th}$ actuator. Note that the system is completely decoupled when $e_j(t)=0$ for all j and t. The coupled system differential equation is then

$$\ddot{x}_j(t) + k_1\dot{x}(t) + k_2(x_j(t) - \sum_{i \neq j} x_i(t) r_i(j)) = \beta_{j1} + \beta_{j2} e^{-T/\tau_j}$$

where we have assumed that the actuator forcing is of damped exponential form as shown in figure 2.3.3.

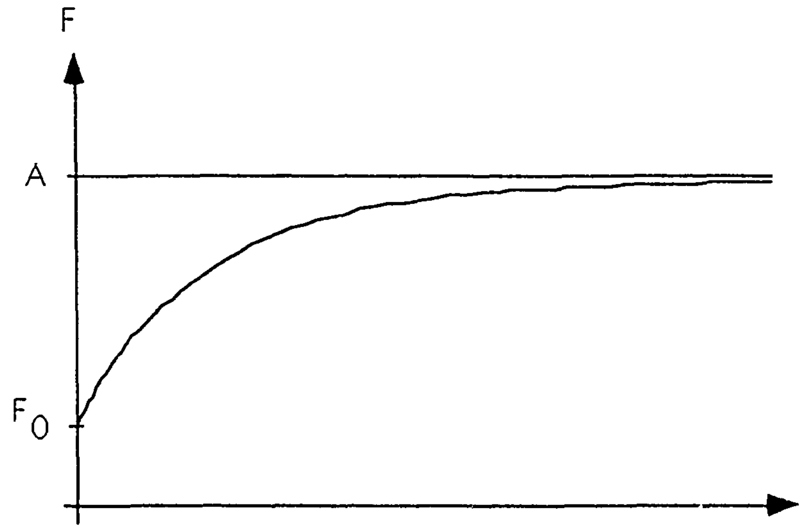


Figure 2.3.3
Actuator Forcing Function

To develop a state equation representation of this system we choose actuator position and velocity as system states. Thus we define

$$\begin{aligned} z_{2i-1} &= x_i \\ z_{2i} &= \dot{x}_i \end{aligned} \qquad \text{for } i = 1,2,\ldots,N \tag{22}$$

where N is the total number of actuators. Now from the system of differential equations we have

$$z_i = z_{i+1}$$

$$z_{i+1} = -k_2 z_i - k_1 z_{i+1} + k_2 \sum_{j \neq 1} z_{2j-1} r_{2j-1}(i-1) + \beta_{j+1,1} + \beta_{j+1,2} e^{-T/\tau_{j+1}}$$

for 1=1,3,5,...,2N-1. In matrix form this gives

$$\dot{\bar{z}} = A\bar{z} + B\bar{u} \tag{23}$$

where

$$A = \begin{bmatrix} 0 & 1 & 0 & 0 & 0 & 0 & 0 & 0 & & 0 \\ A21 & A22 & A23 & 0 & A25 & 0 & A27 & 0 & & 0 \\ 0 & 0 & 0 & 1 & 0 & 0 & 0 & 0 & & 0 \\ A21 & A22 & A23 & 0 & A25 & 0 & A27 & 0 & \cdots & 0 \\ 0 & 0 & 0 & 0 & 0 & 1 & 0 & 0 & & 0 \\ & & & & \vdots & & & & \ddots & \\ A21 & A22 & A23 & 0 & A25 & 0 & A27 & 0 & & 0 \end{bmatrix}$$

$$A_{ij} = \begin{cases} -k_1 & i=j \quad i=2,4,\ldots,2N \\ -k_2 & i=j+1, \quad j=1,1,\ldots,2N \\ K_2 r_{i/2}((j+1)/2) & \text{otherwise} \end{cases}$$

$$B = \begin{bmatrix} 0 & 0 & 0 & 0 & & 0 \\ 1 & 0 & 0 & 0 & & 0 \\ 0 & 0 & 0 & 0 & & 0 \\ 0 & 1 & 0 & 0 & \cdots & 0 \\ 0 & 0 & 0 & 0 & & 0 \\ 0 & 0 & 1 & 0 & & 0 \\ 0 & 0 & 0 & 0 & & 0 \\ & \vdots & & & & \\ 0 & 0 & 0 & 0 & & 1 \end{bmatrix}$$

$$\bar{u} = \begin{bmatrix} \beta_{11} + \beta_{12}e^{-t/\tau_1} \\ \beta_{21} + \beta_{22}e^{-t/\tau_2} \\ \vdots \\ \beta_{N1} + \beta_{N2}e^{-t/\tau_N} \end{bmatrix}$$

B is a 2N by 2N input matrix and u is a N by 1 vector where $\beta_{ij}$ contain the actuator voltage commands and the exponentials represent the forcing response.

System output is given as

$$\bar{y}(t) = C\bar{z}(t) = \bar{x}(t) \tag{24}$$

where C is a N by 2N output matrix given by

$$C = \begin{bmatrix} 1 & 0 & 0 & 0 & & 0 \\ 0 & 0 & 0 & 0 & & 0 \\ 0 & 1 & 0 & 0 & & 0 \\ 0 & 0 & 0 & 0 & \cdots & 0 \\ 0 & 0 & 1 & 0 & & 0 \\ 0 & 0 & 0 & 0 & & 0 \\ & & \vdots & & & \\ 0 & 0 & 0 & 0 & & 0 \end{bmatrix} \tag{25}$$

Note that system output is a vector of actuator displacements.

It is clear that the resulting state space representation is extremely large (the system matrix can be as large as 160 by 160 for a deformable mirror containing 80 actuators). The most feasible approach to the solution of this control problem is to attempt to view the system as decentralized and apply the theory of large scale systems.

Although the second order model had been derived to consider interactuator coupling effects it seemed reasonable to also apply the model to the uncoupled case in the event that coupling effects proved to be negligible. When the actuator coupling effects have been determined to be negligible, system matrix, A, is diagonal and we have one differential equation for every actuator

$$\ddot{x}(t) + k_1\dot{x}(t) + k_2x(t) = F(t) \tag{26}$$

The solution to the homogeneous part of the equation is given by

$$x_H(t) = \alpha_1 e^{t\tau_1} + \alpha_2 e^{t\tau_1} \tag{27}$$

where

$$\tau_1 = -\frac{k_1}{2} - \frac{1}{2}\sqrt{k_1^{\,2} - 4k_2}$$

$$\tau_2 = -\frac{k_1}{2} + \frac{1}{2}\sqrt{k_1^{\,2} - 4k_2} \quad .$$

The solution exhibits oscillatory behavior when

$$k_1 < 2\sqrt{k_2} \quad . \tag{29}$$

Since the assumed forcing function is of the form

$$F(t) = \beta_1 + \beta_2 e^{t\tau} \tag{30}$$

where $\beta_1$, and $\beta_2$ and $\tau < 0$ are measured constants, the particular solution will be of the form

$$x_p(t) = A_0 + A_1 e^{t\tau} \quad . \tag{31}$$

substitution of $x_p$ into the differential equation gives

$$A_0 = \frac{\beta_1}{k_2}$$

$$\tag{32}$$

$$A_1 = \frac{\beta_2}{\tau^2 - k_1\tau + k_2} \quad .$$

Note that $F(0) = \beta_1 + \beta_2 = F_0$. The response of the uncoupled actuator system is

$$x(t) = A_0 + A_1 e^{\tau t} + \alpha_1 e^{\tau_1 t} + \alpha_2 e^{\tau_2 t} . \tag{33}$$

If the system is overdamped and

$$x(t) = A_0 + A_1 e^{\tau t} + e^{\tau_1 t}(\alpha_1 \cos(\tau_2 t) + \alpha_2 \sin(\tau_2 t))$$

where

$$\tau_1 = - \frac{k_1}{2}$$

$$\tau_2 = \sqrt{4k_2 - k_1^{\;2}} \tag{35}$$

when the system is underdamped. Initial conditions for the overdamped case give

$$x(0) = A_0 + A_1 + \alpha_1 + \alpha_2 = x_0$$

$$x(0) = A_1 \tau + \alpha_1 \tau_1 + \alpha_2 \tau_2 = v_0 \tag{36}$$

$$\alpha_1 = \frac{1}{\tau 1 - \tau 2} [v_0 + A_1 \tau + (A_0 + A_1 - x_0) \tau_2]$$

$$\alpha_2 = x_0 - A_0 - A_1 - \alpha_1$$

and for the underdamped case

$$\alpha_1 = x_0 - A_0 - A_1$$

(37)

$$\alpha_2 = \frac{1}{\tau_2} [v_0 - A_1\tau - (x_0 - A_0 - A_1)\tau_1]$$

## 2.4 Noise and Model Uncertainty

The last week of the summer research effort was spent considering other possible control problem aspects. These aspects were discused with Mike Roggemann and Sal Cusamano. Dr. Cusamano noted that the frequencies at which oscillatory behavior or "ringing" would occur are generally much higher than the bandwidth at which the deformable mirror typically operates and as a result the effects of actuator coupling could be considered negligible. This would suggest that the first order model would be sufficient. The main concern here was that any model would contain uncertainty with respect to the actual behavior of the deformable mirror. A simplified statement of the problem would be: what is the exact position of the deformable mirror at any given time? This requires an understanding of the uncertainty between the observation of the deformable mirror at any given time by the interferometer device and the transformation of that observation into current actuator positions.

It was also noted that the deformable mirror itself is not perfect in that the mechanical properties of the mirror-actuator system do not produce the desired result exactly. An actuator "nulling" is usually required to flatten the mirror before specific aberration deformations can be applied and that commanded actuator displacements are applied in addition to these nulling commands. It would seem that this effect could be neglected since feedback control is used. Further consideration on all these effects is needed.

# 3.0 Future Activity

As previously mentioned, it is intended that this research will provide a foundation for a technical article and a masters degree thesis. Further work will be conducted throughout the fall and spring semesters at the University of New Mexico to achieve these goals. It is anticipated that a concentration of this effort will be on the topics described in the above section 2.4 as more is understood about the types of disturbances and uncertainties involved. It is also hoped that a form of emergent computation can be applied to this problem.

# SINGLE QUANTUM WELL, GRIN-SCH SEMICONDUCTOR OPTICAL AMPLIFIER GAIN CHARACTERIZATION

Keith W. Ver Steeg

Power gain measurements were made on a single quantum well (SQW) graded index - separate confinement heterostructure (GRIN-SCH) optical power amplifier (PA). At low input power, the amplifier exhibited better efficiency for vertically polarized input than for horizontal polarization, even though more power can be coupled into the cavity with horizontal polarization. Higher input powers damaged the amplifier, resulting in large leakage currents.

## I. Introduction

Semiconductor laser amplifiers serve an important role in optical fiber communications, laser imaging, and optical computing. Characterization of the power gain performance as a function of input wavelength, input power, and amplifier structure is useful in order to assess how well the amplifier will work for a particular application.

This report is a summary of my work done while at Philips Laboratory, Kirtland AFB, NM. Power gain characteristics of SQW GRIN-SCH semiconductor optical amplifiers were measured. The amplifiers were manufactured by Hughes Research Co. to be used as an amplifier array in a Phase Conjugate - Master Oscillator Power Amplifier (PC-MOPA) system. While power versus injected current data exists on the amplifiers, there is no data available on their gain efficiency.

## II. Experiment

The power amplifiers (hereafter referred to as PA) are grown as a 1x11 array mounted p-side down on to a metal heat sink. Each amplifier was an AlGaAs single quantum well with an active region of 100 $\mu$m wide by 500 μm long. The center to center distance between adjacent amplifiers was 500 μm. The rear facet of each facet was coated for high reflectivity (>95%) while the front facet was antireflection coated. This made the amplifier into a 2-pass system. The negative leads of the amplifiers in the were joined in parallel to a precision current controller, also manufactured by Hughes.

For low pump power measurements, a temperature tuned Spectra Diode Lab SDL-5410-C diode laser was used as a pump source (hereafter referred to as the Master Oscillator, or MO) . It could deliver up to 100 mW CW power at low temperature, with a tunability of 814-834 nm. The temperature of the SDL laser was kept to within $\pm$ 0.02° C by a temperature controller of a Hughes research design.

The PA array and MO were first characterized spectrally using a .5 meter spectrometer. The SDL laser output wavelength was temperature calibrated, and the PA output calibrated to heat sink temperature and injected current. Injected current versus output power measurements were made on both the PA array and the SDL pump laser.

The PA gain experiment setup is shown in Figure 1. After measuring the PA's reverse biased photocurrent ($I_{rev}$), measuring the PA's incremental slope efficiency ($\eta$), and knowing the frequency of the amplifier's emission ($\nu$), the power coupled to the amplifier is found by

$$P_c = I_{rev}\eta h\nu \quad (1)$$

With the MO blocked, the current to the PA array is stepped from 0 to 2.2 amps (0 to 200 mA per individual amplifier) and $PA_{split}$ and $PA_{xmit}$ are measured. The total PA output ($PA_{tot}$) is $PA_{split} + PA_{xmit}$. With this data, $PA_{tot}$ is calibrated to $PA_{split}$. Scattered light from the PA facet is measured by turning off the current to the PA and measuring the scattered light arriving at detector A as a function of MO power. Next, the PA is blocked, and the MO power transmitted through the beamsplitter ($MO_{xmit}$) and $MO_{split}$ are measured while stepping the MO power from its minimum to maximum value. Since

$$MO_{tot} = MO_{xmit} + MO_{split} \qquad (2)$$

$M_{tot}$ can be calibrated to $MO_{xmit}$.

Two lightmeters were used to measure the PA and MO powers. The first was an International Light IL1350 and the second was a Newport model 815. The first half-waveplate/polarizing beamsplitter combination is used to continuously vary the MO power. A second half-waveplate is used to rotate the MO polarization. A CCD camera connected to a vidicon is used to roughly align the MO beam with PA active region. Two MO power ranges were investigated for both horizontally and vertically polarized MO beams, the first from 0 to 26 mW, and the second from 0 to 1000 mW (using a Ti:Sapphire MO laser). The SDL MO power was low due to the attenuation caused by the two optical isolators and many beam shaping optics.

The MO light was focused onto the amplifier facet with a Newport F-L20 laser diode collimating lens. The beam size on the facet was approximately 5$\mu$m in diameter.

## III. Results

Figure 2a shows the spontaneous emission spectrum of one of the PAs. The MO, which has a linewidth of less than .4 Angstrom, is temperature tuned to the peak of the PA emission. The PA emission peak does not noticeably shift as the injected current varies from 0 to 2.2 watts. In figure 2b, the incremental quantum efficiency of amplifier #7in the array is calculated to be .48. This number will be used in Equation 1 to calculated the optical power coupled to the amplifier.

The absolute power in versus power out is shown in Figures 3a and 3b for amplifier #7. These figures are corrected for scattered MO light reflecting off the PA facet. The "signal in" axis refers to the actual power coupled into the amplifier, as calculated by Equation 1. It is interesting to note that more power can be coupled into the amplifier for the MO beam polarized horizontally (E-field parallel to amplifier facet plane) than for vertical polarization of the MO beam. However, the amplifier output is greater for a vertically polarized MO beam. Also, the amplifier gain never rises above unity for either polarization, possibly due to low injection current, or insufficient MO power coupling into the cavity.

Since these first low power measurements did not yield sufficient information about the PA performance past unity gain, a higher power MO was utilized. A tunable titanium sapphire ring laser having an output power of 1.25 watts was used as a new MO. After tuning the Ti:sapphire laser to the PA emission peak of 820 nm, we were able to deliver approximately 1 watt to the PA facet. At these higher input powers to the PA, damage to the active region occurred. After a few hundred milliwatts MO incident on the PA facet, its reversed biased current dropped significantly, and the amplifier showed a significant dark current, indicating that some sort of damage had occurred. Figure 4 is a photo of the MO beam and the PA facet both before and after damage occurred. The circular beam is the MO, and has a diameter of about 5$\mu$m. It is offset from the facet image intentionally in order to show the damaged areas, which appear as dark regions in Figure 4b.

**IV. Conclusion**

It appears that the higher MO powers cause some sort of change in the PA. Either the facet itself is fused together, or internal changes to the amplifier occur when the incident MO power is increased above a few hundred milliwatts. To avoid these catastrophic local heating effects, the MO beam must be better matched to the mode volume of the PA active region. A short focal length cylindrical lens could be used, however it will not collimate light which diverges in the plane of the lens. Proper calibration of the emitted light would circumvent this problem.

The time scale of the study did not allow further iterations to be made to the experimental method in order to adequately probe higher MO powers. Future studies should include a closer inspection of the curious polarization dependence of the MO coupling and amplifier output.

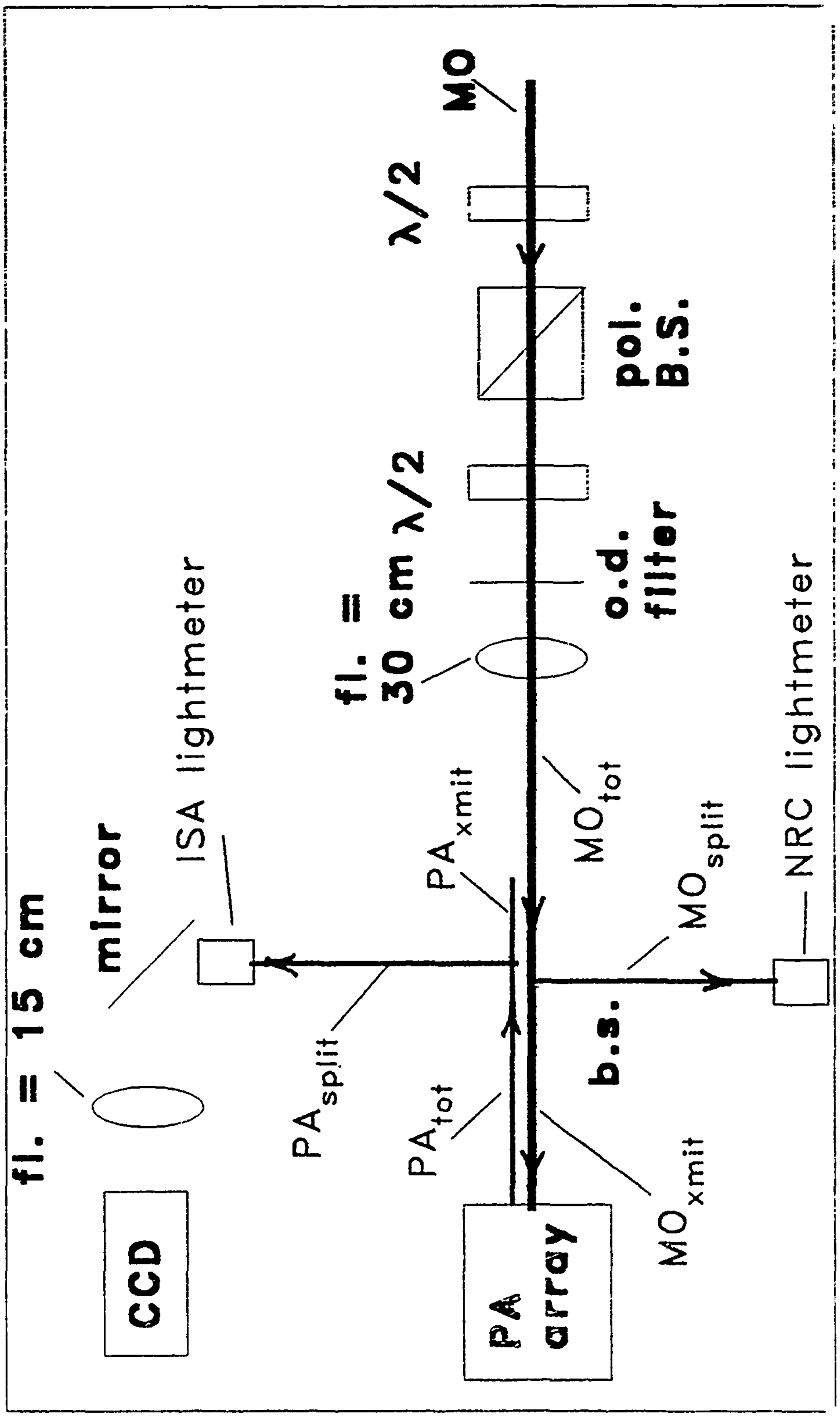


Figure 1. Experimental setup

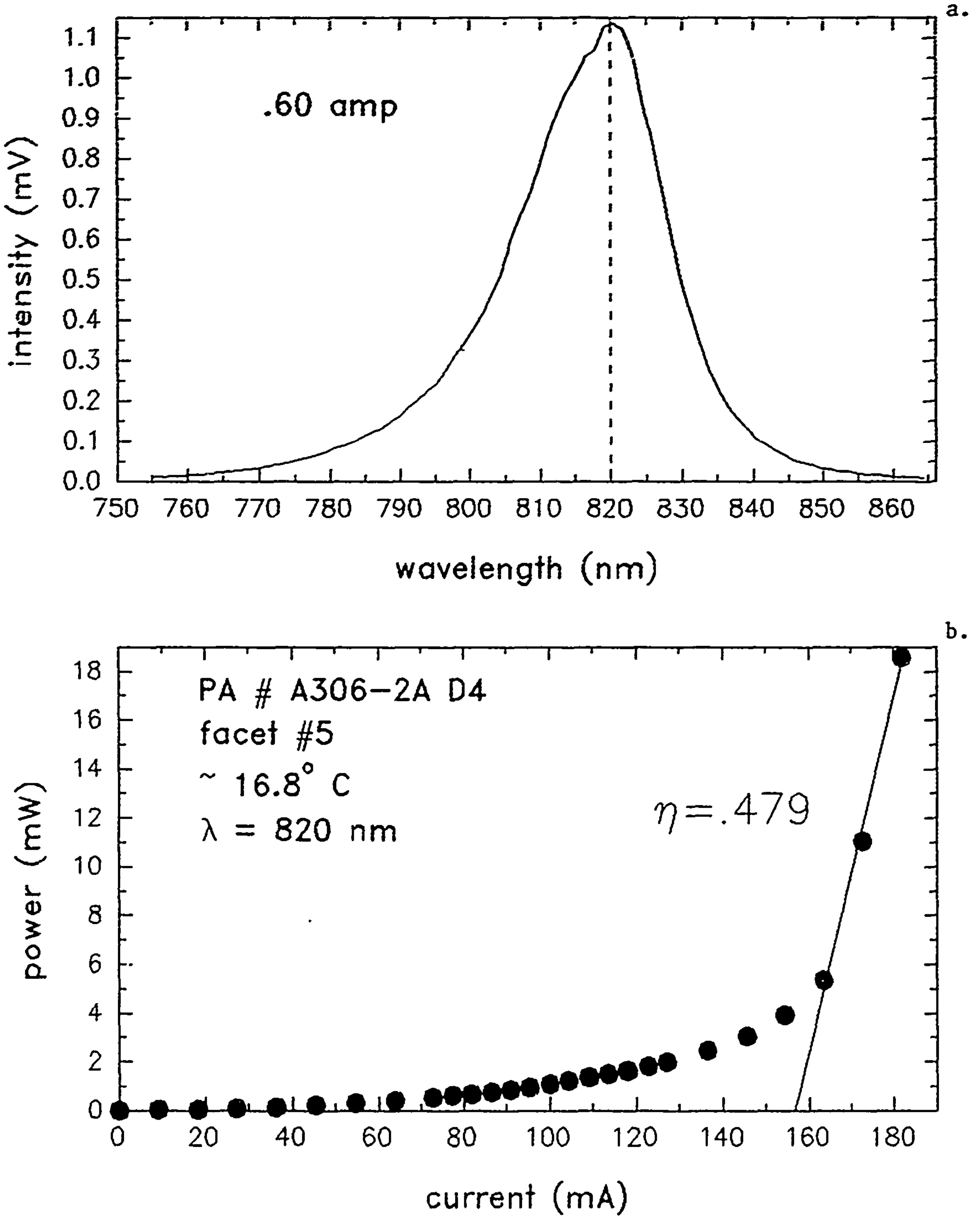


Figure 2. a: Emission spectrum of a power amplifier with .60 amp forward bias applied to the array. The dashed line denotes the MO pump wavelength

b: P versus I diagram for a single PA

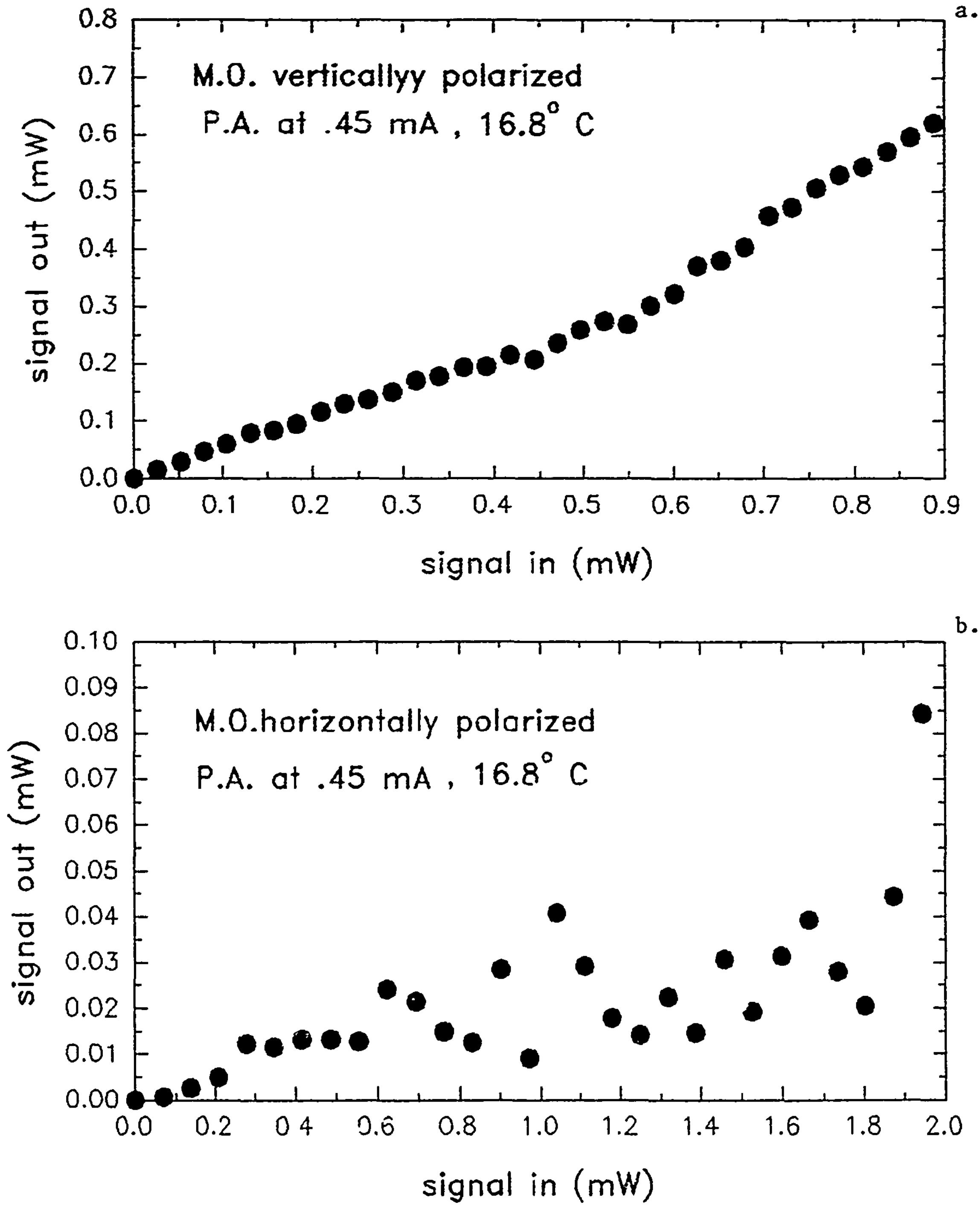


Figure 3. a: Power in versus power out of a PA for a horizontally polarized MO

b: Power in versus power out of a PA for a vertically polarized MO a.

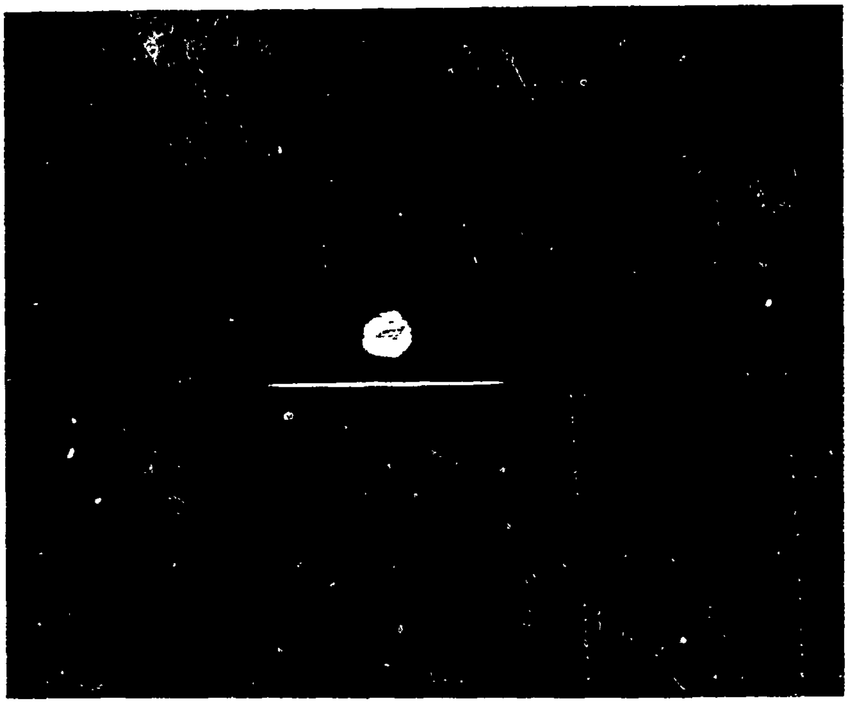

b.

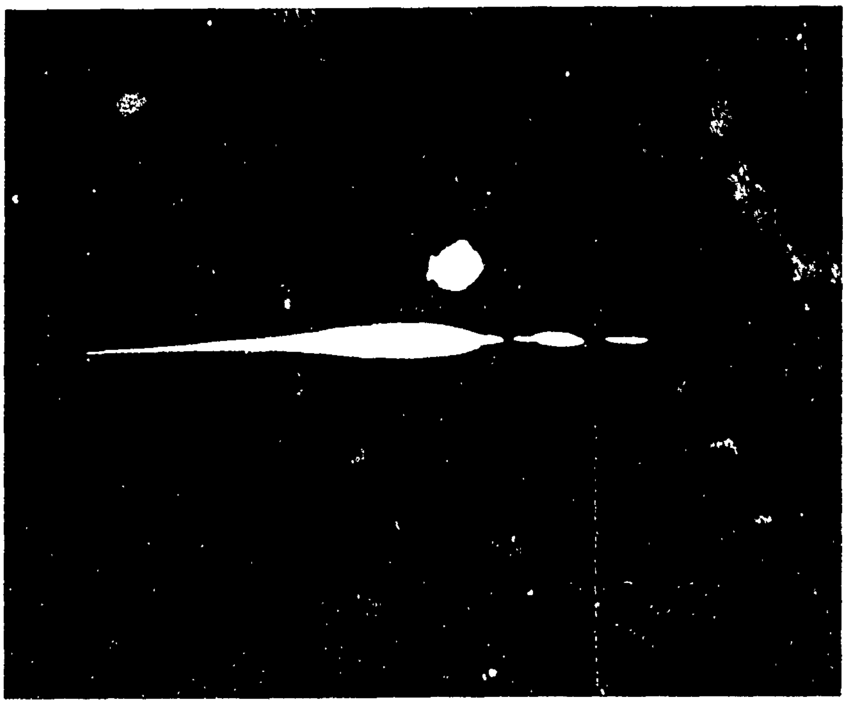

Figure 4. Photographs of the PA facet (horizontal line) and MO beam (circle). The MO beam is 5um in diameter.
a: Before damage
b: After damage. The dark gaps in the facet are the damaged areas

**NEURAL NETWORK PROGRAMS INSTALLED ON THE KHOROS ENVIRONMENT**

**Paul H. Wheeler**

**Abstract:** The Phillips Lab Neural Computation Research group developed a number of Neural Network programs for research into pattern recognition applications. These programs were written for a specific research topic, but were nearly useless for use for general research. These programs were revised so that they would operate on a visual processing environment called KHOROS, which is supported by the University of New Mexico. This paper describes in detail on how the neural network programs operate within KHOROS and how they were tested.

## I. INTRODUCTION

The Phillips Lab Neural Computation Research group, lead by Capt S. A. Anderson at Kirtland Air Force Base in Albuquerque, NM is researching neural network applications to recognize the angle at which a laser beam is incident on an optical fiber based on the light intensity pattern at the fiber back optical plane. Last summer, researchers developed and tested programs that ran neural network and pattern recognition algorithms. These programs modeled a two-layer perceptron, a bidirectional associative memory, an Anderson's associative memory, a convex-mean clustering algorithm, and a vector quantization algorithm. Additionally a powerful program, NETS, that modeled the backpropagation algorithm was also used as a research tool. All of these programs (except NETS) were written to test each algorithm's ability to recognize the patterns and classify them according to angle.

Since these programs were written with a specific purpose in mind, they had a number of problems that prevented them from being a general research tool. First, the input data had to be in a special format that was specific to the programs. Although the researchers made sure that they were consistent with each other as far as input data format, the format was not consistent with any common file format. This meant that not only did large data sets have to be converted into their format, but also had to be converted to more common formats if a user wanted to try signal conditioning (such as FFT's) on the data. A programmer would have to have knowledge of both file formats to write a converter and even then that might not be enough if, say, the researcher wanted to try some other signal conditioning program: it might use still another file format. Along these lines, there was no capability for the programs to display data visually.

Another problem with these programs is that they were inefficient with memory allocation. These program were written in FORTRAN, which does not allow dynamic array allocation. To allow for users to test arbitrary sized data sets, the programs were compiled with arrays allocated to some maximum size. This would increase both the time and cost of running each neural network program. If a user wanted to avoid this problem, he would have to recompile each program every time he changed the size of the data set.

Finally, only users who were intimately familiar with both the program and the program's algorithm could use it as a research tool. Although the programs were documented to some degree, the documentation was not generally available with the programs. Essentially the programs were only useful to the people who wrote them.

All of these problems can be addressed by placing these programs in an environment that provides for signal processing, visual display, and an online help manual. The University of New Mexico developed such an environment, called KHOROS for research into visual processing. Any program implemented on KHOROS would have access to a vast library of signal processing, visualization, and data conversion routines. Additionally, KHOROS provides for an online help facility which can be used to provide specific information regarding the neural network program. Thus the summer project was to revise the neural network programs written last summer to operate under KHOROS.

This paper will briefly discuss the KHOROS environment and how each program was implemented onto the environment. It will also discuss how the neural networks were tested, and what problems were encountered.

## II. GENERAL INFORMATION

Programs that operate under KHOROS operate as "commands" in a visual language. Figure (1) shows a KHOROS workspace that contains a visual program.

Each box, called a "glyph" represents either a data file or an executable file. The lines between the boxes, called "glyph connections" show how data flows from one box to another. In this example, data flows from the "DATA" glyph and the "asc2viff" glyph to a program called "zclus_t". "zclus_t" operates on

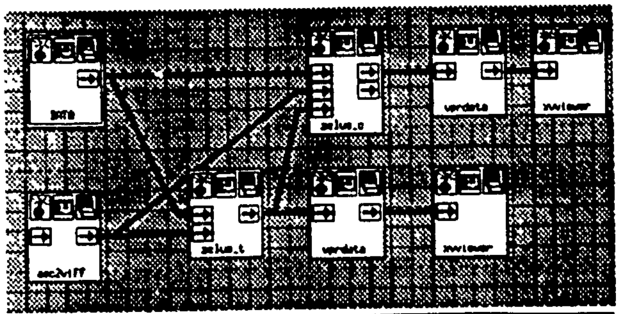

Figure 1

these two sets and sends it to two other programs, "vprdata" and "zclus_c". Ultimately the process is completed at the "xvviewer" boxes, which allow for visualization of the output data. The whole idea is that the user can define these connection however he wishes allowing for almost unlimited pre- and post-processing of data.

How each program processes the data can be changed by the user. Each one of the glyphs can be opened into a box called a pane or a window. Figure (2) shows the pane produced from opening the "zclus_t" glyph. These panes contain pane parameters that allow the user to modify the program's operation. The files indicated in the input images and the output image are temporary files that are automatically created when a user constructs the worksheet. Additionally, a user can manually change the filenames to any permanent file.

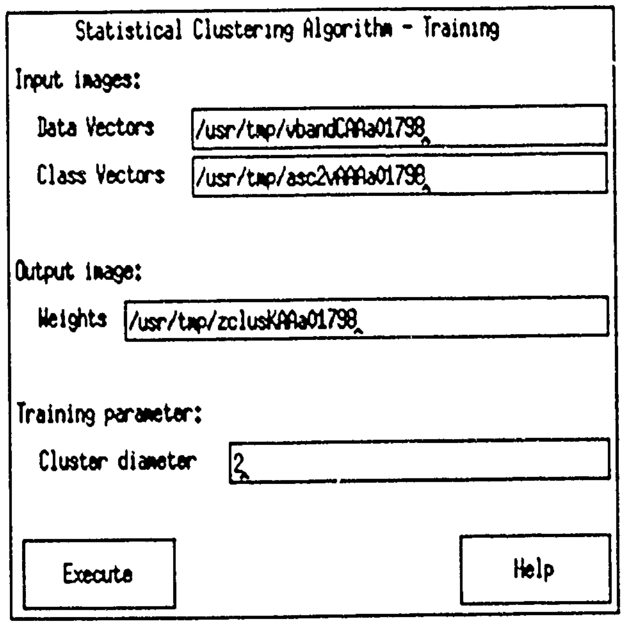


Figure 2

Thus KHOROS provides for all input and output for any program operating in its environment. To provide consistency a data format, KHOROS uses an internal file format called a VIFF format. The VIFF format was especially designed to contain visual images, however a VIFF file can contain any kind of array. More on this will be discussed later.

Each of the neural network simulation programs were menu driven fortran programs designed to operate in a VMS operating system environment. The programs had to be revised so that the neural networks routines could be called and serviced only by the KHOROS environment. The research group revised each program, using one of two methods, so that the neural network routines could be extracted without the menu or the input/output routines that are provided by KHOROS.

The first method involved merely rewriting the fortran program so that the programs were in a modular format. In the modular format, each subroutine in the program would perform input/output or it would perform neural network operations. The research group would then extract the neural network subroutines and call them from a C driver for KHOROS. This particular method had the advantage that the original author's code is mainly preserved and that if the program is upgraded in future, it is easy to update the KHOROS implementation. The disadvantage of this approach is that any bugs in the original source may be carried to KHOROS. The neural network group had a great deal of difficulty tracing and removing these bugs where they occured because the program were not well documented and the author was generally unavailable.

Another problem is that arrays and some variables do not pass well between Fortran and C. For example C stores a double-dimensioned array in memory in columns, but Fortran will reference that array in rows thus a programmer must reverse the indexing notation when accessing C arrays in Fortran. Another example is that the C compiler passes floating point variables as type DOUBLE to subroutines; but a FORTRAN subroutine cannot access a DOUBLE variable. Thus any floating point variable had to be explicitly cast as type FLOAT before the variable's pointer was passed to the FORTRAN subroutine.

Also when calling the Fortran subroutines, only pointers to variables can be passed in the argument list: a side effect to this is that any changes the Fortran subroutines make to any of the variables in the argument list gets passed back to the calling C driver. This means that sometimes extra variables had to be declared to recall values changed by the subroutine.

Lastly, portability problems may be increases because both the portability of C and FORTRAN must be considered. Although FORTRAN is known to be very portable, how it interacts with a version of C may not be portable, thus more care may be needed when porting this code to another system.

The other method involved recoding the algorithm in C. This method was used if the neural network subroutines were short or if there were many bugs with the program. If the subroutines are short, the subroutines can be more efficiently run in C because the additional code needed to make the variable compatable is not needed. Also if the original program had many bugs, the group could more efficiently recode the algorithm than debug the program because most of its source will not be used by KHOROS. The disadvantages of this method is that it would be difficult to incorporate upgrades from the original authors and that recoding the algorithm can introduce new bugs that were not present in the original code.

## III. SPECIFIC CHANGES

Each neural net program was implemented as two KHOROS applications; a training application (trainer) and a classifying application (classifier). The training application creates a weight file which is passed on to the classifying application. This method allows the user to construct a logical data flow path separating training from classifying. The user can save the weights file, or he can manipulate it as part of an experiment (for example: An experimenter may want to add some random noise to the weights to test the robustness of training).

All the training applications require an input vector set. The input vector set is a single VIFF file containing all the input images that the network is going to be trained with. Each image is stored in a VIFF file as bands and is used by the program as a single dimensioned array. For example consider an image that shows light intensity on a 100x100 grid. Then even though the VIFF file will store it as a 100x100 grid, it is stored in a single band; thus the program will retrieve it as a 10000 element real array. The training application will automatically size the neural network so that it can train on these arrays (called training vectors). The only requirements are that the application has enough available memory to load all the images at once and that all the images have identical size (number of data points) and identical mapping.

When supervised training (training a network to learn a particular output when given some input) is needed, a class vectors file is required. The class vectors file contains the all the output vectors with each vector stored in a band. Each output vector must be the same size and correspond to an input image. For example: If there are twenty input images in the input vector set and there are twenty output vectors in the class vectors file, the first output vector corresponds to the first image and the second output vector corresponds to the second image and so forth. Each application will a omatically size the network to use the output vectors.

Finally all the training applications require an weights file. This is a VIFF file where the application stores the weight set that is generated during training. The application will only store a weight set once training is complete: If training is aborted, the current value of the weights will not be stored. The size of the weight set depends on the size of an image and the size of an output vector.

The classification applications require as input files an input data set, a weights file, but only optionally use a class vectors file. All these files for a classifier are in the same format as the files for a training application. The classifiers also have two output files: the Image file and the Ascii file.

The Image file is a VIFF file that contains the resulting output vectors that were produced during classification. Each output vector is contained in a band and correspond to an input image (first output vector is from the first image etc). The Ascii file contains the ascii representation of the output vectors, the total number of vectors classified and, if class vectors file is given, information on whether or not a vector has been misclassified.

Lastly, every neural network required a help file. This help file contains all the information necessary to understand and operate the neural network program. Also wherever possible the team included information into determining whether or not a particular neural network is appropriate for a particular application. This help documentation could be recalled from any pane by selecting an appropriate button.

Depending on which neural network is used, additional information is required. The next section will discuss each neural network, how it was implemented, and how it was tested.

## IV IMPLEMENTATION DESCRIPTION

### A. VQ

VQ is a program written by J. Schruben[4] to perform vector quantization. For supervised training the program simply normalizes all the input vectors on a unit hypersphere and sets the first n unit vectors to be the n codewords. Each codeword is a vector that represents a class. "n" is determined by how many elements there are each output class vector. A vector from the remaining vector set is compared to each codeword and the winning (smallest distance) codeword is updated according to the following relationship:

$$m_{t+1}(x) = m_t(x) + f(t) * (x - m_t(x)) \tag{1}$$

where:

$f(t)$ = a * monatonically decreasing function of t
$t$ = discrete time
$x$ = input vector
$m_t(x)$ = nearest codeword to x before update
$m_{t+1}(x)$ = nearest codeword to input x after update

a is -1 if the winning codeword is not in the class defined by the user (the codeword is rotated away from x); a is +1 if the winning codeword is in the class defined by the user. To prevent one codeword from always winning (called "dominating the competition"), the distance is weighted by the sqrt(number of times a codeword has won). Thus the more times a codeword wins, the closer x must be to that codeword before it wins again. This is known as DeSieno's Method of Conscience.

For unsupervised learning, the user selects the number of classes and the application randomly selects points on the unit hypersphere to start as codewords. Codewords are then updated according to the same rule as for supervised learning, except a is always +1 (the user does not define the classes).

When the classifier is run, each vector is compared to all the codewords. Since each codeword corresponds to a particular class, the output vector is the class vector for the winning codeword. The final output is a list of class vectors which correspond to the input vectors.

The pane items for the training application includes those listed in section III plus:

Threshold(Thr)[Training and classifying]: Any value above the threshold retains its value; any value below the threshold is zero. This was a part of the initial program and was kept to preserve the Author's original algorithm. It is not clear whether changing the threshold from zero will enhance performance. The classifier should use the same threshold the weight set was trained with.

Number of Classes(ncl)[Training]: This button is mutually exclusive from the Class vectors button. If this button is selected, then you must enter the number of classes. The application will then perform unsupervised training with the total number of classes = ncl. If this button is not selected then you must enter the name of the class vectors file and the network will perform supervised learning.

Number of iterations(niter)[Training]: The number of times the network will train with a vector set. This allows user flexibility to control the accuracy or speed of training (As accuracy increases, speed decreases)

ASCII statistics[Training and classifying]: An optional file that stores information regarding the classes, the average error, and the current settings. If this is not selected, the output will be sent to stdout.

Print iteration(piter)[Training]: The rate (print at every 'piter' iteration) at which statistics are printed in the ASCII statistics file. This allows the user to record training statistics at a convenient rate.

Random number seed(seed)[Training]: The seed for the random number generator. Used when performing unsupervised training.

Testing the network was done using five of the images showing light intensity patterns at different angles. So the group could differentiate between bugs with the program versus limitations of the algorithm, the same vectors used to train the network were used to classify. Using this method the network was tested using both the supervised and unsupervised modes. In both cases, the network was able to classify each vector correctly.

**B. BAM**

"bam.for" is a program written W. J. Zimmermann[7] which simulates a Bidirectional Associative Memory (BAM). A BAM is a simple two layer Neural Network with the output of the first layer providing the input to the second layer and the output of the second layer providing an input to the first layer (see figure 3). If the sum into a neuron is greater than zero, then the output is 1; if the sum is less than zero, the output is zero; and if the output is equal to zero, than the neuron retains its value.

Training a bidirectional associative memory is done by forming the correlation matrix:

$$M=\sum b_i * a_i^T \qquad (2)$$

where:

$a_i$ = The bipolarized input vector

$b_i$ = The bipolarized output vector

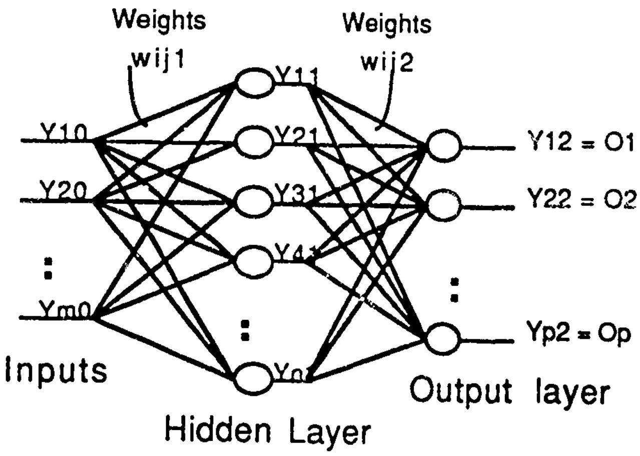


**Figure 3** - The BAM

The input vector is bipolarized by comparing the each element in a real vector to a threshold. If the element is greater than the threshold, then that value is replaced by one, otherwise it is replaced by -1. Similarly, the output vector is a bipolarized class vector with a threshold of 0.5.

$$a \rightarrow a': \; b = f(M*a) \qquad (3)$$
$$a' = f(M^T*b)$$

A vector is classified by placing a bipolarized vector a at the input of the first layer. The network performs the function shown in equation (3) where f(x) causes all elements in x greater than 0 to be one; less than 0 to be zero;

and equal to zero to retain its value (assume that the neurons initially start as zero). The resulting vector b is then passed in the reverse direction to produce an a' (equation (3)). The process of a -> a' is called resonation. Resonation will continue until the final resonation, a* -> a*. The solution of (3) for a* is b* which is the final output of the BAM given an input a.

The panes for BAM include those discussed in section III plus:

Threshold(Thr)[Training]: This contains the threshold value that determines how the input vector is bipolarized. This value is passed as a part of the weights file to the classifier.

Testing the BAM was done using an example found in Kosko's paper.[4] The reason why the group did not use actual image data as was done for VQ is that the BAM could not learn that data set. Thus Kosko's example was used because it showed the vectors and the proper weight matrix. The BAM training application constructed the proper weight matrix and the BAM classifier was able to reproduce the correct output vectors given a set of input vectors.

**C. AND**

"and.for" is a program written by W. J. Zimmermann[7] that simulates an Anderson's Associative Memory (AND). AND is a single layer neural network that produces a class vector output.

Training AND is similar to training BAM (see equation 2), except that the input vector is normalized to a length of 1 instead of bipolarized. Classifying a vector using AND does not use resonation as in BAM. Instead the unchanged input vector a produces an output b by the below function:

$$b = f(M*x) \tag{4}$$

Where:

b = Class vector
x = raw input vector
M = weight matrix
f(x)= y s.t.

if $x^T = [\, x_1\ x_2 \ldots x_n \,]$ and kth element of x, $x_k = \max\{x_1, x_2, \ldots, x_n\}$

then

$y^T = [\ldots 0\ 1\ 0 \ldots]$ where the kth element of y is 1 and the remaining n-1 elements are 0.

There are no addition pane items for AND that were not mentioned in section III.

AND was tested successfully using the same data set as VQ.

## D. ZCLUS

"zclus.for" is a vector clustering p·ogram developed by W. J. Zimmermann.(7) The algorithm starts with a subset of randomly selected vectors from the input space. A vector is arbitrarily selected from this subset and is made into the first codeword. Another vector is selected from the subset and is compared to the codeword using equation (5). If (5) is true, then the codeword is updated

$$d<|x_1-c_1|+|x_2-c_2|+|x_3-c_3|+\ldots+|x_n-c_n| \quad \textbf{(5)}$$

Where

$C$ = Codeword
  $= [\ c_1\ c_2\ c_3\ \ldots\ c_n\ ]^T$
$X$ = input vector
  $= [\ x_1\ x_2\ x_3\ \ldots\ x_n\ ]^T$
$d$ = cluster diameter

by adding the vector to the old codeword. If (5) is false, then the input vector becomes a new codeword. The remaining vectors are compared to every codeword in this manner: if (6) is true for a codeword, then that codeword is updated;

$$d<|x_1-\frac{1}{n_i}c_{1i}|+|x_2-\frac{1}{n_i}c_{2i}|+\ldots+|x_n-\frac{1}{n_i}c_{ni}| \quad \textbf{(6)}$$

Where

$C_i$ = ith Codeword
  $= [\ c_{1i}\ c_{2i}\ c_{3i}\ \ldots\ c_{ni}\ ]^T$
$n_i$ = The number of times the ith codeword has been previously updated.

otherwise if (6) is never true, then the vector becomes a new codeword. Training is complete once all the vectors from the subset have been compared.

The codewords are then weighted by $1/n_i$ where $n_i$ equals the number of times the ith codeword has been updated + 1. The codewords are then stored as columns of the codeword matrix.

So far the training has been unsupervised, because the computer decides which codeword corresponds to which class. The computer will classify a vector as being in the same class as its nearest codeword. To provide for supervised learning, the application will classify the vectors in the subset and will construct a correlation matrix mapping the codewords to the desired output

The items in the ZCLUS pane include those discussed in section III plus the following items:

Cluster diameter(cld)[Training]: The cluster diameter defines d shown in equation (5) and (6).

Zclus successfully classified the same data set as used with VQ.

**E. Twolayer**

Twolayer is a program written by W. J. Zimmermann[7] that simulates backpropagation in a two layer perceptron (TLP). A two layer perceptron, shown in figure (4), is a neural network capable of distinguishing convex open or closed regions. Each neuron produces an output shown in equation (7).

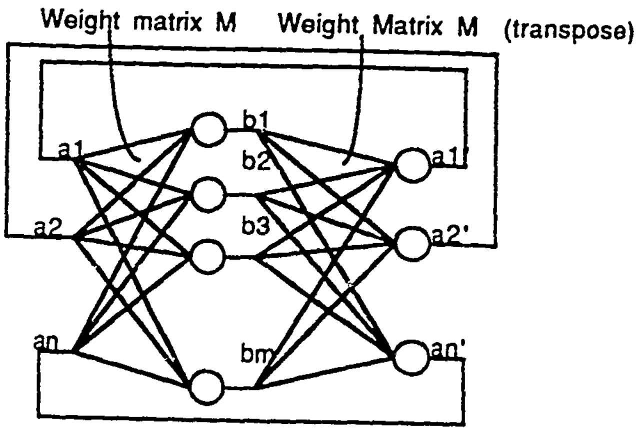


**Figure 4 - A Two-layer Perceptron**

$$Y_{1k}=f(\omega_{11k}Y_{1(k-1)}+\omega_{21k}Y_{2(k-1)}+\cdots$$

*where*:

$$f(x)=\frac{1}{(1+e^{-\alpha x})} \qquad (7)$$

and:

$\alpha$ = steepness
$Y_{ik}$=ith neuron in the kth layer, k>0
=ith input, k=0
$\omega_{ijk}$ = weight from neuron i (or input i) to the jth neuron in the kth layer

The perceptron is trained using supervised learning over some arbitrary subset of the input space. All the weights in the network are randomized and then the first vector is placed at the input. After the output is produced, all the weights are updated using the update rule shown below. This process is

$$\Delta\omega_{ijk} = -\eta \frac{\partial E}{\partial \omega_{ijk}} \tag{8}$$

Where:

$$E = \frac{1}{2}\left[(D_1-O_1)^2 + (D_2-O_2)^2 + \ldots + (D_n-O_n)^2\right] \tag{9}$$

and:

E = error
$\omega_{ijk}$ = weight from neuron i (or input i) to the jth neuron in the kth layer
$D_j$ = jth desired output
$O_j$ = jth output from the network
$\eta$ = learning gain ($\eta$>0.0)

continued until the error reaches some small value, or a maximum number of iterations is reached. Note that unlike the other networks, training is repeated over the entire subset until a desired error is reached.

Unfortunately, although this network can theoretically learn to classify an open or closed convex region, it will not always converge to that region. This is because equation (8) may be trapped by local minima so that error is not reduced by updating the weights, even though the error is large. There are a number of methods that deal with this problem, but they were not included in the algorithm.

Backpropagation is notoriously slow in converging to a minimum error solution- much slower than any of the other networks described in this paper. There are a number of methods that can reduce convergence time. First if there are a large number of neurons in the hidden layer, reduce the "steepness" of the non-linear function f(x) (see figure (5) ) and increase the learning gain. Other methods include varying the number of hidden layers and the value of the learning gain. Much improvement in speed can be made just by experimenting with the training parameters for example- When the group trained the neural net to learn the AND gate function using default parameters, the network took some 800 iterations over the set of four training vectors for it to converge to an average error of 0.05. The group then experimented with the parameters until it was discovered that with 5 hidden layers, $\eta$= 2.71, and $\alpha$ = 1.0, the network converged within 60 iterations

The items on the TLP panes include those discussed in section III plus:

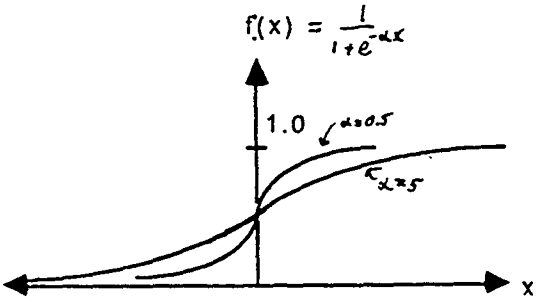


Figure 5 Varying the Steepness of f(x)

<u>Sigmoid Steepness(alpha)[Training and Classifying]</u>: The steepness of the nonlinear function. Included in both the training and classifying panes so that a user can experiment with a varying steepness sigmoid after training.

<u>Weight Matrix Threshold(wcut)[Classifying]</u>: wcut allows the user to constrain the weight matrix so that any weight that is less than the threshold becomes equal to the threshold. If a neural network is able to successfully classify using this constraint, it may be possible to revise the training program to improve training performance.

<u>Learning rate(eta)[training]</u>: eta is the value used as the learning gain for training. Although Lippmann suggests that this value should be limited to (0,1), the group found that performance can be improved if eta could be greater than 1. <u>Threshold(Thr)[Training]</u>: Thr is the value that determines the cutoff for an input vector. Any element in an input vector that is smaller than Thr will be zero, otherwise it retains its value.

<u>Hidden Layer Nodes(nfln)[Training]</u>: nfln determines the number of neurons in the hidden layer.

<u>Max avg error(merr)[training]</u>: merr determines the maximum average euclidean distance between the desired output and the actual output. The error

is averaged over the entire set of training pairs and then reset. Because of the nature of the error function, it was thought that it would be useful to use the Euclidean distance, though it may speed up training if program is changed to use the square of the distance.

Maximum number of iterations(ntcy)[training]: maxiter limits the number of times the network will train over the learning set. If the total number of iterations exceeds ntcy, then training stops regardless of the average error.

Print interval(iter)[training]: iter set the rate at which error statistics are printed. Statistics will be printed every "iter'th" iteration.

Testing was done using an AND gate test set. The reseach group used the AND gate test set because it was simple, and because a two-layer perceptron was known to converge to it. The group also tested the network using an original data set, but the network converged to a local minimum instead of a global, low error minimum. Although this seems to disagree with the perceptron results from last summer, no real comparison can be made because the perceptron training used last summer may have involved improved methods of convergence (such as momentum, varying learning gains, and biases). "tlp" is not designed to use these variations of backpropagation, although it can be modified to do so.

V. NETS

NETS is a program written by the programming group at the Johnson Space Center (JSC) to simulate arbitrary size and configuration neural networks. The user defines the neural network by writing a configuration file that contains information on the number of layers, the number of neurons in each layer, and the mapping of each layer to other layers. Once this configuration file has been read by NETS, the network prompts the user on information layer by layer regarding training parameters such as momentum, learning rate, biases, and so forth. NETS then trains the network using backpropagation until it converges to a specified error or it fails to converge within a specified number of iterations.

The research group wanted to install this program on KHOROS because, of all the neural network programs available, it was the most powerful in terms of user degrees of freedom. This power also presented some unique problems because KHOROS does not seem to have the capability to produce "open ended windows" for a user interface. An open ended window is a pane whose total number of inputs can be varied during runtime. An open ended window is necessary because the size of the neural network is defined by the user, not by the program and the number of training parameters depends on the size of the neural network. Although the configuration file could have contained these parameters, the research group wanted to maintain the "feel" of the KHOROS graphical environment when inputing training parameters for a neural network.

Although KHOROS does not provide for open ended windows, it does provide for turning "on" or "off" parameters in a pane. To use this capability, the program must to be able to produce its own window instead of Cantata providing the window. The procedure in developing a program with this capability is somewhat different than the procedures used to develop the other neural networks and is explained in (3), under XV routines.

Since input parameters could be turned on or off in a pane, a template pane was designed which contained enough parameters for 5 layers. If a network had less than five layers, the program would shut off those parameters that are unneeded. If there are more than five parameters, then the pane describes a page which shows five layers at a time. The user can then page up or page down to see and adjust parameters to fit his/her needs. The algorithm is shown below:

Each layer requires a learning rate, a momentum value, a scaling factor, and a logical which determines whether or not constant learning rate is used. Each parameter shown on the pane are stored in a special data structure (the pane structure) which contains a pointer to its value and its location on the pane. Since pane only shows at most five layers at a time, a larger data structure (the net structure) is developed that contains pointers to all the parameters for the neural network. Lastly, an boolean array (the control array) is created which controlled what parameters were on or off on the window. If a value on the array was "on", then the parameters for a layer set would be turned on by routine provided by KHOROS, otherwise the parameters would be turned off. Control was done at the layer level rather than at the parameter level because it provided sufficient control resolution: At no time was it necessary to just shut off a single parameter in a layer.

When the program is run, the nets structure contains the pointers to each training parameter of the first five layers and the control array contains only "on" values. If there were less than five layers in a network, the first n elements of the control array would be on, where n is the number of layers. The user can the adjust these parameters as necessary. When the user decides to page forward, the parameter values from the pane structure are saved onto the net structure and then the pointer to the net structure is incremented so that the next five layer parameters can be accessed. The current values of the net structure are placed onto the pane structure which show up as the default values on the pane. The user can page forward or backward using buttons on the pane to access different layers. Thus even though KHOROS does not support an open ended windows structure, the same effect could be acheived using fixed size windows.

This is as far as group got on implementing NETS on KHOROS. What remains to first revise NETS so that all its input/output and weights file are in a structure similar to the other Neural Network implementation. Second is to revise NETS so that a user can configure a Neural Network without creating a configuration file. The difficulty with the former is that each layer has its own weight matrix, which may be of different dimensions than another layers weight matrix. Since the KHOROS VIFF structure requires that the data is stored in a matrix whose dimensions are constant, not only does the weights file have to contain the weights, but also information on how the weights are mapped (i.e. the first 20 weights belong to layer 1 and map to layer 2, 3, and 4; the next 100 weights belong to layer 2 and so forth). More information about using VIFF is found in (1) and specifically using VIFF with nets is found in (2) where mapping solutions are discussed.

## VI. CONCLUSION

The Neural Network group was able to implement five neural network programs (VQ, ZCLUS, BAM, AND, and TWOLAYER) onto KHOROS and to solve one problem involved with implementing NETS with KHOROS. Each program was tested with, whenever possible, data from the fiber optic experiment. If a neural network did not work well with that data set, a simple data set was contrived that was well known to work on a neural network. When the neural networks were installed, the author's original program was preserved as much as possible. Where it was not preserved, the research group insured that the implemented algorithm was consistent with well known technical papers approaches to Neural Networks.

## BIBLIOGRAPHY


1. Anderson, Steven A. et al, "Neural Network Environment for Signal Processing and Pattern Recognition of Large Scale Data," Proceedings of the Second Workshop on Neural Networks: Academic/Industrial/NASA/Defense, pp 483-489, Feb 11-13 1991

2. Argiro, Danielle, et al. "The KHOROS User's and Programmer's Manual," University of New Mexico, Albuquerque, 1991

3. Croft, Charles R. III "Weekly Progress Report," July 27

4. Kosko, Bart, "Bidirectional Associative Memories," IEEE Transactions on Systems, Man and Cybernetics, Vol 18, Jan/Feb 1988

5. Lippmann, Richard P. "An Introduction to Computing with Neural Nets," IEEE ASSP Magazine, 4-22, April 1987

6. Schruben, J. S. and Anderson, S. A. "From Counterpropagation to Vector Quantization: Neural Networks for Pattern Recognition," Final summer report for AFOSR F49620-88-C-0053, August 1990

7. Zimmermann, W. J. and Anderson, S. A. "Pattern Recognition using Associative Neural Networks," Final summer report for AFOSR F49620-88-C-0053, August 1990

# INTEGRATING NEURAL NETWORK ALGORITHMS INTO THE KHOROS ENVIRONMENT

Carla S. Williams

**ABSTRACT**

Many of the Air Force laboratories are interested in providing an environment supporting signal processing research using neural network algorithms for pattern recognition and classification that does not require domain expertise for the application engineer in neural computation. This paper presents the results of the Neural Computation Research Group's implementation of several generic neural network configurations, developed and tested on relatively large scale data, within the Khoros visual programming environment.

## BACKGROUND

### Neural Algorithms

The Neural Computation Research Group (NCRG) headed by Capt. Steven Anderson, which is a part of the USAF Phillips Laboratory Space Technology Diractorate, has been investigating the use of neural networks to perform pattern recognition/classification of laser intensity values measured on the back focal plane of an optical fiber. The fiber is illuminated with coherent light which resonates down the core and cladding to the back focal plane. The resulting spectral intensity pattern resembles a cardioid (see Figure 1) which can be classified into the corresponding frontal focal plane incidence angle [1]. The specific algorithms implemented for this project had originally been coded during the summer of 1990 as stand-alone Fortran programs. They include:

Statistical clustering algorithm (ZCLUS) [2],

Bidirectional associative memory (BAM) [2],

Anderson associative memory (AND) [2],

Two-layer perceptron (TLP) [2], and

Vector quantization (VQ) [3].

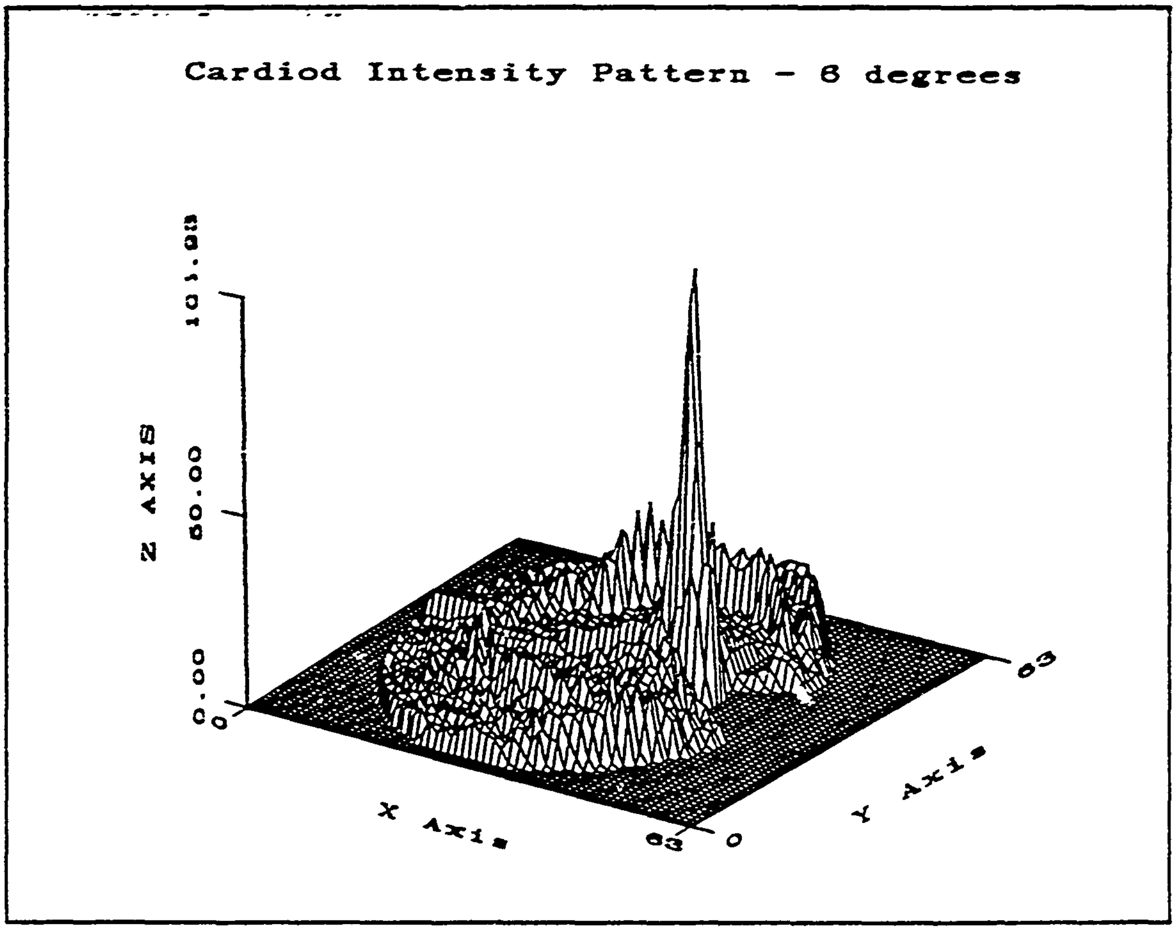


Figure 1 xprism3 plot of cardioid spectral intensity pattern.

Khoros

The Khoros system [4], implemented at the University of New Mexico as an ongoing research project, is an integrated software development environment for multidimensional information processing and data visualization. The system consists of a number of specialized tools for building programming applications. These include an editor for specifying the user interface for applications, code generators to create all the user interface code for both graphical and command-line user interfaces, and source configuration and management tools. Applications created with the tools and supported as part of the Khoros system include over 260 programs for processing image/signal information and for data display and manipulation. The most significant component of the Khoros system in the visual language, **cantata,** which provides a graphical programming interface to the applications.

*Visual programming* [5] is a subject of current active research aimed at reducing some of the difficulties involved in creating and using computer programs. It represents an attempt to exploit our nonverbal capabilities by combining the disciplines of interactive graphics, computer languages, and software engineering. Visual languages have the potential to dramatically enhance the communication between human and computer by providing a more intuitive interface to programming. As used in **cantata**, programs are constructed as *data flow graphs*, or block diagrams, which are already familiar to scientists and engineers. The nodes represent block processes of large granularity, such as filtering or classification algorithms, so that solutions to problems can be configured at a high level without the user needing intimate knowledge of the details of implementing a specific algorithm.

Figure 2 illustrates a typical neural network problem using two programs that were developed for this project, **zclus_t** and **zclus_c**. Input pairs are fed into the **zclus_t** node for training the network. The result (a weight matrix) is input to the **zclus_c** node, along with the vector(s) to be classified and an optional desired output vector, for testing. Classification results are shown in the ASCII text window. The

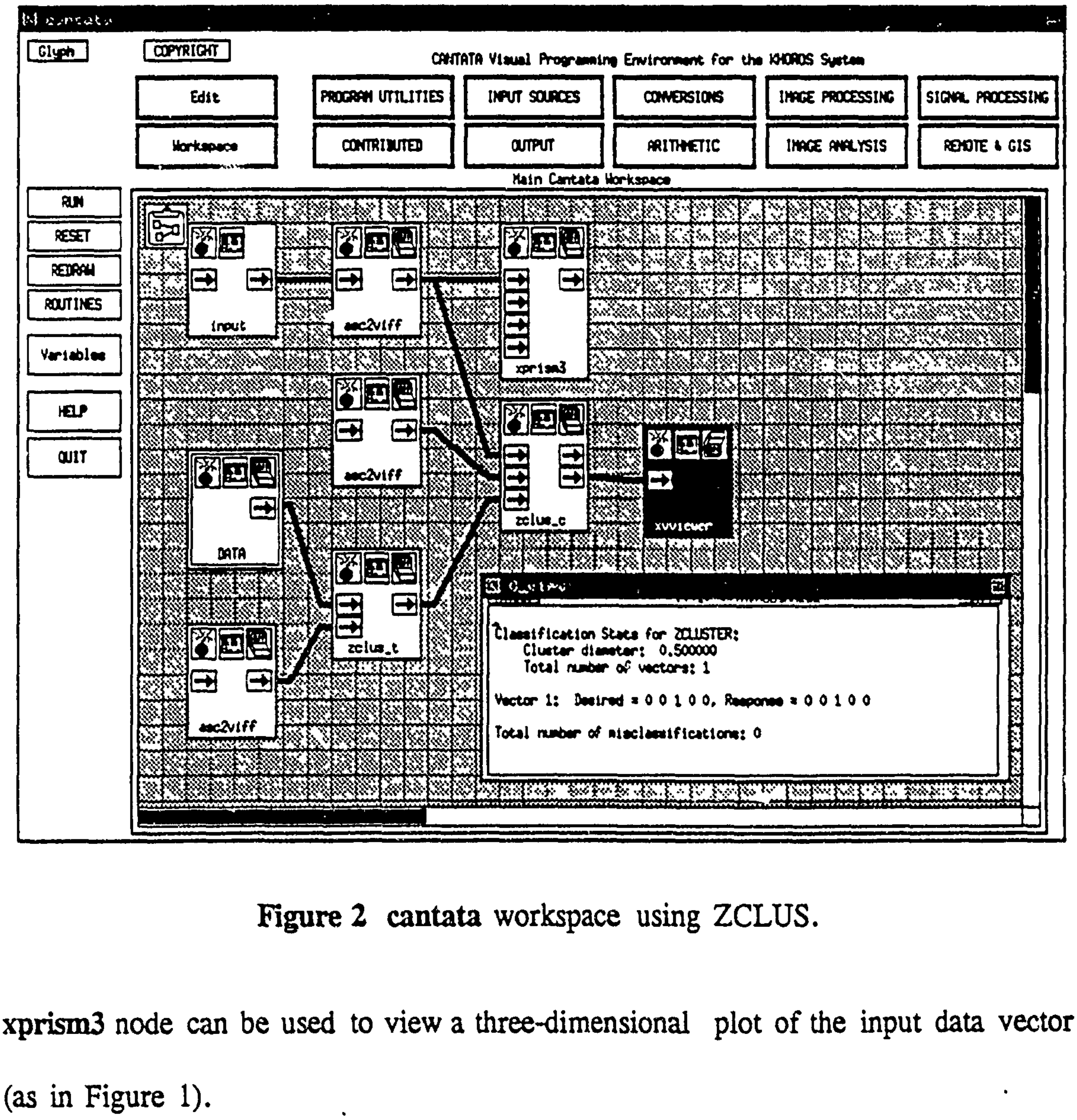


**Figure 2 cantata** workspace using ZCLUS.

**xprism3** node can be used to view a three-dimensional plot of the input data vector (as in Figure 1).

## APPROACH

To integrate the Fortran programs into the Khoros environment, the following steps were identified (which are described in more detail below):

(1) Break the original Fortran code up into two programs, one for *training* and the second for *classification.*

(2) Create a *Graphical User Interface* (GUI) for the programs which will be used to collect the input parameters.

(3) Write a *C driverprogram* to input and output the data (in the form of a VIFF structure) and do any error checking, preprocessing, and initialization required, then call the Fortran routines to actually do the training and classification.

(4) Use the *Khoros tools* to generate all the code to interface the above components and create executable programs which can be accessed via the **cantata** visual language component of Khoros.

(5) Write *documentation* on how to use the programs.

(1) The original Fortran programs consisted of an interactive menu portion during which the user could enter algorithm parameters and I/O data filenames, select training or testing mode, and display output. Since all of this was to be replace by the **cantata** graphical user interface code, the only portion of the original code

that was needed was the part to actually accomplish the *training* and *classification* for the neural algorithm. These functions comprise two distinct steps; therefore, I decided to implement them as two different modules. Another advantage of this separation is that once a network has been trained, the resulting weight matrix can be saved, then used to classify any number of sets of test data.

(2) The graphical user interface (GUI) utilized by processing routines implemented under Khoros consists of a *subform/pane*. Each subform contains the information for a group of related routines from the Khoros libraries. Figure 3 shows the 'Neural Network' subform created for this project. The pane for the 'Statistical Clustering Algorithm - Training' program, **zclus_t**, is shown on the right side of the subform. The GUI is defined by a *User Interface Specification* (UIS) which is an ASCII file composed of a sequence of lines following a strict syntactical structure, each of which describes a separate part of the user interface. The parameters in each line control the data type, position, size, default values, variable names, command-line switches, and action controls for that item. Figure 4 gives an excerpt of the UIS for the 'Neural Network' subform with the **zclus_t** pane. All the input parameters needed to configure the neural network for training are listed, their values to be filled in when the module is selected for use.

A UIS may be created in one of two ways, or (as often happens) a combination of both. The Khoros graphical UIS editor composer can be used by an application developer to interactively select appropriate options describing the

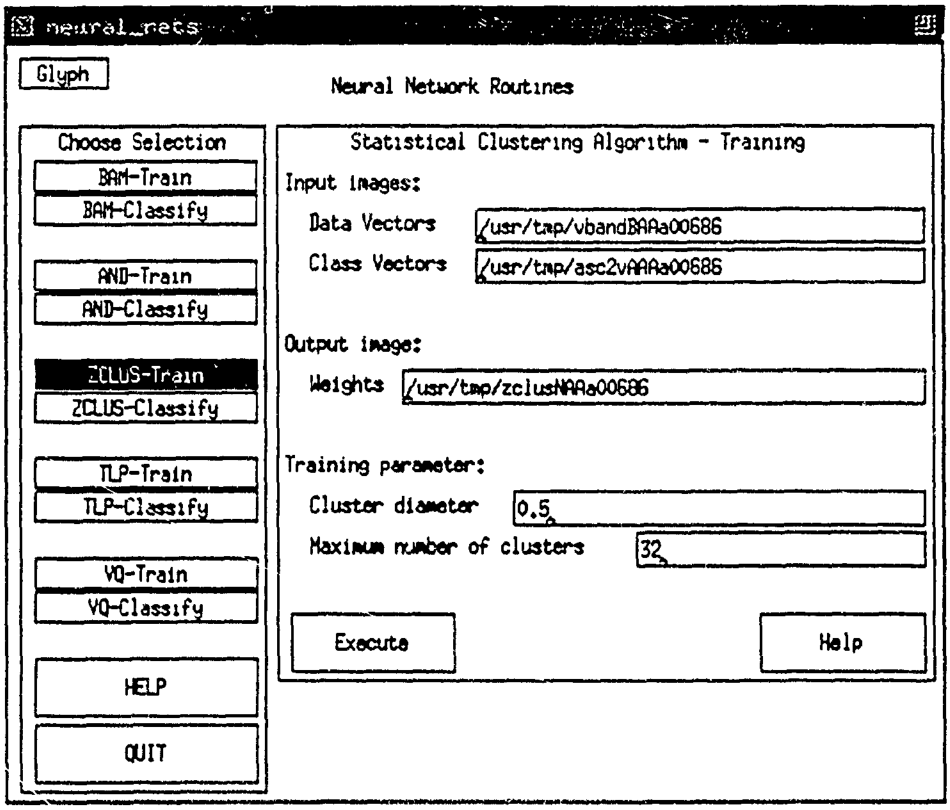


**Figure 3** Subform for neural network algorithms.

desired user interface, which are automatically translated into the UIS file format, then interpreted and displayed on the screen. Alternately a standard text editor can be used to create the UIS file directly (often starting with a previously defined UIS from a similar application). In this case, a prototype of the graphical interface can be interpreted and then displayed by the UIS **preview** program and modified until its appearance is as desired. Syntax checking is automatically done on each entry for the new form and erroneous or illegal specifications are rejected.

(3) The next step is to create the program code that contains the actual functionality of the operator. The Khoros processing routines are typically written

```
-M 1 0 100x40+10+20 +25+1 'Neural Network Routines' neural_nets
 -G 1 20x38+1+2 +2+0 'Choose Selection'
  -g 1 1 18x1+1+1 'BAM-Train'
  -g 1 0 18x1+1+2 'BAM-Classify'
  -g 1 0 18x1+1+4 'AND-Train'
  -g 1 0 18x1+1+5 'AND-Classify'
  -g 1 0 18x1+1+7 'ZCLUS-Train'
  -g 1 0 18x1+1+8 'ZCLUS-Classify'
  -g 1 0 18x1+1+10 'TLP-Train'
  -g 1 0 18x1+1+11 'TLP-Classify'
  -g 1 0 18x1+1+13 'VQ-Train'
  -g 1 0 18x1+1+14 'VQ-Classify'
  -H 1  18x2+1+16 'HELP' 'guide help' KHOROS_CONTRIB/doc/cantata/subforms/neural_nets/help
  -Q 1 0 18x2+1+18 'QUIT'
 -E

 -P 1 0 80x38+22+2 +3+0 'Statistical Clustering Algorithm - Training' zclus_t
  -b +0+1 'Input images:'
  -I 1 0 0 1 0 1 50x1+2+2 +0+0 ' ' 'Data Vectors ' 'training data' i1
  -I 1 0 0 1 0 1 50x1+2+3 +0+0 ' ' 'Class Vectors' 'output classes' i2
  -b +0+5 'Output image:'
  -O 1 0 0 1 0 0 50x1+2+6 +0+0 ' ' 'Weights' 'weights file' wt
  -b +0+8 'Training parameter:'
  -f 1 0 0 1 0 50x1+2+9 +0+0 1 1 0 'Cluster diameter' 'cluster diameter' cld
  -i 1 0 0 1 0 50x1+2+10 +0+0 2 2 32 'Maximum number of clusters' 'max no. clusters' mcl
  -R 1 0 1 13x2+1+12 'Execute' 'do operation' zclus_t
  -H 1  13x2+39+12 'Help' 'man page for zclus_t' KHOROS_CONTRIB/doc/manpages/zclus_t.1
 -E


-E
```

**Figure 4** *UIS* file for 'Neural Network' subform.

as a main program which then calls a library routine. The structural organization I chose for the neural routines is as follows:

MAIN: Input/output of data and parameters plus error checking.

LIBRARY: Preprocessing of data and memory allocation. Main loop for training/testing of input vectors.

FORTRAN: Train or classify (a vector).

To be compatible with the image/signal processing routines currently available within Khoros, new modules need to use the same data structure for input/output data. The *Khoros Visualization/ Image File Format* (VIFF) and internal data

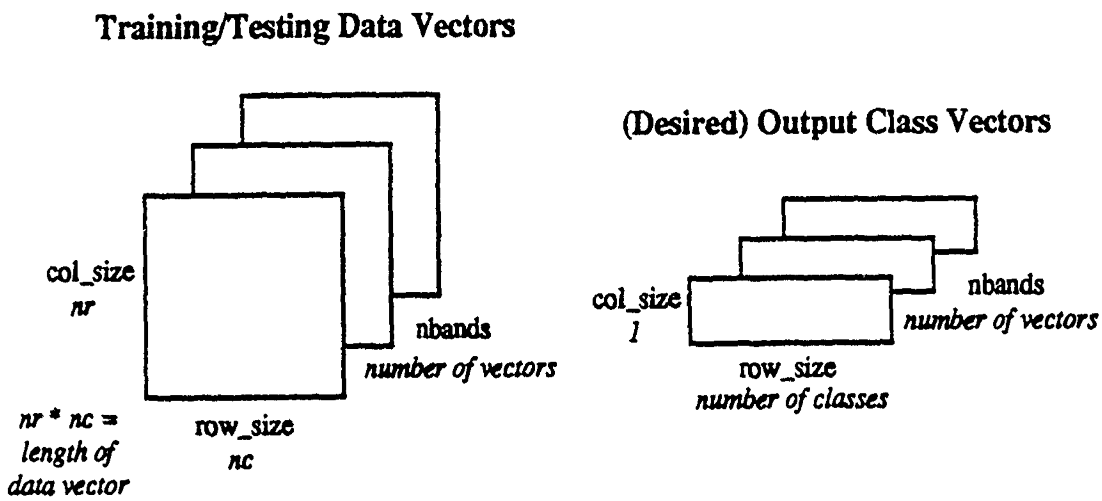


**Figure 5** VIFF image data structure and neural network input vector interpretation.

structure was designed to facilitate the exchange of data, not only between Khoros routines, but also between researchers exchanging data. Data input/output for a module is done in the main driver program (written in C) using the Khoros utilities to read, write, and manipulate the VIFF data structure. The VIFF structure is organized as 1024 bytes of header followed by map(s), location, and image data. An image is a two-dimensional, multiband array of data which may be interpreted as in Figure 5.

Input training and testing data for a neural network routines consists of pairs of vectors: the data and the desired output classification. To store this information in the VIFF structure, I chose to represent the vectors as multiband images. Since the original test data for the project consists of intensity values over a two-dimensional area, this produces an very natural representation with individual vectors converted to VIFF images then combined together (see Figure 5). The library routine then extracts the vectors from the image structure to pass to the Fortran subroutines for processing.

(4) The C code for the main driver and library are included in a *Program Specification* file, which may be created with the assistance of **composer** or by using a standard text editor. In this file, the application developer provides additional information that cannot be included in the UIS, such as program documentation, syntax for library calls, as well as the specific code segments that are to appear in the application program. Figure 6 gives the Program Specification for **zclus_t**. This is used, along with the UIS (Figure 4), by the code generators to create the complete code for the new module.

The code generators for Khoros act as programmer's assistants by providing aid in the tasks that prove to be invariant across applications. These include generation of modular code to extract user input from the user interface, and creation of the C structures needed to mediate between the application program and the user interface, plus the code to initialize these structures. Also generated are the generic application drivers, as well as consistently formatted manual pages and usage statements.

Continuing with the ZCLUS training algorithm as an example, the code generator **ghostwriter** takes as input the UIS file (`zclus_t.pane`) and Program Specification (`zclus_t.prog`) and produces the following files:

```
-AUTHORS
W J. Zimmermann, Carla Williams
-AUTHORS_END

-SHORT_PROG_DESCRIPTION
A statistical clustering algorithm
-SHORT_PROG_DESCRIPTION_END

-SHORT_LIB_DESCRIPTION
A statistical clustering algorithm
-SHORT_LIB_DESCRIPTION_END

-MAN1_LONG_DESCRIPTION
.LP
1.  Introduction
.PP
The zclus_t program is the training portion of a vector clustering
program written by W J Zimmermann  The clustering algorithm clusters
vectors within a user specified diameter and then classifies vectors according
to which cluster it falls into.
.sp
.LP
2.  Theory:
.PP
The vector clustering algorithm determines vector length using a
one-norm (|x| is defined as sum(abs(xi)) for all i=n where n is the dimension
of x)  During classication an input vector (dim n) is compared to the columns
of a weight matrix (dim nxm).  The closest column to the weight matrix is
defined below:
.DS

given
     W = nxm weight matrix = (w1:w2:w3:   :wm)
     X = n dim input vector

    wc = closest column
       = wk s.t  |X-wk| = min (|X-w1|,|X-w2|,     |X-wm|)
         and wk is a column of W
         and |X| is defined as the one-norm of X

.DE
.LP
Since X is closest to the column wc, X is considered to be in the same cluster
as wc.
.sp
.PP
The weight matrix is developed by defining a "cluster diameter" (to be
explained later).  A vector is arbitrarily selected from the set of vectors to
establish the first cluster (i e  w1 = X1)   The remaining vectors are then
compared to the column of the weight matrix.  If the one-norm of the difference
of a vector X and the column is less than the cluster diameter,  then the column
is updated by adding the vector   If the one-norm of the difference is greater
than the cluster diameter, then the vector defines its own cluster.  This vector
will form a new column in the weight matrix   Vectors are then tested against
both columns  creating new columns or adding to the closest column, until the
vector set is exhausted.  At this point, each column is divided by the total
number of vectors added into the column  producing a sort of "mean" vector per
column   The desired effect is that each column of the weight matrix defines the
center of a cluster of vectors which has a diameter equal to the cluster
diameter
.sp
.PP
The actual cluster diameter you should choose depends entirely on the
input vector set and the number of classes you want   The number should be small
enough such that there is definition between vectors, but large enough so that
each vector does not define its own cluster   Finding this number may take some
experimentation or some analysis
.sp
.PP
After the weight matrix has been developed, a correlation matrix is
formed    Each input vector is again compared against the columns of the first
weight matrix and another vector (the first layer output) is generated which has
a dimension equal to the number of columns in the weight matrix   All the
elements of the first layer output are zero except the element that corresponds
to the nearest column of the weight matrix, which is 1   The program then finds
the outer product of the first layer output and the desired output for the
particular vector   A correlation matrix is then found by summing all the outer
products over the entire vector set   The correlation matrix simply maps the
computer's clustering output to the desired output
.sp
.PP
The computer classifies by comparing an unknown vector to each column
of the weight matrix.  The first layer output is generated and is multiplied by
the correlation matrix.  The resulting output is the output class vector
consistent with the user's classification scheme
.sp
.PP
The major problem with this particular algorithm is that if, during
training, the user specifies that two vectors are in separate classes but they
both lie within the same cluster  the algorithm will be unable classify any
vector within that cluster properly   The user must be consistent with the
computer as far as which vectors lie in separate clusters
.LP
3  Program parameters:
.PP
DATA VECTORS: a VIFF image that contains the input
portion of the training pairs.  Each vector defines a band where the
total number of elements in each vector = number of rows * number of columns.
.PP
CLASS VECTORS: a VIFF image that contains the output portion of the training
pairs   Each vector defines a band with the elements stored in a column
The order and number of class vectors must match that of the input vectors
.PP
WEIGHTS: a VIFF image which is used to store the derived weights
This file is to be used as an input to the classification program
.PP
CLUSTER DIAMETER: a floating point number which is used by the program to
the "size" of the vector clusters (see discussion above)
-MAN1_LONG_DESCRIPTION_END

-MAN1_EXAMPLES
zclus_t -i1 invect av -i2 outvect av -wt weight av -eld 1 6
-MAN1_EXAMPLES_END

-MAN1_RESTRICTIONS
All input images MUST be of data storage type FLOAT.
The output "weight" image is data storage type FLOAT.
-MAN1_RESTRICTIONS_END

-MAN1_SEE_ALSO
zclus_c(1)
-MAN1_SEE_ALSO_END

-MAN3_LONG_DESCRIPTION
(same as MAN1_LONG_DESCRIPTION)
-MAN3_LONG_DESCRIPTION_END

-MAN3_RESTRICTIONS
All input images MUST be of data storage type FLOAT
The output "weight" image is data storage type FLOAT
 MAN3_RESTRICTIONS_END

-MAN3_SEE_ALSO
lzclus_c(3)
-MAN3_SEE_ALSO_END

-USAGE_ADDITIONS
-USAGE_ADDITIONS_END

-INCLUDE_INCLUDES
-INCLUDE_INCLUDES_END

-INCLUDE_ADDITIONS
-INCLUDE_ADDITIONS_END

-INCLUDE_MACROS
-INCLUDE_MACROS_END

-MAIN_VARIABLE_LIST
struct xvimage  *data,        /* input training data */
                *vect,        /* desired output vectors */
                *wtimg,       /* output weight matrix */
                *readimage(),
                *createimage();

int    netv,                      /* number of training pairs */
       LOA,                       /* length of data vector */
       LOB,                       /* length of output vector */
       NELL=33;                   /* size of hidden layer? */
char   *program = "zclus_t";
-MAIN_VARIABLE_LIST_END

-MAIN_BEFORE_LIB_CALL
   if (check_args())
   {
      fprintf (stderr,"%s:  Illegal arguments on command line.\n"  program);
      exit(1);
   }

/*  Read and error check input training data  */
   if ((data = readimage (zclus_t->i1_file)) == NULL)
   {
      (void) fprintf (stderr,"%s:  Cannot read training data (%s) \n",
                         program, zclus_t->i1_file);
      exit(1);
   }
   if ( !(propertype (program, data, VFF_TYP_FLOAT, TRUE)) )
   {
      fprintf (stderr,"%s:  Data storage type for training data must be FLOAT "
               program);
      exit(1);
   }
   (void) proper_num_images (program, data, 1, TRUE);
   (void) proper_map_enable (program, data, VFF_MAP_OPTIONAL  TRUE);

   netv = data->num_data_bands;
   LOA = (data->col_size) * (data->row_size);

/*  Read and error check desired output vectors  */
   if ((vect = readimage (zclus_t->i2_file)) == NULL)
   {
      (void) fprintf (stderr "%s:  Cannot read class vectors (%s) \n"
                         program, zclus_t->i2_file);
      exit(1);
   }
   if ( !(propertype (program  vect, VFF_TYP_FLOAT, TRUE)) )
   {
      fprintf (stderr,"%s:  Data storage type for class vectors must be FLOAT "
               program);
      exit(1);
   }
   (void) proper_num_images (program, vect, 1, TRUE);
   (void) proper_map_enable (program  vect, VFF_MAP_OPTIONAL, TRUE);

/* Check that number training vectors equals number desired output vectors */
   if ( !(netv == vect->num_data_bands) )
   {
       fprintf (stderr "%s:  Output vector image does not contain correct number
       fprintf (stderr, "Should have %d bands, but contains %d bands\n",
               netv, vect->num_ ata_bands);
       exit(1);
   }
   LOB = vect->row_size;

/*  Create the weight image  */
   wtimg = createimage ((unsigned long) NELL,
                        (unsigned long) 1,
                        (unsigned long) VFF_TYP_FLOAT,
                        (unsigned long) 1,
                        (unsigned long) (LOA+LOB),
                        "Weight image created by zclus_t",
                        (unsigned long) 0,
                        (unsigned long) 0,
                        (unsigned long) VFF_MS_NONE,
                        (unsigned long) VFF_MAPTYP_NONE,
                        (unsigned long) VFF_LOC_IMPLICIT,
                        (unsigned long) 0);
   if (wtimg == NULL)
   {
      (void)fprintf(stderr "%s:  Unable to allocate weight image:\n",
                    program);
      exit(1);
   }
   wtimg->fspare1 = zclus_t->eld_float;
   free (wtimg->imagedata);
 MAIN_BEFORE_LIB_CALL_END

-MAIN_LIBRARY_CALL
   if (! lzclus_t (data, vect  wtimg, zclus_t->eld_float  NELL))
   {
      (void)fprintf(stderr "%s:  lzclus_t failed \n",program);
      exit(1);
   }
-MAIN_LIBRARY_CALL_END

-MAIN_AFTER_LIB_CALL
/*  Output weight image  */
   writeimage(zclus_t->wt_file, wtimg);
-MAIN_AFTER_LIB_CALL_END

-LIBRARY_INCLUDES
-LIBRARY_INCLUDES_END

-LIBRARY_INPUT
 IP "data" 15
the input data vectors used for training
 IP "vect" 15
the desired output vectors corresponding to the input data
 IP "clustdia" 15
the cluster diameter value
 IP "NELL" 15
the maximum number of clusters
-LIBRARY_INPUT_END
```

Figure 6  *Program Specification* for zclus_t.

```
-LIBRARY_OUTPUT
 IP "wtimg" IS
the resulting weight matrix after training.
-LIBRARY_OUTPUT_END

-LIBRARY_DEF
int  lzclus_t (data, vect, wtimg, clustdis, NELI)

struct  xvimage  *data, *vect, *wtimg;
float   clustdis;
int     NELI;
-LIBRARY_DEF_END

-LIBRARY_CODE
{
   int    notv, LOA, LOB, NOC, sizeW, i, j, k, index, index2;
   int    *IBvec, *LIV  *noelinec;
   float  *At, *Avec  *Bvect;
   float  *W, *Wt1, *Wt2, *Txnorm, clusterdis;
   char   *program = "lzclus_t";

   void  mat1gen_(), genliv_(), mat2gen_();

/*  Store clustdis as a float value for call to FORTRAN routine
    (was upcast to double when passed to library routine)  */
   clusterdis = (float)clustdis;

/*  Extract training data from image structure  */
   At = (float *) data->imagedata;
   notv = data->num_data_bands;                       /* number training vectors */
   LOA = (data->col_size) * (data->row_size);  /* length of data vector */

/*  Extract desired output vectors from image structure  */
   Bvect = (float *) vect->imagedata;
   LOB = vect->row_size;                              /* length of output vector */

/*  Allocate memory for weight matrices and initialize to zeros  */
   sizeW = NELI * (LOA + LOB);
   if ((W = (float *)malloc((unsigned)sizeW*sizeof(float))) == NULL)
   {
      (void)fprintf(stderr,"%s:  unable to allocate W matrix \n",program);
      exit(1);
   }
   for (i=0; i<sizeW; i++)
      W[i] = 0.0;
   Wt1 = W;
   Wt2 = & W[LOA*NELI];

/*  Allocate memory for Fortran arrays  */
   if ((IBvec = (int *)malloc((unsigned)LOB*sizeof(int))) == NULL)
   {
      (void)fprintf (stderr,"%s:  Unable to allocate IBvec array \n" program);
      exit(1);
   }
   if ((LIV = (int *)malloc((unsigned)NELI*sizeof(int))) == NULL)
   {
      (void)fprintf (stderr,"%s:  Unable to allocate LIV array \n" program);
      exit(1);
   }
   if ((noelinec = (int *)malloc((unsigned)NELI*sizeof(int))) == NULL)
   {
      (void)fprintf (stderr,"%s:  Unable to allocate noelinec array \n" program)
      exit(1);
   }
   if ((Txnorm = (float *)malloc((unsigned)NELI*sizeof(float))) == NULL)
   {
      (void)fprintf (stderr,"%s:  Unable to allocate Txnorm array \n",program);
      exit(1);
   }

/*  Process input data training vectors, one at a time  */
   NOC = 0;                                /* counter for number of clusters */
   for (k=0; k<notv; k++)
   {
     /*  Set desired output vector values as 1 or 0  */
      for (j=0; j<LOB; j++)
      {
         index = k*LOB + j;
         if (Bvect[index] > 0.2)
            IBvec[j] = 1;
         else
            IBvec[j] = 0;
      }
      Avec = & At[LOA*k];

      (void) mat1gen_(&LOA, &clusterdis, &NELI, &NOC, Avec, Wt1  noelinec, Txnor
      (void) genliv_(&LOA, &NELI, &NOC, Avec, Wt1, LIV, Txnorm);
      (void) mat2gen_(&LOB, &NELI, &NOC, Wt2, LIV, IBvec);
   }

/*  Compact weight matrices and insert weights into image structure  */
   if (NOC < NELI)
   {
      for (j=0; j<LOB; j++)
         for (i=0; i<NOC; i++)
         {
            index = LOA*NOC + j*NOC + i;
            index2 = j*NELI + i;
            W[index] = Wt2[index2];
         }
   }

   wtimg->imagedata = (char *) W;
   wtimg->col_size = NOC;
   wtimg->num_data_bands = LOA + LOB;
   wtimg->subrow_size = LOB;

/*  Cleanup  */
   if (IBvec != NULL)  free ((char *)IBvec);
   if (LIV != NULL)  free ((char *)LIV);
   if (noelinec != NULL)  free ((char *)noelinec);
   if (Txnorm != NULL)  free ((char *)Txnorm);

   return(1);
}
-LIBRARY_CODE_END

-LIBRARY_MODS
-LIBRARY_MODS_END
```

Figure 6 (cont.) *Program Specification* for zclus_t.

Main program source: `zclus_t.c`

Library routine source: `lzclus_t.c`

Header file: `zclus_t.h`

Main program manpage: `zclus_t.1`

Library routine manpage: `lzclus_t.3`

Template configuration file: `zclus_t.conf`

plus *make* utility files: `Imakefile` and `Makefile` for compiling the programs.

(5) Documentation for the new modules was provided by Paul Wheeler and then included in the Program Specification to be used to generate manual pages and on-line help, as described above.

(6) Installing the program into the Khoros environment should be merely a matter of running the installation program to automatically put all the files in the correct place in the Khoros directory structure. Unfortunately, the **kinstall** program does not yet work correctly with contributed routines, therefore, the installation had to be done manually. This problem should be addressed by the Khoros development group for the next patch to the system.

## PROBLEMS

In retrospect, the first step should have been to verify and document the original Fortran programs. We had assumed that the programs were complete and correct as they stood, but apparently they had not bee thoroughly debugged and tested. Consequently, we ended up rewriting some of the Fortran code during the middle of transforming a routine. This caused some doubt about the reliability of the final programs.

One of the major difficulties encountered in trying to separate the original Fortran code was the that there was no clean separation between input/output of data and the actual processing. This is required for Khoros modules, and so those portions of the code had to be rewritten as part of the C Library routine. In addition, the data file format required by the Fortran programs for the input training/testing pairs assumed that the data and desired output vectors were mixed together. This would require the duplication of raw data into another format. I felt it would be much more reasonable to be able to input original data independently of the desired output classes, and so this modification had to be included in the code rewrite.

The exclusive use of common blocks of global values in the Fortran code instead of passing arguments, made it difficult to identify required parameters (as opposed to bogus variables) and to determine the interdependencies of values. There do exist software tools to assist with tasks of this nature, but they were not readily available for our use.

Since Fortran does not support dynamic allocation of memory, all arrays in the original Fortran programs were dimensioned to some fixed maximum size. I felt this could pose a severe limitation on the usefulness of the developed routines, so decided to replace them with variable dimensioning. This mean that all arrays had to be declared and memory allocated in the C Library portion of code, then passed to the Fortran subroutines.

The lack of adequate documentation in the original code often left me guessing as to the intended purpose of several segments of code.

Final note--as is usual when working with newly release software, there were several bugs in the Khoros programs which initially caused frustration in trying to use the system. In addition the computer on which the work was done had inadequate secondary memory to contain all the software needed for a complete working environment (the X Windows and Khoros systems), and an older version of the operating system introduced incompatibilities until it was replaced half-way through the project.

## CONCLUSION

The Khoros system offers many advantages for supporting the desired neural network environment. The **cantata** visual programming language provides an intuitive design platform conducive to "what if" experimentation and learning. The software development tools facilitate the importation of new algorithms as operators within the visual language. The new neural processing modules can be used in conjunction with an extensive library of routines for image/signal processing and data visualization.

On a personal level, the work I did was interesting and relevant to my Ph.D. research, which was to identify features needed by a developmemt environment for a visual programming language to aid in the design and implementation of operators for new application domains.

## REFERENCES


[1] S. A. Anderson, W. J. Zimmermann, J. Schruben, A. S. Heger, T. L. Payne, "Neural Network Environment for Signal Processing and Pattern Recognition of Large Scale Data," *Proceedings of the Second Workshop on Neural Networks: Academic/Industrial/NASA/Defense*, February 11-13, 1991, pp. 483-489.

[2] W. J. Zimmermann and S. A. Anderson, "Determination of Angle of Arrival Using Associative Neural Networks," *Proceedings of the Second Workshop on*

*Neural Networks: Academic/Industrial/NASA/Defense*, February 11-13, 1991, pp. 499-507.

[3] J. S. Schruben and S. A. Anderson, "Detection of Laser Beam Incidence Angle via Vector Quantization," *Proceedings of the Second Workshop on Neural Networks: Academic/Industrial/NASA/Defense*, February 11-13, 1991, pp. 491-497.

[4] J. R. Rasure and C. S. Williams, "An Integrated Data Flow Visual Language and Software Development Environment," *Journal of Visual Languages and Computing*, Vol. 2, No. 3 (Sept. 1991), to appear.

[5] B. Myers, "The State of the Art in Visual Programming and Program Visualization," *Journal of Visual Languages and Computing*, Vol. 1, No. 1 (Mar. 1990), pp. 97-123.

APPROVED

# STRESS WAVE TRANSMISSION IN PARTIALLY SATURATED SOILS

Kara L. Olen
Graduate Student
Master of Science Program
Virginia Polytechnic Institute and State University

## ABSTRACT

Centrifuge testing was conducted at Tyndall Air Force Base to study stress wave transmission through partially saturated sands under blast loading conditions. A total of 24 tests were conducted in moist soil. Specimen saturation levels ranged from 17% to 70%. Charge weights of 220 mg, 440 mg, 660 mg, and 880 mg were utilized. The weight of the charge, depth of the explosion, and level of acceleration were varied for each test to model 1-g explosions ranging from 15 lbs. to 500 lbs. and occurring at a depth of 30 ft. Test results show that there is a definite correlation between the saturation level of the soil and the peak stress and velocity of the transmitted wave.

## INTRODUCTION

The study of stress wave transmission in partially saturated soils under blast loading conditions is of great importance to the United States Air Force. Many strategic structures are buried ones which require compacted backfill around and above them. The study and evaluation of stress waves generated by penetrating explosive weapons in such backfill is therefore crucial in assessing the safety of these underground structures. Extensive centrifuge modeling was conducted at Tyndall Air Force Base to study the relationship between soil saturation level and stress wave transmission.

DISCUSSION

Partially saturated sand specimens, each containing a buried charge, were accelerated to various g- levels and detonated. Instrumentation buried in the sample at several locations measured both the voltage and acceleration of the blast wave induced by the explosion. Voltage was converted to stress using the stress calibration regression curve (figure 1) and wave acceleration was converted to velocity by integration.

The test sands utilized were Tyndall base sand and Ottawa 20/30 sand. The Tyndall base sand was collected from a deposit near the laboratory facility and was a very fine grained uniformly graded beach sand with $D_{50}$= 0.25 mm (+/-). The Ottawa 20/30 sand was obtained from a supplier in Ottawa, Illinois and was a medium grained, spherical, uniformly graded sand with $D_{50}$= 0.75 mm (+/-). The sand was placed in lifts into a circular aluminum container with dimensions D= 18" and h= 12". A vibrating motor with an attached circular aluminum plate was used to compact each layer from the top down to a dry unit weight of 95 pcf. Surcharge weight was added as needed to compact each lift to the inal thickness required to achieve this density.

Instrumentation was placed a distance of eight inches above the bottom of the bucket. This consisted of six or more 1000 ohm resistors and 3 20,000- g accelerometers placed in a log spiral pattern as shown in figure

2. The amount of cover over the instrumentation varied with each test. The completed sample was then loaded onto the centrifuge. A small hole was carefully drilled in the center of the moist sample and the charge was placed in it at the same depth as the instrumentation. The instrumentation was wired to a data acquisition system and the charge was wired to an electronic detonator which was triggered from the control room.

A total of 24 tests were conducted with specimen saturation levels ranging from 17% to 70%. Charge weights varied from 220 mg to 880 mg. Samples were accelerated from 19-g to 80-g? (+/-). All testing simulated 1-g explosions between 15 and 500 lbs. occurring 30 ft. beneath the ground surface. For all tests, the stress and velocity at all instruments in the specimen were calculated and recorded for evaluation.

ADDITIONAL STUDIES

Additional studies on cratering and attenuation of reflection waves were also conducted during testing.

Cratering:

Crater dimensions and volumes were measured and recorded for each test explosion. These values were compared to those obtained by previous researchers. Results of this study can be found in the AFSOR Final Report by Dr. Teresa Taylor, 1991.

Wave Attenuation:

When testing confined samples a problem often encountered is that of boundary effects. For instrumentation placed near the bucket wall, the plots of voltage vs. time showed the presence of reflection waves. Reflection waves directed back into a soil sample can frequently interfere with the incident waves and produce inaccurate data. As an additional study, several experimental materials were utilized in an attempt to attenuate reflection waves in the sample bucket. These materials will be referred to as material A, B, and C.

Material A was "No Slip" brand carpet liner. This was a foam coated elastic netting intended to be placed under carpets to prevent them from sliding on bare floors. Two layers of this material were utilized as a boundary material. When applied to the side of sample bucket (see figure 3A) it was theorized that a stress wave contacting this material would be reflected as a tension wave and a wave contacting the bucket wall would be reflected as a compression wave. In this manner the two reflection waves would cancel each other out.

Material B was "Bubble Wrap" brand packaging material. Every other bubble was deflated so that when the material was applied to the bucket wall it created a matrix pattern of alternating air pockets and aluminum surfaces as shown in figure 3B. It was again believed that tension and compression reflection waves would be generated and cancel each other out.

Material C consisted of uniformly shaped styrofoam cones approximately 3/4" tall as shown in figure 3C. It was theorized that the incident wave would be refracted within the layer of cones without re-entering the soil specimen.

All boundary materials were cut into rectangular shapes approximately 5" X 8" and were taped to the wall of the specimen bucket. For each test two of the resistors were placed a distance of 8" from the center of the bucket (approximately 1" from the wall); one being placed in front of the bucket wall and the other being placed in front of the boundary material (see figure 2).

Limited success was achieved with these materials as is shown in figures 4A, 4B, 5A, 5B, 6A, and 6B. In each of the plots of voltage vs. time where no boundary material was utilized (figures 4A, 5A, and 6A), a reflection wave can be seen immediately after the incident wave, followed by a secondary wave. When the boundary material was placed against the bucket wall (figures 4B, 5B, and 6B), these reflection waves appear to have been attenuated. However, these results are preliminary ones based on very limited testing.

It can be noticed that, for each test, wave amplitudes and arrival times of both plots are not coincident as was expected. These variations could be the result of either: 1) inconsistencies in gage placement (ie: both gages were not placed precisely eight inches from the center so that arrival times and peak voltages were not coincident); or 2) moisture variations within the sample (ie: degree of saturation was not consistent throughout the sample) due to the compaction process or desaturation of the sample during centrifuging. Further research is necessary to devise a method of more accurately placing gages, compacting moist samples without causing desaturation and assessing the desaturation characteristics of the in flight sample.

## CONCLUSION

For all tests, peak stress, peak velocity, charge weight, and scaled distance were grouped according to saturation level. From this data plots of attenuation coefficient vs. saturation level were prepared and are shown in figures 7A and 7B. These plots illustrate that the effectiveness of stress wave transmission through soil is dependent on the degree of saturation of the soil. It can be seen that the largest stress waves and highest velocities occur between 17% and 55% saturation for the Tyndall sand. Similar results were reported by Ross (1989) and Charlie and Pierce (1988) through Split Hopkinson Pressure Bar Testing. Additional testing of the Ottowa sand is necessary to determine the saturation range for optimum transmission.

STRESS CALIBRATION REGRESSION

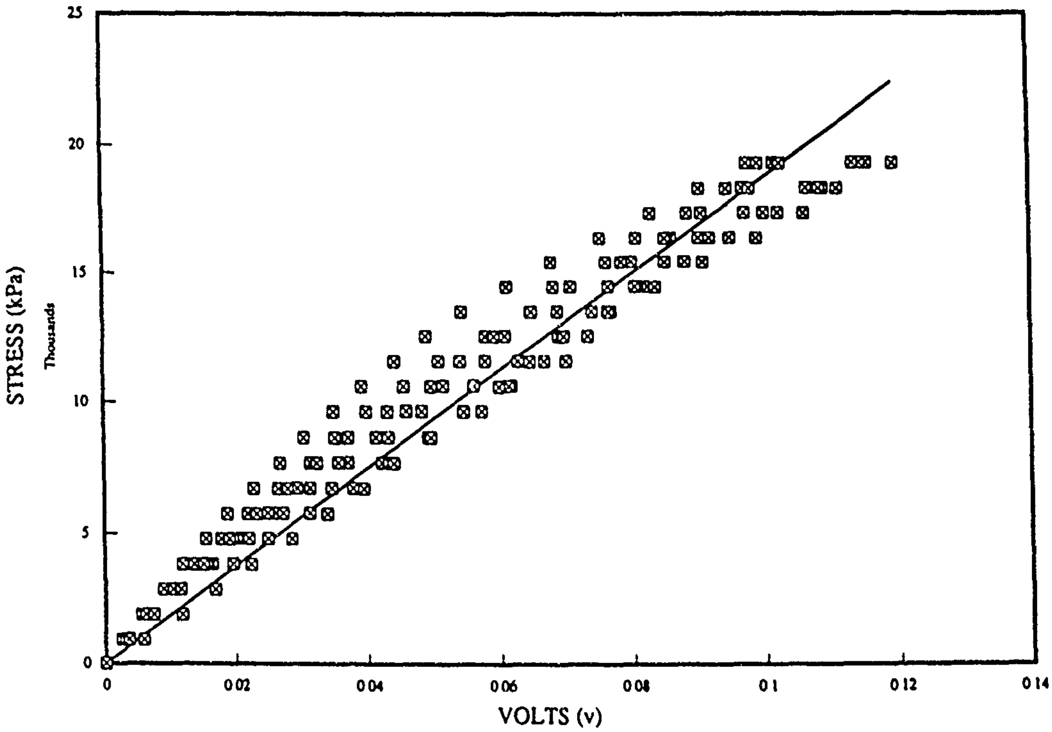


—— REGRESSION EQU: STRESS=VOLTS*187261.1

EIGHT RESISTORS PLOTTED
REGRESSION FORCED THROUGH ZERO

X COEFFECIENT : 187261.1
CONSTANT : 0
R SQUARED : 0.9469

STD ERROR OF Y EST : 1331.8
STD ERROR OF COEFFICIENT : 1718.4

FIGURE 1

Plot prepared by Andy Wals

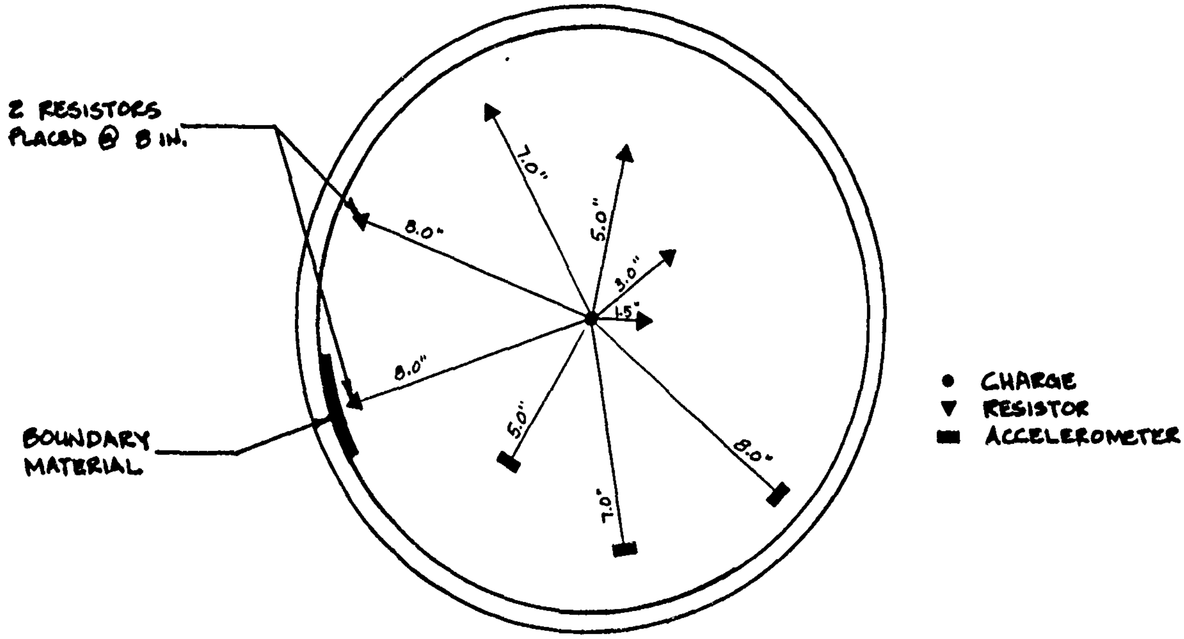


PLAN

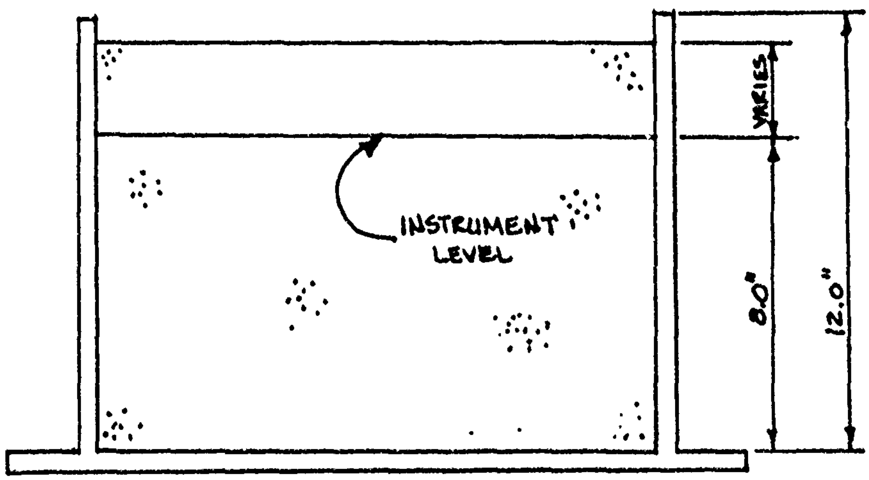


SECTION

FIGURE 2
N.T.S.

FIG. 3A

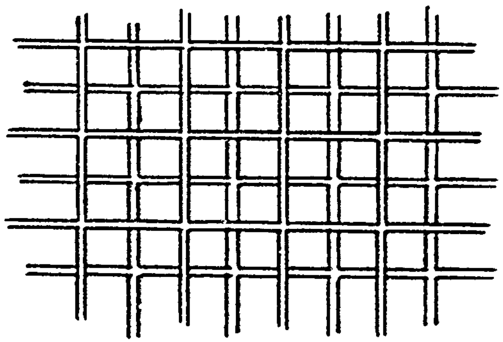

MATERIAL A

FIG. 3B

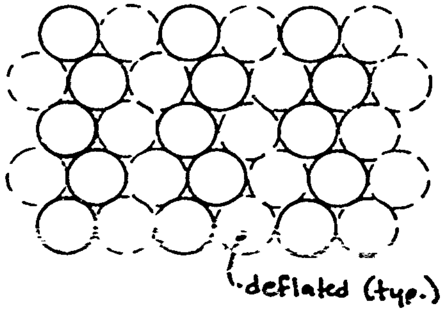


MATERIAL B

FIG. 3C

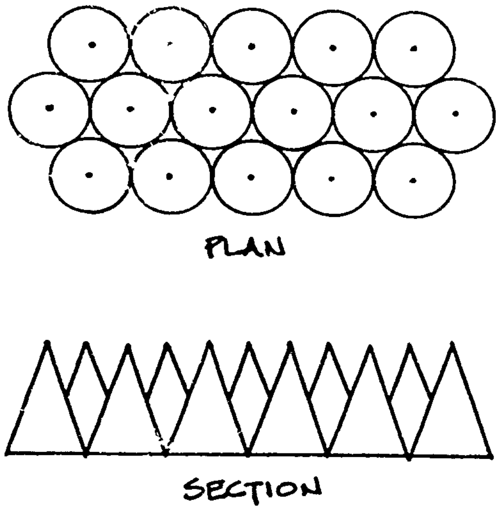


MATERIAL C

FIGURE 3 A,B, & C

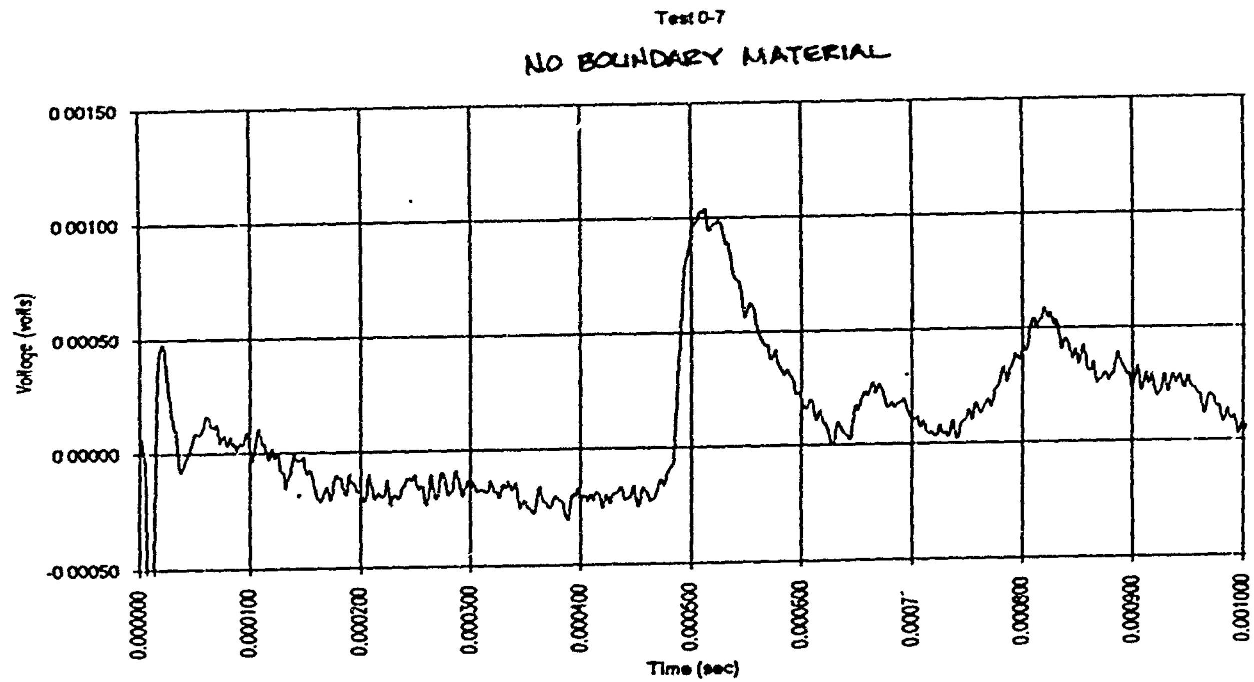
Test 0-7
NO BOUNDARY MATERIAL
0.00150
0.00100
0.00050
0.00000
-0.00050
Voltage (volts)
0.000000
0.000100
0.000200
0.000300
0.000400
0.000500
0.000600
0.0007
0.000800
0.000900
0.001000
Time (sec)

FIGURE 4A

Test 0-7

MATERIAL A

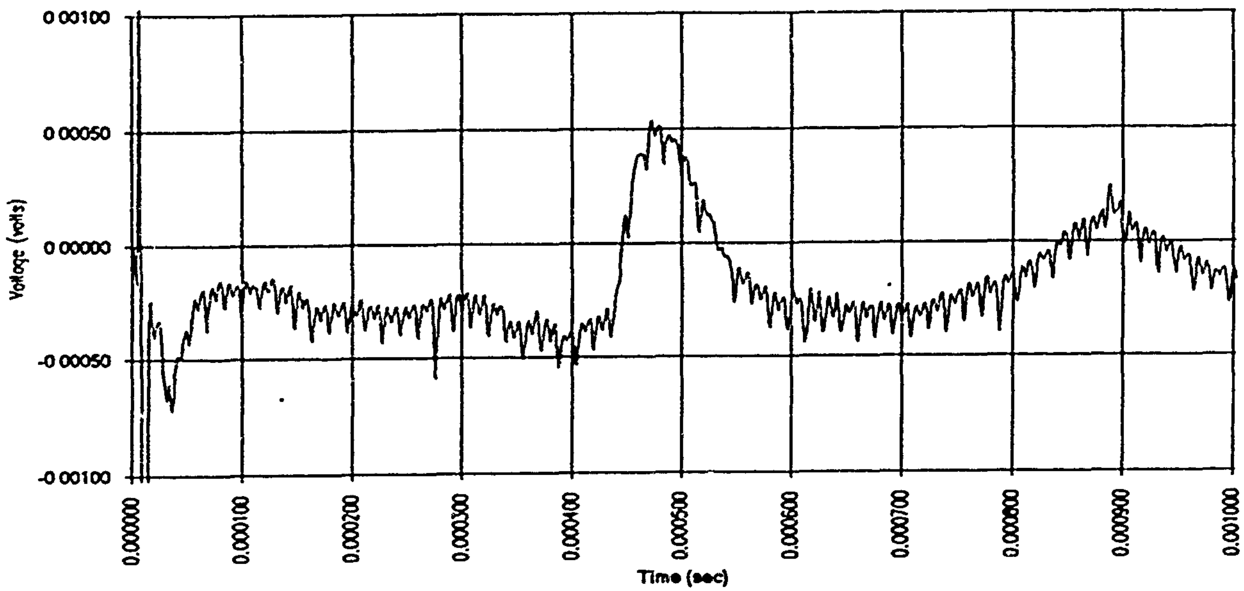


FIGURE 4B

Test 70-2

NO BOUNDARY MATERIAL

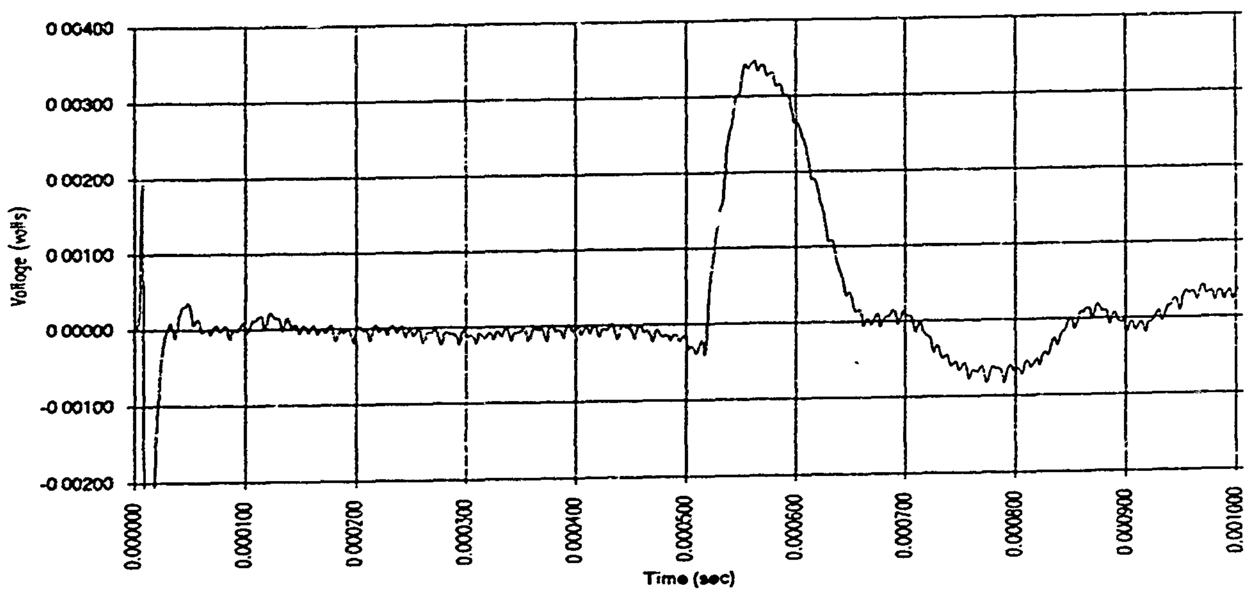


FIGURE 5A

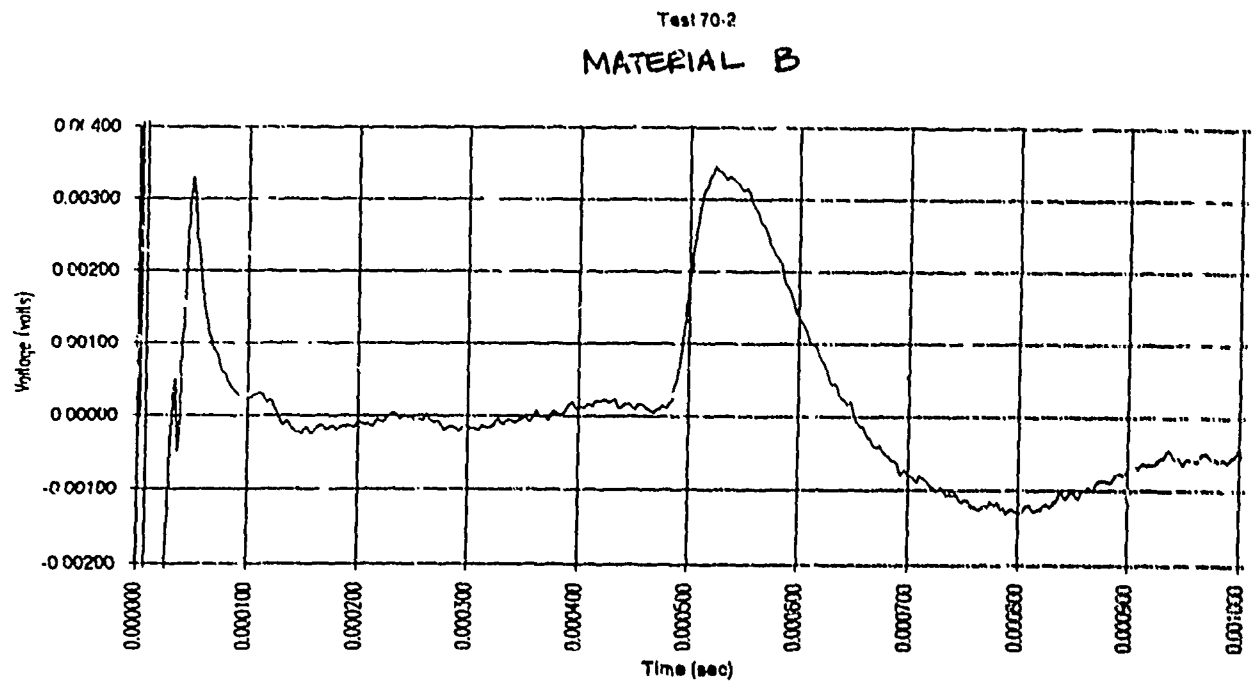

Test 70-2
MATERIAL B
Voltage (volts)
0.00400
0.00300
0.00200
0.00100
0.00000
-0.00100
-0.00200
0.000000
0.000100
0.000200
0.000300
0.000400
0.000500
0.000600
0.000700
0.000800
0.000900
0.001000
Time (sec)


FIGURE 5E

Test 70-3

NO BOUNDARY MATERIAL

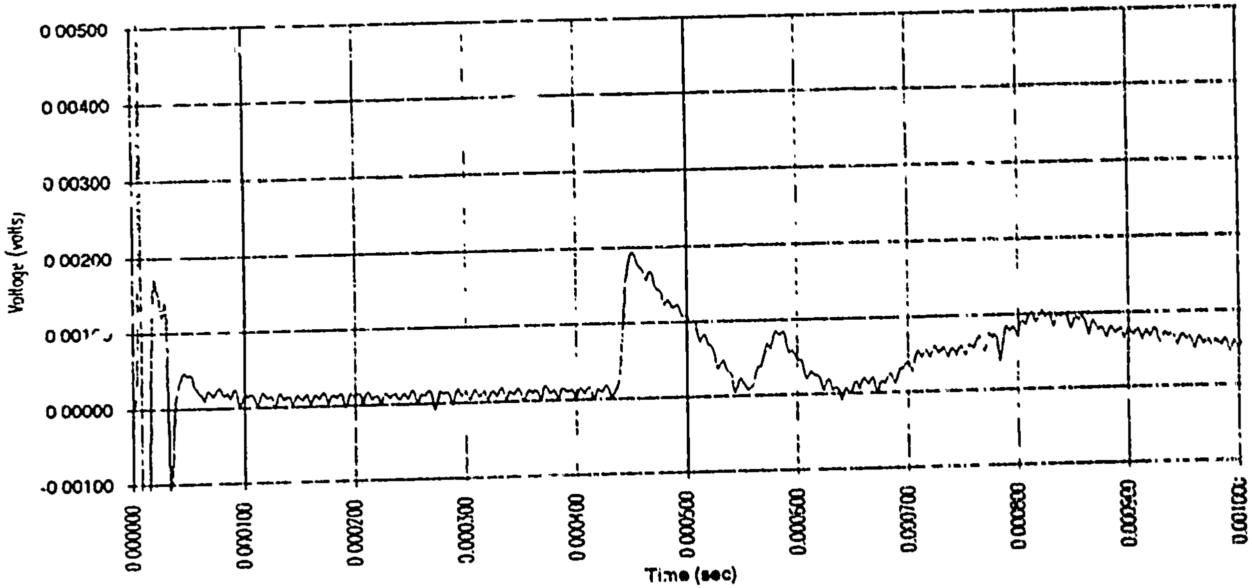


FIGURE 6A

Test 70-3

MATERIAL C

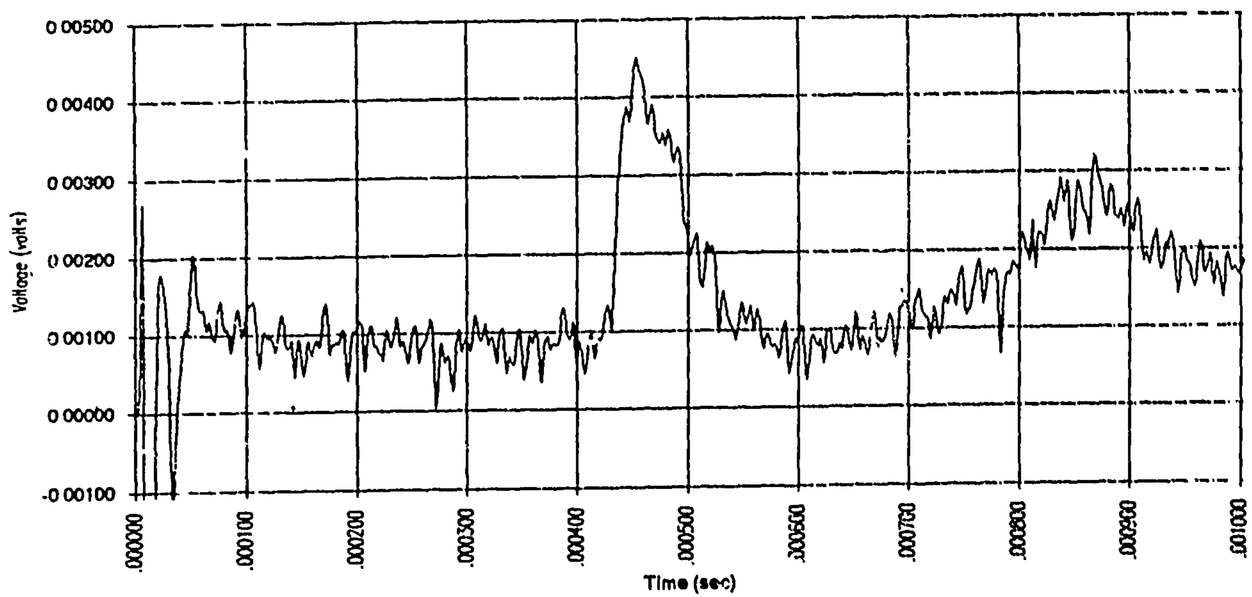


FIGURE 6B

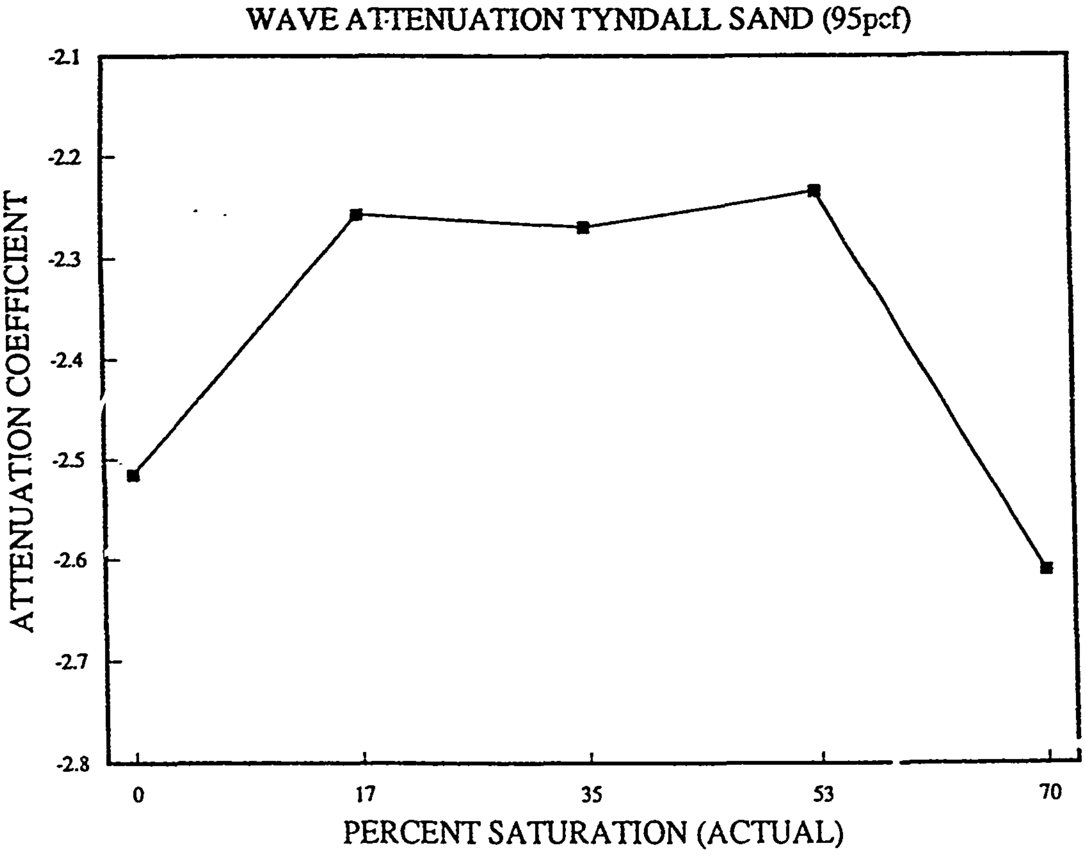


Plot prepared by Andy Walsh

FIGURE 7A

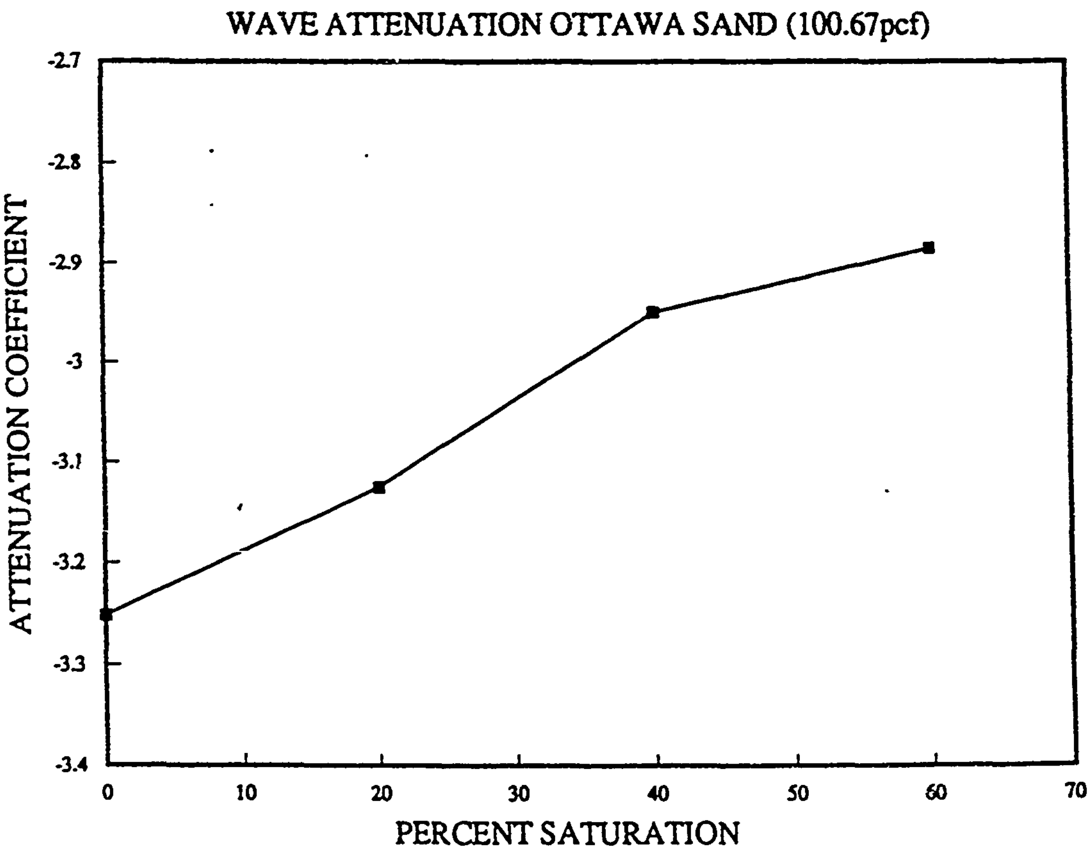


Plot prepared by Andy Walsh

FIGURE 7B

# ESTIMATION OF CONTAMINANT TRANSPORT PARAMETERS FROM LABORATORY STUDIES: BATCH AND COLUMN TECHNIQUES WITH SORBING ORGANIC SOLUTES

William P. Ball
Assistant Professor
Dept. of Civil and Environmental Engineering
Duke University
Durham, NC 27706

Dirk F. Young
Graduate Student
Dept. of Civil and Environmental Engineering
Duke University
Durham, NC 27706

## ABSTRACT

Batch and column experiments were performed with halogenated organic solutes and sandy aquifer solids. Column results were analyzed with two solute transport models that incorporated nonequilibrium sorption as a) first-order mass transfer and b) Fickian spherical diffusion. The diffusion model was able to predict the column results using input parameters from prior independent batch tests. On the other hand, the first-order model required 3 to 4 parameters to be varied for good simulation, and fitted parameters were often not in good agreement with the batch results.

## INTRODUCTION

Laboratory batch and column experiments are frequently used to predict pollutant transport at the field scale. Batch experiments are able to isolate fundamental grain-scale processes, but are unable to asses flow-dependent processes. Columns can better replicate flow-dependent processes and will provide some measure of the effects of heterogeneity on transport.

However, with columns, isolation of grain-scale properties is more difficult. Comparison of these two laboratory processes using the same sorbent material and solutes may provide useful insight into the most appropriate means of establishing the correct input parameters for groundwater models. Such comparison was a major motivation for the research described here. More specific objectives of this research follow:

1. Determine the extent to which contaminant fate parameters (sorption equilibrium and rate) measured in batch experiments can predict behavior in a flowing column.
2. Determine the extent to which appropriate transport parameters can be "backed out" by model fitting of column experiments.
3. Long-term goal: Determine which types of experiment are most useful in field-scale modeling efforts.

## BACKGROUND

**Solute Transport With Sorption.**

The transport equation for one-dimensional flow and linear equilibrium between the sorbed and aqueous phase can be expressed as follows:

$$R\, dC/dt = D\, d^2C/dx^2 - v\, dC/dx \tag{1a}$$

$$R = (1 + pK_d/\theta) \tag{1b}$$

where $R$ = retardation factor, [--]
$C$ = solute concentration in aqueous phase, [$kg/m^3$]
$D$ = dispersion coefficient [$m^2/s$]
$t$ = time, [s]
$x$ = position, [m]
$p$ = bulk density of solids, [$kg/m^3$]
$K_d$ = partitioning coefficient, [$m^3/kg$]
$\theta$ = porosity, [--]
$v$ = velocity, [m/s]

Recent work has suggested that sorption and desorption can be slow processes, thus putting the equilibrium assumption into question. For example, batch work on Borden aquifer solid by Ball and Roberts (1991a,b) showed that equilibrium may require months to years to be attained. In such cases, modeling solute transport with the local equilibrium assumption would be invalid, and a transport model which includes mass transfer should be used.

**Modeling Transport and Mass Transfer.**

Current models which account for mass transfer assume the existence of two regions--a mobile and an immobile region. Convection and dispersion are assumed to occur only in the mobile region, whereas transport into the immobile region is by diffusion only. Sorption sites are distributed throughout the mobile and immobile regions (though not necessarily evenly), with sites in the mobile region being at equilibrium with the mobile water. The governing equation for this model follows (Goltz and Roberts, 1986):

$$R_m\theta_m \, dC_m/dt = \theta_m D_m \, d^2C_m/dx^2 - \theta_m v_m \, dC_m/dx - \theta_{im} R_{im} \, dC_{im}/dt \tag{2a}$$

$$R_m = 1 + \frac{fpK_d}{\theta_m} \tag{2b}$$

$$R_{im} = 1 + \frac{(1-f)pK_d}{\theta_{im}} \tag{2c}$$

where

$C_i$, $C_{im}$ = average concentrations in mobile and immobile zones, [kg/m$^3$]

$\theta_m$ , $\theta_{im}$ = pore volumes of mobile and immobile water, ($\theta_m+\theta_{im} = \theta$)

f = fraction of sites in direct contact with mobile water

$D_m$ = dispersion coefficient for the mobile zone, [m$^2$/s]

The last term in Equation 2a represents the mass transfer into the immobile region and has been accounted for in several ways. The two most common models are a first-order model which uses an empirical first-order mass transfer coefficient and a mechanistic model which assumes Fickian diffusion.

**First-order model.** The first-order model assumes that rate of solute mass transfer is a linear function of the concentration difference between the mobile and immobile regions, and thus uses a first-order mass transfer coefficient to approximate solute mass transfer. Since concentration gradients are assumed to be nonexistent in the immobile region, an average immobile concentration is used. Under these conditions, the last term in Equation 2a, which represents mass transfer to the immobile region, would be replaced with the following:

$$\theta_{im} R_{im}\, dC_{im}/dt = \alpha(C_m - C_{im}) \tag{3}$$

where $\alpha$ = first-order rate constant, $[s^{-1}]$.

As shown by Parker and van Genuchten (1984), the two-region model is mathematically equivalent to a two-site model in which all sorption sites are in contact with mobile water, but a fraction of these sites are kinetically limited. In this conceptualization, $S_1$ and $S_2$ are the sorbed-phase concentrations [kg/kg] in the equilibrium and rate-limited region, respectively, and F is the fraction of sites in the equilibrium region. The sorption rate equations for each type of site follow:

$$dS_1/dt = FK_d dC/dt \tag{4}$$

$$dS_2/dt = \alpha[(1-F)K_d C - S_2] \tag{5}$$

Under these conditions, the transport equation becomes

$$\left(1 + \frac{FpK_d}{\theta}\right) dC/dt + \frac{\alpha p}{\theta}\,[(1-F)K_d C - S_2] \tag{6}$$

This equation can be represented in nondimensional terms as follows (Parker and van Genuchten 1984):

$$ßR\ dC^*/dT = 1/Pe\ d^2C^*/dz^2 + (1-ß)R\ dS/dT \tag{7a}$$

$$(1-ß)R\ dS/dT = w(C^*-S) \tag{7b}$$

where

| | |
|---|---|
| $T = vt/L$ | Pore Volumes Fed |
| $z = x/L$ | Dimensionless Length |
| $Pe = vL/D$ | Peclet Number |
| $ß = \dfrac{\theta + FpK_d}{\theta + pK_d}$ | Fraction of retardation due to instantaneous equilibrium |
| $w = \alpha(1-ß)RL/v$ | Dimensionless Rate Constant |
| $S = S_2/[(1-F)K_dC_o]$ | Dimensionless sorbed concentration in the rate-limited region |
| $C^* = C/C_o$ | Dimensionless Concentration |

Parker and van Genuchten (1984) and van Genuchten (1980) developed a computer program (CXTFIT) which employs such a first-order model and fits transport models to experimental data. In the research described subsequently, CXTFIT is used to interpret column breakthrough curves generated in the laboratory.

**Diffusion model.** The diffusion model assumes that the regions of immobile water are spherical, and solute mass transfer into these spherical zones occurs by Fickian diffusion, with the concentration at the outer radius of the immobile water equal to the concentration of the mobile water. Such a model may be applicable, for example, to intraparticle diffusion in sand grains, as assumed by Ball and Roberts (1991a,b). The immobile region concentration is described as follows (Rao et al., 1980):

$$C_{im}(x,t) = 3/a^3 \int_0^a r^2 C_{im}(x,r,t)dr \tag{8a}$$

$$C_{im}(x,a,t) = C_m(x,t) \tag{8b}$$

$$R_{im} dC_{im}/dt = D_e/r^2 \, d(r^2 \, dC_{im}/dr) \tag{8c}$$

where

$C_{im}(x,r,t)$ = concentration at position r within each sphere, [kg/m$^3$]

$D_e$ = the effective diffusion coefficient within the immobile zone, [m$^2$/s]

r = radial coordinate within sphere, [m]

a = radius of sphere, [m]

Combining the above equations with the transport equation (Equation 2) gives the diffusion model as described by Goltz and Roberts (1986), Rao et al. (1980), and Nkedi-Kizza et al. (1982). A solute transport code incorporating this model, identical to that used by Goltz (1986), was used in this research to predict column behavior for the Borden 40-60 material, using diffusion rate parameters previously published by Ball and Roberts (1991b).

## BATCH EXPERIMENTS

**Sorbents and Solutes.**

The aquifer materials used in these experiments were a 40-60 mesh size fraction of Borden aquifer material from the same batch of material as that used several years prior by Ball and Roberts (1991a,b) and bulk Borden material from the same batch as that used by Burris and Goltz (1991). Both pulverized (<200 mesh) and unpulverized samples of both materials were used. Pulverization was accomplished with a mortar and pestal.

Solutes used were 1,2,4-trichlorobenzene (TCB) and tetrachloroethene

(PCE). Unlabeled TCB was HPLC grade from Fisher Scientific Co. (Fairlawn, NJ). Radio-labeled TCB came from Sigma Chemical Co. (St. Louis, MO). Unlabeled PCE was Ultrapure grade from Alfa Products (Danvers, MA). Radio-labeled PCE came from Dupont Biomedical Products Dept. (Boston, MA).

**Methods.**

Aquifer material (Borden 40-60 or Box material) was added to flame-sealable ampules, and the quantity was determined gravimetrically. A solution comprising de-ionized water, 0.005M $CaSO_4$, and 0.02% $NaN_3$ was added to the ampules to a level so as to minimize headspace; the exact amount was determined gravimetrically. Each ampule was spiked with the appropriate radio-labeled compound (TCB or PCE) and immediately flame sealed. Sealed ampules were rotated at 5 rpm in a temperature-controlled chamber until they were ready to be analyzed. Quantitative analysis was performed by a scintillation counter. Losses to headspace were accounted for by the use of blanks (ampules without solids).

**Results for Box Material with TCB.**

The isotherm for TCB on pulverized Borden box material equilibrated for 7 days is shown in Figure 1. The figure presents both a Freundlich isotherm and a linear isotherm fit to the experimental data. The Freundlich and linear fit parameters are summarized in Table 1. The linear fit coefficient ($K_d$) was obtained by averaging the $K_d$s from all the data with $C_e$ < 1000 ug/l. As Figure 1 shows, the data are quite nonlinear ($1/n = 0.81$), but are fit well by the Freundlich isotherm. The differences can be seen more dramatically in Figure 2, where the data are shown on a linear plot. Here the low concentration linear fit can be seen to diverge greatly from the data obtained at higher concentrations.

Figure 3 shows isotherms obtained from batch experiments for both pulverized and unpulverized Borden box material at various equilibration times as well as individual points obtained from column studies (discussed later), box studies (Burris, 1991), and batch rate studies (Burris, 1991). This graph shows that, as expected, sorption to unpulverized solids increases with time. It also indicates that if the ultimate $K_d$ for pulverized and unpulverized material is the same, as shown by Ball and Roberts (1991b) using a different solute and different Borden aquifer material, then equilibrium with TCB and unpulverized material still has not been obtained after 46 days. This figure also shows that the uptake capacity as determined from Box experiments (Burris, 1991) tend to be much lower than the capacities determined by batch methods. Long-term (4 to 6 week) column-derived $K_d$s were greater than batch-derived $K_d$s using unpulverized material, but were still lower than the $K_d$s derived from the pulverized material.

**Results for Borden 40-60 with PCE.**

Figure 4 shows the isotherms for both pulverized and unpulverized Borden 40-60 equilibrated with PCE and fitted with both linear and Freundlich fits. This graph reveals the data to be fairly linear, and thus use of a linear model is justified. (Freundlich and linear fit parameters are summarized in Table 1.)

The average linear $K_d$ for the unpulverized material was found to be 0.35 ml/g which differs greatly from the value determined by Ball and Roberts (1991), who determined the $K_d$ to be 1.2 ml/g. The Borden 40-60 aquifer material used in this study, although from the same batch as that used by Ball and Roberts (1991a), had been exposed to the atmosphere about

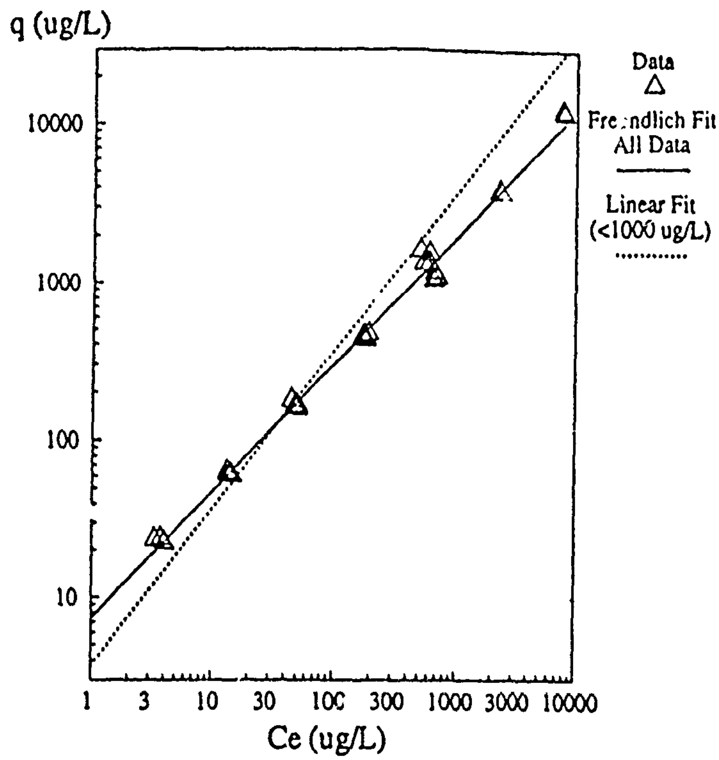


Figure 1. Isotherms (log-log scale) for pulverized Borden box material equilibrated for 7 days with TCB.

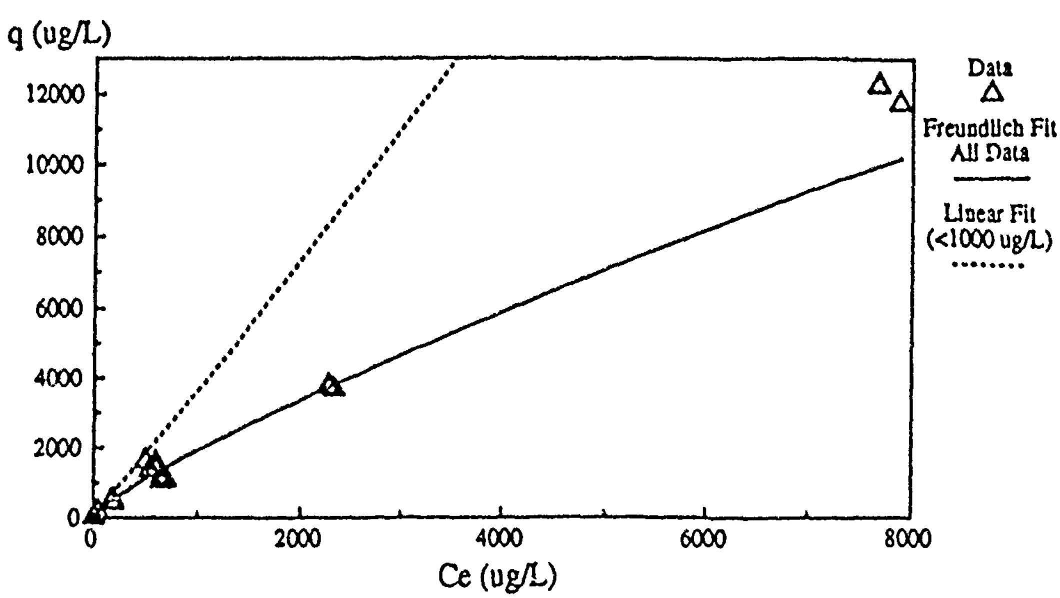


Figure 2. Isotherms (linear scale) for pulverized Borden box material equilibrated for 7 days with TCB.

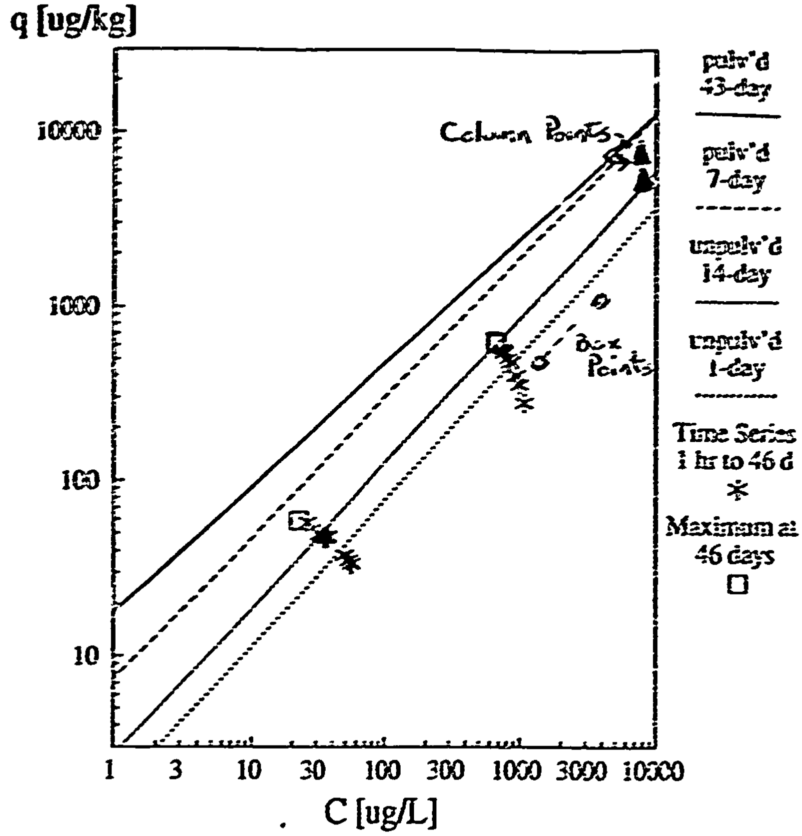


Figure 3. Isotherms for pulverized and unpulverized Borden box material equilibrated with TCB for various times. Data points not shown for clarity. "Column point" was determined from column experiment. "Box points" were determined from box experiment.

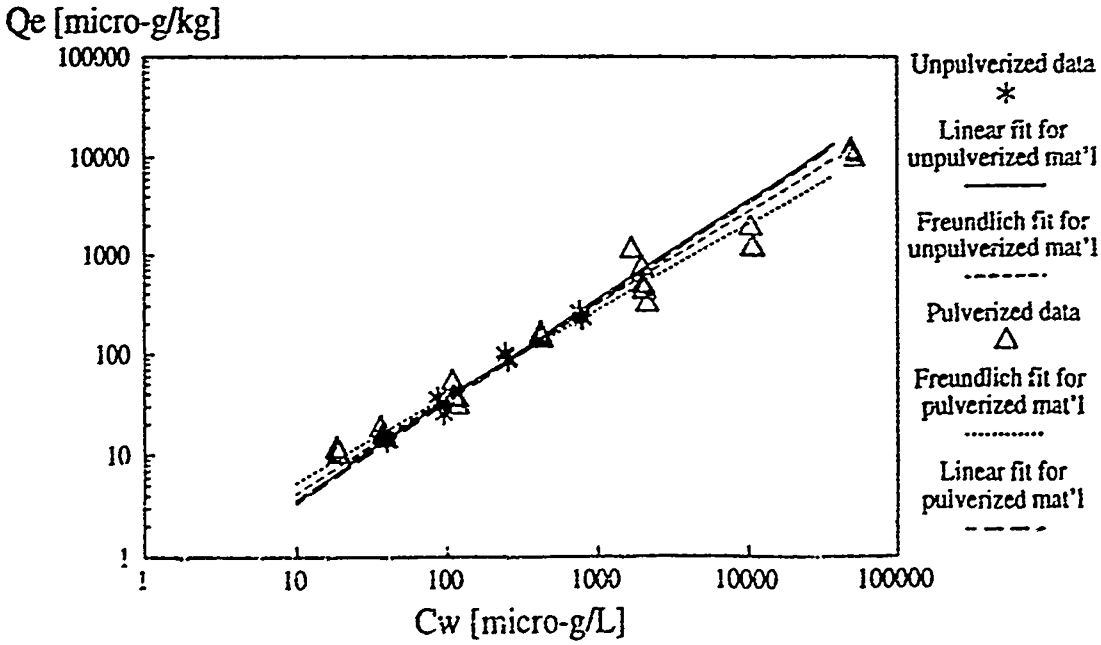


Figure 4. Freundlich and linear isotherms for Borden 40-60 equilibrated with PCE.

Table 1. Summary of the linear and Freundlich parameters as determined from batch experiments.

| Material | Compound | Equilibration Time (days) | Linear $K_d$ (ml/g) | $K_f$* | 1/n |
|---|---|---|---|---|---|
| Borden 40-60 | PCE | 28 | 0.359 | 0.476 | 0.941 |
| Pulverized Borden 40-60 | PCE | 6 | 0.333 | 0.723 | 0.863 |
| Pulverized Borden box | TCB | 7 | 2.94 | 7.35 | 0.806 |
| Pulverized Borden box | TCB | 43 | 5.92 | 17.9 | 0.713 |

* C in ug/l, S in ug/kg

three years longer and may have been altered, perhaps by oxidation of the organic matter. Also, some contamination was present in the radio-labeled PCE; however, even in the extreme case (if the contaminants were completely non-sorbing), the contamination could only count for part of the observed difference.

## COLUMN EXPERIMENTS

### Sorbents and Solutes.

Sorbents used for column experiments were the same as those used in the batch studies. As before, Borden box material was used with TCB as the sorbing solute, while Borden 40-60 was studied using PCE. In addition to the sorbing solutes, tritiated water was used as a conservative tracer for the column work.

### Methods.

The aquifer material was packed into stainless steel columns (2.1 cm ID, 25 cm long). To insure complete saturation, packed columns were purged with bone-dry $CO_2$, slowly filled with degassed working solution (DI water, 0.05M $CaSO_4$, 0.02% $NaN_3$), and allowed to equilibrate by continuing to feed the working solution until the column weight stabilized (2 to 4 days).

A syringe pump (Isco LC 5000, Lincoln, NE) drove flow through the column at fixed flow rates. Solute was pulsed with the use of a 6-port switching valve. Sample fractions were collected with a robotic fraction collector (Gilson 212B, Middleton WI) and analyzed by scintillation counting. Four column experiments were run; the conditions are shown in Table 2.

Table 2. Summary of column experiment conditions

| Column Run No. | Solute | Flow Rate (ml/hr) | Column Porosity (ml/ml) | Velocity[b] (cm/hr) | Pulse Duration (days) | $D_H$[c] ($cm^2$/hr) |
|---|---|---|---|---|---|---|
| 1 | TCB | 4.0 | 0.394 | 2.68 | 3 | 0.15 |
| 2 | PCE | 40 | 0.341 | 30.9 | 0.25 | 0.032 |
| 3[d] | PCE | 40 | 0.341 | 30.9 | 0.25 | 0.032 |
| 4 | PCE | 3.9 | 0.341 | 2.98 | 2.5 | 0.0022 |

[a]Calculated from the empty column volume, the known mass of sand in the column, and the measured solid density of the sand.

[b]Calculated as $v=QL/\epsilon V$, where V=empty column volume, $\epsilon$=porosity, L=column length.

[c]Dispersivity as obtained from fitting model simulations to tritium data

[d]Column run 3 was identical to column run 2 and was used to demonstrate reproducability. Only run 3 data are presented through the remainder of this work.

Fitted parameters for the first-order model were obtained with the fitting program CXTFIT (Parker and van Genuchten, 1984), while a spherical diffusion model (Goltz and Roberts, 1986) was used solely in a predictive mode for runs 2, 3, and 4, using batch equilibrium parameters from this research and rate parameters from Ball and Roberts (1991b).

**Results for Box Material with TCB.**

Figures 5 through 7 show the TCB and tritium BTC data, along with several first-order fits, using the program CXTFIT. The tritium fit (Figure 5) was used to determine the dispersion coefficient for the TCB breakthrough. Figures 6 and 7 show that by fitting only 1 or 2 parameters, only very poor fits could be obtained. A three parameter fit comes much closer, but 4 parameters had to be varied in order to fully match the experimental data. Fitted parameters for all runs are given in Table 3.

Table 3. Fitting parameters for simulations in Figures 6 and 7.

| | v | R | D | ß | w |
|---|---|---|---|---|---|
| Figure 6: | | | | | |
| 3 par fit (D, ß, w) | 2.68 | 7.6 | 2.26 | 0.306 | 0.168 |
| 2 par fit (D, w) | 2.68 | 7.6 | 1.79 | 0.132 | 1.08 |
| 2 par fit (ß, w) | 2.68 | 7.6 | 0.143 | 0.275 | 0.287 |
| 1 par fit | 2.68 | 7.6 | 0.143 | 0.132 | 1.11 |
| Figure 7: | | | | | |
| 4 par fit (D, R, ß, w) | 2.68 | 3.1 | 1.19 | 0.689 | 0.461 |
| 3 par fit (R, ß, w) | 2.68 | 2.9 | 0.143 | 0.639 | 1.11 |
| 3 par fit (D, ß, w) | 2.68 | 7.6 | 2.26 | 0.306 | 0.168 |
| 2 par fit (ß, w) | 2.68 | 7.6 | 0.143 | 0.132 | 1.11 |

After breakthrough (3 days, 8 pore volumes), this column was stopped, and the ends were capped. Pore water samples were subsequently taken at 2, 4, and 6 weeks by eluting the column through the addition of one-fifth pore volume of clean solution at each time cited. At these time intervals, a mass balance was performed on the last one fifth of the column, and implied $K_d$s were determined. The results are shown in Table 4 (and in Figure 2). For the first four weeks, as time increased, the $K_d$s increased, which implies that the solids are continuing to uptake TCB, and that the column was not at

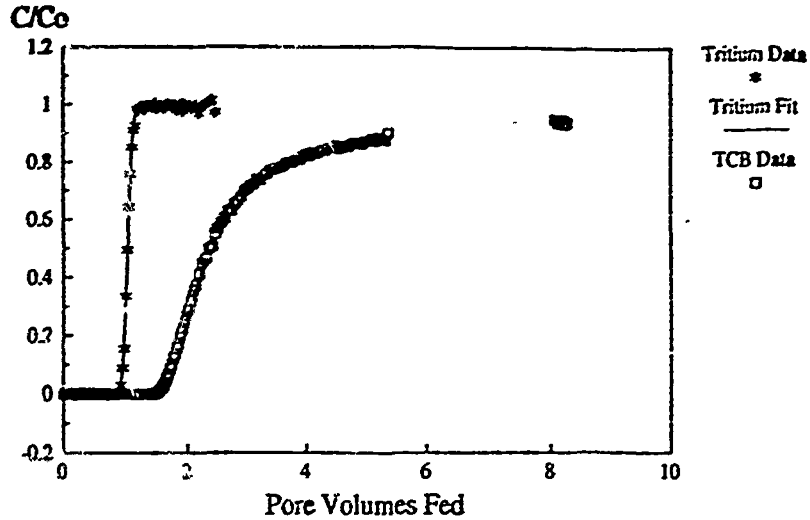


Figure 5. TCB and tritium with Borden box material (v = 3 cm/hr).

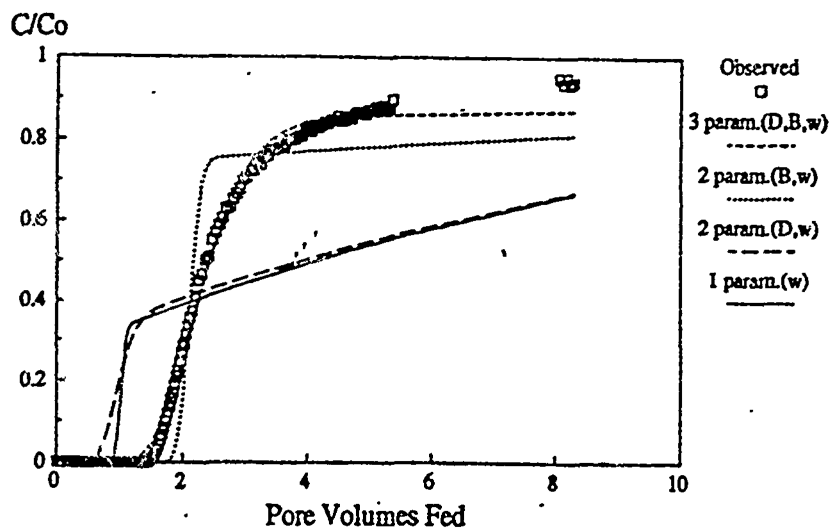


Figure 6. First-order fits for TCB and Borden box material (v = 3 cm/hr).

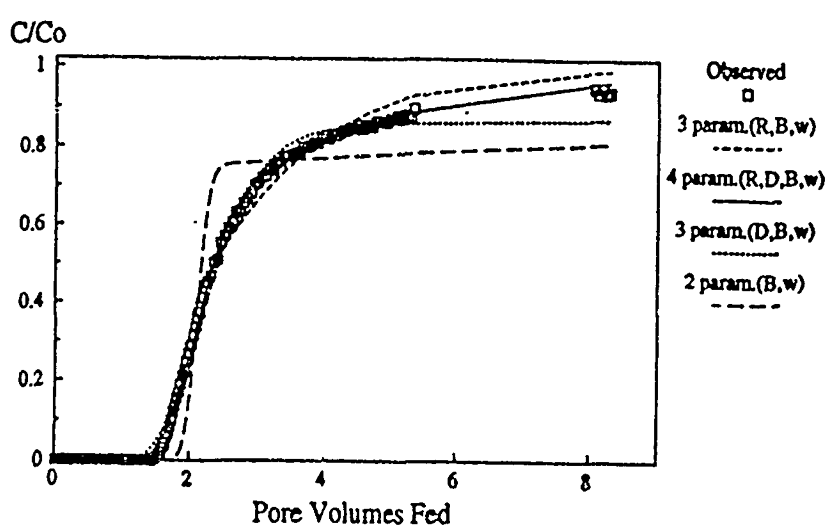


Figure 7. First-order fits for TCB and Borden box material (v = 3 cm/hr).

equilibrium. However, at the 6-week interval, the $K_d$ decreased, which may reflect the initially incomplete breakthrough, with higher aqueous concentrations near the inlet of the column. Note that the results should not be affected by TCB diffusing back toward the column clean water at the inlet, since this effect was minor for tritium (Table 4), and back diffusion of tritium should be much more rapid.

Table 4. TCB intermittent uptake by Borden box material.

| Time | Effluent Conc. (C/C$_o$) $^3H$ | $^{14}C$ | Implied $K_d$ (ml/g) |
|---|---|---|---|
| 3 days | 1.0 | 0.96 | 0.46 |
| 2 weeks | 0.95 | 0.81 | 0.84 |
| 4 weeks | 0.93 | 0.69 | 1.0 |
| 6 weeks | 0.90 | 0.76 | 0.91 |

**Results for Borden 40-60 with PCE.**

Figure 8 shows the PCE and tritium breakthrough data for the column run with a pore water velocity of 2.98 cm/hr. Also shown is the tritium fit (CXTFIT), from which the dispersion coefficient (D) was determined.

With the batch data from this research, two predictions of column breakthrough were made using the spherical diffusion model--one using the batch data from this work and one using the batch data from Ball and Roberts (1991a). Both predictions used rate data from Ball and Roberts (1991b). As shown by Figure 9, the prediction using the batch data from this experiment ($K_d$ = 0.35) exhibits excellent agreement with the column data, whereas the prediction using the data of Ball and Roberts (1991a) ($K_d$ = 1.2) does not. Thus, the column data appear to reflect the equilibrium uptake exhibited in the current batch work. Possible reasons for the discrepancy with the results of Ball and Roberts (1991a) have been previously discussed.

Fits using the first-order model are shown in Figure 10, and parameter values are given in Table 5. For the two parameter fit (ß and w varied), the fitted w is within 33 percent of that implied by $D/a^2$ determined by Ball and Roberts ($D/a^2$=0.026 $s^{-1}$, w=22.5$D/a^2$ = 0.59), but the model did not fit the data very well. A better fit was obtained by allowing R to vary, as the 3-parameter fit shows. To obtain an excellent fit, however, four parameters (B, w, R, D) had to be allowed to vary.

Figure 11 shows the data for the high velocity column (30.9 cm/hr) along with the diffusion model prediction using the batch equilibrium data from this work. As the figure shows, the diffusion model prediction is again in generally good agreement with the data.

The first-order model simulations of the high velocity column using 2- and 3-parameter fits are shown in Figure 12. The first-order fits all required that w be much higher than the value determined by Ball and Roberts (1991b), from which w was estimated to be 0.056. The 2-parameter fit also was not in good agreement with the data, but a reasonable fit was obtained by also allowing R to vary (3-parameter fit); however, the value of w is then off by an order of magnitude. Also shown in Figure 12 is a prediction using the first-order model and parameters derived from the low velocity column. The prediction from the low velocity data, which used w = 0.79, also gives a poor fit. These results suggest that for high velocity experiments differences of breakthrough shape with diffusion and first-order models are sufficiently severe to make the first-order models act as poor means of estimating diffusion-based rate constants.

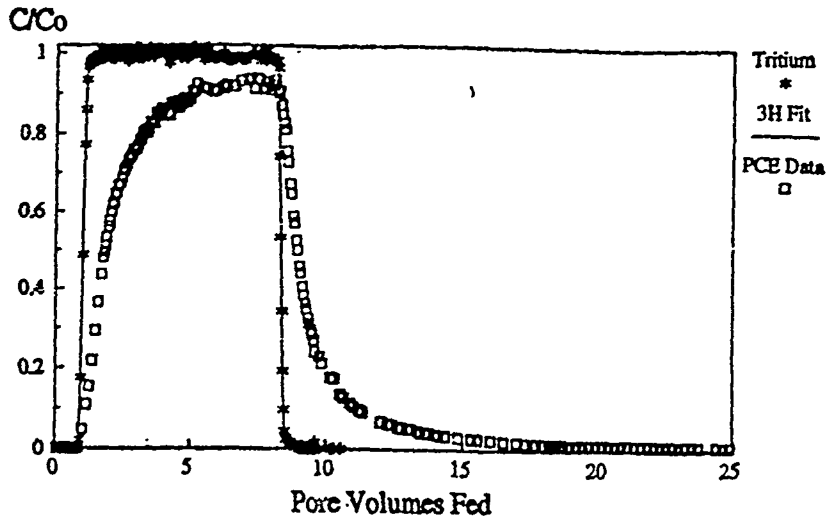


Figure 8. PCE and tritium with Borden 40-60 (v = 3 cm/hr).

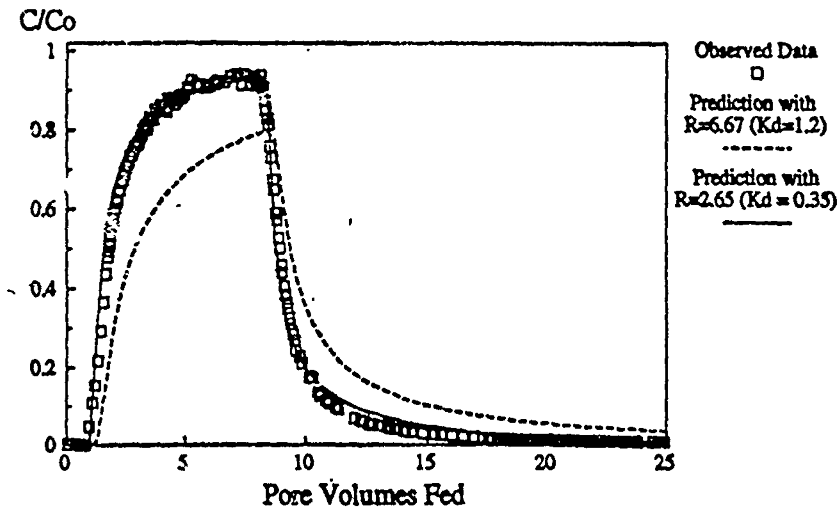


Figure 9. Diffusion model predictions for PCE and Borden 40-60 (v = 3 cm/hr)

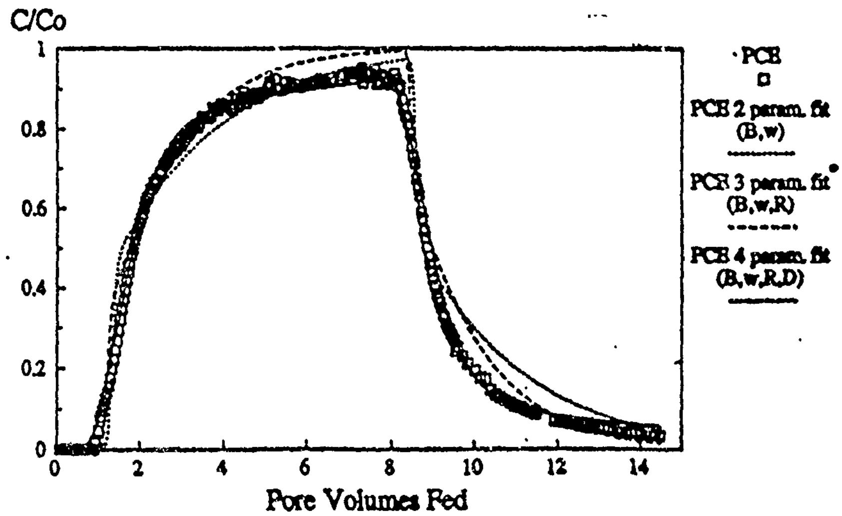


Figure 10. First-order fits for PCE and Borden 40-60 (v = 3 cm/hr)

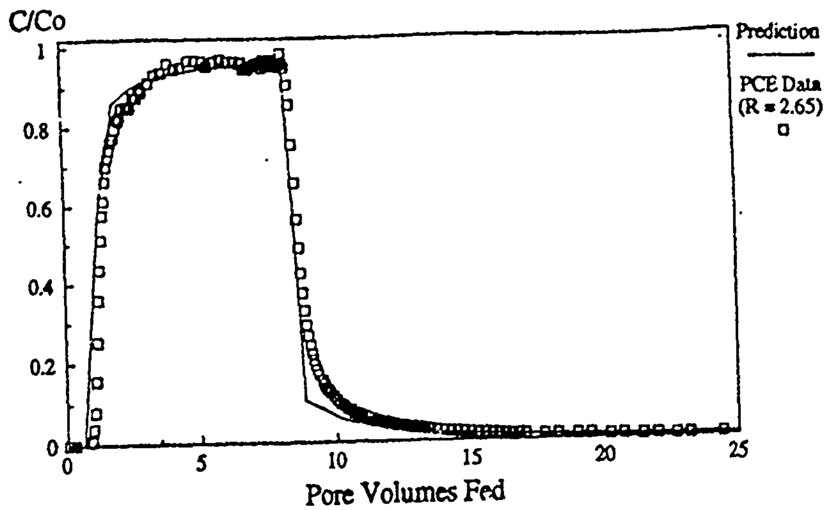


Figure 11. Diffusion model prediction for PCE and Borden 40-60 (v = 30.9 cm/hr).

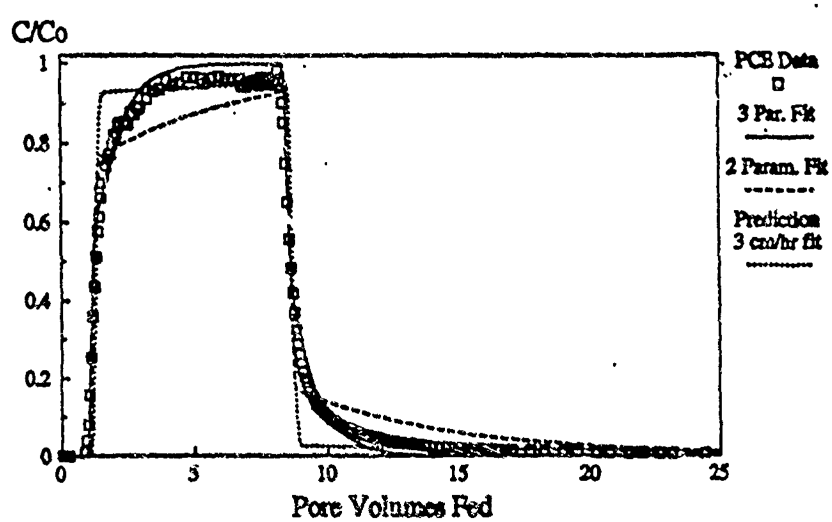


Figure 12. First-order fits for PCE and Borden 40-60 (v = 30.9 cm/hr).

Table 5. Fitting parameters for simulations in Figures 10 and 12.

| | v | R | D | ß | w |
|---|---|---|---|---|---|
| Figure 10: | | | | | |
| 4 par fit (ß, w, R, D) | 0.0496 | 3.0 | 0.0932 | 0.591 | 0.202 |
| 3 par fit (R, ß, w) | 0.0496 | 2.3 | 0.00218 | 0.520 | 1.13 |
| 2 par fit (ß, w) | 0.0496 | 2.7 | 0.00218 | 0.502 | 0.787 |
| Figure 12: | | | | | |
| Prediction from col4 | 0.515 | 2.65 | 0.229 | 0.506 | 0.79 |
| 3 par fit (R, ß, w) | 0.515 | 1.56 | 0.229 | 0.724 | 0.772 |
| 3 par fit (D, ß, w) | 0.515 | 2.65 | 0.229 | 0.474 | 0.251 |

## CONCLUSIONS

From this study the following conclusions were drawn:

- The Borden box material exhibits very slow uptake of TCB. At least four weeks is required to attain equilibrium, and batch studies with pulverized material suggest that an even longer equilibration time may be required.
- The diffusion model describes the breakthrough data quite well for Borden 40-60 with PCE, and batch-based rate and equilibrium data served as good predictors of column results.
- The first-order fit was sufficiently inappropriate as to lead to misestimation of the sorption rate coefficient w, especially at higher velocities.
- The simultaneous fitting of ß and R gives better data matches but is physically meaningless and leads to greater error in the estimation of w.

## ACKNOWLEDGEMENTS

This work was conducted in the laboratories of the Environics Division of the Engineering and Services Center, Tyndall AFB, FL as part of a 10-week summer research program. Dr. Thomas Stauffer was the focal contact for the research. Dr. David Burris provided valuable assistance with the

experimental aspects, and Dr. Kirk Hatfield (University of Florida) assisted with the application of the CXTFIT computer program. We would like to thank Dr. Stauffer and his staff for their considerable efforts toward making our visit enjoyable and productive.

## REFERENCES


Ball, W. P., and P. V. Roberts, 1991a. "Long-Term Sorption of Halogenated Organic Chemicals -- Part 1. Equilibrium Studies", Environ. Sci. Technol. 25(7), 1223-1237.

Ball, W. P., and P. V. Roberts, 1991b. "Long-Term Sorption of Halogenated Organic Chemicals -- Part 2. Rate Studies", Environ. Sci. Technol. 25(7), 1237-1249.

Burris, D.B., 1991. Personal communication, Air Force Engineering and Services Center, Tyndall Air Force Base, Panama City, FL.

Burris, D.B. and Goltz, M.N., 1991. "Use of a Physical Box Model to Examine the Role or Rate-Limited Sorption on Aquifer Remediation" AGU-MSA 1991 Spring Meeting, Baltimore, MD., American Geophysical Union and the Mineralogical Society of America.

Goltz, M.N. 1986. "Three-Dimensional Analytical Modeling of Diffusion-Limited Solute Transport", Ph.D. Dissertation, Stanford University, Stanford CA, 172pp.

Goltz, M.N. and Roberts P.V., 1986. "Interpreting Organic Solute Transport Data from a Field Experiment Using Physical Nonequilibrium Models", J. Contaminant Hydrology, 1(1), 77-93.

Nkedi-Kizza, P, Rao, P.S.C., Jessup, R.E., and Davidson, J.M., 1982. "Ion Exchange and Diffusive Mass Transfer during Miscible Displacement Through an Aggregated Oxisol" Soil Sci. Soc. Am. J., 46, 471-476.

Parker, J.C. and van Genuchten, M. Th., 1984. "Determining Transport Parameters from Laboratory and Field Tracer Experiments", Bulletin 84-3, Virginia Ag. Exp. Stn., Virginia Polytechnic Institute and State University, Blacksburg, VA.

van Genuchten, 1980. "Determining Transport Parameters from Solute Displacement Experiments" Research Report No. 118, U.S. Salinity Lab., Riverside, CA.

Rao, P.S.C., Ralston, D.E., Jessup, R.E. and Davidson, J.M., 1980 "Solute Transport in Aggregated Porous Media: Theoretical and Experimental Evaluation" Soil Sci. Soc. Am. J. 44, 1139-1146.